Selective laser melting of glass-forming alloys

Von der Fakultät Maschinenwesen der Technischen Universität Dresden
zur Erlangung des akademischen Grades
Doktoringenieur (Dr. -Ing.)
angenommene

DISSERTATION

von
Master of Engineering
Liang Deng
geboren am 05.05.1989 in Harbin, Heilongjiang Province, China

TECHNISCHE UNIVERSITÄT DRESDEN

Leibniz-Institut für Festkörper- und Werkstoffforschung Dresden

Tag der Einreichung: 26.02.2020

Tag der Verteidigung: 29.07.2020

1. Gutachter: Prof. Dr.-Ing. Martina Zimmermann

2. Gutachter: Prof. Dr.-Ing. habil. Christoph Leyens

3. Gutachter: Prof. Dr. Xin Lin

Contents

Abstract

Bulk metallic glasses (BMGs) are known to have various advantageous chemical and physical properties. However, the condition of producing BMGs is critical. From a melt to congealing into a glass, the nucleation and growth of crystals has to be suppressed, which requires a fast removal of the heat. Such high cooling rates inevitably confine the casting dimensions (so-called critical casting thickness). To overcome this shortcoming, additive manufacturing proves to be an interesting method for fabricating metastable alloys, such as bulk metallic glasses.

Selective laser melting (SLM), one widely used additive manufacturing technique, is based on locally melting powder deposited on the powder bed layer by layer. During the SLM process, the interaction between laser beam and alloys is completed with a high energy density (10^5 - 10^7 W/cm^2) in very short duration (10^{-3} - 10^{-2} s), which results in a high cooling rate (10^3 - 10^8 K/s). Such high cooling rates favour vitrification and to date, various glass-forming alloys have been prepared. The approach to prepare bulk metallic glasses (BMGs) by SLM bears the indisputable advantage that the size of the additively manufactured glassy components can exceed the typical dimensions of cast bulk metallic glasses. Simultaneously, also delicate and complex geometries can be obtained, which are otherwise inaccessible to conventional melt quenching techniques. By using such advantages of SLM, $Ti_{47}Cu_{38}Zr_{7.5}Fe_{2.5}Sn_2Si_1Ag_2$ (at.%) and $Zr_{52.5}Cu_{17.9}Ni_{14.6}Al_{10}Ti_5$ (at.%) BMGs have been successfully fabricated via SLM in the current work. The SLM process yields material with very few and small defects (pores or cracks) while the conditions still have to render possible vitrification of the molten pool. This confines the processing window of the fully amorphous SLM samples. By additively manufacturing different BMG systems, it is revealed that the non-linear interrelation is differently pronounced for varied compositions. The only way to obtain glassy and dense products is optimizing all the process parameters. However, it is difficult to obtain fully dense sample (100%). The relative density of the additively manufactured BMGs can reach 98.5% (Archimedean method) in current work. The residual porosity acts as structural heterogeneities in the additively manufactured BMGs.

The structures of BMGs are sensitive to the thermal history, i.e. to the cooling rate and to the thermal treatment. During SLM process, the laser beam not only melts the topmost powder, but also the adjacent already solidified parts. Such complicated thermal history may lead to locally more/less relaxed structure of the additively manufactured BMGs. Thus, systematic and extensive calorimetric measurements and nanoindentation tests were carried out to detect these

structural heterogeneities. The relaxation enthalpies, which can reveal the free volume content and average atomic packing density in the additively manufactured BMGs are much higher than that in the as-cast samples, indicating an insufficient duration for structural relaxation. The nanoindentation tests indicate that the structure of additively manufactured BMG is more heterogeneous than that of as-cast sample. Nevertheless, no obvious heat-affected zone which corresponds to the more/less relaxed structure is visible in the hardness map. In order to reveal the origin of such heterogeneity, the thermal field of the additively manufactured BMGs was simulated via finite volume method (FVM). Owing to the different process parameters and varied thermophysical properties of $Ti_{47}Cu_{38}Zr_{7.5}Fe_{2.5}Sn_2Si_1Ag_2$ and $Zr_{52.5}Cu_{17.9}Ni_{14.6}Al_{10}Ti_5$ BMGs, the heat-affected zone (HAZ) is differently pronounced, resulting in the varied heterogeneities of both additively manufactured BMGs.

Afterwards, the physical and chemical properties of the additively manufactured BMGs were systematically studied. The additively manufactured BMGs tend to fail in a premature manner. The heterogeneities (defects, crystalline phases and relaxed/rejuvenated regions) can determine the mechanical and chemical properties of the BMGs. In the current work, the additively manufactured BMGs are fully amorphous. Thus, the effects of crystalline phases can be ruled out. The effect of residual porosity and more/less relaxed state on the deformation of additively manufactured and as-cast BMGs has been studied. The analysis of the observed serrations during compressive loading implies that the shear-band dynamics in the additively manufactured samples distinctly differ from those of the as-cast glass. This phenomenon appears to originate from the presence of uniformly dispersed spherical pores as well as from the more pronounced heterogeneity of the glass itself as revealed by instrumented indentation. Despite these heterogeneities, the shear bands are straight and form in the plane of maximum shear stress. Additive manufacturing, hence, might not only allow for producing large BMG samples with complex geometries but also to manipulate their deformation behaviour through tailoring porosity and microstructural heterogeneity. Different from the compressive tests, the heterogeneities of additively manufactured BMGs have no significant effect on the tribological and corrosion properties. The similar specific wear rate and the worn surfaces demonstrate that similar wear mechanisms are active in the additively manufactured and the as-cast samples. The same holds for the corrosion tests. The anodic polarization curves of SLM samples and as-cast samples illustrate a similar corrosion behaviour. However, the SLM samples have a slightly reduced susceptibility to pitting corrosion and reveal an improved surface healing ability, which might be attributed to an improved chemical homogeneity of the additively manufactured BMGs.

In order to improve plasticity, bulk metallic glasses composites (BMGCs) have been developed, in which crystals precipitate in a glassy matrix. The crystalline phases can alter the local stress state under loading, thereby, impacting the initiation and propagation of the shear bands. However, it is difficult to control the crystalline volume fraction as well as the size and spacing between the crystals by using the traditional melt-quenching method. One approach is to mix glass-forming powder with conventional alloy powder. In this way, a large degree of freedom for designing the microstructure can be gained. Thus, SLM was chosen to prepare such "ideal" BMGCs in the present work. The β-phase stabilizer Nb powder was mixed with $Zr_{52.5}Cu_{17.9}Ni_{14.6}Al_{10}Ti_5$ powder. After SLM processing, the irregular-shaped Nb particles are distributed uniformly within the glassy matrix and bond well to it. At the higher Nb content, diffusion of Nb during processing locally deteriorates the glass-forming ability of the matrix and results in the formation of several brittle intermetallic phases around the Nb particles. The size of these precipitates covers a wide range from nanometres to micrometres. Despite the fact that the soft Nb particles increase the heterogeneity of the glassy matrix, none of the samples deforms plastically. This is attributed to the network-like distribution of the intermetallic phases, which strongly affects the fracture process. Besides the *ex-situ* method of mixing powders, designing i*n-situ* ductile phases and controlling the fraction of the crystalline phases by altering process parameters can also prepare optimized BMGCs. $Cu_{46}Zr_{46}Al_8$ (at.%) was processed via SLM to produce *in-situ* BMGCs. It is revealed that the microstructure of the nearly fully dense additively manufactured BMGs is strongly affected by the energy input. By increasing the energy input, the amount of the crystalline phases was raised. By optimizing the energy input, the B2 CuZr phase was particularly deliberately introduced. Due to the residual porosity and brittle phases, no plasticity is visible in the additively manufactured samples. Generally, selective laser melting opens a gateway to design the microstructure of the BMG matrix composites.

Kurzfassung

Massive metallische Gläser (MMGs) haben zahlreiche vorteilhafte chemische und physikalische Eigenschaften. Ihre Herstellung ist jedoch äußerst herausfordernd, da während der Schmelzabschreckung, die heutzutage die konventionelle Standardmethode ist, die Keimbildung und das Wachstum von Kristallen kinetisch unterdrückt werden muss. Dabei muss die Wärmemenge der unterkühlten Schmelze sehr schnell entzogen werden. Dies kann nur durch das Aufbringen von hohen Abkühlraten erreicht werden, die aber die erreichbare Gußgeometrie (den sogenannten kritischen Gießdurchmesser) einschränken. Um diesen prozesstechnologischen Mangel zu überwinden, eignet sich die additive Fertigung als Methode zur Herstellung von metastablien Legierungenm wie den massiven metallischen Gläsern.

Selektives Laserstrahlschmelzen (engl. Selective Laser Melting (SLM)), ist eine weit verbreitete pulverbett-basierte additive Fertigungsmethode, bei der eine lokal begrenzte Pulvermenge geschmolzen wird, erstarrt und sich dabei mit einem bereits erstarrten Bereich vereinigt. Somit wird schichtweise ein Bauteil additiv heregstellt. Während des SLM-Prozesses interagiert der Laserstrahl mit dem metallischen Pulver und dabei herrschen hohe Energiedichten (10^5 - 10^7 W/cm^2) innerhalb sehr kurzer Zeitdauern (10^{-3} - 10^{-2} s) und anschließend sehr hoher Abkühlraten (10^3 - 10^8 K/s) vor. Bei solch hohen Abkühlraten wird die Glasbildung begünstigt, so dass bisher zahlreiche glasbildende Legierungen mittels SLM verarbeitet wurden. Diese Vorgehensweise massive metallische Gläser (MMGs) mittels SLM herzustellen, ist sehr vorteilhaft, da somit MMG-Komponenten mit Abmessungen jenseits des kritischen Gießdurchmessers der Legierung additiv gefertigt werden können. Diese Technologie ermöglicht es aber auch extrem dünne und geometrisch komplizierte MMGs zu fertigen, die mittels der konventionellen Schmelzabschreckungsmethode nicht herstellbar sind.

Im Rahmen dieser Arbeit wurden aus Folgenden Legierungen MMGs erfolgreich mittels SLM additiv gefertigt: $Ti_{47}Cu_{38}Zr_{7.5}Fe_{2.5}Sn_2Si_1Ag_2$ und $Zr_{52.5}Cu_{17.9}Ni_{14.6}Al_{10}Ti_5$. Der mittels SLM hergestellte Werkstoff weist wenige und kleine Defekte, wie beispielsweise Poren und Risse, auf und konnte für beide Legierungen vollständig amorph hergestellt werden. Es sollten nicht nur möglichst dichte, also fehlerfreie, sondern auch noch amorphe Werkstoffe hergestellt werden. Diese zusätzliche Anforderung schränckt das geeignete optimale Prozessfenster weiter ein. Durch die additive Fertigung von verschiedenen glassbildenden Legierungen wird gezeigt, dass die Dichte des erzeugten Werkstoffs und die Prozessparameter nicht linear miteinander zusammenhängen und dieser nicht-lineare Zusammenhang zudem für jede Legierung unterschiedlich ausgeprägt ist. Daher müssen alle Prozessparameter einzeln indentifiziert

werden, um dichte und amorphe Werkstoffe zu erhalten. Bisher konnte weltweit noch kein MMG mit 100%-iger Dichte additiv gefertigt werden. In dieser Arbeit wurden Bauteile mit einer relativen Dichte (Archimedesmethode) mit bis zu 98.5% hergestellt werden. Die mit SLM in den MMG-Werkstoff eingebrachte Porosität kann als strukturelle Heterogenität verstanden werden.

Das Gefüge von MMGs hängt stark von der thermischen Vorgeschichte ab, wie beispielsweise die effektive Abkühlrate und anschließende Wärmebehandlung. Während des SLM-Vorganges wird nicht nur die oberste Pulverschicht geschmolzen, sondern auch noch der daran angrenzende bereits erstarrte Werkstoff. Solch eine eher komplexe thermische Vorgeschichte könnte zu lokal mehr oder weniger relaxierten amorphen Struktur von additiv gefertigten MMGs führen. Daher wurden systematische und umfangreiche differenzkalorimetrische Messungen und Nanoindetierungsexperimente durchgeführt, die strukturellen Heterogenitäten nachzuweisen. Dabei wurden Relaxationsenthalpien, die den Gehalt an freiem Volumem, also den Anteil an weniger dicht gepackten amorphen Bereichen, qunatifizieren, von additiv gefertigten und Gußwerkstoffen, die als Refrenz dienen, bestimmt. Die mittels SLM gefertigten Werkstoffe zeigen deutlich höhere Relaxationsenthalpien auf. Dies ist auf die ebenfalls deutlich höheren Abkühlraten und die wenig ausgeprägte strukturelle Relaxation zurückzuführen. Die Nanoindentierungsversuche belegen, dass das Gefüge des additiv gefertigten MMGs dennoch heterogener als das der Gußreferenz ist. Trotzdem zeigen die Härtemappen keine Wärmeeinflusszone (engl. heat-affected zone (HAZ)) zugehörig zu den mehr oder weniger relaxierten Gefügebereichen. Um den Ursprung dieser strukturellen Heterogenitäten zu ergründen, wurde das Wärmefeld für die beiden Legierungen mittels finite Volumenmethode (engl. finite volume method (FVM)) simuliert. Bedingt durch die unterschiedlichen Prozessparameter und thermophysikalischen Eigenschaften beider glasbildenden Legierungen ($Ti_{47}Cu_{38}Zr_{7.5}Fe_{2.5}Sn_2Si_1Ag_2$ und $Zr_{52.5}Cu_{17.9}Ni_{14.6}Al_{10}Ti_5$), ist die HAZ unterschiedlich ausgeprägt, so dass die additiv hergestellten MMGs beider Legierungen unterschiedlich strukturelle Heterogenität aufweisen.

Anschließend wurden die physikalischen und chemischen Eigenschaften der additiv gefertigten MMGs, die vorzeitig versagen, systematisch untersucht. Dabei können die strukturellen Heterogenitäten (Defekte, kristalline Phasenberieche, mehr oder weniger relaxierte Bereiche) die mechanischen und chemischen Eigenschaften der MMGs beeinflussen. Da in dieser Arbeit vollständig amorphe MMGs additiv hergestellt wurden, können kristalline Bereiche als Einflußgrößen ausgeschlossen werden. Auswirkungen der Prosität und relaxierten Bereiche wurden untersucht. Eine nähere Analyse der Spannungs-Dehnungskurven und der

einzelen Spannungsabfällen während der plastischen Verformung, belegt, dass die Scherbanddynamik in den additiv gefertigten MMGs sich von denen der gegoßenen MMGs unterscheidet. Dieser Unterschied beruht auf dem Vorhandensein von gleichmäßig verteilten sphärischen Poren und von der ausgeprägteren strukturellen Heterogenität der additiv gefertigten MMGs wie Nanoindentierungsversuche belegen. Trotz des Vorhandenseins der Heterogenitäten, können gerade und nicht abgelenkte Scherbänder, die entlang der maximalen Schubaspannugsrichtung verlaufen, in plastisch verformten MMGs beobachtet werden. Strukturelle Heterogenitäten haben keinen bedeutsamen Einfluss auf die Verschleiß- und Korrosionseigenschaften von additiv gefertigten MMGs. Gleiche spezifische Verschleißraten und abgenutzte Oberflächen ziegen, dass gleiche Verschleißmechanismen in additiv gefertigten und gegoßenen MMGs aktiv sind. Die Korrosionsversuche belegen ebenso keine Unterschiede zwischen additiv gefertigten und gegoßenen MMGs. Die anodischen Polarizationskurven der SLM- und Gußproben belegen ein ähnliches Korrosionsverhalten. Nichtsdestotrotz, ziegen die SLM-Proben eine leicht geringere Neigung zur Ausbildung von Lochfraßkorrosion und lassen somit auf eine verbesserte Oberflächenheilung schließen, die wiederum auf chemisch homogenere additiv gefertigte MMGs schließen lässt.

Eine sehr effektive Weise die plastische Verformbarkeit von MMGs zu verbessern, ist das Einbringen von Kristallen in die amorphe Matrix, so dass massive metallische Glas-Matrix-Komposite (MMKs) entstehen. Unter Belastung werden durch die kristalline Phase lokale Spannungszustände verändert, die die Initiierung und Ausbreitung von Scherbändern beeinträchtigen. Um ein möglichst effektives Ergebnis zu erzielen, ist die exakte Einstellung des Volumenanteils und Größenverteilung der kristallinen Phase wichtig. Im konventionellen Schmelzabschreckungsverfahren ist dies nicht möglich. Die additive Fertigung bietet hierzu eine vielversprechende Alternative, in dem glasbildendes Pulver mit hochschmelzendem Pulver einer anderen Legierung bzw. Elements vermischt wird. Diese Vorgehensweise bietet einen hohen Freiheitsgrad das resultierende Gefüge einzustellen, da Volumenanteil und Partikelgrößenverteilung genau eingestellt werden können. Daher wurde SLM ausgewählt, um damit “ideale” MMKs in dieser Arbeit herzustellen. Als kristalline Phase wurde das *b*-stabilisierende Nb-Pulver asugewählt und mit glasbildenden $Zr_{52.5}Cu_{17.9}Ni_{14.6}Al_{10}Ti_5$-Pulver vermischt und mittels SLM prozessiert. Die irregulär geformten Nb-Partikel sind dabei gleichmäßig innerhalb der amorphen Matrix verteilt und gut mit ihr verbunden. Bei höherem Nb-Gehalt, diffundiert es während des SLM-Prozesses in die Matrix und senkt ihre Glasbildungsfähigkeit, was die Bildung von mehreren intermetallischen Phasen nach sich zieht, die um die Nb-Partikel angeordnet sind. Das Ausmaß der intermetallischen Phasen erstreckt

sich von mehreren Nano- bis Mikrometer. Daher ist das resultierende MMK spröde, obwohl die Nb-Partikel plastisch verformbar sind. Die intermetallischen Phasen sind innerhalb des MMK netzwerkartig angeordnet, so dass wenn Risse entstehen, diese sich leicht durch den gesamten Werkstoff ausbreiten können. Außer dieser *ex-situ*-Methode, die sich durch das Mischen des Ausgangspulver auszeichnet, können MMKs mittels SLM auch *in-situ* hergestellt werden. Dabei können duktile kristalline Phasen entstehen, deren Volumenanteil mittels veränderten Prozessparametern eingestellt werden kann, um optimierte MMKs herzustellen. Um dieses Konzept umzusetzen, wurde die $Cu_{46}Zr_{46}Al_8$ (at.%) glasbildende Legierung mittels SLM prozessiert, so dass *in-situ* MMKs hergestellt werden können. Es werden nahezu vollständig dichte Gefüge der *in-situ* MMKs erzeugt, wobei deren Einstellung sehr stark vom Energieeintrag bestimmt wird. Ein höherer Energieeintrag führt zu einem ebenso höheren Volumentanteil der kristallinen Phase. Durch eine Optimierung des Energieeintrages, kann die duktile B2 CuZr phase *in-situ* in die Matrix gezielt eingebracht werden. Das resultierende *in-situ* MMK ist jedoch spröde, aufgrund der vorhandenen Porosität. Obwohl noch Herausforderungen, insbesondere die Minimierung der Porosität, bewältigt werden müssen, zeigt diese Arbeit das SLM das Potenzial besitzt das Gefüge von MMKs maßzuschneidern.

Symbols and abbreviations

List of symbols

$\mathbf{A_c}$	the projected contact area of the indenter tip
$\boldsymbol{d}$	single track width (mm)
$\boldsymbol{d_{50}}$	median powder particle diameter (µm)
$\boldsymbol{D_P}$	diameter of powder particles (m)
$\boldsymbol{E}$	Young's modulus (GPa)
$\boldsymbol{E_V}$	volume energy density (J/mm^3)
$\boldsymbol{E_{corr}}$	corrosion potential (V)
$\boldsymbol{E_{pit}}$	pitting potential (V)
$\boldsymbol{E_R}$	repassivation potential (V)
$\boldsymbol{F}$	applied load in wear test (N)
$\boldsymbol{F_0}$	view factor in FVM simulation
$\boldsymbol{\Delta G}$	free energy
$\boldsymbol{H}$	Hardness (GPa)
$\boldsymbol{\Delta H_{crys}}$	crystallization enthalpy (J/g)
$\boldsymbol{\Delta H_{relax}}$	relaxation enthalpy (J/g)
$\boldsymbol{\Delta H_{mix}}$	mixing enthalpy (kJ/mol)
$\boldsymbol{h}$	hatch distance (mm)
$\boldsymbol{i_{corr}}$	corrosion current density (mA/cm^2)
$\boldsymbol{K_w}$	specific wear rate
$\boldsymbol{L}$	sliding distance (m)
$\boldsymbol{l}$	layer thickness (mm)
$\boldsymbol{m}$	Weibull modulus
$\boldsymbol{N(s)}$	statistical number of stress drop
$\boldsymbol{P}$	laser power (W)
$\boldsymbol{R_c}$	critical cooling rate (K/s)

s	normalized stress drop magnitude
s_c	cut-off stress drop
T_m	melting temperature (K)
T_g	glass-transition temperature (K)
T_x	crystallization temperature (K)
T_l	liquidus temperature (K)
T_P	temperature of powders (K)
ΔT_x	supercooled liquid region (K)
v	scanning velocity (mm/s)
ν	Poisson's ratio
V	loss volume (mm^3)
β	scaling exponent
κ_g	thermal conductivity of the ambient gas ($W\ m^{-1}\ K^{-1}$)
κ_s	thermal conductivity of the solid ($W\ m^{-1}\ K^{-1}$)
κ_r	radiative heat transfer among powder particles
τ	shear stress (Pa)
σ_e	Stefan-Boltzmann constant
$\rho(D)$	local particle density at distance D
ρ_0	average density of the system
Φ	overlapping rate

List of abbreviations

3D	three-dimensional
AM	additive manufacturing
ASTM	American Society for Testing and Materials
bcc	body-centred cubic
BMG	bulk metallic glass
BMGCs	bulk metallic glass matrix composites
BSE	back-scattered electron
CAD	computer aided design
CCT	continuous cooling transformation
COF	coefficients of friction
DSC	differential scanning calorimetry
DMLS	direct metal laser sintering
EBM	electron beam melting
EDS	energy-dispersive X-ray spectroscope
fcc	face-centred cubic
FEM	finite element modelling
FVM	finite volume method
GFA	glass-forming ability
HAZ	heat affected zone
HCRZ	high-cooling-rate zone
HRTEM	high-resolution TEM
IBA	inverse bremsstrahlung absorption
ICP-OES	inductively-coupled plasma-optical emission spectroscopy
LCRZ	low-cooling-rate zone
MD	molecular dynamics
OCP	open circuit potential
SAED	selected area electron diffraction

SCE	saturated calomel electrode
SE	secondary electron
SEM	scanning electron microscope
SHS	selective heat sintering
SLM	selective laser melting
SLS	selective laser sintering
SOC	self-organized criticality
STZ	shear transformation zone
TEM	transmission electron microscope
XRD	X-ray diffraction
μ-CT	micro-computed tomography

Aims and objectives

Over the past decades, bulk metallic glasses (BMGs) have attracted scientific attention because of their desirable properties, such as high yield strength, good toughness, relatively low Young's modulus, outstanding friction and corrosion resistance unmatched by most conventional alloys. Some BMG systems have found their way into industrial application. However, owing to the required high cooling rates, their critical casting thickness warranting amorphicity is limited as is their plastic deformability at room temperature. These aspects still constitute some of the major obstacles exacerbating their large-scale use to date. Selective laser melting (SLM) is a viable process technology to produce bulk metallic glass (BMG), since high cooling rates (10^3 -10^8) are effective. During the last few years, Fe-, Al-, and Zr-based BMGs have been successfully prepared via SLM. This relatively new fabrication method is capable of overcoming the geometrical limitations of BMG-components.

The advantageous physical properties of BMGs result in a high load-bearing capability and can reduce stress-shielding or the formation of wear debris, which is crucial when being used as implants. Due to their biocompatibility, Ti and its alloys have been already used in biomedical sector for decades and also additively manufactured components have been investigated for this field of application. Thus, it appears natural to study the fabrication of Ti-based BMGs via SLM. In the current work, $Ti_{47}Cu_{38}Zr_{7.5}Fe_{2.5}Sn_2Si_1Ag_2$ (at.%) was chosen to assess the suitability of Ti-based BMGs for selective laser melting and investigate the effect of the processing route on the density and microstructure.

As mentioned above, some BMG systems have been successfully produced via SLM. However, the new challenges arise inherent to the layer-by-layer synthesis, such as the heterogeneous structure of additively manufactured BMGs. Thereby, the extent of the structural heterogeneities can range from micro- to nanometres, represented by pores, crystals and amorphous regions with different atomic packing density. Such heterogeneities can play a decisive role on the mechanical properties. The reported additively manufactured BMGs trend to fail in a premature manner. The underlying mechanism is still unknown. Only when the performance of the bulk metallic glass is not adversely affected by additive manufacturing, can selective laser melting of glass-forming alloys be considered a viable route for the production of bulk metallic glasses on a larger scale, e.g. for commercial applications. Therefore, comprehensive characterization of bulk metallic glasses obtained by SLM combined with a direct comparison with as-cast material of the same composition is of paramount importance. $Zr_{52.5}Cu_{17.9}Ni_{14.6}Al_{10}Ti_5$ (at.%) was selected to systematically investigate the interrelation

between processing conditions and properties. This covers investigation of structural heterogeneity, deformation behaviour upon compressive loading and wear as well as corrosion properties. In addition, the extent of heterogeneity for $Ti_{47}Cu_{38}Zr_{7.5}Fe_{2.5}Sn_2Si_1Ag_2$ and $Zr_{52.5}Cu_{17.9}Ni_{14.6}Al_{10}Ti_5$ were compared to study the effect of the thermal history on the structure of BMGs.

Bulk metallic glasses composites (BMGCs) have been developed to enhance the mechanical properties. Yet, it is difficult to properly design the structure of BMGCs by using the traditional melt quenching method. Using SLM to process the powder mixtures becomes a choice to design a desired structure of BMGCs. Thus, two different blends of the $Zr_{52.5}Cu_{17.9}Ni_{14.6}Al_{10}Ti_5$ powder and the Nb powder were produced and the processes at the interface investigated with regard to the diffusion-dependent microstructural evolution. As-cast samples of both compositions were also prepared for comparison and the mechanical properties of all samples were determined and compared. The work aims at understanding the metallurgical processes during selective laser melting and at correlating them with the materials properties. Apart from adding the second phase to synthetize BMGCs, controlling the process parameters of SLM can also obtain BMGCs. Thus, a glass-forming $Cu_{46}Zr_{46}Al_8$ (at.%) powder was chosen to fabricate BMGCs containing B2 CuZr phase via SLM. The influence of process parameters on structural heterogeneities were systematically investigated to reveal the possibility of controlling the volume fraction of crystalline phase(s) and their distribution in the deliberately crystallized additively manufactured BMGCs.

CHAPTER 1 Metallic glasses and selective laser melting

In the past decades metallic glasses have been prepared via many different processing methods, such as vapor deposition [1], mechanical alloying [2], plasma processing [3], spray deposition [4] and rapid quenching of the melt [5]. Among these methods, rapid quenching of a melt is the most commonly applied [5]. In this chapter, the formation of the metallic glasses fabricated by quenching will be discussed first. Afterwards, the mechanical properties and the corrosion behaviour, as well as the underlying mechanisms of metallic glasses are addressed. Finally, a relatively recent approach for producing metallic glasses, selective laser melting, will be introduced.

1.1 Formation of metallic glasses from the melt

Metallic glasses can be generally formed by suppressing nucleation and growth of crystals during cooling of a melt [6-8]. Consequently, vitrification competes with the precipitation of crystals [6-9]. Fig. 1.1 schematically depicts the changes of given system properties (volume or entropy) as a function of temperature. As the liquid is cooled, its volume or entropy decreases continuously until reaching the melting point (T_m). Whether the melt crystallizes or is supercooled instead, then depends on the cooling rate and the alloy composition. As shown in Fig. 1.1, when crystallization (a first-order phase transformation [10, 11]) sets in, the volume of the system is reduced abruptly because of the high atomic packing density in the crystalline state. In the case crystallization is suppressed, the liquid becomes gradually supercooled and volume or entropy continue to be lowered steadily. On supercooling the viscosity of the system increases dramatically [7, 12] and atomic movements become more difficult and sluggish. Below a certain temperature, the glass-transition temperature, T_g, the supercooled liquid eventually “freezes” and transforms into the glassy state [7, 12]. This transition is of kinetic rather than thermodynamic nature [7, 12].

The so-called “free-volume” concept has been developed in order to explain the observed viscous behaviour at the glass transition [13-15]. Free volume is defined as part of the system volume, which can form voids without energy cost and, consequently, enables atomic movements [14]. When the temperature of the supercooled liquid decreases, structural relaxation usually annihilates free volume and increases the atomic packing density (Fig. 1.1). As shown in Fig. 1.1, the cooling rate has a strong effect on the transition from the supercooled liquid to the glass. With the decrease of the cooling rate, T_g occurs at lower temperatures ($T_{g.1}$, $T_{g.2}$). In other words, depending on the thermal history, the glass transition occurs within a

temperature range and there are several ways to determine the glass-transition temperature (T_g) [7, 12]. In order to avoid the intrinsic difficulties in determining T_g, the glass-transition temperature is defined as the temperature at which the system reaches a viscosity of 10^{12} Pa s [7, 12].

When the cooling rate is high leading to a higher T_g ($T_{g.2}$ in Fig. 1.1), the system traps more free volume. As shown in Fig. 1.1 (red dash line), when the BMGs are annealed, the free volume is annihilated. This structural relaxation can be detected by isochronal calorimetric measurements for example and reflects in the enthalpy of relaxation. The amount of free volume in the glass has an impact on the plasticity of metallic glasses. The underlying mechanism will be discussed in the section 1.2.2.

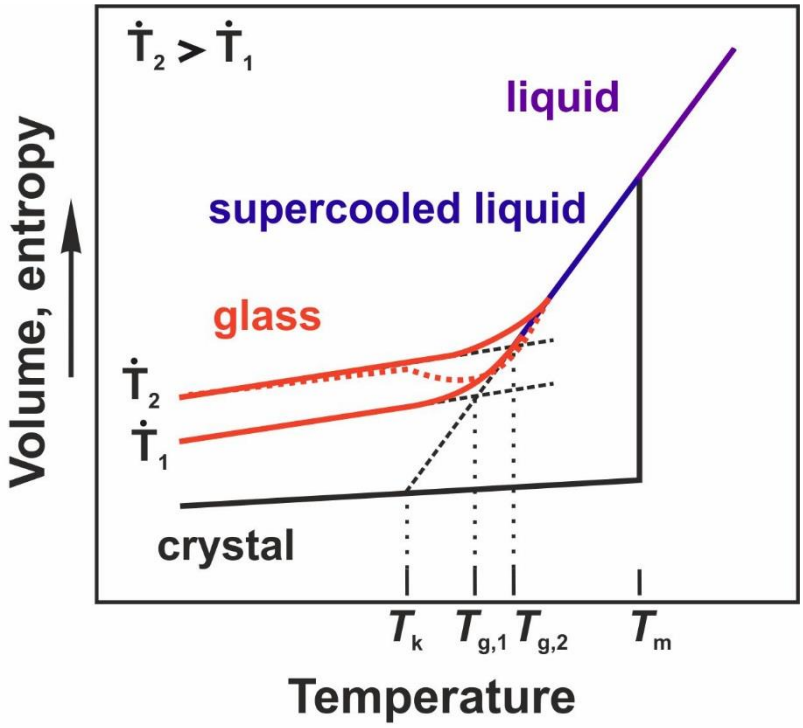

Figure 1.1: Change of volume or entropy as a function of temperature and cooling rate. T_m is the thermodynamic melting point. On increasing the cooling rate, the glass transition occurs earlier. Adapted from [16].

During solidification, the driving force for crystallization is given by the difference of the free energy between supercooled liquid and the crystal, ΔG [8, 17]. ΔG rises with supercooling and represents the thermodynamic aspect of crystallization/vitrification [8]. As mentioned above, the crystallization process is also strongly influenced by the viscosity of the system. During undercooling, atomic movements are hampered, which can even suppress the formation and growth of nuclei [8]. This constitutes the kinetic aspect of solidification. The interplay of thermodynamics and kinetics for crystallization of supercooled liquid result in the typical

continuous cooling transformation (CCT) curves shown in Fig. 1.2, in which the solid-liquid boundary has a nose-like shape [17]. If the alloy system has a high glass-forming ability (GFA), the nose is located more to the right-hand side (i.e. towards larger times).

The minimum cooling rate to suppress crystallization and to form metallic glasses instead is defined as critical cooling rate (R_c), which is the slope of the curve in Fig. 1.2. R_c is largely determined by the alloy composition and can range between 10^{-2} K/s and 10^{6} K/s [18-21]. A lower R_c means a larger critical casting thickness for metallic glasses [8, 22, 23].

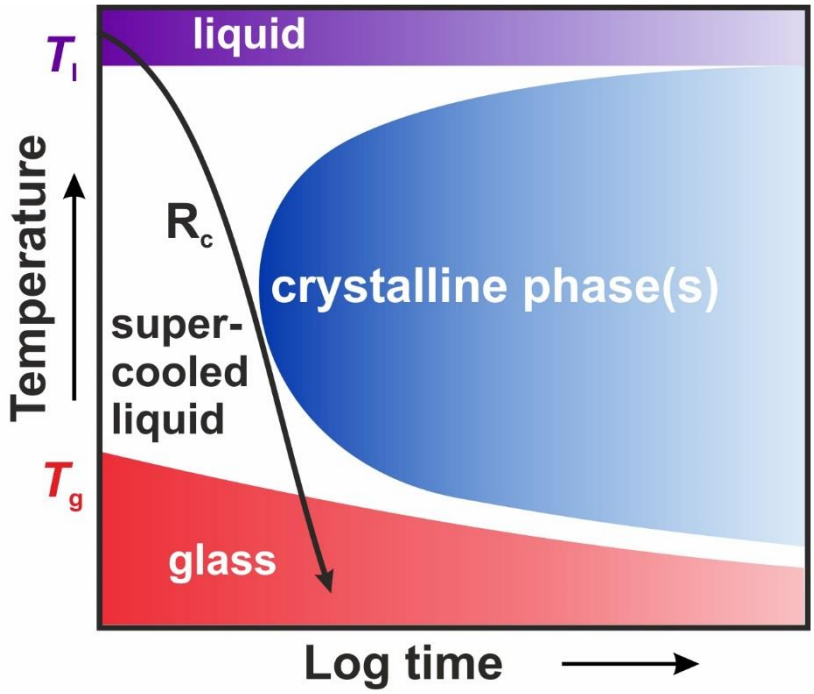

Figure 1.2: A schematic continuous cooling transformation (CCT) diagram demonstrating the conditions for glass formation on quenching of the melt. R_c represents the critical cooling rate. Adapted from [17].

After the Au-Si alloy [24] has been produced as amorphous structure by a method called gun technique [25], the different routes to fabricate metallic glasses have been widely studied. Melting spinning [26], flux melting [20], water quenching [27], high-pressure die casting [28], Cu mould casting [29, 30], cap-casting [31], suction/injection casting [32], squeeze casting [33], unidirectional zone melting [34], electromagnetic vibration process [35] and thermoplastic forming in combination with granulation [36] have been developed for synthesizing metallic glasses.

Moreover, in order to increase the dimensions of metallic glass samples, a large number of different glass-forming systems have been developed over the past decades [20, 37-39]. Especially after Inoue *et al.* have successfully prepared centimetre-scaled bulk metallic glasses

(BMGs) [27]. However, despite all recent advances the typical size of glassy alloys is still limited due to the fact that the heat has to be extracted quickly from the system on cooling. A technique, which allows for producing BMGs without size limitation and which, moreover, enables the fabrication of BMGs with complex geometry, is needed. Additive manufacturing, a relatively new approach, which is widely used to produce conventional crystalline alloys, bears the potential to solve these problems. The fabrication of BMGs via additive manufacturing will be discussed in the section 1.5.

1.2 Mechanical properties of BMGs and their composites

To evaluate the application potential of materials, the mechanical properties usually play a decisive role. Owing to their unique structure [40-42], BMGs have advantageous mechanical properties, such as high yield strength, low Young's modulus, high hardness and good wear resistance [17, 43-46]. However, BMGs have not been widely used as structural materials so far because of their inherent brittleness in tension [44-46]. In this section, the mechanical properties of BMGs and their composites are briefly discussed.

1.2.1 Shear banding in metallic glasses

Since the first study on mechanical behaviour of Pd-Si metallic glasses has been reported [47], the mechanical properties of BMGs have drawn a lot of attention in the academic field [46]. Unlike conventional crystalline alloys, BMGs approach the theoretical limit for strength [18, 48]. When BMGs are loaded, they usually undergo elastic deformation, then fail or deform plastically in compression or bending at room temperature [49].

Plastic deformation is highly localized in shear bands [48-52]. Shear band initiation and propagation are the critical steps during plastic flow of metallic glasses [49]. The first stage of shear localization in metallic glasses is the activation of so-called shear transformation zones (STZs) [49, 53]. Small clusters of atoms reorganize spontaneously and cooperatively under loading and form a shear transformation zone (STZ) [52, 54]. STZs preferentially form in the regions with a higher free volume content or, equivalently, more pronounced structural disorder [49, 53]. Such structurally heterogeneous regions are generally considered to be fertile sites for shear transformations [49].

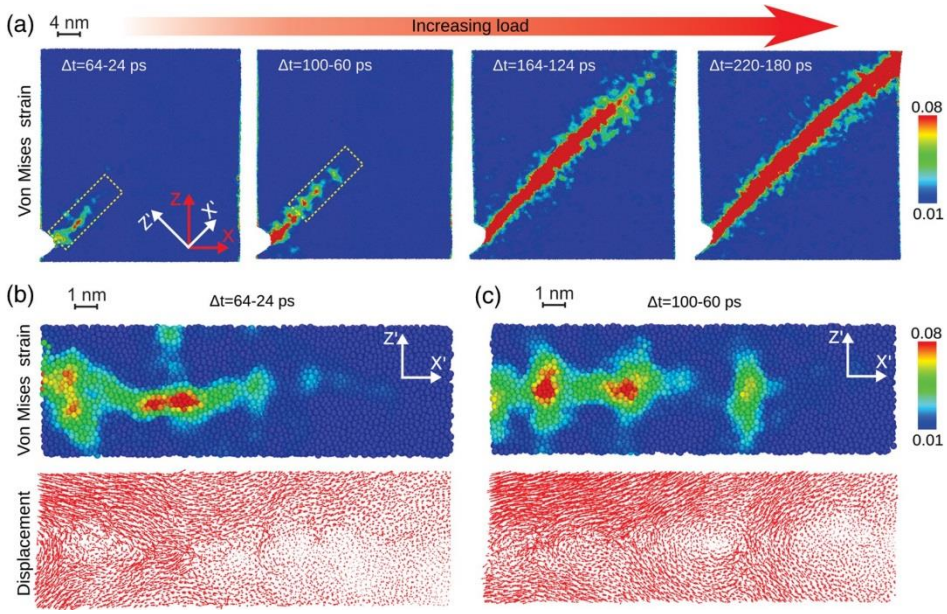

Figure 1.3: Structural variations in the molecular dynamics (MD) simulated notched metallic glass during the early stages of shear banding (a) Overall evolution of the atomic von Mises strain built up within consecutive time frames of 40 ps. (b)Δt = 64-24 ps, (c) Δt = 100-60 ps. Taken from [55].

Since the STZs are hard to detect experimentally, computer simulations are often used to reveal the atomic-level mechanism of shear band formation and propagation [49, 55-57]. Such simulations consistently reveal that existing STZs stimulate the activation of STZs in their vicinity [49, 55-57] and eventually form a shear band by percolating along the plane of maximum shear stress [56, 58]. Sopu *et al.* have studied the atomic-level mechanism of the STZ percolation process in a simulated glass containing a notch [55]. Fig. 1.3 shows the evolution of the atomic von Mises strain. Since the stress is concentrated at the notch root, the shear band propagates along the plane of maximum shear stress after its initiation at the notch. On the tip of the developing shar band, there exist the circular displacements of the atoms, resembling a vortex like motion (Figs. 1.3 (b) and (c)). It is notable that the shear band initially is discontinuous and comprises isolated vortices with high strain.

In order to discuss the underlying mechanism, the vortex is considered as a structural entity, which transfers the stain from one STZ to the next. Fig. 1.4 reveals the mechanism of STZ percolation. When the load is low, the distortion of the STZ near the notch is small and the effect on the neighbouring matrix is negligible (Fig. 1.4 (a)). Upon raising the load, the STZ is activated and its atomic configuration is changed, which first induces elastic deformation of the neighbouring STZ (Fig. 1.4 (b)). When the load reaches a certain value, the adjacent STZ is activated (Fig. 1.4 (c)). Such repetition of the two-unit STZ mechanism results in the percolation of STZ along a certain direction and the formation as well as the propagation of shear band.

Thus, with increasing load, more STZs initiate/form and eventually coalesce into a shear band [54, 59, 60]. The STZ theory can be considered as an extension of the free volume concept to explain the initiation of shear band [15, 61].

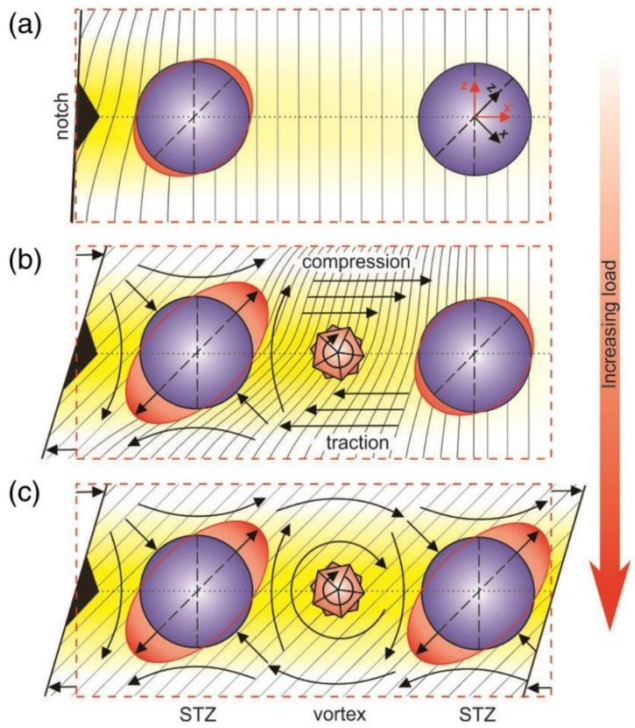

Figure 1.4: Schematic representation of the STZ percolation mechanism. The nonactivated STZs are represented by purple circles, whereas STZ distortions are shown as orange ellipse. The black arrows indicate atomic motion. Taken from [55].

As the increasing the load on the BMGs, more and more shear bands will be activated. When the stress arises to a certain value, yielding will occur with macroscopic shape change, followed by the formation of a shear band [49]. The shear band thickness is ranging from 10 to 50 nm [62]. As illustrated in Fig. 1.5, the compressive loading results in the tensile stresses in the central part of the shear band. Voids initiate throughout the shear band due to the excess free volume caused by the plastic flow and tensile stresses. When the dilatation force exceeds the critical shear fracture stress, a break or split will form. The coalescence of the voids leads to the formation of crack. The different elastic constants and the susceptibility to flowing destabilize the interface between the shear band and the neighbouring undeformed region. Therefore, the small cracks propagate along these interfaces. When the cracks reach a critical length and become unstable, the catastrophic failure will occur. The local melting during the fracture results in the typical vein like pattern in BMGs [63].

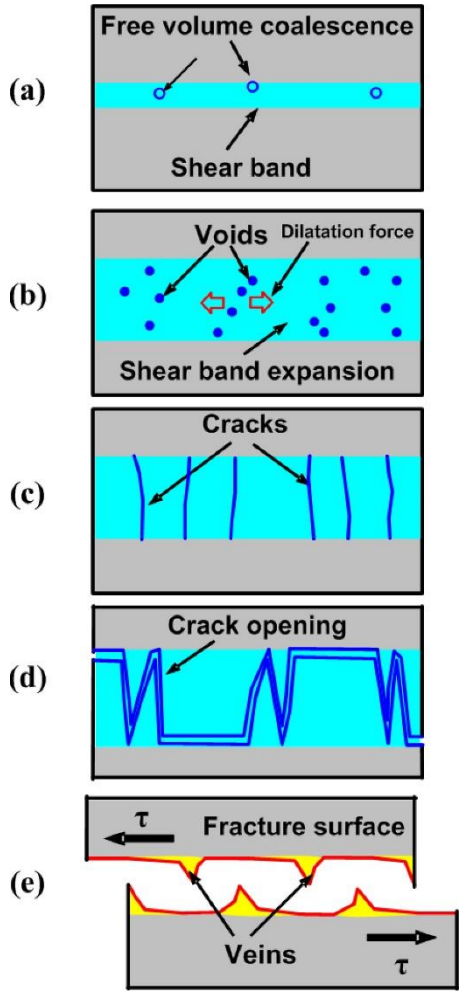

Figure 1.5: Schematic illustration of crack initiation and fracture development in a shear band: (a) Formation of voids by coalescence of free volume within the shear band. (b) Increase in the number of voids by cyclic strain localization in the primary shear band. (c) Crack initiation and shear band fragmentation by connecting voids. (d) Crack propagation. (e) Fracture with vein patterns on the fracture surface. Taken from [63].

1.2.2 Effect of structural heterogeneities on plastic deformation

Shear bands can be either nucleated homogeneously or heterogeneously [49]. Homogeneous nucleation of shear bands is induced by structural fluctuations inherent to the amorphous material itself [49]. Moreover, during preparation of BMG specimens, defects, voids, pores and surface imperfections are difficult to avoid [49]. These defects can serve as stress concentrators, around which the stress is above the average in the sample [49]. Thus, defects can act as heterogeneous nucleation sites for shear bands [49] (Fig. 1.3).

Wada *et al.* have introduced the hydrogen bubbles to a Pd-based BMG and obtained samples with a porosity of up to 3.7% [64]. The compressive plasticity of these samples is significantly improved [64]. Similar reports also indicated that uniformly dispersed, relatively small pores can elevate the plastic deformability [65, 66]. The underlying mechanism of such results can be

concluded as following. The stress concentration promotes the formation of shear bands. Moreover, as loading these porous BMGs, the pores introduce the stress gradient, which can stabilize the propagation of shear bands [65, 66]. Additionally, the pores interact with the shear bands [65, 66], hampering the development of a runaway shear band, which may induce the catastrophic failure.

Apart from the defects, the local free volume, the *in-situ* and *ex-situ* crystalline phases also can act as preferential spots of heterogeneous nucleation for shear bands [67, 68]. Moreover, the heterogeneities not only can affect the formation, but also can influence the propagation of the shear bands [49, 69, 70]. In this section, the effect of free volume and crystalline phases on deformation of glass forming alloys will be focused on.

1.2.2.1 Nanoscale heterogeneities

As discussed in section 1.2.1, the STZs which eventually coalesce into a shear band preferentially initiate in the regions with a higher free volume content. The adjustment of free volume may introduce more shear bands under loading to enhance the plasticity. One method to adjust the free volume content is to solidify the metallic glasses at different cooling rate. By using different casting conditions, BMGs adapt different structural states. As mentioned above, a higher free volume content can be obtained from the fast cooling of supercooled liquid with high temperature (Fig. 1.1). Shen *et al.* have cast Ti-Cu-based BMGs at various cooling rates [71]. According to their calorimetric measurements, the relaxation enthalpy of the samples increases on faster cooling, indicating the free volume content increases. In the subsequent compression tests, samples with a higher free volume content have shown a larger plastic strain. More shear bands are found on the lateral surfaces of the samples with high free volume content. Besides casting with different cooling rates, cryogenic cycling is also an effective method to introduce free volume [72]. After cryogenic cycling, the rejuvenated samples contain more free volume than the as-cast samples. During deformation, the rejuvenated samples show a larger plasticity and more shear bands are found in the rejuvenated BMGs [72]. Additional finite element modelling (FEM) [73] reveals that the overall free volume leads to low activation stress of shear band.

Not only the overall amount of free volume determines plastic flow but also the distribution of free volume. It is now widely accepted that metallic glasses are structurally heterogeneous and this can be regarded as a non-uniform distribution of local free volume [71, 73]. The non-uniform distribution of free volume has been found to promote the multiplication of shear bands [69]. The free volume-enhanced regions, which are more prone to structural rearrangements, can act as preferred sites for the initiation of shear bands [69]. Kosiba *et al.* have introduced

free volume into a CuZr-based BMG and controlled its distribution by means of ultrafast inductive heating followed by quenching ("flash-annealing") [70]. The highly rejuvenated BMGs exhibit better plasticity than the as-cast sample. By controlling the ejection temperature, the differences in cooling rates between the outer and inner regions of the samples can be altered. As a result, the distribution of free volume is non-uniform, which is reflected in the distribution of the corresponding hardness values [70]. Moreover, Molecular Dynamics (MD) simulations have been carried out to investigate the effect of an "interface" between structurally dissimilar glassy regions (i.e. relaxed or rejuvenated regions) on the stress field under the compressive loading. In the uniformly hard sample (Fig. 1.6 (a)), the number of STZs is comparatively low. The shear band forms along the plane of maximum shear stress and propagates quickly, resulting in a more brittle behaviour of the sample. The uniformly soft sample (rejuvenated sample) has a lower barrier for STZ activation (Fig. 1.6 (b)). The density of STZs is obviously increased. The strain is clearly less localized than in the uniformly hard sample. The delocalization of strain hampers the formation of a runaway shear band. Thus, the fracture of the sample is retarded and plasticity enhanced, in agreement with experimental results [70].

Even though the free volume content is lower in the non-uniform sample than the uniformly soft sample, the plasticity of the glass with a non-uniform distribution of free volume is larger [70] . The "interface" between the soft and the hard regions apparently influences the formation and propagation of the shear band (Fig. 1.6 (c). The shear band, which initiates in the hard region, becomes wider and bifurcates at the interface. The strain in this shear band is much lower in the soft region than that in the hard region. Moreover, shear bands intersect at the interface. Therefore, fracture is effectively retarded and plasticity is enhanced.

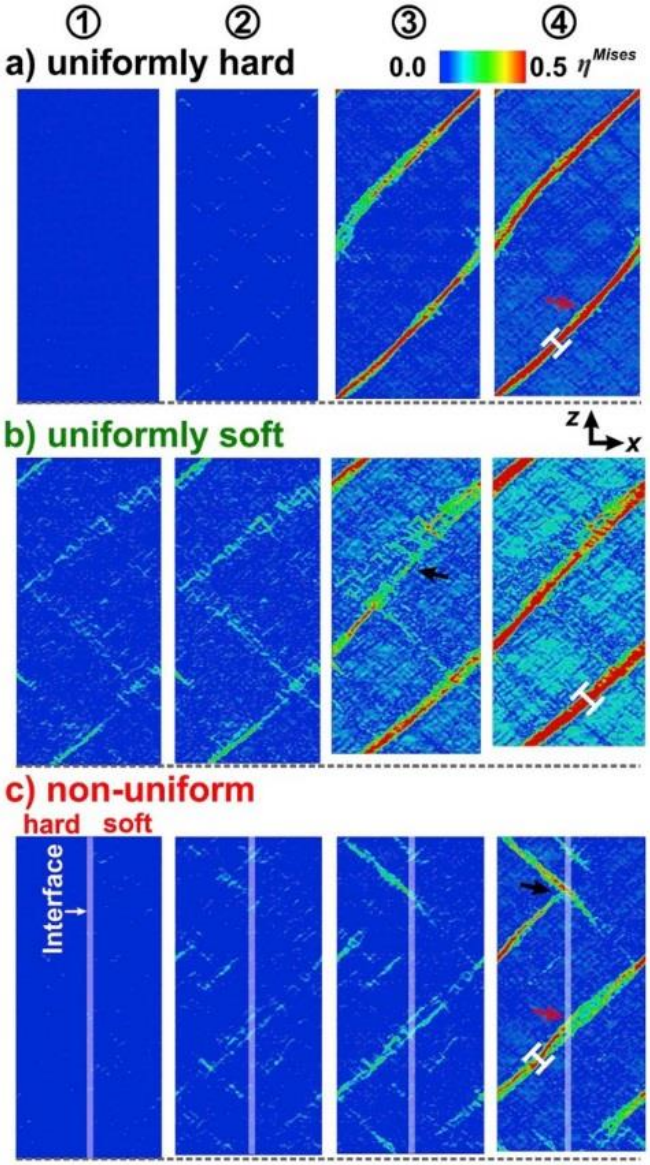

Figure 1.6: Maps of atomic von Mises strain for three different structures in BMGs: (a) uniformly hard (relaxed), (b) uniformly soft (rejuvenated) and (c) half hard and half soft. Taken from [70].

The vortex mechanism outlined above [55], can qualitatively explain the behaviour of the shear band at interface. An active STZ stimulated an adjacent STZs through a vortex-like motion of atoms. However, the stress field resulting from the activity of a STZ is changed at the interface due to the elastic mismatch (between relaxed and rejuvenated glass). The obstruction for the cooperative activation of STZs and the reduction of the strain localization in the rejuvenated part promotes bifurcation of the shear band and increase its width. Only when the strain becomes relatively large (at the later stages of deformation), the STZs near the interface can be activated and the mature shear band forms. Such a shear band can propagate through the sample and cause failure. These investigations reveal how the interface between heterogeneities and matrix enhances the plasticity [70]. The aspects discussed above could be

summarized as "nano-scale effect" of the heterogeneities on deformation. In the following paragraphs, also the effect of micro-scale heterogeneities on the deformation process of metallic glasses shall be addressed.

1.2.2.2 Microscale heterogeneities

It has proven to be a feasible way to introduce crystalline particles to metallic glasses to form BMG matrix composites (BMGCs) in order to elevate plasticity [68, 74-85]. Because the crystalline particles effectively block the propagation and trigger the initiation of the shear bands, failure of the glass forming alloys can be retarded [68, 74-85]. The methods of preparing BMGCs can be generally divided into two categories, *ex-situ* and *in-situ* glass matrix composites. For the *ex-situ* BMGCs, insoluble particles with high melting point such as SiC, WC, Ta and W are added to the glass-forming melt [49, 86]. The thermal expansion coefficients of the additions should be similar to the matrix in order to reduce the mismatch stress during cooling [49, 87]. The interfacial strength of the additional particles in the matrix should also be considered [49, 87]. *Ex-situ* BMGCs show increased yield strength and plastic strain [49]. Moreover, by optimizing the particle size and volume fraction, the mechanical properties of BMGCs can be tuned to some extent [88]. However, the distribution of the particles added are generally very difficult to control.

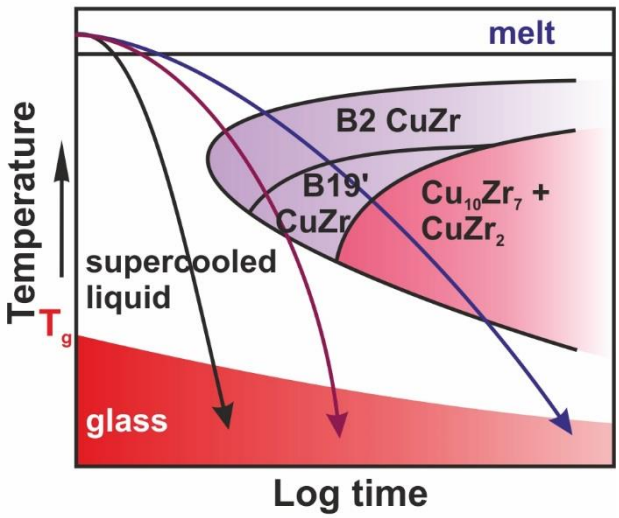

Figure 1.7: A schematic CCT diagram demonstrating the influence of varying cooling rates on the phase formation in the CuZr-based alloy system. Adapted from [16].

In case of the *in-situ* BMGCs, the crystalline phases precipitate during the solidification process. Depending on the alloy composition and the cooling rate, the crystalline phases can take on different shapes (dendritic, spherical, cellular etc.) [16, 89, 90] or sizes (nanometres to hundreds of micrometres) [16, 89, 90]. In comparison to the *ex-situ* BMGCs, the *in-situ* BMGCs

generally have a stronger interfacial bonding between the particles and the glassy matrix [49, 91]. By tailoring the composition, β-type TiZr-based BMGCs with a tensile ductility over 10% at room temperature have been prepared [89]. Also in other ZrTi-based BMGCs average fracture strains up to 8.3% in compression have been measured [77]. In these studies, the β-dendrites promote the initiation, bifurcation and deflection of the shear bands and, with it, limit the shear band length. Crack development is avoided at the early stage of deformation in this way and strain localization reduced [89].

Next to the family of β-type BMGCs, CuZr-based BMGCs have been also developed in the recent years [92-97]. The B2 CuZr phase precipitates polymorphically in these glass formers, a phase, which is thermodynamically stable only at high-temperatures [98, 99]. During slow cooling, the B2 CuZr phase decomposes into the low-temperature equilibrium phases, $Cu_{10}Zr_7$ and $CuZr_2$ (Fig. 1.7). High cooling rates are required to retain the B2 CuZr phase also at room temperature. The B2 CuZr phase is interesting as reinforcing phase because it martenistically transforms on mechanical loading [100]. The diffusionless transformation from B2 CuZr to B19' and B33 CuZr results in a pronounced work-hardening capability [96, 101]. The volume expansion, which accompanies the martensitic transformation, facilitates and promotes initiation of additional shear bands [96] (Fig. 1.8 (a)). In addition, the shear bands are blocked by the crystalline particles (Figs. 1.8 (c) and (d)), leading to an enhanced ductility.

The effect of B2 CuZr phase on the plasticity depends on the particle size and the distribution of the particles [93, 97, 102]. A relatively small particle size in combination with a uniform distribution of the B2 CuZr crystals has been reported to be most effective for elevating the plastic deformability [93, 97, 102]. Unfortunately, it is generally very difficult if not impossible to precisely control the size and distribution in *in-situ* CuZr-based bulk metallic glass matrix composites by using the traditional melt-quenching method [103-105]. The outcome is a non-uniform crystal distribution and a relatively wide range of B2 CuZr particle sizes [103-105].

To solve this problem, various methods such as a dedicated re-melting treatment and laser scanning were carried out [97, 106]. Only recently, Kosiba *et al.* were able to control the particle size of B2 CuZr phase in BMGCs by flash-annealing [107]. Generally speaking, it is usually a tedious procedure to find the optimized processing parameters in order to properly control the distribution (homogeneity and distance between crystalline particles) and the particle size of the crystals [90, 97, 106]. A new and effective method of preparing BMGCs is required and additive manufacturing could be suitable approach, as we will outline in section 1.5.2.

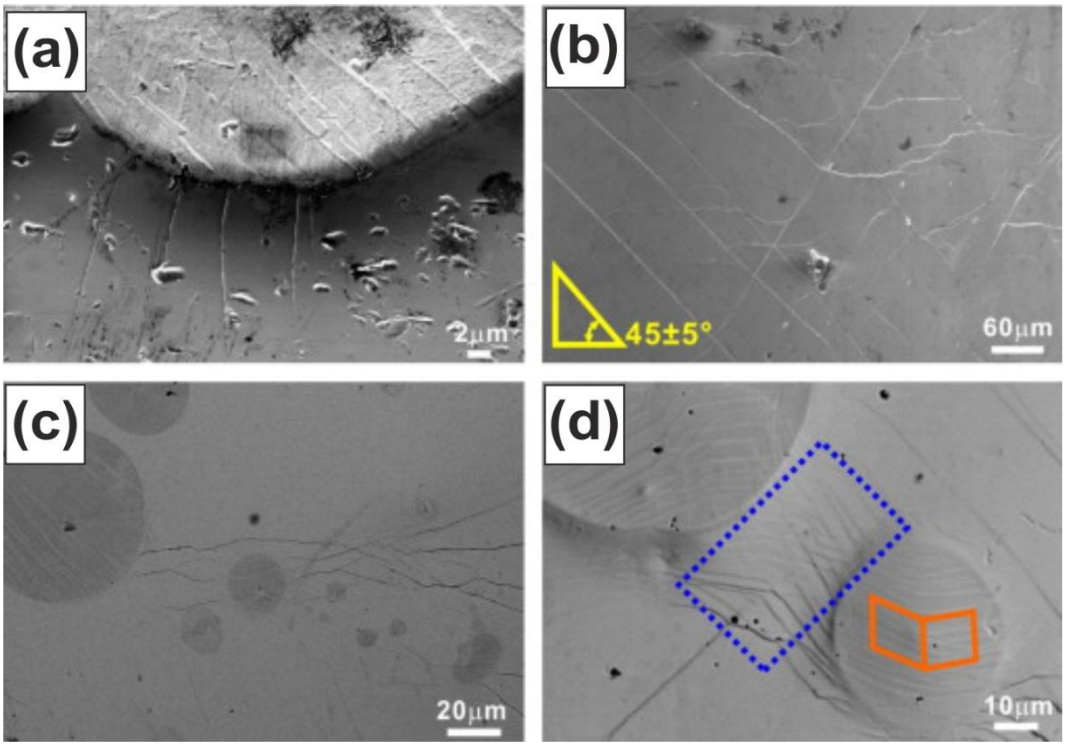

Figure 1.8: Shear band behaviour of $Cu_{47.5}Zr_{47.5}Al_5$ BMGCs under compressive loading (a) at the second yielding and (b-d) at around 1160 MPa. The shear bands initiate at the surrounding regions of the crystalline particles. The shear bands are blocked by the crystalline particles during their propagation. Taken from [96].

1.2.3 Shear band dynamics

The generation and propagation of shear bands during plastic flow (see section 1.2.2) leads to characteristic sudden stress drops in the stress-strain curve [108-111] (Fig 1.9). Then the alloy recovers elastically and this process repeats until the sample fractures (Fig. 1.9 (a)). This phenomenon is called serrated flow (Figs. 1.9 (b - d)) [108, 110, 112]. A single serration can be the result of a single shear-band operation [113]. Serrations originate from a stick-slip motion [113]. During the “stick state”, the shear band remains stationary. In this state, both the load and the elastic energy stored in the sample increase. At a critical limit, the energy is released into the shear band to drive its propagation. During the “slip state”, the system is under decreasing load. The shear band will be arrested until the low stress limit is reached [49]. The stick-slip process of shear banding is influenced by various intrinsic and extrinsic factors, such as the structure of the glass, the free volume content as well as the strain rate, sample size and the stiffness of the testing machine [110, 114, 115]. By analysing the size and the number of serrations (i.e. their frequency) during plastic flow, conclusions can be drawn regarding the shear band dynamics [108-112].

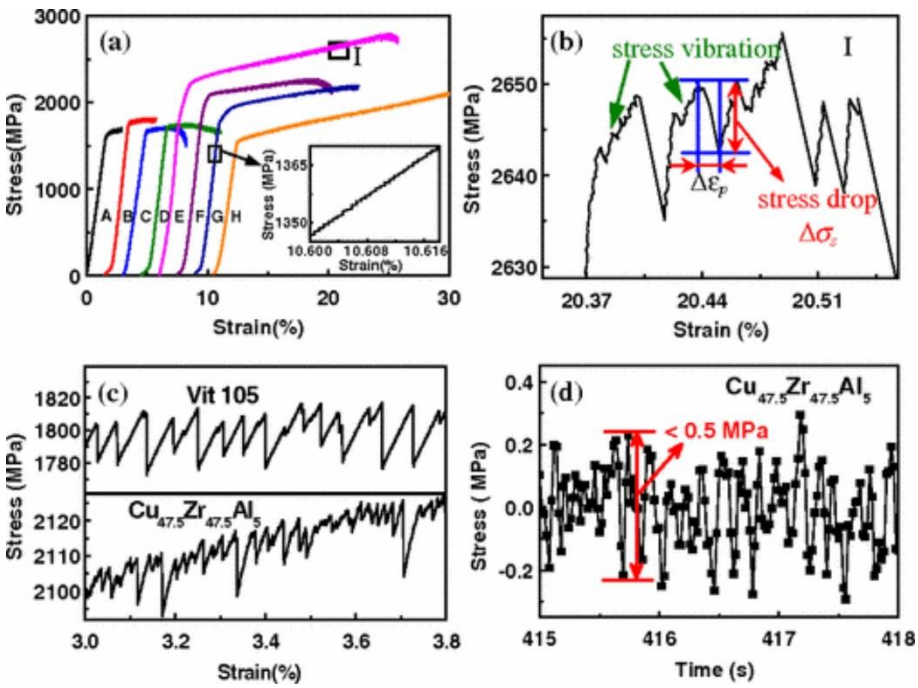

Figure 1.9: (a) Compression stress-strain curves of typical BMGs. Curve B and F are Vit105 and $Cu_{47.5}Zr_{47.5}Al_5$ BMGs, respectively. The inserted curve is an enlarged elastic part showing the stress vibrations due to the machine. (b) Enlarged serrations from region I, showing the stress drops of a serration. (c) Comparison of the serrated flow of Vit105 and $Cu_{47.5}Zr_{47.5}Al_5$ BMGs at the same strain range. (d) An example of the stress vibrations due to the machine. Taken from [116].

Sun *et al.* have statistically analysed the serrated flow of different BMGs in order to reveal the details of their deformation mechanism [116]. The stress drop magnitudes (Fig. 1.9 (c)) are normalized using a linear regression fit through the stress drop vs. time diagram. In order to exclude the influence of the vibrations (Fig. 1.9 (d)) from the testing machine, the serrations with small values are ignored. Then the distribution histograms of the normalized stress drops are analysed. As shown in Fig. 1.10 (a), the stress drop magnitude found in Vit105 displays as Gaussian distribution, which indicates that the serration size has a characteristic length scale, the system's shear band dynamics are a chaotic state [108, 110, 116]. BMGs with a chaotic serrated flow behaviour generally show very limited plastic deformability [108, 110, 116]. The histogram of the stress drops for the ductile $Cu_{47.5}Zr_{47.5}Al_5$ BMG shows a monotonic decrease, instead. Moreover, the cumulative probability distribution follows a power-law distribution with a squared exponential decay function [108, 116]. It reveals that the system has adopted a state of self-organized criticality (SOC) [116]. This means that motion of multiple shear bands occurs cooperatively in ductile $Cu_{47.5}Zr_{47.5}Al_5$ BMGs [108, 110, 116].

As discussed in section 1.2.2, heterogeneities can affect the initiation and propagation of shear bands, altering serrated flow. Statistical analysis of the serrations provides valuable information regarding the shear band dynamics [117].

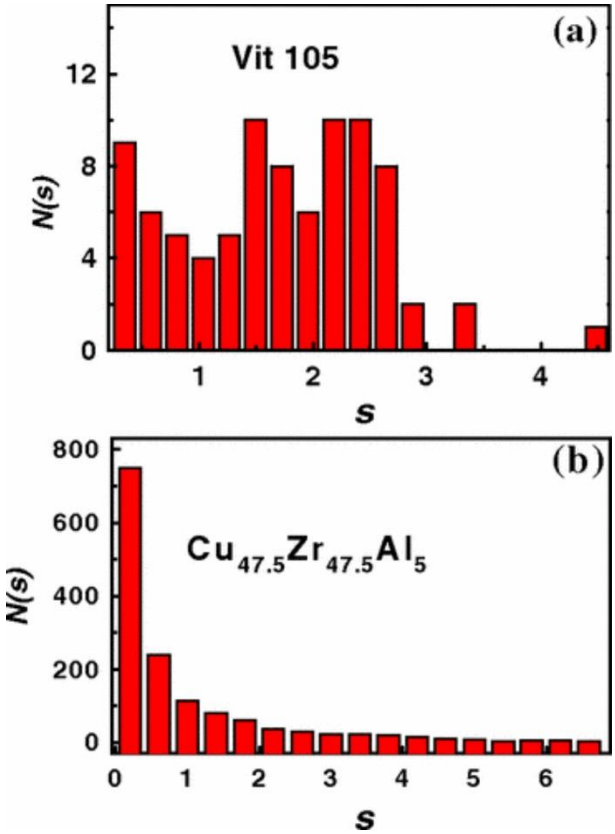

Figure 1.10: The stress drop (shown in Fig. 1.9) distribution of statistical number N(s) vs. normalized stress drop magnitude *s* for (a) Vit 105 and (b) $Cu_{47.5}Zr_{47.5}Al_5$ BMGs. Taken from [116].

1.2.4 Tribological properties of BMGs

Owing to their unique structure, bulk metallic glasses have many advantageous properties, such as high strength and high hardness, indicating the great potential for industrial application [40, 45]. Among them are the tribological properties as well, which directly result from their high hardness in combination with the lack of a conventional microstructure [118, 119]. For a plethora of engineering applications tribology plays a vital role [119]. Thus, BMGs with high hardness are very attractive for applications involving contact sliding [119-121]. In the following, selected aspects of the tribological properties of BMGs are briefly discussed.

It has been reported that Ni-based BMGs have a much higher wear durability than conventional carbon tool steels [122]. Zr-based, Cu-based and Ti-based BMGs also show excellent wear resistance [118, 120, 121, 123-128]. Huang *et al.* have demonstrated that the cooling rate is one important parameter affecting the wear performance of BMGs [123]. The relatively lower cooling rate reduces the free volume content (see section 1.1) and leads to a

more ordered atomic configuration, resulting in the better wear resistance [123]. Rahaman *et al.* have studied the wear mode of the BMGs at different sliding speeds [120]. On the increasing the sliding speed, the frictional heat rises, the wear mode changes from brittle to ductile, and then to mixed (brittle and ductile) stage. Because during this process, the temperature increases to a certain degree and the BMG becomes softer and ductile. As the temperature rises further, the nanocrystals forms [120]. These results reveal that the heterogeneities such as nanocrystals and free volume enhanced regions may influence the wear mode.

1.3 Corrosion behaviour of bulk metallic glasses

The corrosion behaviour is one of the decisive factors for judging the environmental stability of a material [129, 130]. Especially when the alloys are used in aggressive and hostile environments such as oxidizing atmospheres and aqueous corrosion. A chemical reaction between a surrounding medium and the material usually degrades the materials and deteriorates the mechanical properties as well. When bulk metallic glasses are considered for practical applications (e.g. for biomedical applications and/or as structural materials), the corrosion behaviour is one crucial aspect.

Since metallic glasses are usually solidified at a relatively higher cooling rate (see section 1.1) in order to circumvent crystallization, they are thermodynamically in a state of higher energy than their crystalline counterparts. As a consequence, according to the Tafel law [131], the corrosion current rate should be expected to be higher. However, metallic glasses usually show a better corrosion resistance than crystalline alloys of identical or similar composition [130, 132]. Because of the high cooling rates, metallic glasses solidify into a single phase. Abundant atomic diffusion and, hence, solute partitioning are generally suppressed during quenching. Therefore, metallic glasses are chemically and structurally rather homogeneous [17]. In the absence of chemical heterogeneities and structural defects such as grain boundaries, dislocations, galvanic corrosion can be avoided. Passive films on metallic glasses are relatively uniform, which reduces localized chemical attack (e.g. pitting corrosion) [133, 134]. These factors are beneficial for the overall corrosion resistance.

The alloy composition, i.e. the reactivity of the constituent elements, also plays an important role on the corrosion behaviour of metallic glasses [130, 133, 135-141]. The corrosion behaviour of Cu-, Fe-, Mg-, Ni-, Ti- and Zr-based metallic glasses have been widely studied in the past decades [130, 133, 135-141].

Next to the chemical composition of the glass, structural and/or chemical heterogeneities affect the corrosion behaviour. Gas pockets (pores) sometimes form during casting of metallic

gasses [9]. In the vicinity of such pores, the heat removal is slowed down and crystals might precipitate [9]. Such heterogeneities are hard to be avoided completely. Heterogeneities or the crystal-glass interface are considered as preferential spots for initiation of pitting corrosion [133, 142-144].

Before introducing the corrosion behaviour, the methods for evaluating the corrosion behaviour will be discussed among which the potentiodynamic polarization curve is the most widely used. In this thesis, the room-temperature aqueous corrosion of Ti- and Zr-based metallic glasses will be focused on.

Ti-based alloys have already been used in the aerospace and biomedical sector due to their unique physical and chemical properties [129, 132]. Owing to their potential, the corrosion behaviour of Ti-based bulk metallic glasses has been widely studied in different solutions such as acid, akaline and simulated body solutions [139]. In comparison with commercial Ti-based alloys (e.g. Ti-6Al-4V), the Ti-based metallic glasses show better corrosion resistance due to the single-phase nature [139]. As shown in Fig. 1.11, the $Ti_{46}Cu_{27.5}Zr_{11.5}Co_7Sb_3Si_1Ag_4$ metallic glasses exhibit a higher corrosion potential and lower corrosion current density than Ti-6Al-4V, which is widely used as a conventional alloy in all the solutions [139]. Ti-Zr-Ni-Be, Ti-Cu-Zr-Fe-Sn-Si-Ag, Ti-Cu-Zr-Ni, Ti-Zr-Cu-Pd-Nb and Ti-Zr-Cu-Pd glasses all have good corrosion performance [129, 132, 145-147]. Due to their high affinity towards oxygen, the enrichment of Ti and Zr is found in the passive films, which can protect alloys from corrosive environments [148]. Thus, Ti and Zr content is considered to improve the corrosion resistance of the metallic glasses [129, 132, 145-147].

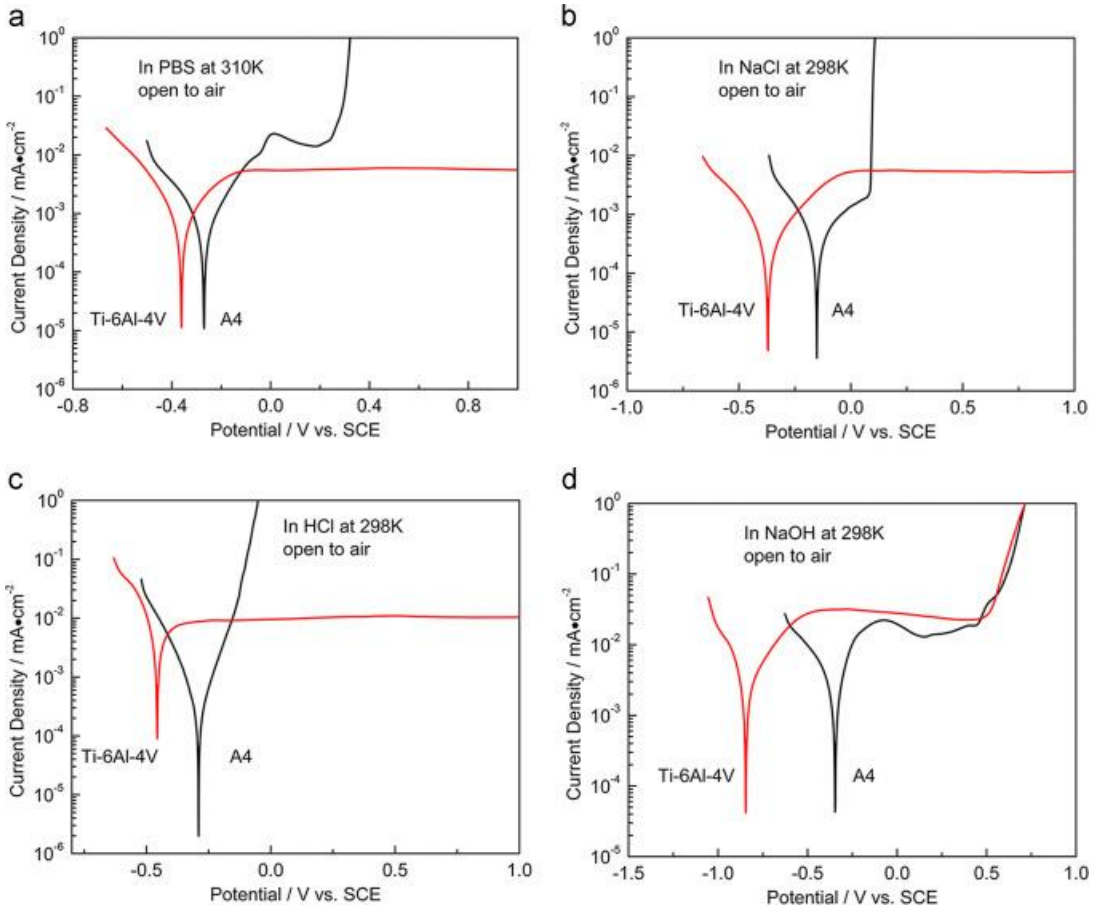

Figure 1.11: Potentiodynamic polarization curves of the Ti-based BMG and the Ti-6A-4V alloy in (a) PBS (phosphate buffered saline, pH = 7.4), (b) 0.9 wt % NaCl, (c) 1mol/L HCl and (d) 1 mol/L NaOH solutions. Taken from [139].

Zr-based BMGs have been widely investigated as well since their critical casting thickness is on the order of centimetres [45], which makes them attractive candidates for applications. In order to evaluate the stability of Zr-based BMGs in a given environment, cast bulk metallic glasses, in particular transition metal-based bulk glass-forming alloys, like Zr-Cu-based multicomponent alloys, have been subject of numerous fundamental corrosion studies [130, 133, 135-138]. In water-based solutions they exhibit low free corrosion rates and spontaneous and stable anodic passivation, both generally superior to crystalline alloys with comparable compositions [149]. The latter is based on the formation of very thin barrier-type oxide layers, which are mainly composed of the valve-metal oxides (Zr-, Ti-, Nb-, Al-oxides) [138, 143, 150]. The systems of Zr-Cu-Al-(Ni-Nb, Ni-Ti, Ag), which have a comparatively high glass-forming ability, show good pitting resistance [137]. It is notable that the pitting and repassivation potentials decrease with the increase of the Cu content. The corrosion products mainly include Cu, O and Cl species. The systems with low Cu and high Nb or Ti content show better pitting resistance [137]. Thus, Cu can be considered a critical alloying element with respect to the corrosion behaviour of Zr-based BMGs.

The corrosion morphology is usually dictated by different local corrosion rates, which can be influenced by structural and chemical heterogeneities. The regions, which corrode at low rates, usually appear as hills, and the regions with high corrosion rates exhibit as valleys.

In BMGs, corrosion is accelerated, when there is chemical heterogeneity (chemical segregation) or inherent porosity [136]. Fig. 1.12 shows three different morphologies of corrosion pits at early stage of development in Zr-Cu-Al-Ni-Ti system. At the beginning, the corrosion pits at the surface are more or less hemispherical, indicating stable dissolution (Fig. 1.12 (a)). As corrosion proceeds, terraces develop at the edge of the pit, because of the local composition changes (enrichment of Cu) and corrosion products (Fig. 1.12 (b)). In Fig. 1.12 (c), the "opening" of the hole in the central part can be seen, revealing that the strong dissolution also occurs below the surface. A possible explanation is that there exists a porous structure that renders the electrolyte attack possible in the bulk region.

Since porosity is inherent in additively manufactured alloys, the pores most certainly influence the corrosion behaviour. Thus, the effect of such heterogeneities in additively manufactured BMGs on corrosion behaviour is also subject of this thesis (Sections 3.1.4 and 3.2.5).

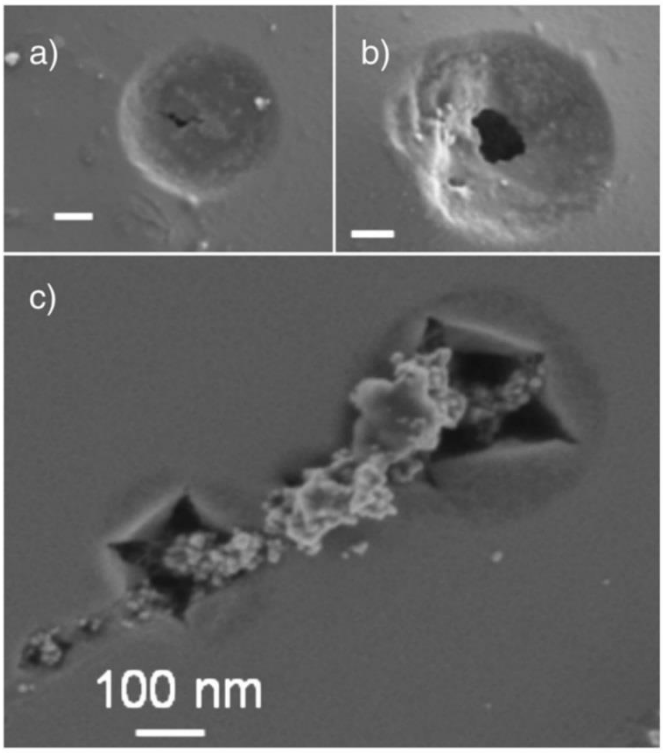

Figure 1.12 Pit development of $Zr_{59}Cu_{20}Al_{10}Ni_8Ti_3$ metallic glasses immersed for 100 s in 0.1% HF. The sequence (a), (b), (c) indicates the temporal development of pits. The scale bar in all figures is 100 nm. Taken from [136].

1.4 Selective laser melting (SLM)

Additive manufacturing (AM), colloquially also called “3D printing”, is a relatively new concept of sample and component fabrication. Depending on the processed materials and machine technologies, the individual techniques differ from each other. The American Society for Testing and Materials (ASTM) group classifies the additive manufacturing processes into seven categories: VAT Photopolymerisation, Material Jetting, Binder Jetting, Material Extrusion, Sheet Lamination, Directed Energy Deposition and Powder Bed Fusion [151, 152]. The commonly used techniques of Powder Bed Fusion include direct metal laser sintering (DMLS), electron beam melting (EBM), selective heat sintering (SHS), selective laser sintering (SLS) and selective laser melting (SLM) [151, 152]. In the present work, SLM is employed for processing of glass-forming alloys and will be, hence, discussed in the following sections.

1.4.1 The SLM process

Selective laser melting (SLM) has been developed by F & S Stereolithographietechnik GmbH and Fraunhofer ILT and has become a promising method to fabricate metals for industrial applications [153, 154]. SLM uses a high-intensity laser as energy source and a 3D computer aided design (CAD) file as software source to selectively fuse the metallic powder on the base plate layer by layer and to, thus, produce a three-dimensional part [153].

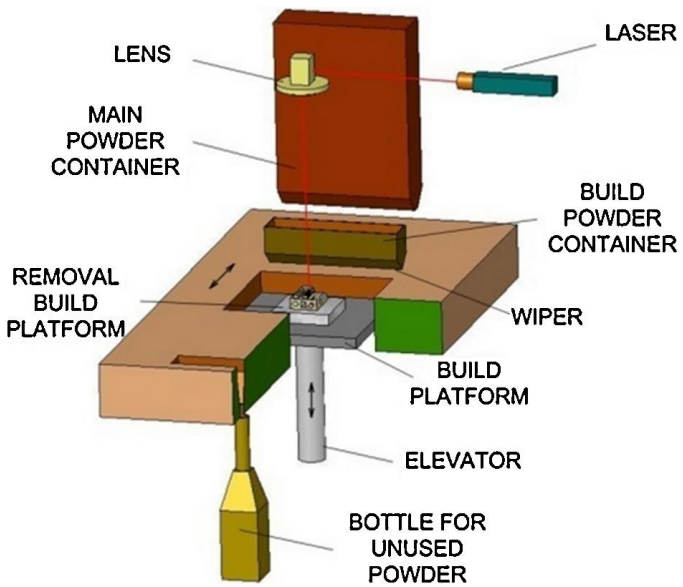

Figure 1.13: Schematic of a SLM system. Taken from [155].

As displayed in Fig. 1.13, the main parts of the SLM system comprise a laser source, the lenses, a powder container, a wiper and a removable build platform. The processing steps start with the CAD file design and end with the removal of the SLM part [155]. First, CAD models

of the components/parts are created. Afterwards, they are uploaded into the software for processing, such as slicing, setting the processing parameters and the scanning strategy. Then the production of the actual parts begins with a thin layer of powder deposited on a suitable substrate. A high-energy laser is used to selectively melt the powder according to the CAD files. After the first layer is completed, the substrate is lowered by a certain distance corresponding to the layer thickness set in the controlling software. Subsequently, the recoater sweeps over the substrate and deposits a new powder layer. The laser beam scans the new powder layer and the process repeats until the final part is obtained. Afterwards, the loose powder on the substrate is removed. The substrate then is removed from the device and the final parts are detached from the substrate [156].

1.4.1.1 Powder properties

The powder properties significantly influence the quality of the additively manufactured component [157-159]. The relevant powder properties include the density of the alloy, thermal conductivity, melting temperature, boiling temperature, thermal capacity, latent heat of fusion, dynamic viscosity, thermal expansion coefficient, laser absorptivity, morphology, particle size and purity. Depending on these factors, the process parameters have to be adjusted, which, in turn, determines the formation and the distribution of defects, the microstructures as well as the physical and chemical properties of the SLM alloys [155, 160-162].

The energy density of the laser deposited in the material during selective laser melting is primarily determined by the thermal properties such as melting temperature, thermal capacity and latent heat of fusion [160, 163]. According to these factors, the energy density is set to ensure complete fusion of the powder. The laser power should be carefully selected for alloys with low boiling temperatures in order to avoid evaporation, which may induce the formation of keyholes [160, 163].

The thermal conductivity is very important for the heat balance (heat flow) during processing and leaves its footprints in the so-called heat affected zone (HAZ) [163, 164]. The dynamic viscosity has a pronounced bearing on the melt pool and the morphology of the single scanning track and, thereby, on the generation of defects (i.e. pores, cracks etc.) [165]. The thermal expansion coefficient is a decisive factor for the generation of internal stresses in the SLM parts in the course of solidification [163, 164]. To release the stresses here, different scanning strategies are carried out as introduced in section 1.4.1.2.

The factors discussed above are determined by the material of choice processed by SLM. However, the morphology, particle size distribution and purity can be tailored in order optimize the SLM process. The shape and the size of the particles strongly affect the flowability of the

powder during powder deposition [162, 166]. It is generally accepted that the highly spherical powder particles have a higher packing density, which is conducive to the flowability of the powder, resulting in the decrease of the defects and higher density for SLM products [162, 167]. In contrast, powder with an irregular shape generally has a lower compaction leading to a lower density of SLM alloys [162, 167, 168]. In addition, the particle size distribution is also important for the flowability of the powder [169, 170]. A certain volume fraction of small particles can fill the voids between larger particles, which is helpful to improve the quality of the SLM parts in terms of reduced porosity [169, 170]. However, when the fine particles are most frequent in the powder, particle agglomeration occurs, leading to a negative effect on the flowability [171]. Another factor, which should be taken into consideration, is the layer thickness, which is primarily defined by the particle size [169]. If the particle size is relatively large, the layer thickness should be accordingly large.

A sufficient energy density is required to melt the large powder particles, which may lead to the evaporation of the fine powder. Thus, the powder size distribution should be carefully selected and the processing parameters adjusted accordingly (see next section). Eventually, the purity of the powder is another decisive factor of the final properties of selectively laser-melted alloys [172]. The level of powder contamination as well as the amount of oxygen and hydrogen usually has adverse effects on the quality of the powder and final parts [172]. Therefore, the purity of the powder should be constantly monitored and strictly controlled to obtain the SLM products with a high quality.

1.4.1.2 Process parameters

Many parameters can be adjusted during selective laser melting, which consequently offers a large degree of freedom during processing. All of these parameters affect the energy input and the distribution of heat and, thus, the thermal history of the additively manufactured component. The thermal history, in turn, has a strong impact on the microstructure and, thus, on the properties of the material. This is rather obvious for conventional metallic alloys processed by SLM [165, 173-179].

The most important process parameters affecting the quality of the final parts are laser power (P), scanning velocity (v), layer thickness (l) and hatch distance (h). By optimizing these parameters, products with high quality can be fabricated [165, 173-179]. The SLM process parameters are shown in Fig. 1.14.

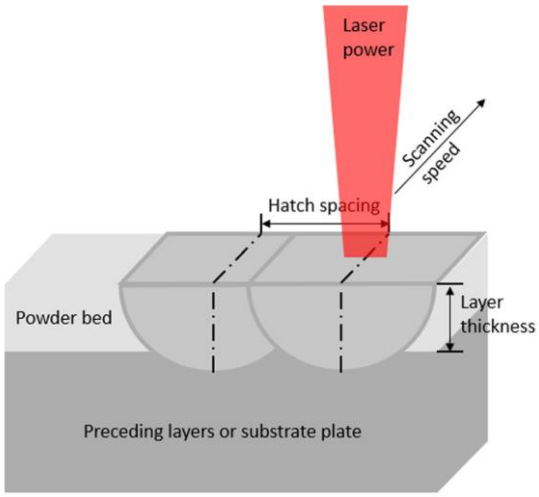

Figure 1.14: Schematic of SLM process parameters. Taken from [153].

The volume energy density (E_V) is often used to estimate the energy input and for many alloy systems, there is an apparent correlation between E_V and the relative density [180, 181]. An insufficient E_V may lead to incompletely melting, decreasing the density of the final part. When E_V is too high, evaporation of the powder occurs and pores form [180, 181]. The energy deposited in the material by the laser (i.e. the thermal history of the component) directly governs the microstructures of conventional metallic alloys and with it, their chemical as well as their physical properties [181, 182]. The volumetric energy density, E_V, is often estimated as:

$$E_V = \frac{P}{v \times l \times h} \tag{1.1}$$

where P is laser power (W), v is scanning velocity (mm/s), l is layer thickness (mm) and h is hatch distance (mm), as mentioned above [183].

In order to obtain a relative dense SLM product, researchers usually optimize the parameters as follows. First of all, the layer thickness is set according to the powder size. Then single tracks are produced by the laser in order to adjust/optimize the laser power and scanning velocity [165]. Based on the width of the single tracks, the hatch distance (the distance between two adjacent tracks) is selected. In optimizing the hatch distance, the track overlap has to be taken into consideration. It plays an important role in keeping strong bonding between the neighbouring tracks. The overlapping rate (Φ) can be described as [184]:

$$\Phi = \frac{d - h}{d} \times 100\% \tag{1.2}$$

where d is the single track width (mm) and h is hatch distance (mm). Too high an overlap causes excessive heat input and may deteriorate the surface quality, increase the residual stress and decrease the relative density of the SLM part [185]. Too low an overlap, in turn, results in an insufficient energy input and may reduce the density and form defects too [185].

Apart from the above mentioned four main processing parameters (P,v,l and h), the scanning strategy is another variable in the SLM process, which also can significantly influence porosity, microstructures and properties of additively manufactured materials [165, 186-190]. Fig. 1.15, depicts some examples of scanning strategies, which are widely used for fabricating SLM parts. As an ordinary scanning strategy, unidirectional scanning vectors can be employed, which are rotated by a certain degree (e.g. 45°, 67°, 90°) in neighbouring layers. This approach is usually carried out to decrease the porosity and improve the defect distribution (Figs. 1.15 A and B) [189, 191]. Fig. 1.15 C displays the scanning strategy of unidirectional scanning vectors (single melt), which are kept constant along the entire height of the sample. This strategy is usually conducted only for the production of single melt tracks or the investigation of formation of defects [165]. The offset scanning strategy, which fuses the powder from outside to the central part of the SLM specimen, is shown in Fig. 1.15 D. Fig. 1.15 E indicates the chessboard (island) scanning strategy, which is usually used to decrease the thermal stress and alter the microstructures of the SLM samples [186].

The last scanning strategy to be listed here is the implementation of a re-melting step during processing (Fig. 1.15 F). Since a re-melting step modifies the thermal history to the additively manufactured alloy, it can be used (Fig. 1.15 F) to design microstructures while not sacrificing the relative density [192-194]. It has been reported that the re-melting scanning is helpful to increase the relative density and improve the surface roughness [194, 195]. In other words, the scanning strategy can change the size and the distribution of defects formed in the SLM process and also affects the microstructures. This is one of the reasons why selective laser melting is such a powerful tool for manipulating microstructures and materials properties.

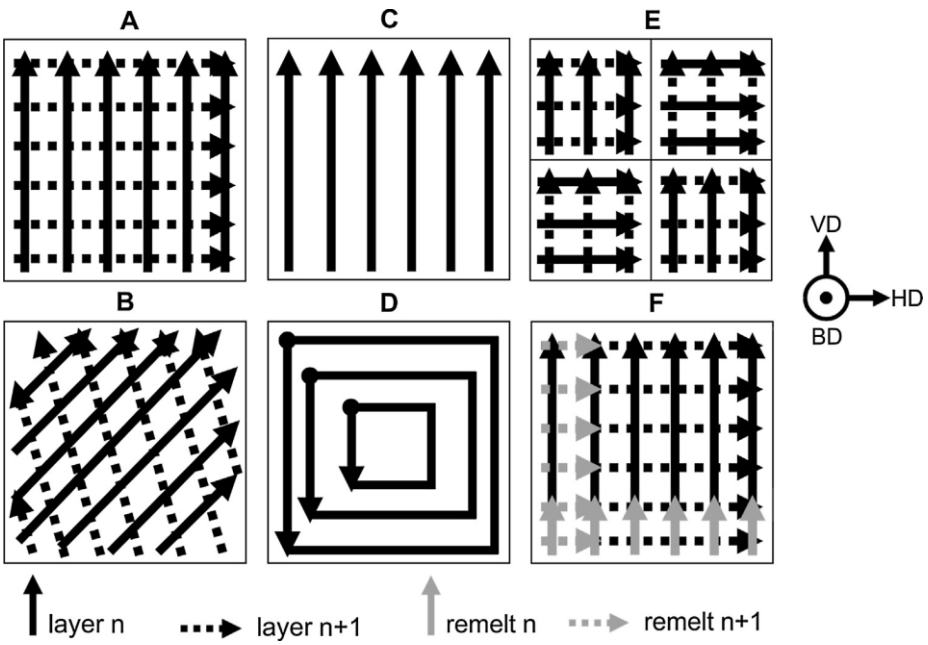

Figure 1.15: Overview of the scanning strategies: unidirectional scanning vectors with rotation in neighbouring layers (A and B), unidirectional scanning vectors (C), offset scanning (D), chessboard scanning (E), re-melting strategy (F). Taken from [165].

1.4.2 Solidification and thermal history

Selective laser melting is a rapid manufacturing technology based on a laser beam. The energy transfer and the thermal transmission during the process is based on the inverse bremsstrahlung absorption mechanism (IBA) [196]. During the SLM process, the interaction between the laser beam with a high energy density (10^5 - 10^7 W/cm^2) and the alloy powder is completed in very short duration (10^{-3} - 10^{-2} s). Under certain circumstances, this energy transfer is sufficiently effective to melt and even evaporate the alloy in a very short time [197-200]. When evaporation or incomplete melting is avoided, the small melt pool produced by the laser solidifies quickly, leading to high cooling rates (10^3 - 10^8 K/s) [197-200].

Pauly et al. have investigated the microstructure of the eutectic Al-33Cu (wt.%) alloy fabricated via SLM with different two different parameter sets but the same energy input to determine the cooling rate of SLM [198]. Their investigation reveals that the cooling rate of SLM is of the order of 10^4 - 10^5 K/s [198].

The different process parameters at a constant energy density are known to result in various cooling rates [198]. In any case, the cooling rates achieved during SLM are usually higher than for conventional casting [197-200]. Such rapid solidification may result in a substantially different microstructure of the additively manufactured alloy from compared to traditionally prepared alloys, which opens a gateway to even locally tailor the physical and chemical properties of the alloys [156].

The high inherent cooling rates are also inevitable for obtaining a glassy state from a metallic melt. As discussed above (section 1.2), local variations in the thermal history could result in the formation of heterogeneities in metallic glasses, which should reflect in the mechanical properties [70]. While crystals are relatively straightforward to detect, structural heterogeneities (i.e. local differences in free volume, see section 1.1) in monolithic glasses are difficult to probe. When dealing with glass-forming alloys produced by SLM it is, therefore, imperative to have a closer look at the thermal history of the process, which shall be done in the following.

The determination of the cooling rate in an individual melt track has been studied by investigation of the corresponding microstructures [201]. It has been revealed for Al-Cu alloy that the cooling rate decreases from the central part to the boundary of the melt track [201]. Similar studies have been also carried out by using other Al alloys and their composites [202-205]. All these works arrive at the same conclusion: the cooling rate decreases from the central part of the melt pool towards its margins [202-205].

The laser beam is a highly concentrated heat source and depending on the energy input, already solidified layers are partially or fully re-melted during selective laser melting of a fresh powder layer [206]. Moreover, the region around each melt track is subjected to an additional heat treatment. Wang *et al.* have used Al-Cu alloys to study microstructural differences in multilayers owing to local variations in the cooling rate [207]. In their work, a high-cooling-rate zone (HCRZ), a low-cooling-rate zone (LCRZ) and a heat-affected zone (HAZ) have been defined (Fig. 1.16) [207]. The HAZ is the additionally heat-treated solidified region around the melt track [207]. As mentioned above, the size of the HAZ depends on the alloy composition, due to different thermal conductivities and reflectivities of the electromagnetic radiation.

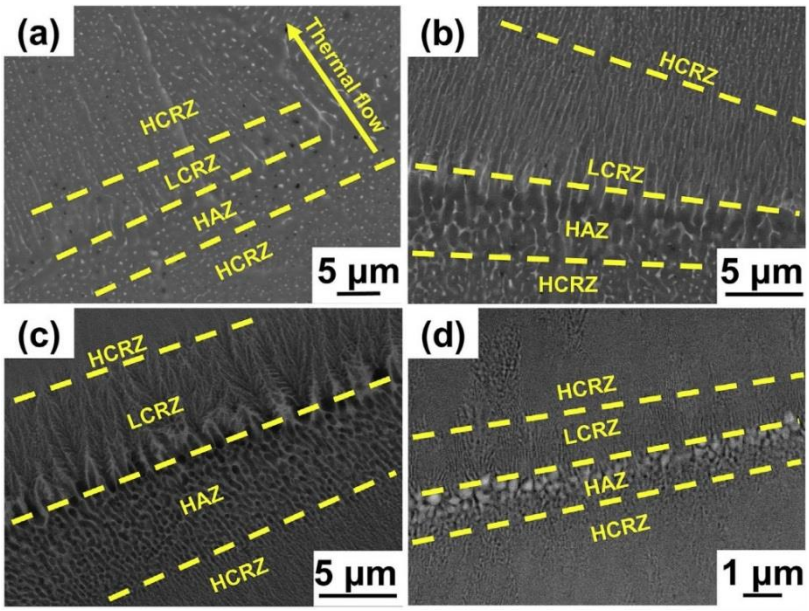

Figure 1.16: Microstructures of SLM Al-Cu alloys, (a) Al-4.5Cu, (b) Al-6Cu, (c) Al-20Cu, (d) Al-33Cu. Taken from Ref. [207].

Since the SLM process is a layer-by-layer process, its unique thermal history leads to a specific solidification behaviour [153, 156, 208]. Unfortunately, it is extremely challenging to monitor the spatial temperature distribution during selective laser melting. Simulation is an effective way to gain deeper insights into the thermal history. There are numerous works about the numerical investigation on temperature evolution and thermal behaviour during SLM process [208-216]. As displayed in Fig. 1.17, the melt pool is semi-elliptical. The temperature decreases with increasing distance from the centre of the molten pool. The part around the molten pool is the heat affected zone (HAZ) [206]. The temperature rise in already processed and solidified layers is substantially heated (Fig. 1.17). When SLM is used to produce BMGs, the additional heat from subsequently processed layers may induce structural relaxation or even crystallization in the already solidified glassy parts [217] (see section 1.1).

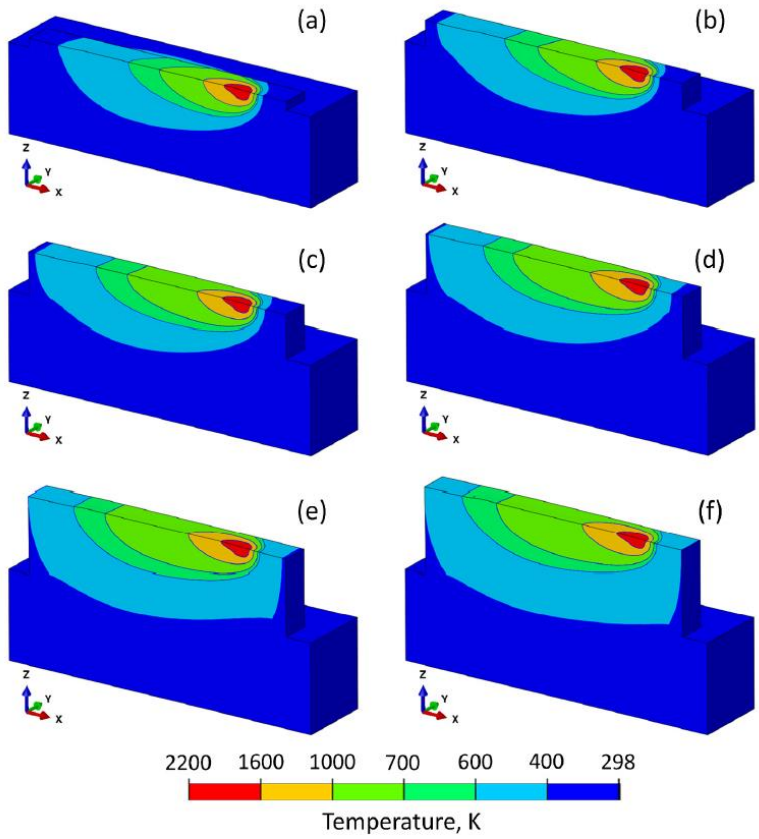

Figure 1.17: Temperature distribution of (a) 1st (b) 3rd (c) 5th (d) 7th (e) 9th and (f) 10th layer. Taken from [206].

1.5 Selectively laser-melted glass formers

As discussed above, selective laser melting (SLM) entails high cooling rates (10^3 - 10^8 K/s) [197-200], which is a prerequisite for glass formation. Simultaneously, the layer-by-layer processing allows for the production of delicate and complex geometries, which are otherwise inaccessible to conventional melt quenching techniques [218]. For conventionally cast BMGs, only simple geometries, such as rods and plates can be obtained with ease [9]. It is hard, yet, to obtain BMGs with complex geometries. This makes SLM a very promising approach in terms of making BMGs accessible to practical applications, which are still largely confined owing to their small as well as usually simple geometries [40].

1.5.1 Selective laser melting of a single alloy powder

Because of their unique potential mentioned above (see section 1.4), different glass-forming alloys such as Fe-based, Cu-based, Zr-based and Al-based alloys have been processed by SLM to date [128, 200, 217, 219-239]. The respective alloy compositions including some remarks are summarized in Table 1.1.

Table 1.1 Summary of the glass-forming compositions processed by SLM to date.

Composition (at.%)	Year	Remarks	Ref.
$Zr_{55}Cu_{30}Al_{10}Ni_5$	2012	Partially crystalline, line scan	[226]
$Fe_{74}Mo_4P_{10}C_{7.5}B_{2.5}Si_2$	2013	Partially crystalline, cracks	[200]
$Al_{86}Ni_6Y_{4.5}Co_2La_{1.5}$	2014	Partially crystalline, line scan	[225]
$Fe_{68.3}C_{6.9}Si_{2.5}B_{6.7}P_{8.7}Cr_{2.3}Mo_{2.5}Al_{2.1}$	2015	Fully amorphous, cracks	[227]
$Zr_{52.5}Cu_{17.9}Ni_{14.6}Al_{10}Ti_5$	2016	Partially crystalline, crack-free	[219]
$Zr_{55}Cu_{30}Al_{10}Ni_5$	2017	Partially crystalline, crack-free	[128, 217]
$Zr_{52.5}Cu_{17.9}Ni_{14.6}Al_{10}Ti_5$	2017	Fully amorphous, crack-free	[220]
$Fe_{43.7}Co_{7.3}Cr_{14.7}Mo_{12.6}C_{15.5}B_{4.3}Y_{1.9}$	2018	Partially crystalline, cracks	[228, 229]
$Zr_{59.3}Cu_{28.8}Nb_{1.5}Al_{10.4}$	2018	Fully amorphous, crack-free	[222, 230]
$Fe_{54.35}Cr_{18.47}Mn_{2.05}Mo_{13.93}W_{5.77}B_{3.22}C_{0.9}Si_{1.32}$	2019	Partially crystalline, cracks	[233]
$Fe_{71}Si_{10}B_{11}C_6Cr_2$	2019	Partially crystalline, cracks	[234]
$Cu_{50}Zr_{43}Al_7$	2019	Partially crystalline, crack-free	[231]
$Zr_{60.14}Cu_{22.31}Fe_{4.85}Al_{9.7}Ag_3$	2019	Fully amorphous, crack-free	[239]
$(Ti_{0.65}Zr_{0.35})_{90}Cu_{10}$	2019	Partially crystalline, crack-free	[238]
$Zr_{57.4}Ni_{8.2}Cu_{16.4}Ta_8Al_{10}$	2019	Partially crystalline, crack-free	[235]
$Fe_{73.7}Si_{11}B_{11}C_2Cr_{2.28}$	2019	Partially crystalline, cracks	[237]
$Fe_{55}Cr_{25}Mo_{16}B_2C_2$	2019	Fully amorphous, cracks	[236]
$Cu_{46}Zr_{47}Al_6Co_1$	2020	Partially crystalline, crack-free	[232]

As shown in Table 1.1, only a few fully amorphous BMGs have been obtained by SLM. Most of the additively manufactured BMGs contain crystalline phases and, thus, represent BMG matrix composites. The precipitation of crystals can be attributed to two main reasons: (i) the

quality of the initial powder [233] and (ii) the additional heat treatment arising in heat-affected zone (HAZ) [128, 217]. Both shall be briefly discussed in the following.

Initially partially crystalline powder may retain its microstructure after the SLM process [200, 223, 226]. In order to investigate the formation of crystals in the powder, Nong *et al.* [233] have identified the phases found in the powder with different particle sizes. Those particles with sizes ranging between 2 and 53 µm have fewer crystals than particles with the sizes between 53 and 150 µm. The cooling rates during gas atomization depend on the particle size, and lower cooling rates (i.e larger particle sizes) result in a larger crystalline volume fraction [233]. During the SLM process, the partially crystalline powder is completely melted and subsequently solidifies in a very short time (see section 1.4.2). One could thus expect that the melt congeals into a glass, which is sometimes the case (see section 1.1) and sometimes not [128, 217]. The retention (or precipitation) of the crystalline phase in the final SLM parts may be due to an insufficient overheating. By selecting a finer powder fraction and/or using optimized process parameters (i.e. an increased energy input), the formation of fully glassy samples might be facilitated.

In certain additively manufactured metallic glasses, the crystalline phases are exclusively found in the HAZ [128, 217]. Ouyang *et al.* [128] have used fully glassy $Zr_{55}Cu_{30}Al_{10}Ni_5$ powder to produce a crack-free Zr-based BMG via SLM. As shown in Fig. 1.18, there is an obvious boundary between the molten pool and the heat-affected zone. The selected area electron diffraction (SAED) pattern shows broad and diffuse rings, suggesting a fully amorphous structure in the central part of the molten track. Yet, nanocrystals can be revealed in the HAZ. The same phenomenon has been also found in Cu- and Zr-based BMGs produced by SLM [219, 231]. Li *et al.* [219] have argued that crystallization was caused by the non-uniform melt flow at high energy densities. The resulting chemical heterogeneity of the supercooled liquid leads to crystallization. Since crystallization is non-polymorphic in most glass formers [97, 240] extended atomic diffusion is generally required for the precipitation of crystals [220]. Thus, chemical heterogeneity might be a consequence of crystallization rather than its origin [220]. Another explanation, hence, would be that excess heat in the heat-affected zone is the reason for the precipitation of the crystals: The individual anneals resulting from the processing of subsequent layers continuously nucleates crystals in the supercooled liquid and stimulates their growth.

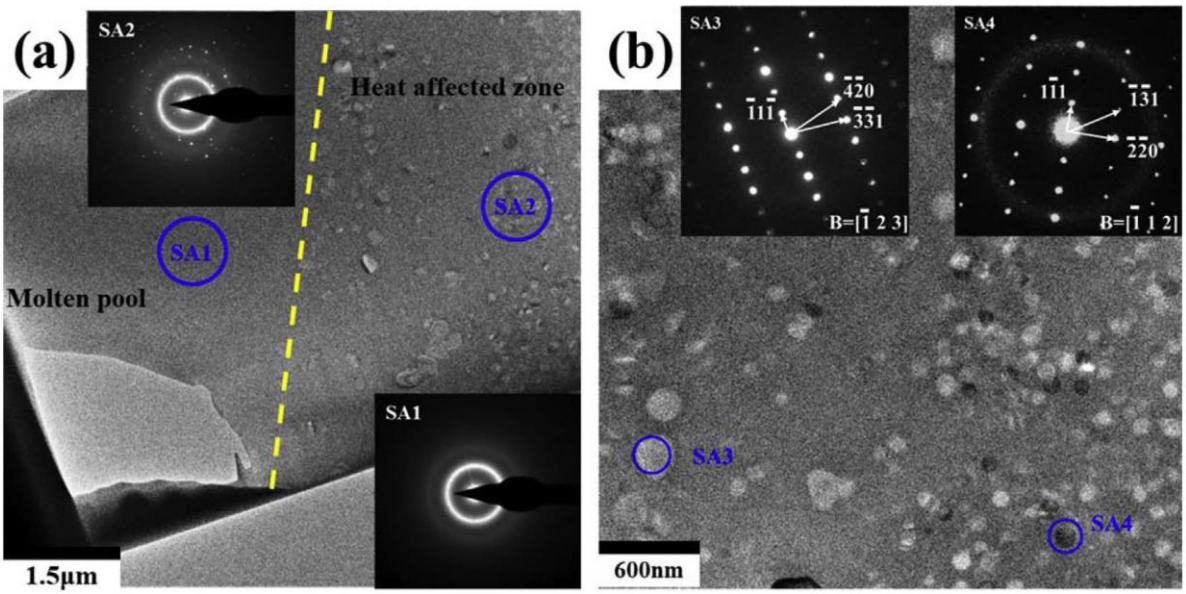

Figure 1.18: TEM images and associated SAED patterns of the interface between molten track and HAZ (a), selected region in HAZ (b). The broad and diffuse rings indicate a fully amorphous structure in SA1. There exist nanocrystals in HAZ. Taken from [128].

In order to better understand the thermal history of a melt track and its surroundings, FEM has been carried out to simulate the thermal field in glass-forming alloys [128, 228, 241]. The temperature distribution and its temporal evolution calculated in Zr-based BMGs reveal that the melt pool solidifies at high rates (10^4 K/s) as to ensure the formation of monolithic glasses [128]. However, the temperature in the HAZ can exceed the crystallization temperature (T_x). Depending on how long such elevated temperatures prevail, crystals may precipitate or not in the HAZ (see section 1.1 and Fig. 1.17). Simulations suggest that this time span, at which the temperature is above the crystallization temperature, can reach up to 5 ms [128]. Such short anneals do not provide the time for substantial crystal growth. Consequently, only nanocrystals have been observed in the HAZ of glass-forming alloys [128, 217] (Fig. 1.18).

Apart from avoiding (partial) crystallization in selectively laser-melted BMGs, the fabrication samples with a high relative density is of utmost importance. As displayed in Table 1.1, there are micro-cracks in some additively manufactured BMGs. Porosity and the presence of micro-cracks in additively manufactured BMGs generally leads to poor mechanical properties [49, 227]. The formation of micro-cracks is usually attributed to thermal stresses [242, 243]. A high laser power enhances thermal stresses, often resulting in cracks [225]. Low energy input results in unmelted powder and high porosity, which also may induce the formation of micro-cracks [225].

To eliminate or at least reduce micro-cracks, the mechanism underlying the formation of cracks in Fe-based BMGs produced by SLM has been studied in more detail [229]. It has been

demonstrated that the concentration of thermal stresses around defects is the origin of crack formation. The concentration of stresses is significant at the interface between molten track and HAZ. In a similar way, Xing *et al.* [242] have analysed the residual stress in Zr-based additively manufactured BMGs. Their results indicate that the sample prepared using a XY cross-scanning strategy (unidirectional scanning vectors rotated by 90° in adjacent layers, see Fig. 1.15) contains less residual stresses than the ones fabricated using single directional scanning strategy. Preheating the substrate is also an effective method to reduce residual stress [244]. In addition, the geometry and its orientation with respect to the building direction has a significant influence on the generation of residual stresses [243]. The crucial factors revealed above provide a useful guidance to avoid the formation of micro-cracks and the premature failure of additively manufactured BMGs during processing.

Although (partial) crystallization within the HAZ and the formation of defects are difficult to avoid during selective laser melting, Pauly *et al.* have successfully produced a fully amorphous Zr-based BMG with a high relative density via SLM by optimizing process parameters [220], indicating that SLM is a promising preparation method for BMGs.

1.5.2 Heterogeneities and mechanical properties of additively manufactured BMGs

Table 1.1 lists a number of crack-free Zr- and Cu-based BMGs successfully processed by SLM [128, 219, 220, 223, 231, 239]. Because the mechanical properties of metallic glasses are one of their outstanding features and render them interesting for a variety of applications (see section 1.2), the mechanical properties of these additively manufactured BMGs have been usually also explored under uniaxial compression. It has been observed that these additively manufactured BMGs tend to fail in a premature manner without significant plastic strain [128, 219, 220, 223, 231].

As discussed in section 1.2.3, heterogeneities play an important role for the mechanical properties of BMGs. These heterogeneities can be broadly classified as (i) crystalline phases, (ii) pores and (iii) more/less relaxed amorphous regions (i.e. a heterogeneous distribution of free volume) [128, 219, 220, 223, 231, 245]. The following sections shall illuminate these aspects in a bit more depth.

The fracture strength of additively manufactured, partially crystalline BMGs exhibits a relatively broad scatter due to the varying volume fractions of glass and crystals [128, 223]. When the glassy volume fraction is around 63% in a $Zr_{55}Cu_{30}Al_{10}Ni_5$ BMG, the fracture strength is in the range of 1270 - 1450 MPa. When it reaches 83%, the fracture strength increases to around 1500 MPa [128, 223]. Since in most of the additively manufactured Zr- and Cu- based

BMGs, the crystalline phases were identified as $NiZr_2$, $CuZr_2$ and $Cu_{10}Zr_7$ [128, 223, 231]. Such phases may lead to poor mechanical properties [128, 223, 231]. Thus, the formation of crystalline phases in the HAZ appears to be one of the main reasons for the premature failure of additively manufactured BMGs.

Of the additively manufactured, crack-free BMGs, only $Zr_{52.5}Cu_{17.9}Ni_{14.6}Al_{10}Ti_5$ [220] and $Zr_{60.14}Cu_{22.31}Fe_{4.85}Al_{9.7}Ag_3$ [239] show a small but distinct plastic strain (Fig. 1.19). As displayed in Fig. 1.19, the additively manufactured $Zr_{52.5}Cu_{17.9}Ni_{14.6}Al_{10}Ti_5$ samples trend to fail at lower strains than the corresponding as-cast glass. Even though the relative density for the additively manufactured BMGs can reach 98.5%, there exist pores, some of which stretch over several layers [220]. Often the observed residual porosity of only a few percent is held responsible for the absence of significant plasticity of additively manufactured BMGs [220] .

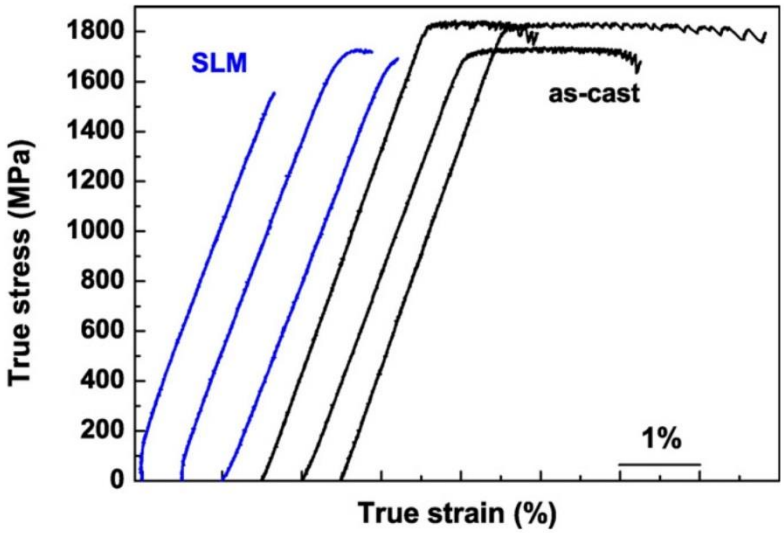

Figure 1.19: Compression stress-strain curves of $Zr_{52.5}Cu_{17.9}Ni_{14.6}Al_{10}Ti_5$ SLM samples and as-cast samples. Taken from [220].

As revealed in section 1.4.2, during SLM, the laser beam does not only melt the topmost powder layer, but also the already solidified layers underneath it. The excessive heat is subsequently dissipated in the surrounding glass. Because the laser beams scan the sample and the component is produced layer by layer, the thermal history of selectively laser-melted alloys is rather complex (see section 1.4.2). Such a complex thermal history is likely to induce structural heterogeneities consisting of more or less relaxed glassy regions. These heterogeneities can be probed with DSC measurements, nanoindentation and X-ray measurements. Best *et al.* [245] have used synchrotron X-ray micro-diffraction and nanoindentation to reveal structural heterogeneities in an additively manufactured $Zr_{59.3}Cu_{28.8}Nb_{1.5}Al_{10.4}$ glass. As shown in Fig. 1.20, small periodic variations of the elastic

modulus have been observed in the order of 40 - 80 µm, which is 2 - 4 times the selected layer thickness (20 µm). This structural variation seems dependent on the local thermal history and it has significant effects on the local mechanical properties. However, in Best's study [245], only one additively manufactured BMG system has been studied. As discussed in section 1.4.2, the size of the molten pool and the HAZ depends on the process parameters and the alloy composition. The following questions naturally arise: Can the heterogeneities also be found in other monolithic BMG systems produced via SLM with different process parameters? How do such structural heterogeneities affect shear banding in compression tests? These questions will be discussed in Chapter 3 (section 3.2.4 and 3.3).

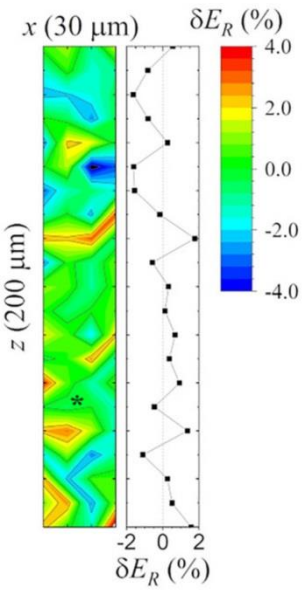

Figure 1.20 Nanoindentation map and line-scan average of the cross section. δE_R is the variation of the mean E_R value. Taken from [245].

Besides structural heterogeneities (crystalline phase, porosity and more/less relaxed regions), which can form in the additively manufactured BMGs produced with single alloy powder, heterogeneities can be also deliberately generated by mixing glass-forming powder with conventional alloy powder.

Generally speaking, the distribution and sizes of the reinforcing particles are difficult to control when traditional melt-quenching techniques are employed [49, 87]. As discussed in sections 1.5.1, SLM offers new possibilities of producing BMGs. By mixing different powders, one gains a large degree of freedom regarding the microstructural design, i.e. the length scales and the distribution of the constituent phases. The first study in this direction has investigated the effect of mixing an intrinsically brittle Fe-based BMG with Cu and Cu-Ni powder prior to selective laser melting [221]. By adding Cu and Cu-Ni alloys as reinforcing phases, micro-

cracking in the SLM parts is alleviated and the fracture toughness could be significantly enhanced. As shown in Fig. 1.21, reactions occurred at the interface of Cu and amorphous matrix and crystalline particles in nano-scale formed. The crystalline phases do not seem to significantly influence the mechanical properties. However, these aspects are of importance in other systems. Diffusion of elements across the crystal-glass interface might affect the glass-forming ability and the phase formation, thus having a large impact on the result of the SLM process and the performance of the material.

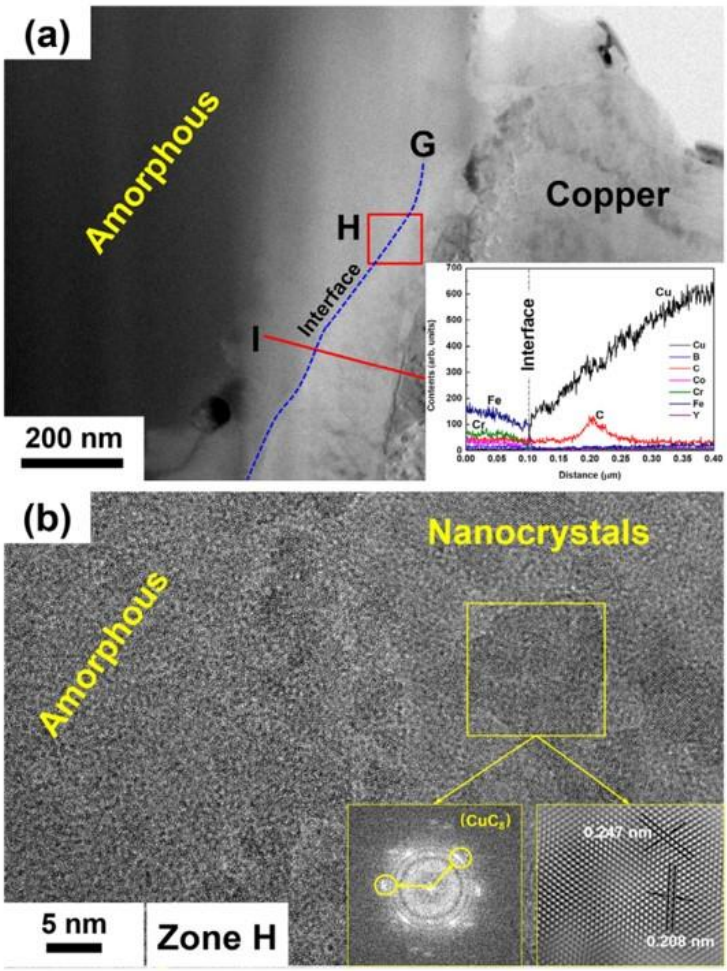

Figure 1.21 (a) TEM micrographs of the interface between amorphous matrix and additional Cu particle in the additively manufactured Fe-based BMGCs reinforced by pure Cu. The inset illustrates the EDXS profile cross the boundary between the BMG-matrix and the Cu particle. The contents of almost all the elements reduce dramatically at the interface. Only C does not change a lot. (b) HRTEM of the boundary zone H. Nanocrystals (CuC_8) formed at the interface. Taken from [221]

CHAPTER 2 Experimental

2.1 Sample preparation

In the present work, glass-forming alloys with nominal compositions of $Zr_{52.5}Cu_{17.9}Ni_{14.6}Al_{10}Ti_5$ (at.%) $Ti_{47}Cu_{38}Zr_{7.5}Fe_{2.5}Sn_2Si_1Ag_2$ (at.%) and $Cu_{46}Zr_{46}Al_8$ (at.%) were fabricated via SLM and, for comparison, via casting. In the following paragraphs, the details of the sample preparation are given.

2.1.1 Arc melting

The elements used in this study have high purities (over 99.9%). The constituent elements (Zr, Cu, Ni, Al, Ti, Fe and Sn) were ground with 800 grit grinding paper to remove surfaces oxides and impurities before alloying. Afterwards, the elements were cut to an appropriate weight (the accuracy is around 0.001g) for alloying. The weight of each ingot was between 20 and 30 g. The employed arc-melter (Edmund Bühler GmbH) consists a melting system and a vacuum system. After placing the elements in the water-cooled Cu hearth, the device was evacuated up to a pressure of 10^{-4} - 10^{-5} mbar. Then the device was flushed with argon. A tungsten electrode was used to melt a Ti getter first for absorbing the residual oxygen in the chamber. The melting time and melting current depend on the compositions. Each ingot was re-melted at least three times to ensure chemical homogeneity.

2.1.2 Suction casting

After alloying the ingots were cracked into pieces. 4 or 7 g pre-alloy pieces were used to cast cylindrical rods with a diameter of 2 or 3 mm and a length of 50 mm. The arc-melter (Edmund Bühler GmbH) has a facility for suction casting (Fig. 2.1). When the chamber was evacuated to 10^{-3} mbar, the under pressure tank which was connected with the Cu mould was closed to form a pressure difference between the chamber and the suction facility. After the pressure reached 10^{-4} - 10^{-5} mbar, the chamber was flushed with argon. When the melt reached a certain fluidity, the under pressure tank was opened. With the pressure difference, the liquid alloy was sucked into the Cu mould.

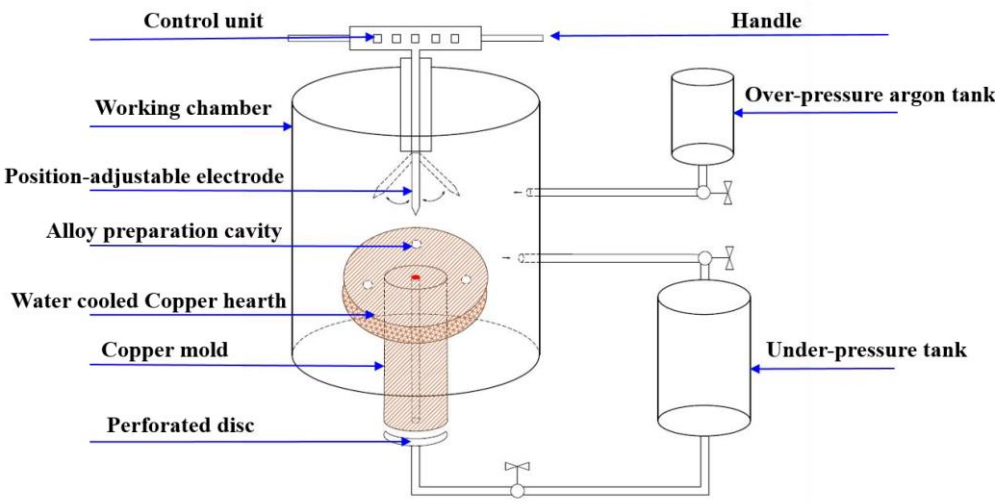

Figure 2.1: Schematic illustration of an arc-melter. The device includes melting system, pressure control system and casting system. Taken from [246].

2.1.3 Gas atomization

The $Zr_{52.5}Cu_{17.9}Ni_{14.6}Al_{10}Ti_5$ (at.%) and $Ti_{47}Cu_{38}Zr_{7.5}Fe_{2.5}Sn_2Si_1Ag_2$ (at.%) ingots with a weight of 50 g were first prepared by arc melting (ALD Vacuum Technologies AG). Afterwards, they were transformed to powder by NANOVAL GmbH & Co. KG via electrode induction-melting gas atomization (EIGA). A $Cu_{46}Zr_{46}Al_8$ (at.%) rod with a weight of 5 kg was prepared at the Institute of Metal Research, Chinese Academy of Science, Shenyang, China. Afterwards the rod was transformed to powder by TLS Technik GmbH & Co. Spezialpulver KG via gas atomization. The particle size distribution was obtained by using dynamic image analysis (CAMSIZER X2, Retsch TECHNOLOGY). After sieving, a particle size below 90 µm was chosen for selective laser melting.

2.1.4 Powder mixtures

In order to study the fabrication of BMGCs via SLM, 2 wt.% and 10 wt.% non-spherical Nb powder (particle size ≤ 63 µm) (AVIMETAL PM) was mixed with the amorphous gas-atomized $Zr_{52.5}Cu_{17.9}Ni_{14.6}Al_{10}Ti_5$ powder in protective argon atmosphere. A drum hoop mixer (JEL PRM Mini-II) was used for 30 min at a speed of 30 rounds per minute.

Figure 2.2: Photograph of the drum hoop mixer.

2.1.5 Selective laser melting (SLM)

The SLM process were carried out using a SLM 50 (Realizer GmbH) equipped with a 120 W fiber laser (spot size: 50 μm) at room temperature. All the SLM samples were prepared on a steel substrate, which was sandblasted prior to the experiment. The rough surface of the substrate is beneficial for the powder deposition of the first few layers, ensuring the quality of the powder bed. High-purity Ar was used to purge the chamber and remain the oxygen content less than 0.01 vol.% throughout the whole process.

Figure 2.3: Photograph of the SLM 50 (Realizer GmbH) system.

For the $Zr_{52.5}Cu_{17.9}Ni_{14.6}Al_{10}Ti_5$ (at.%) SLM samples, a laser power of 109.5 W, a scanning speed of 1000 mm/s, a layer thickness of 40 μm and a hatch distance of 200 μm was employed.

The unidirectional scanning vectors were rotated by 90° in adjacent layers. These parameters represent an optimized process compared to our previous experiments [220]. For the $Zr_{52.5}Cu_{17.9}Ni_{14.6}Al_{10}Ti_5$ glass matrix composites, the laser power was slightly adjusted to 105 W because of the Nb additions. All other process parameters were identical to those used for pure $Zr_{52.5}Cu_{17.9}Ni_{14.6}Al_{10}Ti_5$ powder.

For the $Ti_{47}Cu_{38}Zr_{7.5}Fe_{2.5}Sn_2Si_1Ag_2$ (at.%) SLM samples, a parameter optimization was conducted in order to produce dense specimens. The laser power was varied between 37.5 and 120 W. The range of scanning velocities was between 600 mm/s and 900 mm/s. The layer thickness and hatch distance were fixed as 40 µm and 140 µm, respectively. The unidirectional scanning vectors were also rotated by 90° in neighbouring layers.

For the $Cu_{46}Zr_{46}Al_8$ (at.%) SLM samples, a constant layer thickness of 40 µm was selected for all experiments. The hatch distance was also fixed as 180 µm. The scanning velocity was altered from 800 mm/s to 1200 mm/s with a step size of 100 mm/s. The laser power was changed from 60 W to 120 W with a step size of 3 W at each scanning velocity. The scanning strategy was also kept as unidirectional vectors rotated by 90° in neighbouring layers.

By using the different process parameters, cylindrical specimens with diameters of 2 or 3 mm and a length of 6 mm were produced. To further study the deformation mechanism of additively manufactured BMGs, rectangular samples (dimension of $3 \times 3 \times 6$ mm^3) were also prepared.

2.1.6 Heat treatment

In order to better analyse the crystalline phases, which formed during the SLM process, an additional heat treatment was carried out in an FRH-3-40-500-110 furnace (Linn High Therm.). Prior to the heat treatment, the samples were put in a glass tube, the interior of which was then filled with Argon to avoid the oxidation of the sample. The $Zr_{52.5}Cu_{17.9}Ni_{14.6}Al_{10}Ti_5$ as-cast samples were heat-treated at 973 K and 873 K for 24 h. The as-cast $Zr_{52.5}Cu_{17.9}Ni_{14.6}Al_{10}Ti_5$ samples with 10 wt.% Nb ($Zr_{48.3}Cu_{16.5}Ni_{13.4}Al_{9.2}Ti_{4.6}Nb_8$ (at.%)) were also annealed at 973 K for 24 h. Afterwards, the samples were air cooled. The heat treatment was done with the help of Siegfried Neumann and Juliane Scheiter at IFW Dresden.

2.2 Sample characterization methods

After the synthesis of the BMG samples via casting or SLM, the physical and chemical properties of the materials were analysed by using various methods. In the following sections, these methods and the respective parameters are listed.

2.2.1 Composition analysis

The gas atomization and SLM process may introduce oxygen or other elemental contamination. Moreover, preferential evaporation of certain elements during arc melting may occur. The exact chemical composition and the amount of contaminants, thus, have to be carefully checked. The chemical composition and the oxygen content of the powder, as-cast and SLM specimens were measured using ICP-OES (inductively-coupled plasma-optical emission spectroscopy, IRIS Intrepid II XUV from Thermo Fischer Scientific GmbH) and carrier gas hot extraction (TC-436DR, LECO), respectively. Three independent powder batches were measured to ensure the accuracy and reproducibility of the measurements. The chemical analysis was done by Andrea Voß at IFW Dresden. The oxygen content was measured by Heike Bußkamp at IFW Dresden.

2.2.2 X-ray diffraction

X-ray diffraction (XRD) for phase identification was done on two different devices. One was a D3290 PANalytical X'pert PRO diffractometer with Co-K_α-radiation (λ = 0.17889 nm) in reflection mode. The specimens were sliced into 2 mm thick pieces and ground (800 grit) to ensure that the samples have a uniform thickness. The scanning angle was set between $2\theta = 20°$ and 100°. The device was operated at a voltage of 40 kV and a current of 40 mA. The other diffractometer used in this study is a STOE STADIP diffractometer (STOE & Cie GmbH) with Mo-$K_{\alpha 1}$-radiation (λ = 0.07093187 nm) in transmission mode. The samples were ground to a thickness of 80 - 120 µm. The measurements on the STOE STADIP diffractometer were completed with the help of Dr. Konrad Kosiba.

2.2.3 Calorimetry

The differential scanning calorimetry (DSC) measurements were performed from 313 K to 873 K in a Perkin-Elmer Diamond calorimeter under the argon atmosphere. All the specimens with a weight of about 17 mg were measured at a heating rate of 0.33 K/s and a subsequent cooling rate of 1.67 K/s. In order to get the base line, two consecutive heating cycles were recorded: The samples were held at 313 K for 10 min, then heated up to 873 K at the rate of 0.33 K, afterwards cooled down to 313 K at the rate of 1.67 K/s, held there for 10 min again, heated up to 873 K at the rate of 0.33 K. The Al_2O_3 crucibles were carried out for all the measurements. To investigate the influence of layer-by-layer process method from SLM on the structural relaxation of the glasses, the rods were sliced into the same thickness (about 650 µm) along the building direction, as shown in Fig. 2.4 and measured by DSC. The DSC measurements were done by Birgit Bartusch at IFW Dresden.

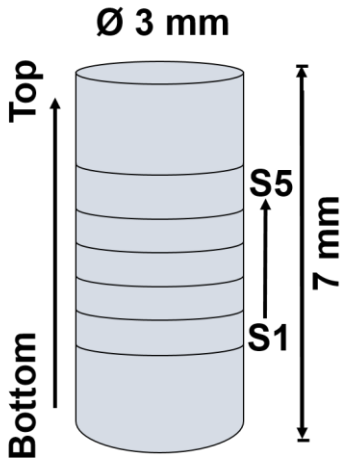

Figure 2.4: Schematic illustration of the DSC samples. The samples (S1 to S5) were taken from bottom to the top of the additively manufactured rods.

2.2.4 Density measurements (Archimedean method)

For SLM samples, density is a decisive factor to evaluate their quality. The density of all the SLM samples was measured by the Archimedean method using a Sartorius density balance (MSA 225S). Samples were first weighed in air and afterwards weighed in distilled water. By using the difference of the two values obtained in air and water, the density of the sample can be calculated.

2.2.5 µ-CT

By analysing the shape and distribution of the defects formed during the SLM process, the process parameters can be optimized. X-ray micro-computed tomography is an effective method to obtain such information. In this study, the shape and distribution of particles and pores, as well as the relative density were analysed by means of a Phoenix nanotom m (General Electric) equipped with a tungsten-diamond target at 130 kV and 100 µA. According to the dimensions of the samples, the voxel size ranged between 1 µm to 5 µm. A part of the analysis was carried out with the help of Dr. Alexander Funk at IFW Dresden.

2.2.6 Scanning electron microscopy (SEM)

The microstructures and fracture surfaces were investigated in a scanning electron microscope (SEM, Gemini 1530, Carl Zeiss AG) in back-scattered electron (BSE) mode and secondary electron (SE) mode. The device is equipped with an energy-dispersive X-ray spectroscope (EDS; Quantax400 with SDD-Detector Xflash4010, Bruker) to analyse the distribution and the contents of different elements. The SE mode was carried out to observe the fracture morphologies, worn surfaces and the surfaces after corrosion tests. The BSE mode was

used to identify the BMG matrix and Nb addition, as well as the interface between them. The device was operated at a voltage of 15 - 20 kV, 60 - 120 µm aperture and the working distance was 10 - 12 mm.

2.2.7 Transmission electron microscopy (TEM)

For more detailed structural investigations, a FEI Tecnai F20 transmission electron microscope (TEM) equipped with a field emission gun was used. The specimens with a diameter of 3 mm were first ground to the thickness of about 45 µm, with P800, P1200, P2500 and P4000 sand paper. Afterwards, the samples were dimpled to reduce the central thickness to about 10 µm, followed by ion-milling until perforation using a Gatan 691 with liquid nitrogen cooling. High-resolution micrographs and selected area electron diffraction (SAED) patterns were used to analyse diffusion processes and the final microstructure of the samples. The sample preparation was achieved with the help of Dina Bieberstein at IFW Dresden, Germany. The sample observation and analysis were done by Dr. Long Zhang at the Institute of Metal Research, Chinese Academy of Science, Shenyang, China.

2.2.8 Hardness measurements

Prior to the microhardness measurements, the samples were ground to 4000 grit and polished. Vickers microhardness measurements were performed on polished samples using an HMV Shimadzu Microhardness tester. Indents were created with a load of 200 g and 10 s of dwell time. The schematic of the location, at which microhardness indents are placed on the cross and longitudinal sections, is shown in Fig. 2.5.

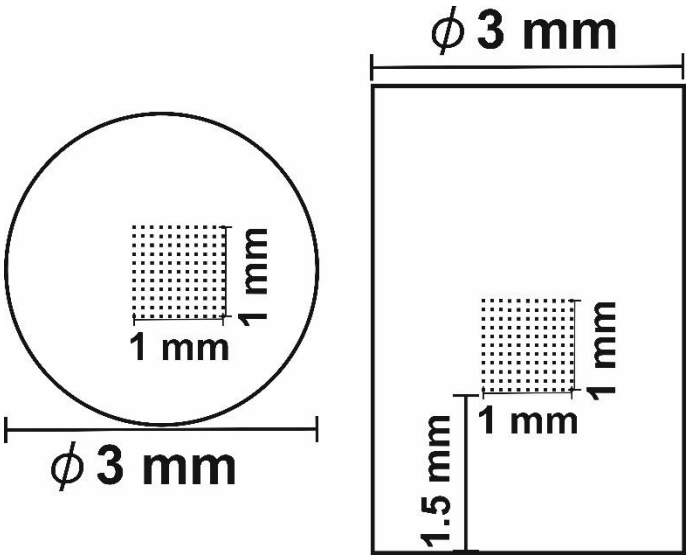

Figure 2.5: Schematic illustraton of locations for the indents.

Nanoindentation testing was performed on both cross and longitudinal sections of the sample using a nanoindenter platform (G200, Agilent Inc.), equipped with a three-sided Berkovich diamond tip. Indents with a maximum load of 10 mN were created at a constant loading rate of 1 mN/s (i.e., a loading duration of 10 s) and with a 5 s dwell time at peak load. 170 indents on longitudinal section as well as 143 indents on the cross section for each sample and the spacing between the individual indents is illustrated in the section 3.1.3.3. The hardness, *H*, was calculated from the load, *P,* divided by the projected contact area of the indenter tip, A_c:

$$H = \frac{P}{\mathrm{Ac}} \tag{2.1}$$

The Young's modulus, *E,* was derived from the reduced elastic modulus, E_r, using the Poisson's ratio, v:

$$E = (1 - v^2)\left[\frac{1}{E_r} - \frac{1-\mathrm{v_i}^2}{E_i}\right]^{-1} \tag{2.2}$$

with:

$$E_r = \frac{S}{2}\sqrt{\frac{\pi}{A_c}} \tag{2.3}$$

where v_i is the Poisson ratio of 0.07 and E_i is the elastic modulus of 1141 GPa [247, 248].

All the nanoindentation measurements and the corresponding analyses were done by Dr. René Limbach at The University of Jena, Germany.

2.2.9 Compression tests

Cylindrical SLM and as-cast $Zr_{52.5}Cu_{17.9}Ni_{14.6}Al_{10}Ti_5$, $Cu_{46}Zr_{46}Al_8$ and $Zr_{52.5}Cu_{17.9}Ni_{14.6}Al_{10}Ti_5$ samples with a length of 6 mm and a diameter of 3 mm were used for uniaxial compression tests. For the $Ti_{47}Cu_{38}Zr_{7.5}Fe_{2.5}Sn_2Si_1Ag_2$ SLM and as-cast samples, the dimension is 2 mm in diameter and 4 mm in length. Prior to the tests, the cylindrical surfaces were ground to ensure that they are parallel and perpendicular to the cylinder axis.

To further investigate the initiation and propagation of shear bands, one lateral side of the rectangular $Zr_{52.5}Cu_{17.9}Ni_{14.6}Al_{10}Ti_5$ SLM samples (dimension of $3 \times 3 \times 6$ mm^3) was polished prior to loading up to (i) the onset of plastic deformation (1400 MPa) and (ii) fracture.

The compression tests were performed at an initial strain rate of 2×10^{-4} s^{-1} in an Instron 5869 at room temperature. The strain was measured directly on the samples using Fiedler laser extensometer. To ensure the repeatability of the results, at least 3 specimens were measured for each condition.

2.2.10 Sliding wear tests

Pin-on-disk friction tests were carried out in a Tribometer (T500, Nanovea) at room temperature with the help of Alexander Schultze at IFW Dresden. The cylindrical as-cast and

additively manufactured $Zr_{52.5}Cu_{17.9}Ni_{14.6}Al_{10}Ti_5$ samples with a length of 20 mm and a diameter of 3 mm, whose surfaces were ground with 4000 grit SiC abrasive paper, and an X210Cr12 steel friction pair were used with a load of 15 N applied on the pin, a 15 mm radius of the wear track, a rotating speed of 240 RPM and a sliding duration of 480 min. The main parts of the device are marked and shown in Fig. 2.6. All the coefficients of friction (COF) data was recorded by the Nanovea Tribometer system. At least 3 samples of each process state were measured to ensure repeatability.

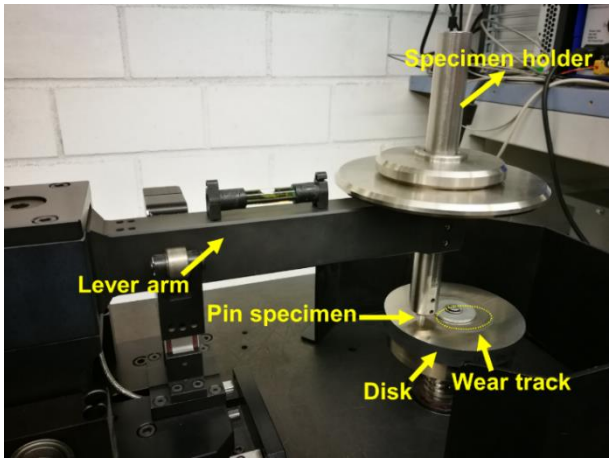

Figure 2.6: Main parts of the Tribometer. Provided by Alexander Schultze.

2.2.11 Corrosion tests

Cylindrical as-cast and additively manufactured $Zr_{52.5}Cu_{17.9}Ni_{14.6}Al_{10}Ti_5$ specimens with a length of 10 mm and a diameter of 3 mm, as well as cylindrical $Ti_{47}Cu_{38}Zr_{7.5}Fe_{2.5}Sn_2Si_1Ag_2$ SLM and as-cast samples, of which the dimensions were 2 mm in diameter and10 mm in length were electrically connected and embedded in epoxy resin for the electrochemical measurements. The cross section, the only part exposed to the corrosive environment of all the samples, was ground to 4000 grit, afterwards the interfaces between the sample and the epoxy resin were coated with a polymer to avoid crevice corrosion [133, 137].

For the $Zr_{52.5}Cu_{17.9}Ni_{14.6}Al_{10}Ti_5$ samples, all polarization tests were performed at ambient temperature in a 0.01 M Na_2SO_4 and 0.1 M NaCl solution with pH 6.5 using a Solartron SI1287 electrochemical interface, which was connected to a standard three-electrode cell with $Zr_{52.5}Cu_{17.9}Ni_{14.6}Al_{10}Ti_5$ specimens as working electrode, a saturated calomel electrode (SCE, E (SHE) = 0.241 V) as reference electrode and a Pt-net as the counterelectrode.

For the $Ti_{47}Cu_{38}Zr_{7.5}Fe_{2.5}Sn_2Si_1Ag_2$ samples, the device and working principle are the same as for the $Zr_{52.5}Cu_{17.9}Ni_{14.6}Al_{10}Ti_5$ samples. The corrosion tests for the as-cast and additively manufactured $Ti_{47}Cu_{38}Zr_{7.5}Fe_{2.5}Sn_2Si_1Ag_2$ as-cast and SLM samples were conducted in

Ringer's solution (8 g/L NaCl, 0.2 g/L KCl, 0.2 g/L $CaCl_2$ and 1 g/L $NaHCO_3$) with pH 7.4 at 310 K (37 °C).

To ensure that the samples of both compositions have reproducible surface states after grinding, they were exposed to air with a relative humidity of around 30% at room temperature for 20 h before they were tested in the electrolyte. The specimens were immersed in the solution for 30 min while monitoring the open circuit potential (OCP). Potentiodynamic polarization measurements were conducted using a scan rate of 0.5 mV/s up to anodic potential values slightly beyond the pitting potential. The polarization direction was reserved when the measured anodic current density reached a defined value of 1 mA/cm^2. The measurement was stopped at -0.5 V versus OCP. Each test was repeated at least five times for the $Zr_{52.5}Cu_{17.9}Ni_{14.6}Al_{10}Ti_5$ samples and two times for the $Ti_{47}Cu_{38}Zr_{7.5}Fe_{2.5}Sn_2Si_1Ag_2$ samples in order to assess the repeatability of the measurement result. By means of graphical extrapolation analysis from each measured curve, the characteristic parameters were determined: corrosion potential E_{corr}, corrosion current density i_{corr}, pitting potential E_{pit} and repassivation potential E_R. The electrochemical corrosion tests were carried out and analysed by Dr. Annett Gebert and Marion Johne at IFW Dresden.

2.2.12 Finite volume method modelling

A three-dimensional finite volume method (FVM) model was established to simulate the thermal evolution of the molten pool during processing of the $Zr_{52.5}Cu_{17.9}Ni_{14.6}Al_{10}Ti_5$ and $Ti_{47}Cu_{38}Zr_{7.5}Fe_{2.5}Sn_2Si_1Ag_2$ SLM samples. The mathematical model was developed using the software FLUENT. The calculations were performed in a domain with a uniformly structured mesh containing 50 000 hexahedral cells and the overall dimension was 2 × 1 × 0.25 mm^3. The loose powder material freely heaps up on the previously processed layer with a high porosity φ of about 40%. The laser beam penetrates the voids between the powder particles described by the multiple reflection mechanisms [249].The simulation was carried out by Hongyu Chen at IFW Dresden.

CHAPTER 3 Selective laser melting of glass-forming alloys

As outlined in section 1.5, selective laser metling (SLM) has great potential for producing glass-forming alloys. In this chapter, the processing route, mechanical and chemical properties of additively manufactured $Ti_{47}Cu_{38}Zr_{7.5}Fe_{2.5}Sn_2Si_1Ag_2$ and $Zr_{52.5}Cu_{17.9}Ni_{14.6}Al_{10}Ti_5$ BMGs will be discussed. Afterwards, the deformation mechanism and the structural heterogeneity of the additively manufactured BMGs will be focused on.

3.1 Selective laser melting of a $Ti_{47}Cu_{38}Zr_{7.5}Fe_{2.5}Sn_2Si_1Ag_2$ BMG

Due to their advantageous physical and chemical properties (see Chapter 1), BMGs have a high load-bearing capability and can significantly reduce stress-shielding or the generation of wear debris, which are important when the alloys are used as implants, for instance [250, 251]. Also the biodegradability of certain Mg-based metallic glasses has been reported to be superior to that of crystalline alloys [252].

For many biomedical applications, however, it is required that the material maintains its structural integrity even after prolonged times in the human body. Due to their limited ion release, bioinertness and beneficial mechanical properties, titanium and its alloys have already been used in the biomedical sector for decades [250]. Therefore, it appears natural to investigate the applicability of Ti-based BMGs as biomaterials in order to exploit their unique properties [253]. The first Ti-based amorphous alloy was reported in 1977 [254] and since then new glass-forming compositions have been discovered such as Ti-Si, Ti-Ni, Ti-Be, Ti-Nb-Si, Ti-Al-Ni, Ti-Zr-Be, Ti-Zr-Cu-Pd-(Sn, Si, Nb) and Ti-Cu-Ni [255] (and references therein). However, only when the toxic element Be is present, does the critical casting thickness of the Ti-based alloys reach relatively high values (above 50 mm in Ti-Zr-Cu-Ni-Be and Ti-Zr-Cu-Fe-Be) suitable for real-world applications [256]. Otherwise, the glass-forming ability (GFA) is inherently low, which represents a major obstacle for most applications. Apart from further alloy optimization, selective laser melting (SLM) can help to overcome this problem.

Here, a Ni-free Ti-based bulk metallic glass with the nominal composition of $Ti_{47}Cu_{38}Zr_{7.5}Fe_{2.5}Sn_2Si_1Ag_2$ (at.%) was fabricated via SLM. This alloy is known to have a high compressive yield strength, low elastic modulus, high corrosion resistance and good biocompatibility [257]. The processing route on the relative density, mechanical properties and corrosion behaviour will be discussed systematically in the following paragraphs.

3.1.1 Powder analysis

The actual chemical composition of the gas-atomized powder is provided in Table 3.1. The actual composition, $Ti_{46.9}Cu_{38.13}Zr_{7.43}Fe_{2.52}Sn_{2.02}Si_1Ag_2$, only marginally deviates from the nominal composition, $Ti_{47}Cu_{38}Zr_{7.5}Fe_{2.5}Sn_2Si_1Ag_2$. This indicates that gas atomization did not result in any significant compositional changes. The oxygen content of the powder is 930 ± 25 ppm. After SLM processing, the alloy contains more oxygen (1250 ± 40 ppm) owing to the high affinity of Ti to oxygen [87].

Table 3.1 Chemical composition of the gas-atomized $Ti_{46.9}Cu_{38.13}Zr_{7.43}Fe_{2.52}Sn_{2.02}Si_1Ag_2$ (at.%) powder.

Element (wt.%)	Ti	Cu	Zr	Fe	Sn	Si	Ag
nominal	37.69	40.45	11.46	2.34	3.98	0.47	3.16
powder	37.44	40.40	11.31	2.35	3.99	0.47	3.59
	± 0.16	± 0.23	± 0.06	± 0.01	± 0.02	± 0.01	± 0.01

The size distribution and morphology of the powder particles are shown in Fig. 3.1. The particle size mainly distributes between 10 and 40 µm (Fig. 3.1 (a)). A relatively large fraction (above 60%) of particles has a diameter below 40 µm. The median powder particle diameter, d_{50} is 37.4 ± 1 µm. This information is important for setting the proper value for the layer thickness. Fig. 3.1 (b) indicates that some of the particles have an irregular, non-spherical shape, which can adversely affect the flowability of the powder (see section 1.4.1.1). In addition, the small powder particles tend to agglomerate and to form satellites sticking to the large powder particles. In some of the particles, pores (Fig. 3.1 (c)) and crystals (Fig. 3.1 (d)) become evident. Both pores and crystals tend to form in the larger particles and are generally found in their centres. The pores may negatively affect the relative density of the SLM samples, resulting in a premature failure upon mechanical loading.

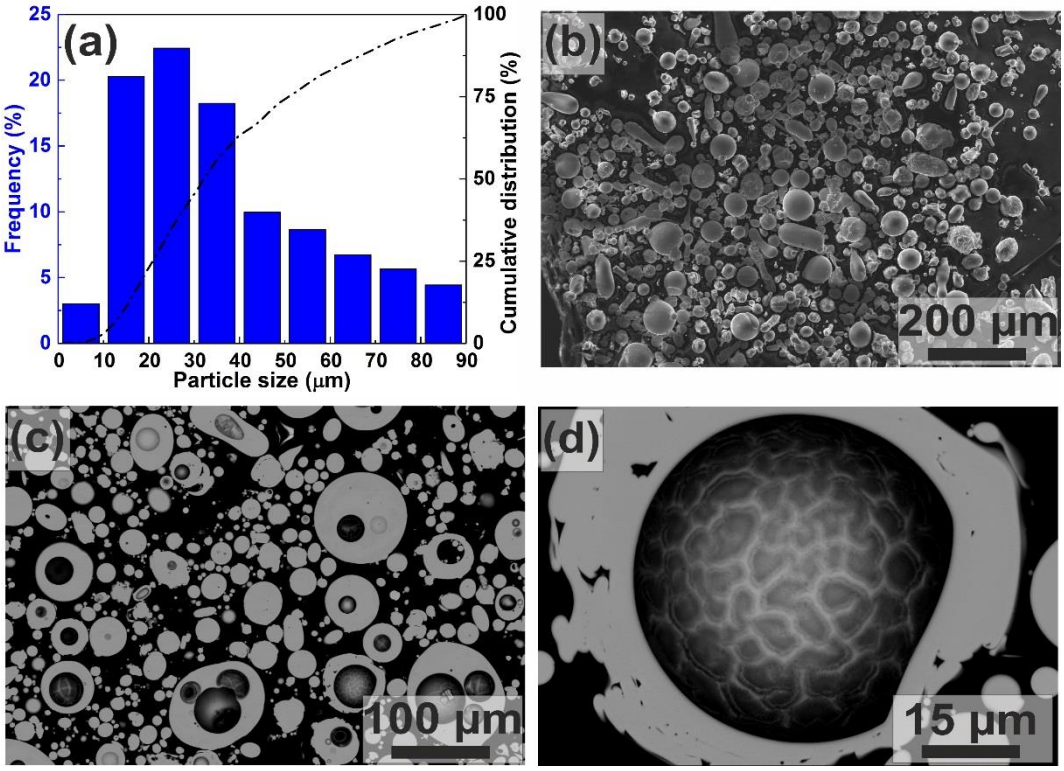

Figure 3.1: (a) Particle size distribution of the $Ti_{47}Cu_{38}Zr_{7.5}Fe_{2.5}Sn_2Si_1Ag_2$ powder. The diameters of the powder particles primarily range between 10 and 40 µm. (b) Morphology of the sieved gas-atomized powder. A part of the particles exhibits non-spherical shapes. Satellites and agglomeration were found for the fine particles. (c) The morphology of the polished powder. The large particles contain pores. (d) A polished particle at high magnification. The dark coral-like patterns are crystals.

3.1.2 Parameter optimization and microstructural characterization

According to the results presented above, the layer thickness and hatch distance were fixed as 40 µm and 140 µm, respectively. In order to investigate the effect of energy input on the microstructure of the SLM samples, $Ti_{47}Cu_{38}Zr_{7.5}Fe_{2.5}Sn_2Si_1Ag_2$ bulk samples were prepared with varying laser powers and scanning velocities. The XRD patterns of eight different SLM samples with a diameter of 3 mm are shown in Fig. 3.2. The energy input of these specimens was selected from low to high (11.2 J/mm^3 - 23.8 J/mm^3). Surprisingly, all SLM samples exhibit a broad scattering maximum and appear to be fully amorphous. In other words, with increasing energy input, the SLM samples still remain amorphous. This result is quite different from the previous study on Zr-based bulk metallic glasses produced by SLM, which partially crystallized on employing relatively high energy inputs [220]. This finding indicates that the $Ti_{47}Cu_{38}Zr_{7.5}Fe_{2.5}Sn_2Si_1Ag_2$ metallic glass has a larger process window, which is generally beneficial for the optimization of the relative density.

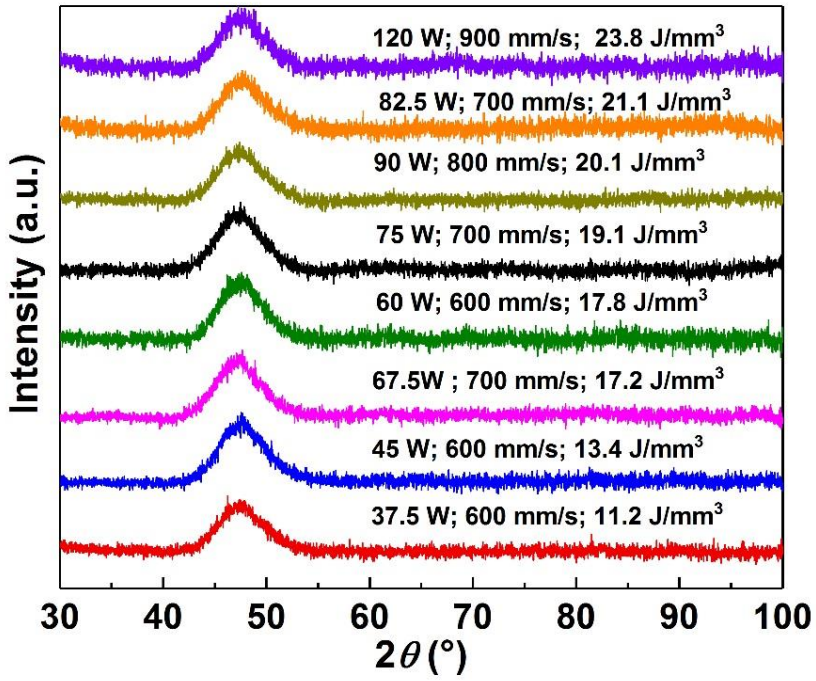

Figure 3.2: X-ray diffraction patterns of the $Ti_{47}Cu_{38}Zr_{7.5}Fe_{2.5}Sn_2Si_1Ag_2$ samples produced by selective laser melting with varying energy inputs at a constant layer thickness of $l = 40$ µm and a constant hatch distance of $h = 140$ µm. The corresponding laser power, scanning velocity and corresponding energy inputs are indicated.

As discussed above, fully glassy samples can be fabricated by selective laser melting once the critical energy input is identified. Because only fully dense SLM samples might be able to compete with as-cast samples in terms of mechanical properties, only glassy SLM samples with a high relative density should be considered. In the first step, therefore, the interrelation between the relative density and the employed process parameters is investigated. Since the layer thickness and hatch distance are kept constant, the laser power and scanning velocity are the only variables of interest here. The relative density is plotted as a contour map as a function of the latter two parameters in Fig. 3.3. It shows the details of the interrelation between these process parameters and the relative density. The black diamonds represent those samples, which were analysed by µ-CT. These samples will be discussed in the following paragraphs. The dashed lines in Fig. 3.3 represent values of constant energy input. Although there is a relatively wide process window for obtaining fully amorphous samples, the process window, which allows obtaining samples with a high relative density (over 98%), is comparatively narrow. High relative densities were only found in the area between 13 J/mm^3 and 16 J/mm^3. Unlike for selectively laser-melted Zr-based BMGs [220], an increase of the laser power first increases the

relative density and then decreases it at a given scanning velocity. Thus, the relative density does not increase linearly with the laser power in the present Ti-based BMG. The same trend is found for varying the scanning velocity at a constant laser power (Fig. 3.3). In other words, there is no single process parameter has a monotonous effect on the relative density of the $Ti_{47}Cu_{38}Zr_{7.5}Fe_{2.5}Sn_2Si_1Ag_2$ samples produced by selective laser melting.

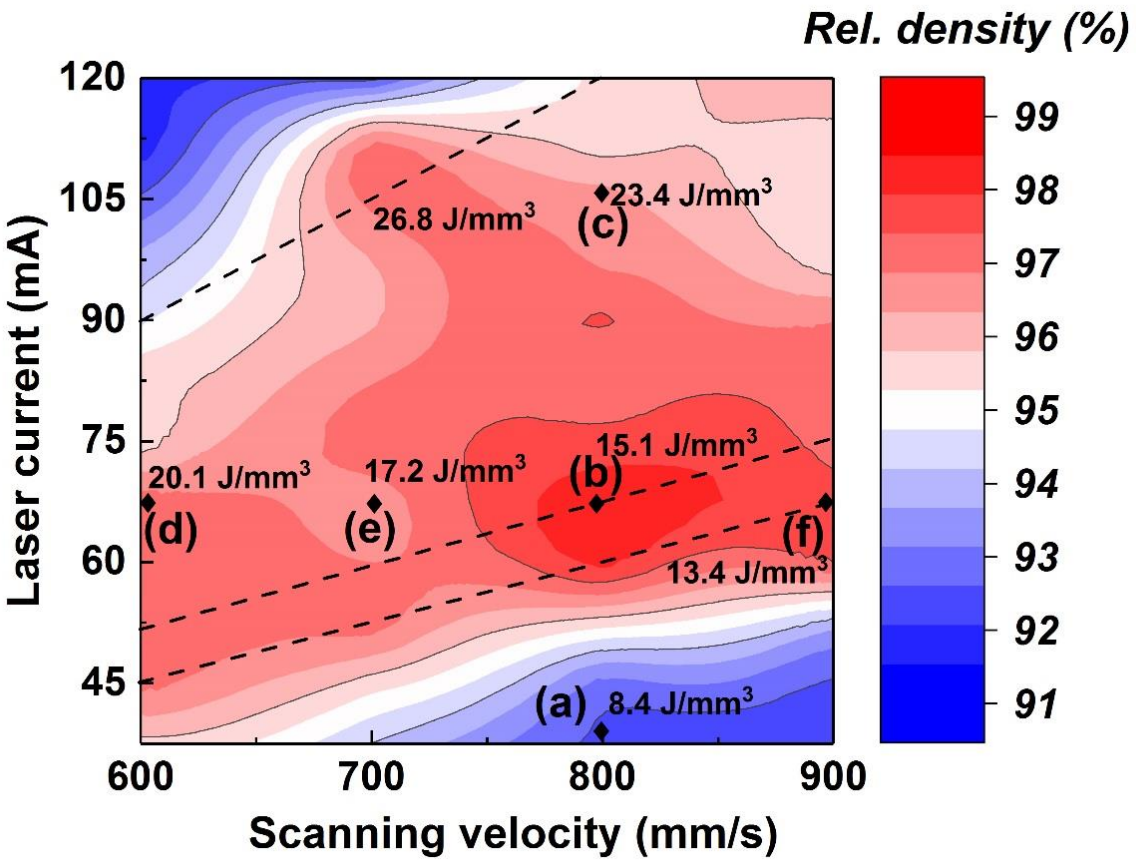

Figure 3.3: Contour map of the relative density of the SLM $Ti_{47}Cu_{38}Zr_{7.5}Fe_{2.5}Sn_2Si_1Ag_2$ samples as a function of scanning velocity and laser power at a constant layer thickness l = 40 µm and hatch distance h = 140 µm. The dashed line indicates values of constant energy input. The black diamond with the corresponding energy input will be discussed in the following paragraphs. µ-CT scans of the cross section for samples produced with the parameters (a) - (f) are shown in the Fig. 3.4.

Fig. 3.4 shows selected but representative cross sections of the SLM samples manufactured with different processing parameters and energy inputs. All the parameters and energy inputs discussed in the following are marked in Fig. 3.3 and the respective µ-CT scans are displayed in Fig. 3.4. When the energy input is only 8.4 J/mm^3 (scanning speed: 800 mm/s, laser power: 37.5 W; point (a) in Fig. 3.3), pores distribute uniformly at the cross sections (Fig. 3.4 (a)). Since the energy input is low, the powder is not completely melted and multiple voids and pores are trapped in the final sample. The pores, especially the large pores have an irregular shape.

As indicated in Fig. 3.3, the relative density just reaches about 92%. Increasing the laser power at a scanning speed of 800 mm/s to a value of 67.5W raises energy input to 15.1 J/mm^3. The big, irregularly shaped pores apparently disappear. Only some small pores can be found at the edges of the cross section (Fig. 3.4 (b)). The corresponding relative density is over 98%, suggesting that enough energy is transferred to the powder in order to fully melt it. By continuously increasing the laser power, the energy input reaches 23.4 J/mm^3 (point (c) in Fig. 3.3). However, the relative density drops to about 96%. As shown in Fig. 3.4 (c), round and relatively big pores can be found in the specimens. Because the high energy input results in evaporation of the alloy (see section 1.4.1.1) such big and round pores appear. When the energy input decreases, the amount of the big round pores also decreases (Figs. 3.4 (d) and (e)). When the laser power is kept constant, a higher scanning velocity (i.e. a decreased energy input) can apparently reduce the formation of round pores in the central part of the cross section (Fig. 3.4 (f)). However, simultaneously, there exist more small pores at the margins of the sample. The shape and distribution of the pores on the cross sections underpin the finding discussed above: no individual process parameter has a monotonous effect on the relative density.

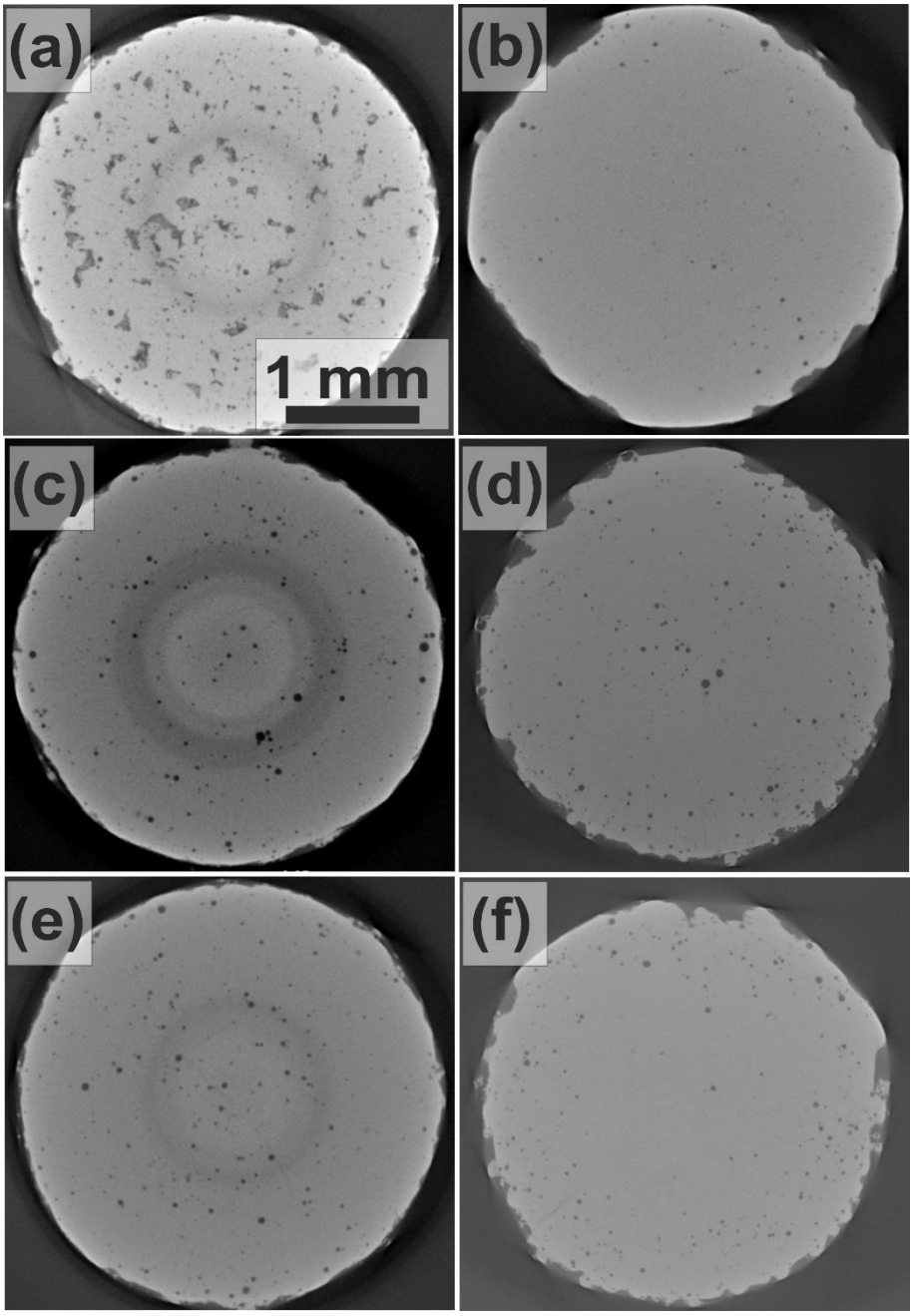

Figure 3.4: Cross sections of the SLM samples produced with different energy inputs. All the samples were prepared with a constant layer thickness, l = 40 µm, and hatch distance, h = 140 µm. The laser power, scanning velocity and corresponding energy inputs for (a) - (f) are marked in Fig. 3.3.

Combining the information of Figs. 3.2, 3.3 and 3.4, a relatively dense (98.5%), fully glassy sample was produced with the energy input of 15.4 J/mm^3 (v = 780 mm/s, hatch distance h = 140 µm, layer thickness l =40 µm, and laser power P = 67.5 W). Afterwards, the microstructure and thermal stability of SLM samples produced with these optimized parameters were compared with the initial powder and as-cast samples.

The diffraction patterns of the powder, a SLM sample and an as-cast rod are displayed in Fig. 3.5 (a). Some sharp reflections superimpose on a broad background typical of metallic

glasses in the case of the powder. The reflections are identified to result from Ti_2Cu, Ti_3Cu_4 and TiCu in agreement with previous reports [257]. Consequently, these are the phases, which constitute the crystals seen in Fig. 3.1 (d). The cooling rate during gas atomization, apparently, is not high enough to suppress crystallization and as a result, partially crystalline powder particles are obtained. This is unexpected because the critical casting thickness has been reported to reach 7 mm [257] and gas atomization with its high intrinsic cooling rates should, therefore, yield fully amorphous powder. In spite of the elevated oxygen content in the powder, no stable or metastable phases with icosahedral order (quasicrystals or the big cube phase) [258, 259] precipitate. In contrast, the diffraction patterns of the SLM sample and the as-cast rod only exhibit a broad scattering maximum and appear to be fully glassy. It is noteworthy that the alloy vitrifies during SLM although the cooling rates should be similar to those of gas atomization [260]. The short lifetime of the molten pool [261] seems sufficient to overcome the slight chemical segregation, which accompanies the formation of the present Ti-rich Ti_2Cu phase and to produce a chemically uniform melt. The subsequent cooling again proceeds sufficiently fast to warrant vitrification.

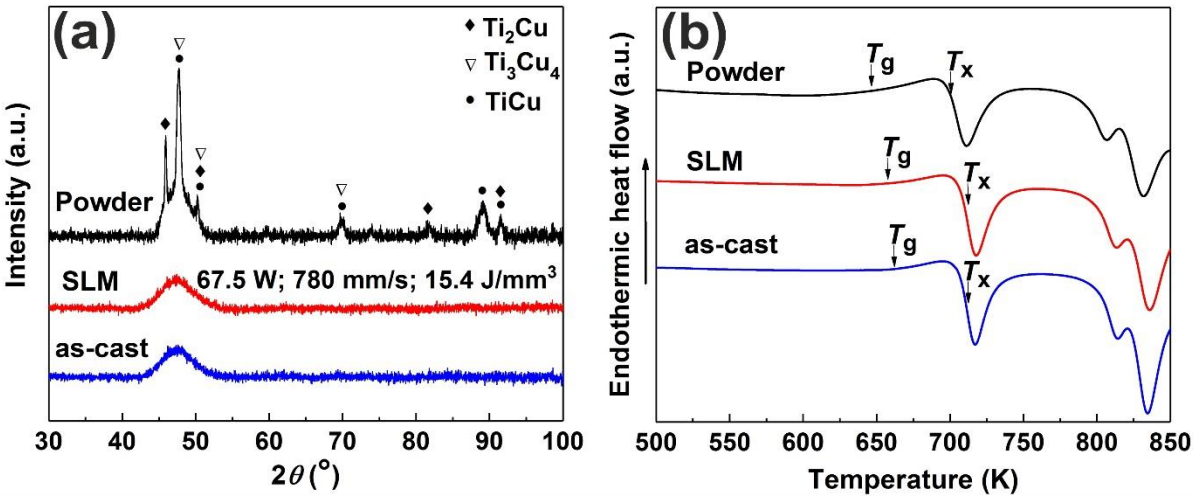

Figure 3.5: (a) X-ray diffraction patterns of the $Ti_{47}Cu_{38}Zr_{7.5}Fe_{2.5}Sn_2Si_1Ag_2$ powder, a cylindrical SLM sample and an as-cast rod. The latter two have a diameter of 2 mm. Crystalline reflections can be only detected in the gas-atomized powder. (b) DSC curves of the $Ti_{47}Cu_{38}Zr_{7.5}Fe_{2.5}Sn_2Si_1Ag_2$ powder, a cylindrical SLM sample and an as-cast rod recorded at a heating rate of 0.33K/s. The glass-transition temperature, T_g and the onset of crystallization, T_x, are marked by arrows.

The thermal stability and crystallization behaviour were analysed on heating and the respective DSC traces are displayed in Fig. 3.5 (b). All the samples show the typical features of metallic glasses, i.e. a distinct glass transition followed by a supercooled liquid region prior to multiple exothermic events associated with crystallization. The glass-transition temperature, T_g, as well as the onset-temperature of crystallization, T_x, are indicated in Fig. 3.5 (b) and these

values are listed in Table 3.2 next to the enthalpy of crystallization, ΔH_{cryst}, of the first crystallization event. The values of T_g, T_x, ΔT_x and ΔH_{cryst} are identical within the experimental error for the as-cast rod and the SLM sample. Only the powder is obviously different due to its partially crystalline nature. More importantly, the SLM samples exhibit a thermal stability identical to the as-cast material and SLM processing or the elevated oxygen content do not measurably deteriorate the glass-forming ability or the stability of the glass against crystallization.

Table 3.2: Glass-transition temperature, T_g, onset-temperature of crystallization, T_x, extension of the supercooled liquid region, ΔT_x, and enthalpy of crystallization of the first crystallization event shown in Fig. 3.5 (b) for the $Ti_{47}Cu_{38}Zr_{7.5}Fe_{2.5}Sn_2Si_1Ag_2$ powder, a SLM sample and an as-cast rod.

	$T_g \pm 1$ (K)	$T_x \pm 1$ (K)	$\Delta T_x = T_x - T_g \pm 2$ (K)	$\Delta H_{cryst} \pm 1$ (J/g)
powder	642	698	56	24.5
SLM	658	708	50	26.7
as-cast	660	706	46	25.9

The relative density plays a decisive role for the deformation behaviour and, consequently, detailed information about the density is critical for understanding irreversible flow in metallic glasses. The relative densities of the specimens as obtained by the Archimedean principle range from 98.5% to 98.7% (Fig. 3.3), but these values do not provide any hints related to the distribution or sizes of the pores. In order to gain more information about these aspects, the densest specimens were investigated by µ-CT. The result is shown in Fig. 3.6. In the cross-sectional view of Fig. 3.6 (a), small pores with a typical diameter of 10 - 30 µm can be found. Only a few larger defects locate at the edge of the sample. As mentioned above, the powder consists a certain amount of small powder particles. Van der Waals forces between these small particles generally enhance their tendency to agglomerate [153], which renders a uniform distribution and dense packing impossible. This in turn increases the probability of the forming small pores during SLM [262]. Moreover, the non-negligible fraction of irregularly shaped particles (Fig. 3.1) may additionally reduce the packing of the $Ti_{47}Cu_{38}Zr_{7.5}Fe_{2.5}Sn_2Si_1Ag_2$ powder which then enhances the formation of pores. The size distribution of defects and the full µ-CT reconstruction (inset) of a SLM sample is depicted in Fig. 3.6 (b). As shown in the histogram, the vast majority of the pores has diameters between 15 µm and 35 µm. The relative density evaluated from the µ-CT reconstruction amounts to 99% to 99.5% which is higher than the values obtained from Archimedean principle mentioned above. Because of the limited

resolution of the device, small pores (less than 10 µm) cannot be detected reliably by µ-CT. In addition, small air bubbles can adhere to the rough surface of the SLM samples which may influence the results of the Archimedean measurement and could account for the observed discrepancy. As shown in the inset of Fig. 3.6 (b), the pores are uniformly distributed in the sample. No obvious pore aggregation is visible.

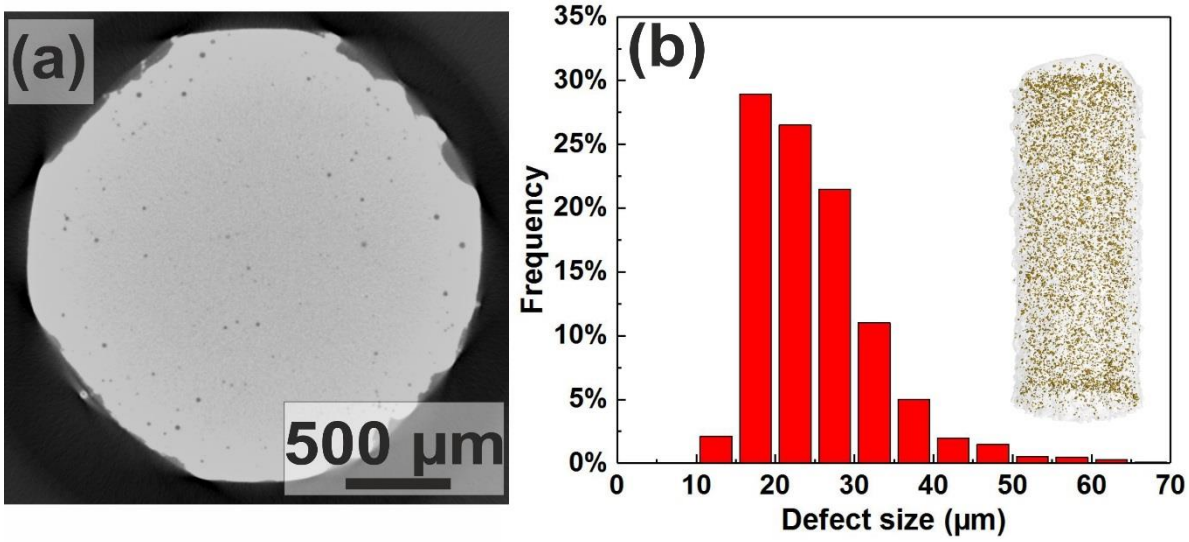

Figure 3.6: (a) Cross-sectional slice of a $Ti_{47}Cu_{38}Zr_{7.5}Fe_{2.5}Sn_2Si_1Ag_2$ sample produced by SLM as obtained by µ-CT. The darker pores are relatively small and uniformly distributed across the sample. (b) Size distribution of defect for SLM sample. Pores have a main size range between 15 µm and 35 µm. Full µ-CT reconstruction of a compression test rod with a diameter of 2 mm produced by SLM (inset). The pores are indicated. Even though the sample appears to be highly porous the relative density is determined to be 99.5% (µ-CT).

3.1.3 Mechanical properties

3.1.3.1 Compression tests

In order to investigate the effect of the processing route on the materials response to mechanical loading, SLM samples and as-cast samples were uniaxially compressed. Fig. 3.7 compares the compressive stress-strain curves for two representative samples. The as-cast $Ti_{47}Cu_{38}Zr_{7.5}Fe_{2.5}Sn_2Si_1Ag_2$ sample yields at stresses around 2000 MPa and exhibits serrated flow in the plastic regime. The Young's modulus of both samples is E =100 ± 5 GPa and the as-cast sample fails after a plastic strain of about 1.8%. The SLM samples, however, fractures at lower stress (1690 ± 50 MPa) without any significant plastic deformation.

After having successfully produced dense and fully glassy $Ti_{47}Cu_{38}Zr_{7.5}Fe_{2.5}Sn_2Si_1Ag_2$ bulk specimens, complex and delicate geometries were also manufactured via SLM (inset to Fig. 3.7) in order to assess the processability of the present powder. The miniature skull and hand, shown in the inset, are fully glassy and have a relatively smooth surface. Even very flimsy details can

be obtained without any macroscopic defects. Since $Ti_{47}Cu_{38}Zr_{7.5}Fe_{2.5}Sn_2Si_1Ag_2$ BMG is proven to have a good biocompatibility, the good processability of this alloy indicates the large potential the present approach has for additively manufacturing Ti-based glasses for biomedical applications.

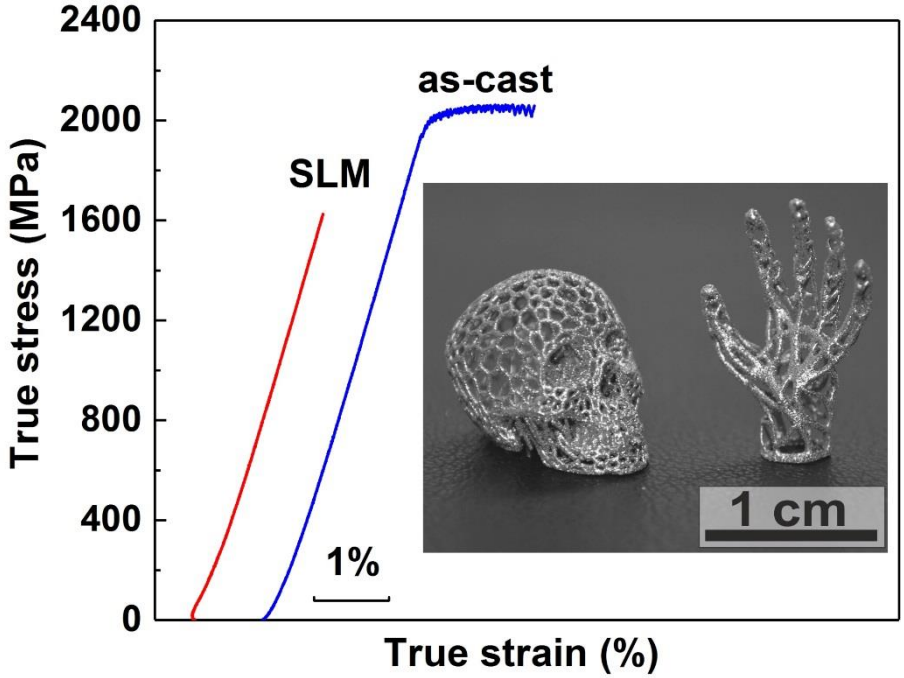

Figure 3.7: Compressive stress-strain curves of glassy $Ti_{47}Cu_{38}Zr_{7.5}Fe_{2.5}Sn_2Si_1Ag_2$ rods with a diameter of 2 mm prepared by casting and SLM. The inset depicts complex structures composed of glassy $Ti_{47}Cu_{38}Zr_{7.5}Fe_{2.5}Sn_2Si_1Ag_2$ produced by SLM.

Although the $Ti_{47}Cu_{38}Zr_{7.5}Fe_{2.5}Sn_2Si_1Ag_2$ sample synthesized by SLM has a high strength, the underlying mechanism for premature failure and the absence of plastic strain needs to be further investigated. Therefore, the fracture surfaces were observed under SEM. Fig. 3.8 depicts the morphology of the fracture surfaces for the additively manufactured (Figs. 3.8 (a) - (c)) and the as-cast (Fig. 3.8 (d)) samples. As shown in Fig. 3.8 (a), unlike the as-cast rods, which have a well-defined, relatively smooth fracture plane inclined by 45 ° with respect to the loading axis (not shown here), the fractured SLM samples appear completely different. The fracture angle is at almost 90 ° with respect to the loading axis, which indicates that the stress state and fracture mode is rather different for the SLM samples. Vein-like patterns can be found on the fracture surfaces of both SLM (Fig. 3.8 (b)) and as-cast (Fig. 3.8 (d)) samples, but one cannot identify a clear fracture plane for the SLM samples. The vein-like patterns are not continuous and the fracture plane is rather rugged, suggesting a different stress state under loading compared to the as-cast sample. The SLM sample fails in a brittle fashion, which can induce severe surface roughness. Moreover, nanoscale periodic corrugations form at the fracture surface (Fig. 3.8 (c)). The presence of the pores results in a complicated directional stress field [49]. This can reduce

the local stress intensity factor, decrease the size of the damage cavity and raise the density of the cavities [263]. The self-assembly of cavities needs a critical density to make the cavities close enough to be within each other's elastic influence range [263]. Therefore, the periodic corrugation pattern forms on the rugged surface. Broadly speaking, the uniform porosity seems responsible for the premature failure and the differences in the fracture morphology.

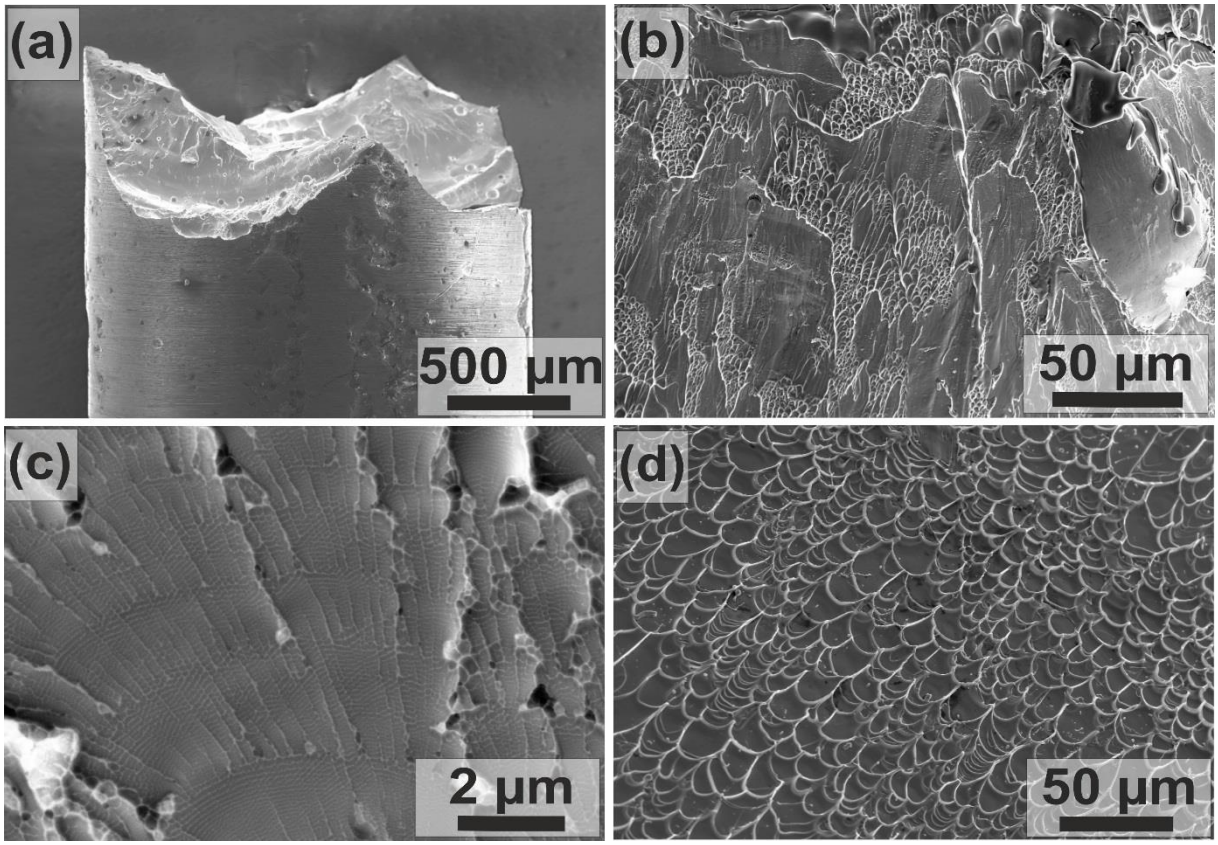

Figure 3.8: Fracture surfaces of $Ti_{47}Cu_{38}Zr_{7.5}Fe_{2.5}Sn_2Si_1Ag_2$ additively manufactured samples ((a) - (c)) and as-cast sample (d). (a) The additively manufactured sample does not fail in a shear mode under an angle of 45 °. (b) The vein-like patterns exist in rugged plane. (c) Nanoscale periodic corrugations are found on the fracture surfaces. (d) The typical vein-like patterns of the as-cast samples.

3.1.3.2 Microhardness and structural relaxation

To further investigate possible structural heterogeneities in the SLM samples and the influence of the layer-by-layer process method on the mechanical properties, microhardness measurements were carried out on both SLM and as-cast samples. Fig. 3.9 depicts hardness maps of the cross and longitudinal section for both SLM and as-cast samples. The schematic of the locations at which indents were taken can be found in section 2.2.8. The cross-section and the longitudinal section of the SLM as well as as-cast sample have similar hardness values ranging between 571 HV0.2 and 596 HV0.2. The cross-section (Fig. 3.9 (a)) and the longitudinal section (Fig. 3.9 (b)) of the SLM sample exhibit quite uniform hardness values

across the whole sample. Except for the few soft or hard areas, the structure seems to be macroscopically homogeneous. The heat-affected zone (HAZ) does not reflect in the hardness map. This could be explained by the fact that the distance between the indents is 100 µm, which is on the order of the HAZ [128].

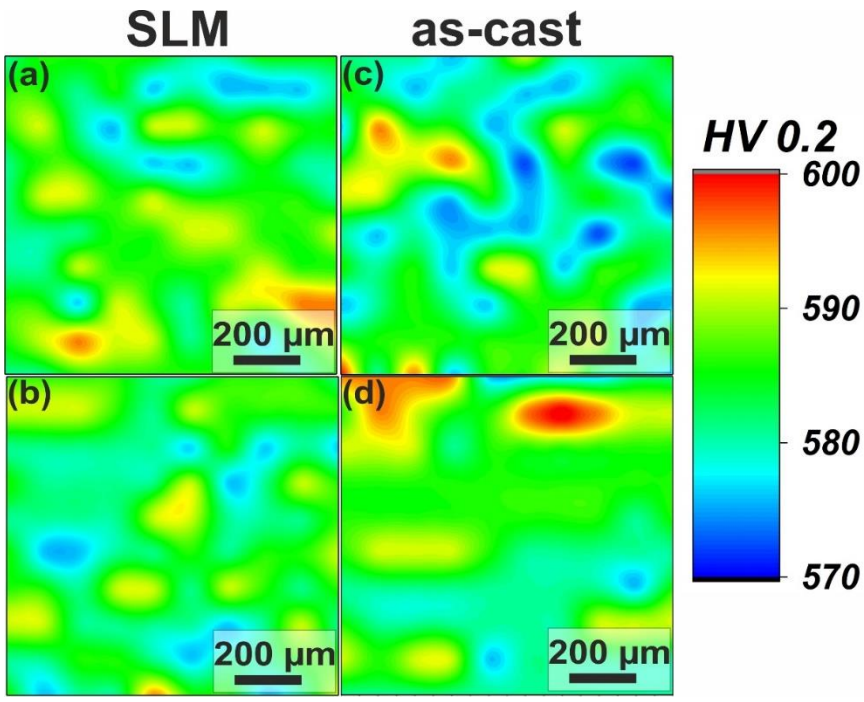

Figure 3.9: (a) and (c) depict the hardness contour maps for the cross section of a SLM and an as-cast sample, respectively. (b) and (d) show the hardness maps for the longitudinal section of SLM and as-cast BMGs, respectively.

The enthalpy of relaxation provides valuable information on the structural state of a glass and its degree of metastability [69, 264, 265], which, in turn, has an effect on the mechanical properties [69, 264]. For this reason, the relaxation behaviour of the $Ti_{47}Cu_{38}Zr_{7.5}Fe_{2.5}Sn_2Si_1Ag_2$ glass processed by selective laser melting was investigated (Fig. 3.10). The relaxation enthalpies of the SLM samples range between $\Delta H_{relax} = 9.22$ J/g and $\Delta H_{relax} = 10.36$ J/g, whereas the as-cast samples display distinctly lower values ($\Delta H_{relax} = 4.86$ - 5.68 J/g). The relaxation enthalpy is a measure for the free volume trapped in the structure of the glass as it vitrifies [266] and, consequently, is a measure for the average atomic packing density [267]. This enthalpy strongly depends on the cooling rate (see section 1.1) [266]. Compared to SLM where cooling rates of about 6.5×10^5 K/s prevail [198], copper-mould casting of rods with 3 mm in diameter are estimated to occur only at about 200 K/s [268]. Thus, the significantly larger relaxation enthalpy measured for the SLM samples seems to result from the faster solidification process. Such a clear trend, however, is remarkable considering the complex thermal history of BMGs prepared by SLM: As outlined in section 1.4.2, the laser beam is a highly concentrated heat

source, which generally does not only melt the topmost powder layer. Instead, already solidified layers beneath it are re-melted [128] and the heat is subsequently dissipated in the bulk material underneath [128], the aforementioned HAZ [128, 229]. According to finite element simulations, the HAZ expands up to 100 µm into the previously fabricated material [128]. In conventional crystalline materials processed by SLM, the HAZ can be directly proven in micrographs because it often leads to a change in the phase composition or the grain morphology [128, 229]. While there is not a microstructure of any kind in metallic glasses being able to reveal the HAZ, the heat treatment could lead, instead, to overall relaxation of the glassy structure (section 1.4.2) [128, 269]. This is obviously not the case (Fig. 3.10) as the relaxation enthalpies suggest. One can speculate that the duration of the temperature rise is too short [128] to cause pronounced relaxation and, therefore, the enthalpy of relaxation remains larger than for the as-cast glass. This finding seems reasonable and has been reported by other groups as well [230]. To further investigate the thermal history of SLM, in section 3.3, the relaxation enthalpies of the slices taken from bottom to the top of the additively manufactured sample will be compared.

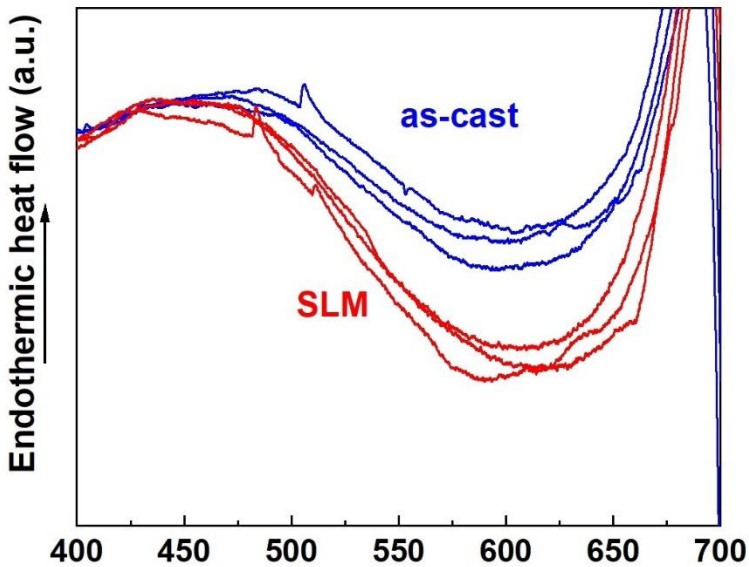

Figure 3.10: DSC curves of as-cast and additively manufactured $Ti_{47}Cu_{38}Zr_{7.5}Fe_{2.5}Sn_2Si_1Ag_2$ samples show exothermic structural relaxation. The relaxation enthalpies of additively manufactured samples are larger than the as-cast samples.

3.1.3.3 Nanoindentation

The experiments discussed so far have a relatively limited spatial resolution and do not allow for detailed information on a small length scale. A more local and commonly applied probe is nanoindentation [270]. As outlined in section 1.4.2, the thermal history of selectively laser-melted alloys is complex and results in locally different microstructures in the case of conventional alloys [207]. Even in the absence of crystallization in the heat-affected zone, the

locally different thermal history imposed on the material during selective laser melting (e.g. in the heat-affected zone (HAZ)), might result in a structurally heterogeneous metallic glass. One could conceive of it as locally more or less relaxed on a micron-scale and could term it "μ-glass" in analogy to the known nanoglasses [271-273]. Such structural differences might be detectable by nanoindentation. Figs. 3.11 (a) and (b) display the hardness maps of the cross section and the longitudinal section for the SLM sample.

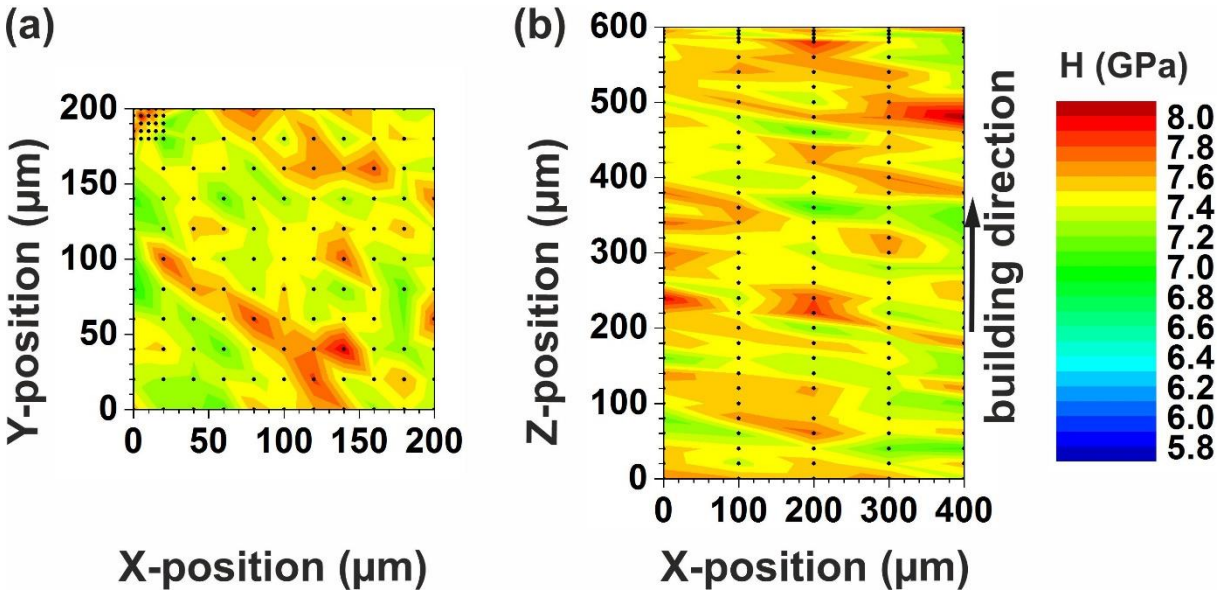

Figure 3.11: Hardness contour maps of cross sections (a) and longitudinal sections (b) of the additively manufactured $Ti_{47}Cu_{38}Zr_{7.5}Fe_{2.5}Sn_2Si_1Ag_2$ BMG based on the indents (black dots) indicated. Both sections show similar hardness values and heterogeneous structure.

The nanohardness maps of the $Ti_{47}Cu_{38}Zr_{7.5}Fe_{2.5}Sn_2Si_1Ag_2$ SLM sample indicate a clearly heterogeneous structure (Fig. 3.11). Both sections show similar hardness values, which range between 7.0 and 8.0 GPa, and they are distributed in a non-uniform manner. The layer-by-layer-like synthesis seems to be reflected in the hardness distribution of the longitudinal section.

In the next step the distribution of hardness values was statistically analysed (Fig. 3.12) in order to get a more quantitative picture. The Weibull modulus of the longitudinal section (m = 53.69 ± 0.96) is higher than the cross section (m = 48.82 ± 0.93). This result indicates that the longitudinal section is slightly more homogeneous. The structural heterogeneity will be discussed in more details in section 3.3 by comparing with the additively manufactured $Zr_{52.5}Cu_{17.9}Ni_{14.6}Al_{10}Ti_5$ samples.

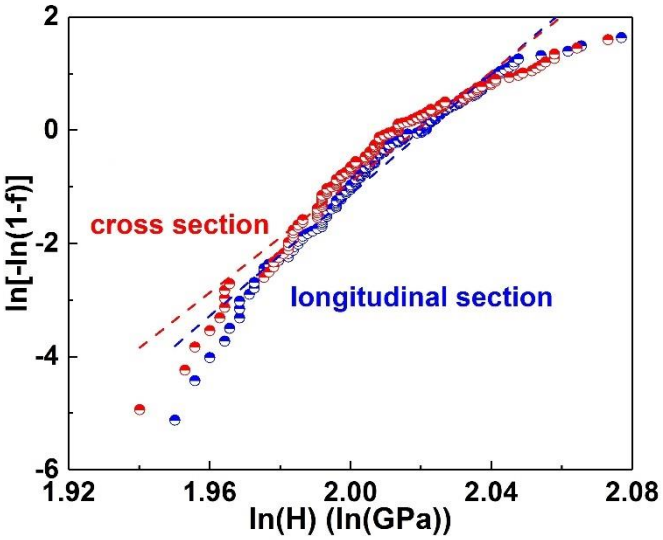

Figure 3.12: Weibull plot of the hardness values for additively manufactured $Ti_{47}Cu_{38}Zr_{7.5}Fe_{2.5}Sn_2Si_1Ag_2$ BMG shown in Fig. 3.11. The Weibull modulus, *m*, is derived from the slope of the linear regression curve of ln[-ln(1-*f*)] over ln(*H*), marked by the dashed lines.

3.1.4 Corrosion properties

The processability and mechanical properties of the $Ti_{47}Cu_{38}Zr_{7.5}Fe_{2.5}Sn_2Si_1Ag_2$ glass prepared by SLM appears promising, its corrosion behaviour -another crucial factor for biomedical applications- is still unknown. In order to demonstrate the feasibility of additively manufactured $Ti_{47}Cu_{38}Zr_{7.5}Fe_{2.5}Sn_2Si_1Ag_2$ sample for the use as implant material, the polarization tests were carried out in a synthetic body fluid, i.e. Ringer's solution. Fig. 3.13 shows anodic polarization curves of both SLM and as-cast samples. In both cases, the corrosion current densities i_{corr} are quite small, i.e. in the range of 0.06 - 0.07 µA/cm² which corresponds low free corrosion rates. The SLM sample has an E_{corr} value of -0.23 V vs. SCE. The E_{corr} value of the as-cast sample is -0.24 V vs. SCE, which is more negative. This can be indicative of a more reactive surface state under free corrosion conditions. During anodic polarization, the current densities of the SLM and as-cast sample increase gradually up to 0.6 µA/cm² and 1 µA/cm², respectively. This indicates very low corrosive dissolution, which is superimposed by anodic growth of passive films with a strong barrier-type effect [137, 274]. Pitting initiation and propagation is evident from a sudden steep rise of the anodic current density for both alloy states at E_{pit} [137]. As shown in Fig. 3.13, the pitting initiation of as-cast samples is retarded according to a more positive E_{pit} value. In both curves, a significant overshoot of the current density above the set value of 1 mA/cm² occurs followed by a wide, high-level current density range in the reverse scan. This suggests strong pit propagation into the glassy matrix and a low repassivation ability. The current density level of the as-cast sample in the reverse scan is higher and the repassivation potential, E_R, is shifted to more negative values corresponding to a

retarded healing of the damaged surface. When comparing the SLM and as-cast sample, the SLM sample shows similar E_{corr}, i_{corr} and $i_{passive}$ values but pitting occurs earlier. These results reveal that the SLM sample has a slightly lower pitting corrosion susceptibility and better surface healing ability. The corrosion property of SLM sample shown here may be attributed to a more pronounced structural or chemical homogeneity.

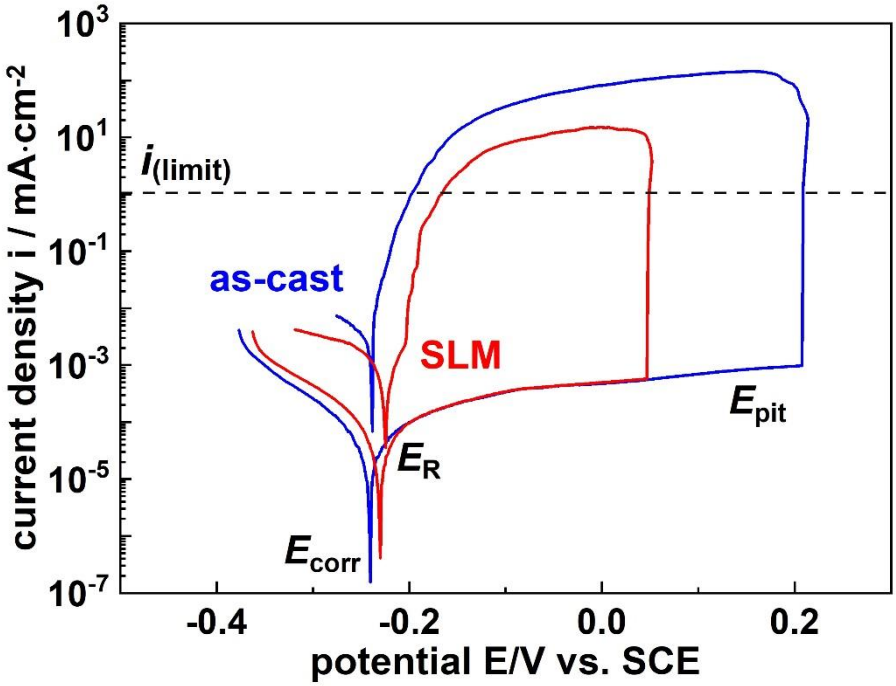

Figure 3.13: Anodic polarization curves recorded for additively manufactured and as-cast $Ti_{47}Cu_{38}Zr_{7.5}Fe_{2.5}Sn_2Si_1Ag_2$ samples in Ringer's solution with pH 7.4 at 310 K. Corrosion potential (E_{corr}), pitting potential (E_{pit}) and repassivation potential (E_R) are marked. Both samples show similar corrosion behaviour. The SLM sample performs slightly better than the as-cast sample during pitting corrosion.

3.2 Selective laser melting of a $Zr_{52.5}Cu_{17.9}Ni_{14.6}Al_{10}Ti_5$ BMG

Relatively dense glassy $Zr_{52.5}Cu_{17.9}Ni_{14.6}Al_{10}Ti_5$ specimens were produced by SLM. The mechanical properties (compression and wear tests) as well as the corrosion behaviour of these samples were assessed and compared with as-cast samples of the same composition. The corresponding results are discussed in the following.

3.2.1 Powder analysis

As shown in Table 3.3, the chemical composition of the gas-atomized $Zr_{52.3}Cu_{18}Ni_{14.6}Al_{10.1}Ti_5$ (at.%) powder is in excellent agreement with the nominal composition $Zr_{52.5}Cu_{17.9}Ni_{14.6}Al_{10}Ti_5$, suggesting that gas atomization does not significantly change the composition of the present alloy. The oxygen content of the original alloy powder (487 ± 5 ppm) is significantly lower than that of the samples after SLM processing (920 ± 20 ppm).

Apparently, residual oxygen in the chamber is absorbed during SLM processing because of the high affinity and solution ability of Zr and Ti for oxygen [87, 275]. In addition, owing to the low oxygen content in the arc-melter, the oxygen content of the as-cast sample is only 77 ± 5 ppm.

Table 3.3 Chemical composition of the gas-atomized $Zr_{52.3}Cu_{18}Ni_{14.6}Al_{10.1}Ti_5$ (at.%) powder.

Element (wt.%)	Zr	Cu	Ni	Al	Ti
nominal	65.67	15.60	11.75	3.70	3.28
powder	65.53 ± 0.26	15.74 ± 0.04	11.75 ± 0.03	3.76 ± 0.01	3.26 ± 0.01

Fig. 3.14 (a) depicts the particle size distribution of the sieved $Zr_{52.5}Cu_{17.9}Ni_{14.6}Al_{10}Ti_5$ powder. Knowledge of the powder size distribution is inevitable for choosing the proper layer thickness and hatch distance. The majority of the particles has a diameter ranging between 20 and 50 µm. The morphology of the powder particles shown in Fig. 3.14 (b) indicates that only some particles have an irregular, non-spherical shape. Moreover, some satellites sticking to the relatively large particles and only few powder agglomerates are visible, which is typical of gas-atomized powder [171]. Yet, these phenomena are not so pronounced as to adversely affect the flowability of the powder in the present case [167, 171].

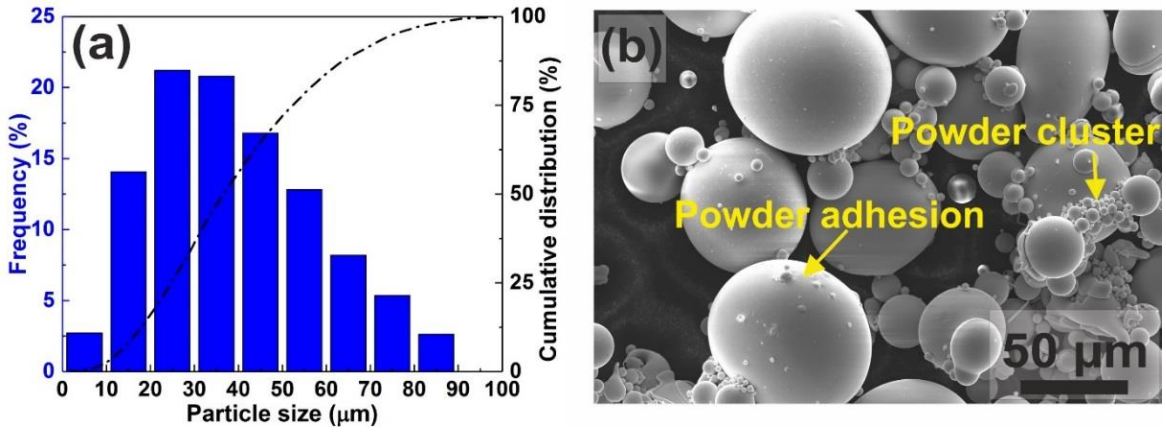

Figure 3.14: (a) Particle size distribution of the $Zr_{52.5}Cu_{17.9}Ni_{14.6}Al_{10}Ti_5$ powder after sieving. The powder diameters mainly distribute between 20 and 50 µm. (b) Scanning electron micrograph of the sieved gas-atomized powder. Some particles display non-spherical shapes. Especially the fine particles tend to form satellites and to agglomerate.

3.2.2 Microstructural characterization

The relative density of all SLM samples exceeds 98.7% according to the Archimedean method. The corresponding XRD patterns of the different samples are displayed in Fig. 3.15 (a). Neither in the XRD patterns of the cross section of the SLM sample nor in the patterns of

the powder (Fig. 3.15 (a)) sharp reflections can be observed indicating the presence of crystalline phases. Instead, only a broad scattering maximum is visible, as found for the as-cast sample. Consequently, bulk amorphous $Zr_{52.5}Cu_{17.9}Ni_{14.6}Al_{10}Ti_5$ samples were fabricated by SLM.

To obtain more details about the glassy nature, the samples were analysed with differential scanning calorimetry. Fig. 3.15 (b) displays the DSC traces of a SLM sample, an as-cast sample as well as of the powder. The glass-transition temperature (T_g) and the crystallization temperature (T_x) are marked by arrows. All samples show a characteristic glass transition and a supercooled liquid region prior to the exothermic crystallization events. However, the trace of the SLM sample appears to be slightly different in terms of the crystallization behaviour. Separating the sequence of crystallization events is not as obvious as for the as-cast samples or the powder, most likely due to the significantly higher oxygen content. In Zr-based BMGs, the oxygen content is the main factor for the formation of the big cube phase and icosahedral crystals, which may result in different DSC traces [276, 277]. However, the crystallization enthalpy determined for the SLM sample ($\Delta H_{cryst} = 55 \pm 2$ J/g) is similar to that calculated for the as-cast sample ($\Delta H_{cryst} = 54 \pm 2$ J/g) and for the powder ($\Delta H_{cryst} = 52 \pm 2$ J/g). Consequently, the presence of crystalline phases should be ruled out as a reason for the variation of the DSC curves of the specimens prepared by SLM. More information of structural relaxation obtained from DSC curves will be addressed in section 3.2.3.

In order to further characterize the structural state of the SLM samples, transmission electron microscopy was carried out. A representative bright-field TEM micrograph and the corresponding selected area electron diffraction (SAED) pattern are displayed in Fig. 3.15 (c). The bright-field TEM image reveals a homogeneous maze-like pattern. Moreover, the SAED pattern (shown as inset) exhibits broad and diffuse rings. These results strongly indicate that the SLM sample is fully amorphous, which is in agreement with the results obtained by XRD and DSC.

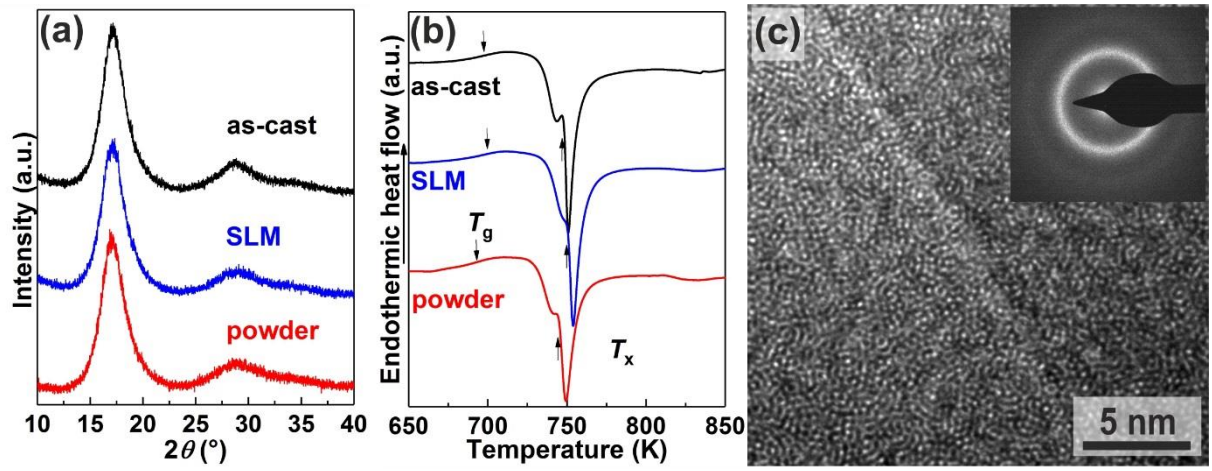

Figure 3.15: (a) X-ray diffraction patterns of the $Zr_{52.5}Cu_{17.9}Ni_{14.6}Al_{10}Ti_5$ powder, as-cast and SLM rods with a diameter of 3 mm. The SLM sample was produced with the optimized parameter set with a laser power of 109.5 W, a scanning speed of 1000 mm/s, a layer thickness of 40 µm, and a hatch distance of 200 µm. Only broad diffraction maximum can be observed, suggesting a fully amorphous structure. (b) DSC traces of representative powder, as-cast and SLM samples. An obvious endothermic glass transition at T_g (marked by arrows), followed by exothermic crystallization can be seen in all traces. (c) TEM micrograph and corresponding SAED pattern (inset) of a SLM sample. A homogeneous maze-like pattern reveals a fully glassy structure for the SLM specimen. The broad and diffuse rings also shown in the inset indicate an amorphous structure.

Fig. 3.16 shows the defect size (i.e. pore size) distribution and a full µ-CT reconstruction of a representative SLM sample for compression test. The pores distribute uniformly across the sample and no pore aggregation can be found, which is different from the previous work [220]. During SLM processing, the formation of pores is inevitable. There are many factors, which promote the formation of defects such as non-ideal powder deposition, the laser power distribution and the quality of the powder particles [167]. The slightly enhanced laser power in combination with the optimized scanning velocity apparently reduces the likelihood to locally not melt powder particles. In addition, the proper amount of relatively small powder particles increases the packing density in the powder bed. The pore size ranges from 10 µm to 70 µm. Most of the defects exhibit a spherical geometry, which reveals that the energy input is sufficient. Furthermore, the largest fraction of pores has dimensions below 35 µm, indicating that the optimized parameter can eliminate pore aggregation and decrease the defect size.

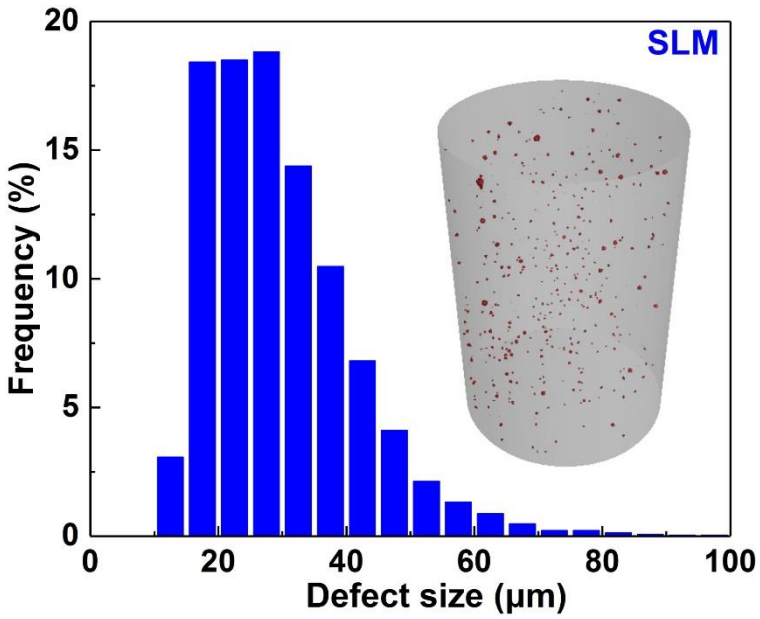

Figure 3.16: Defect size distribution and µ-CT reconstruction (inset) of a $Zr_{52.5}Cu_{17.9}Ni_{14.6}Al_{10}Ti_5$ sample produced by SLM. The pore size is randomly distributed within the sample.

3.2.3 Mechanical properties

3.2.3.1 Compression tests

The SLM samples and the as-cast samples were then uniaxially compressed. Fig. 3.17 (a) depicts the compressive stress-strain curves of three as-cast and three SLM rods. All as-cast samples show a distinct plastic strain after yielding at stresses ranging between 1830 MPa and 1930 MPa as well as a fracture strain of 3.1% to 3.8%. The cylindrical SLM samples show comparatively lower yield stresses (1670 MPa to 1710 MPa) and also show a typical plastic strain of up to 0.5% after yielding.

The fracture surfaces of the SLM samples were investigated in a scanning electron microscope (Figs. 3.17 (b) to (d)). The fracture surfaces are rather smooth and form a distinct plane inclined by 45° with respect to the loading axis (inset of Fig. 3.17 (b)). This is quite different from previous investigations, in which the fracture surface is not a single plane but is reminiscent of an inclined rooftop (see Fig. 3.8). This means that the stress state is different in the present SLM samples and reveals that they predominantly fail in a shear mode [278]. Multiple interlaced planes form only at the edges of the rods, which cannot be found in the as-cast samples (not shown here). At higher magnifications (Fig. 3.17 (c)), it becomes obvious that the areas around the pores have a more rugged morphology possibly due to the different stress state during compression [220]. Moreover, the vein-like pattern, which is characteristic of shear fracture of as-cast BMGs [278] is found in pore-free regions (Fig. 3.17 (d)), suggesting that the

lower porosity contributes to the enhanced plasticity. However, uniformly dispersed, relatively small pores in metallic glasses are known to drastically elevate plastic deformability [64-66]. Such an enhancement of plasticity has been attributed to stress concentrations around the pores leading to shear-band proliferation [49, 65, 66, 279]. As indicated in Fig. 3.16, there are a few exceptionally large pores present and the μ-CT reconstruction implies that some of the pores have an irregular shape. These large pores possibly having sharp edges concentrate the stresses during loading and might, thus, be responsible for early failure [49, 280]. This phenomenon cannot be counterbalanced by the altered stress state and the more uniform shear band generation around the smaller pores. Simultaneously, the fracture stress must be lower for the additively manufactured samples than for the as-cast samples. Another possible explanation for the reduced plasticity of the additively manufactured glass could be its relatively high oxygen content. Oxygen embrittlement has been reported for a variety of glass-forming alloys [281, 282] including Zr-based alloys [283, 284]. However, the mechanism underlying this phenomenon is still subject of debate. Above a certain level, oxygen generally reduces the glass-forming ability by interfering with the crystallization process [284, 285]. In the case of Zr-based bulk metallic glasses, high oxygen contents stabilize a metastable $NiTi_2$-type phase (big cube phase) [277, 286, 287] or oxides [288] and, with it, deteriorate critical casting thickness [283-285]. The precipitation of big cube crystals or oxides is accompanied by a significant reduction of the plastic strain [283, 284, 288]. The oxygen content in the present SLM samples (920 ± 20 ppm) is sufficiently high to favour formation of the big cube phase. However, it only precipitates when the energy input during processing is above 15 J/mm^3 [220]. This is higher than in the present experiments (E_V = 13.7 J/mm^3) and neither the XRD patterns (Fig. 3.15 (a)) nor the enthalpies of crystallization suggest the presence of any crystalline phase. Recent research provides another explanation for the observed oxygen embrittlement in metallic glasses. Completely dissolved oxygen has been found to drastically reduce the fracture toughness of a Zr-based bulk metallic glass [230, 282]. It has been hypothesized that oxygen alters the short- and medium-range order and thereby renders shear transformations, which constitute the early stage of shear banding [49], energetically more unfavourable [230]. In a Cu-Hf-Al bulk metallic glass, in contrast, dissolved oxygen is claimed to only have a marginal effect on the toughness of the glass [281]. In any case, various publications [230, 275, 289, 290] suggest that at or around the oxygen content of interest (920 ± 20 ppm), Zr-based bulk metallic glasses still exhibit a significant plastic strain on compressive loading. Hence, it seems unlikely that oxygen is responsible for the early failure of the present additively manufactured $Zr_{52.5}Cu_{17.9}Ni_{14.6}Al_{10}Ti_5$ samples observed during the compression tests. A more detailed study,

however, would be required to clarify this point. It is notable that the serrated flows of SLM sample and as-cast sample are different in Fig. 3.17 (a). As discussed in section 1.2.3, by analysing the serrated flow the details of deformation mechanism can be revealed. The differences for the serrated flows will be discussed in section 3.2.4.

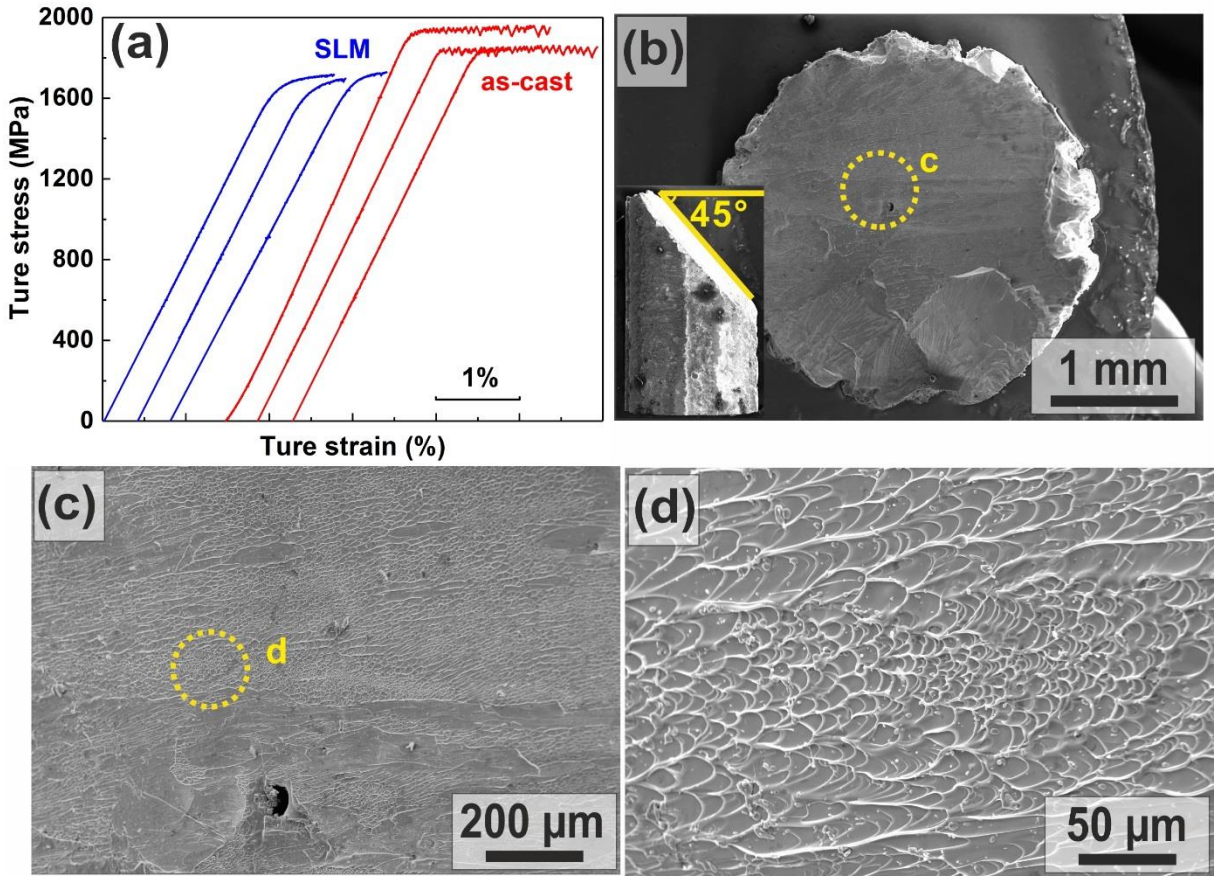

Figure 3.17: (a) True stress-strain curves of $Zr_{52.5}Cu_{17.9}Ni_{14.6}Al_{10}Ti_5$ samples prepared by casting and SLM. Three samples of each manufacturing technique were selected to show the reproducibility of the compression test. All SLM samples yield at stresses lower than the as-cast material and exhibit a smaller plastic strain. (b) Fracture surfaces of the rod samples fabricated via SLM. The fracture angle is about 45° (inset). The morphology of fracture surfaces reveals interlaced fracture planes. (c) Magnified section of the fracture surface shown in (b). The morphology around the pore differs from the remaining fracture surface. (d) Enlarged section in (c) shows that typical vein-like patterns are found in pore-free regions.

3.2.3.2 Microhardness and structural relaxation

As outlined in section 1.2.2, structural heterogeneities are important to the plasticity of BMGs. In order to study the macroscopic structural homogeneity of the SLM samples and the influence of the processing method on the mechanical properties, microhardness measurements were performed on both SLM and as-cast $Zr_{52.5}Cu_{17.9}Ni_{14.6}Al_{10}Ti_5$ samples. Fig. 3.18 displays the respective microhardness maps of the cross and longitudinal section for SLM and as-cast

samples. As shown in Fig. 2.5 (section 2.2.8), the indents were created in the central part of the samples, where the laser works steadily in case of the SLM samples and where the cooling rate does not have a gradient in case of the as-cast samples. All the microhardness maps in Fig. 3.18 show rather uniform values ranging from 496 ± 6 HV0.2 to 524 ± 6 HV0.2. When comparing the cross-section and the longitudinal section of the SLM sample (Figs. 3.18 (a) and (b)), one finds that the hardness values are quite homogeneous across the entire sample. The microhardness measurements do not reveal any features, which could correspond to the heat-affected zone or the margins of a melt track [229, 245]. Since no obvious differences in the hardness maps of the as-cast and SLM samples are present (Figs. 3.18 (c) and (d)), the layer by layer processing inherent in selective laser melting does not seem to significantly relax or rejuvenate the structure (section 1.1), which would otherwise result in higher or lower hardness values. It should be stressed here that the distance between indents is around 100 µm. Thus, the present results only reflect the macroscopic homogeneity/heterogeneity of the SLM samples. This study is complemented and extended by exploring the structure on a more local scale by nanoindentation. The results are discussed in the following section.

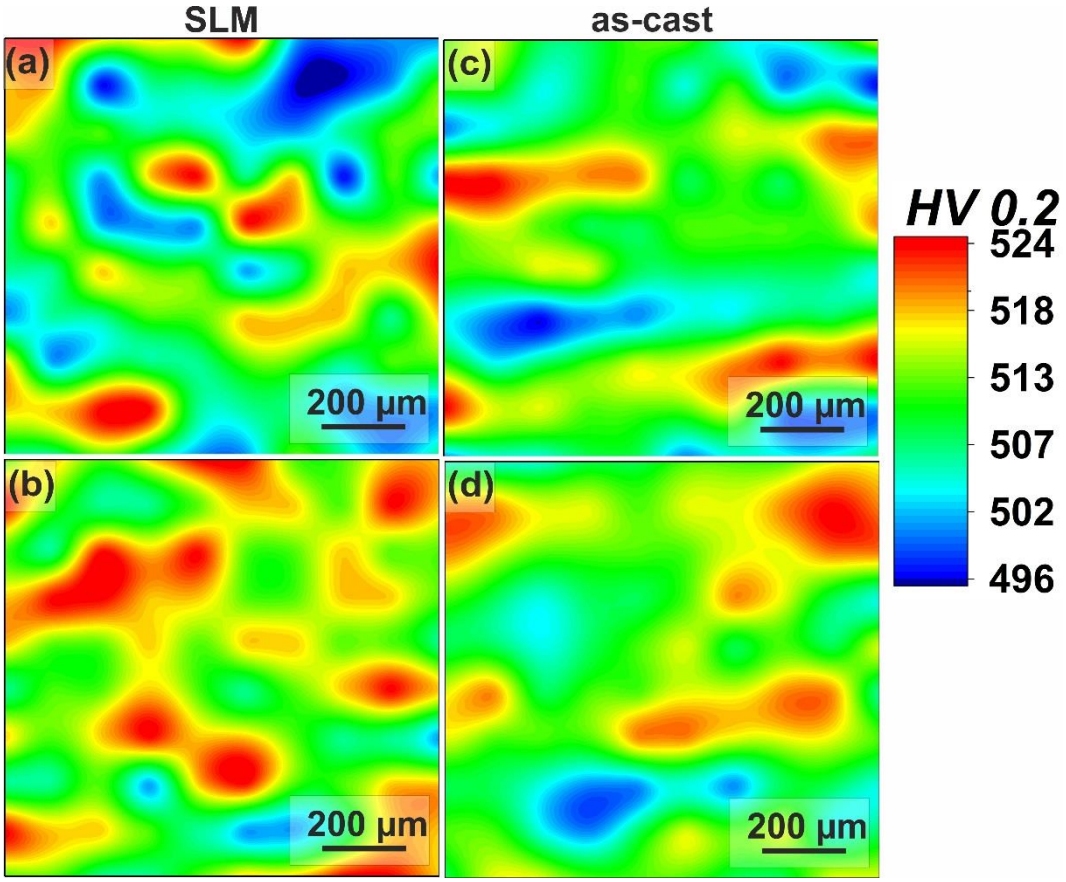

Figure 3.18: (a) and (c) depict the microhardness contour maps for the cross section of SLM and the as-cast sample, respectively. (b) and (d) display the microhardness maps for the longitudinal section of SLM and as-cast BMGs, respectively.

As mentioned above, the SLM samples show yield strengths comparable to the as-cast samples. However, the deformation mechanisms, which might provide conclusions related to the premature fracture of SLM samples, need to be clarified.

Previous works have attributed premature failure either to inherent porosity, crystallization in heat-affected zone (HAZ) or structural relaxation caused by layer-by-layer process method [128, 220, 222]. The question now arises: How homogeneous are the SLM samples on the microscale? Intimately connected with this point is structural relaxation of the glass, which may occur during manufacturing.

According to the microstructural analysis and the thermal data shown in Fig. 3.15 (section 3.2.2), the SLM samples are fully amorphous. Therefore, structural heterogeneity caused by crystallization can be ruled out. In order to further investigate the homogeneity on the microscale, nanoindentation which can indirectly detect the structural differences [270], and a systematic investigation of the relaxation enthalpies was conducted. Therefore, the relaxation enthalpies were analysed (Fig. 3.19). A section of the full DSC trace, which reveals the structural relaxation of the as-cast and SLM samples just below the glass-transition temperature, was selected. The relaxation enthalpies of the SLM samples range between ΔH_{relax} = 9.42 J/g and ΔH_{relax} = 11.38 J/g, whereas the as-cast samples display distinctly lower values (ΔH_{relax} = 3.16 J/g - 4.93 J/g). As in the case of the Ti-based glass (section 3.1.3.2), one can speculate that the durations of the cyclic temperature increases during SLM are too short [128] to cause pronounced relaxation and, therefore, the enthalpy of relaxation remains larger than for the as-cast glass. In order to reveal the thermal history of SLM, the relaxation enthalpies as a function of sample height will be discussed in section 3.3.

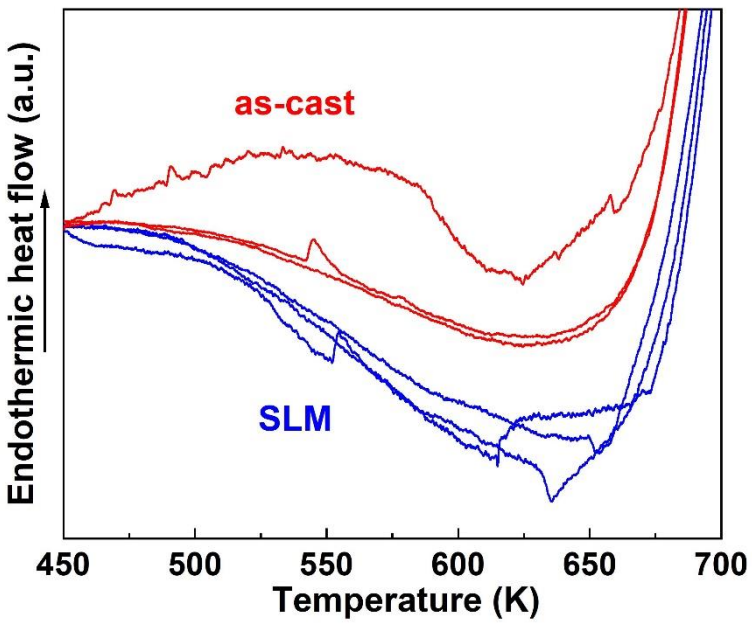

Figure 3.19: DSC curves of as-cast and SLM samples show exothermic structural relaxation. The relaxation enthalpies of SLM samples are larger than for the as-cast samples, indicating a less structurally relaxed state.

3.2.3.3 Nanoindentation

As revealed in section 3.2.3.2, the SLM samples appear macroscopically homogeneous. Nonetheless, the SLM process might lead to a non-uniform distribution of free volume or likewise atomic strains (see section 3.1.3.3). The DSC data (section 3.2.3.2), yet, do not provide any information on whether or not the highly localized, sequential energy input upon SLM. As discussed in section 3.1.3.3, nanoindentation appears to be a suitable tool to detect structural heterogeneities in additively manufactured BMGs.

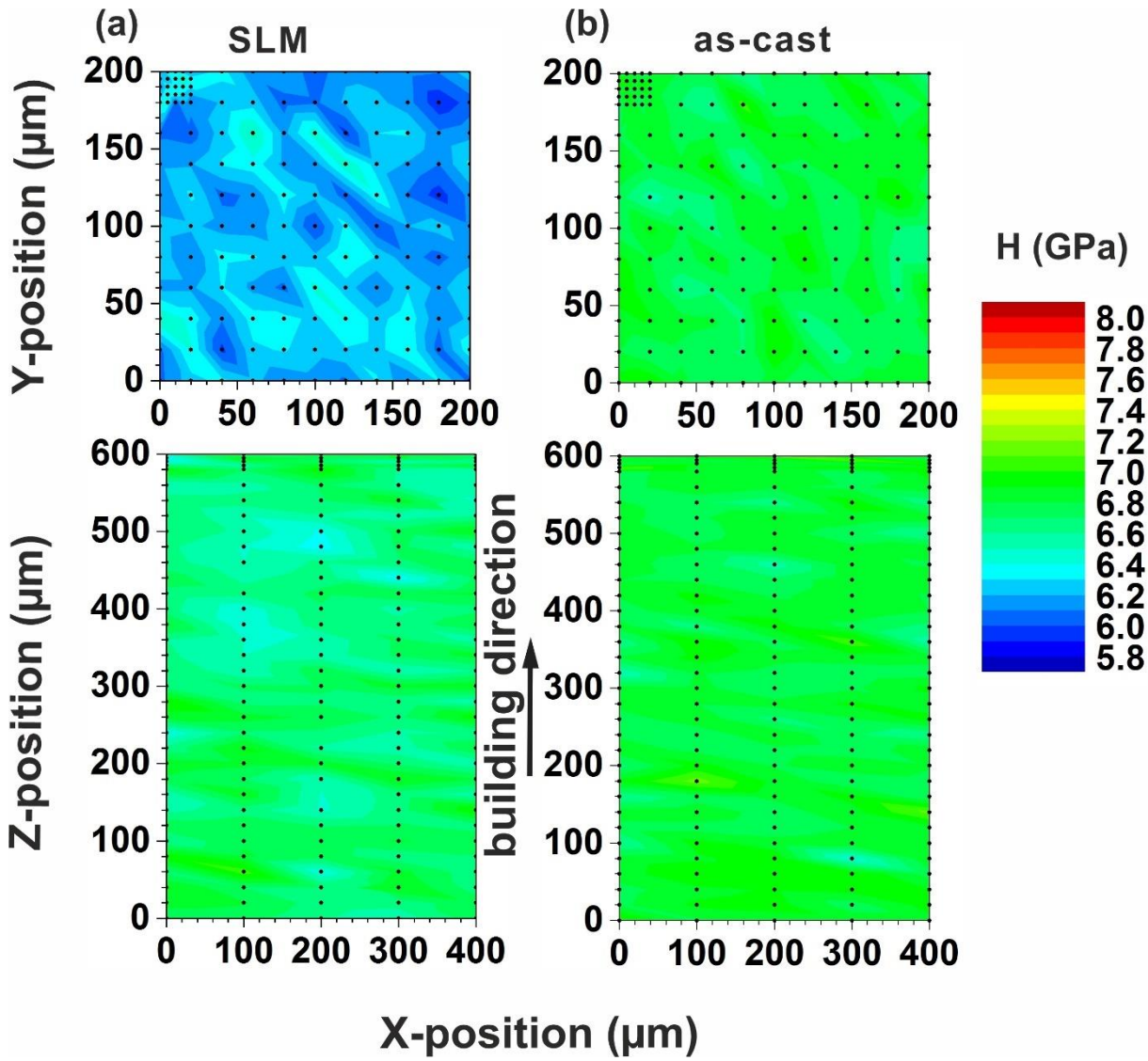

Figure 3.20: Hardness contour maps of the cross section (upper) and longitudinal section (down) of SLM and as-cast $Zr_{52.5}Cu_{17.9}Ni_{14.6}Al_{10}Ti_5$ samples based on the indents revealed as black dots, respectively. The SLM sample is produced with the layer thickness of 40 µm and the hatch distance of 200 µm.

The cross-sectional nanohardness map of the additively manufactured $Zr_{52.5}Cu_{17.9}Ni_{14.6}Al_{10}Ti_5$ BMG (Fig. 3.20 (a), top) yields values ranging from 5.8 to 6.2 GPa. The hardness distribution of the longitudinal section has values ranging from 6.4 to 7.0 GPa, as the corresponding map demonstrated (Fig. 3.20 (a), bottom). Both cross and longitudinal sections of as-cast sample have the similar hardness values ranging from 6.5 to 7.1 GPa. The larger relaxation enthalpy of the SLM samples (see Fig. 3.19) is in accord with the lower hardness value for SLM sample shown in the hardness maps. The longitudinal maps suggest a layer-type arrangement of the hardness values. This could be indeed the case for the SLM sample because the building direction is aligned with the z-axis (Fig. 3.20). For the as-cast sample, in contrast, such a layer-like distribution of hardness values does not seem probable.

Instead, the interpolation of the hardness values might be the origin of this phenomenon since the horizontal distance between indents (100 µm) is larger than their vertical spacing (20 µm). Both probed longitudinal sections are larger than the typical HAZ in metallic alloys [128, 217] and also significantly larger than the melt track dimensions in the present experiments (width about 250 µm). Due to absence of a conventional microstructure, the melt track depth cannot be extracted from microscopy but is expected to be in the range of 60 µm to 100 µm [128, 217]. Nevertheless, no obvious heat-affected zones with significant gradients in hardness (corresponding to more or less relaxed states) are visible within the spatial resolution of the present maps (Fig. 3.20 (a)). This contrasts recent results on a similar Zr-based BMG obtained by selective laser melting [245]. Interestingly, compared to the cross-section, the longitudinal section is overall harder, a behaviour, which could not be found in the Ti-based glass (section 3.1.3.3). One speculation is that different processing parameters and thermal physical properties induced different relaxation behaviours in two systems, leading to such differences. More details will be discussed in section 3.3.

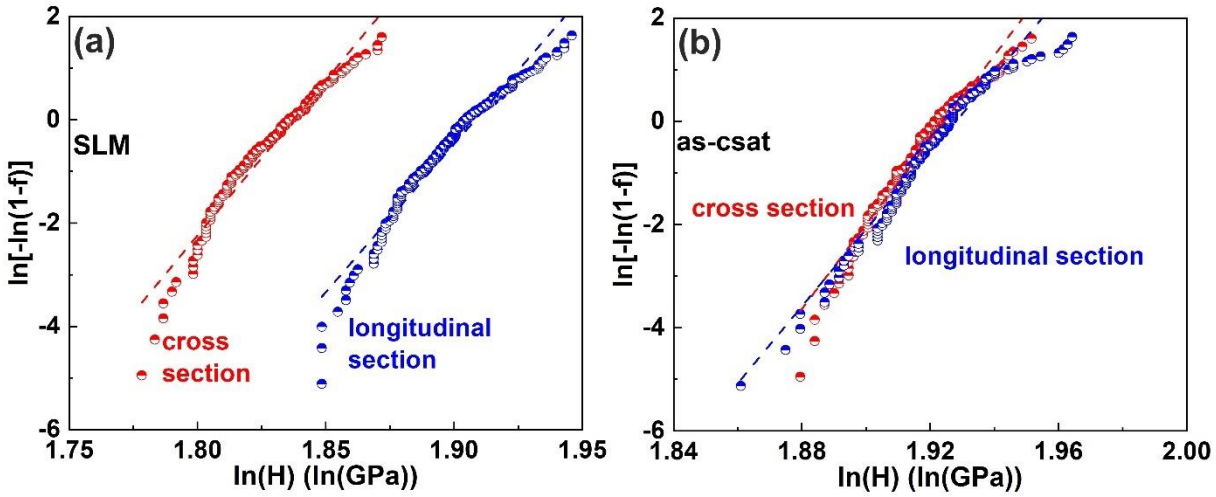

Figure 3.21: Weibull plot of the hardness values shown in Fig. 3.20. (a)Additive manufactured and (b) as-cast $Zr_{52.5}Cu_{17.9}Ni_{14.6}Al_{10}Ti_5$ samples. The Weibull modulus, *m*, is derived from the slope of the linear regression curve of ln[-ln(1-*f*)] over ln(*H*), marked by the dashed lines.

Again, the distribution of the nanohardness was analysed and a Weibull plot was created (Fig. 3.21). The Weibull modulus extracted for the cross section of $Zr_{52.5}Cu_{17.9}Ni_{14.6}Al_{10}Ti_5$ SLM sample ($m = 60.05 \pm 0.95$) is slightly higher than for the longitudinal section ($m = 57.30 \pm 0.95$). This indicates a more heterogeneous structure of the longitudinal section for the SLM sample. The as-cast sample also shows a steeper slope for the cross section than for the longitudinal section. The Weibull modulus of cross section ($m = 81.85 \pm 0.95$) is higher than that of longitudinal section ($m = 74.65 \pm 0.96$). Even though the hardness maps do not allow for the identification of a typical HAZ, the Weibull modulus of as-cast sample is higher than that of

SLM sample in both cross and longitudinal sections. In other words, the structure of BMGs fabricated by SLM is less uniform resulting in larger scattering of the nanohardness values [291]. As discussed in section 1.2.3, the structural heterogeneities can affect shear band generation and propagation. Even though the observed heterogeneities (Fig. 3.20) in SLM sample are not extremely pronounced, they might account for the different serrated flows of SLM and as-cast samples. More information about the serrations will be discussed in section 3.2.4.

3.2.4 Shear band dynamics and shear band propagation

Next to the lower plastic strain of the SLM samples, another characteristic becomes apparent from the stress-strain curves of Fig. 3.17 (a): the serrated flow behaviour is clearly different between the as-cast and the additively manufactured glass. As outlined in section 1.2.3, serrated flow reflects the shear band propagation in metallic glasses and its stick-slip characteristics [49, 108, 111]. Statistical analysis of these serrations provides valuable information regarding the shear band dynamics [108, 112]. Thus, the shear banding behaviour is illuminated in the following paragraphs.

Fig 3.22 shows an enlarged section of the plastic flow regime of the stress-strain curves displayed in Fig. 3.17 (a). Fewer but much larger stress drops occur within a given time interval (strain interval) in the as-cast sample than in the SLM sample (Fig. 3.22 (a)), suggesting that the processing method significantly affects the shear band dynamics. In order to better understand the difference between the two structural states, a statistical analysis of the serrations was carried out. The stress drop magnitude was normalized following the routine of Sun *et al.* [108] (see section 1.2.3). The resulting normalized stress drop magnitude, s, (Fig. 3.17 (b)) was calculated in the stable plastic flow regime. Fig. 3.22 (b) highlights the difference in the stress drop magnitudes and their frequencies for the as-cast and additively manufactured samples. The stress drop magnitude is rather uniform for the SLM samples and s remains below a value of 2.5 MPa. In contrast, the stress drop magnitudes scatter much more in the case of the as-cast sample and values of up to 27 MPa are observed. This is summarized in the according histograms of s (Figs. 3.22 (c) and (d)). Since the stress drop magnitude is an indicator for shear band stability, shear banding should be more stable in the SLM sample [110]. Because of the same strain regime compared here, many more serration events must occur in the SLM samples to accommodate the imposed plastic strain (Fig. 3.22 (a)). The distribution of s provides information on the shear banding process, which can range from chaotic to self-organized critical [108, 110]. If plastic deformation of BMGs is dominated by the propagation of a major shear band, then serrated flow will be chaotic and the corresponding distribution of s has a Gaussian-type shape [108, 110]. BMGs with a chaotic serrated flow behaviour generally show

very limited plastic deformability [108]. When plastic deformation is borne by multiple shear bands, as in malleable BMGs, the cumulative probability distribution of s, $P(s)$, can be approximated by a power law coupled with an exponential decay function [108, 110, 292]:

$$P(s) = As^{-\beta} \exp\left\{-\left(\frac{s}{s_c}\right)^2\right\} \tag{3.1}$$

where β is the scaling exponent and s_c is the cut-off stress drop, which indicates up to which value of s, the power law is valid. In such plastically deformable (malleable) metallic glasses, serrated flow is in a self-organized critical state, which means that shear bands are highly correlated and that the serration magnitude does not have an intrinsic size [108, 110]. Also other complex dynamic processes, such as earthquakes [293] or dislocation avalanches [292] are subjected to self-organized criticality. In order to examine if flow is a self-organized critical phenomenon in the present glasses, the cumulative probability distributions were calculated (Figs. 3.22 (e) and (f)) and fit by equation (3.1).

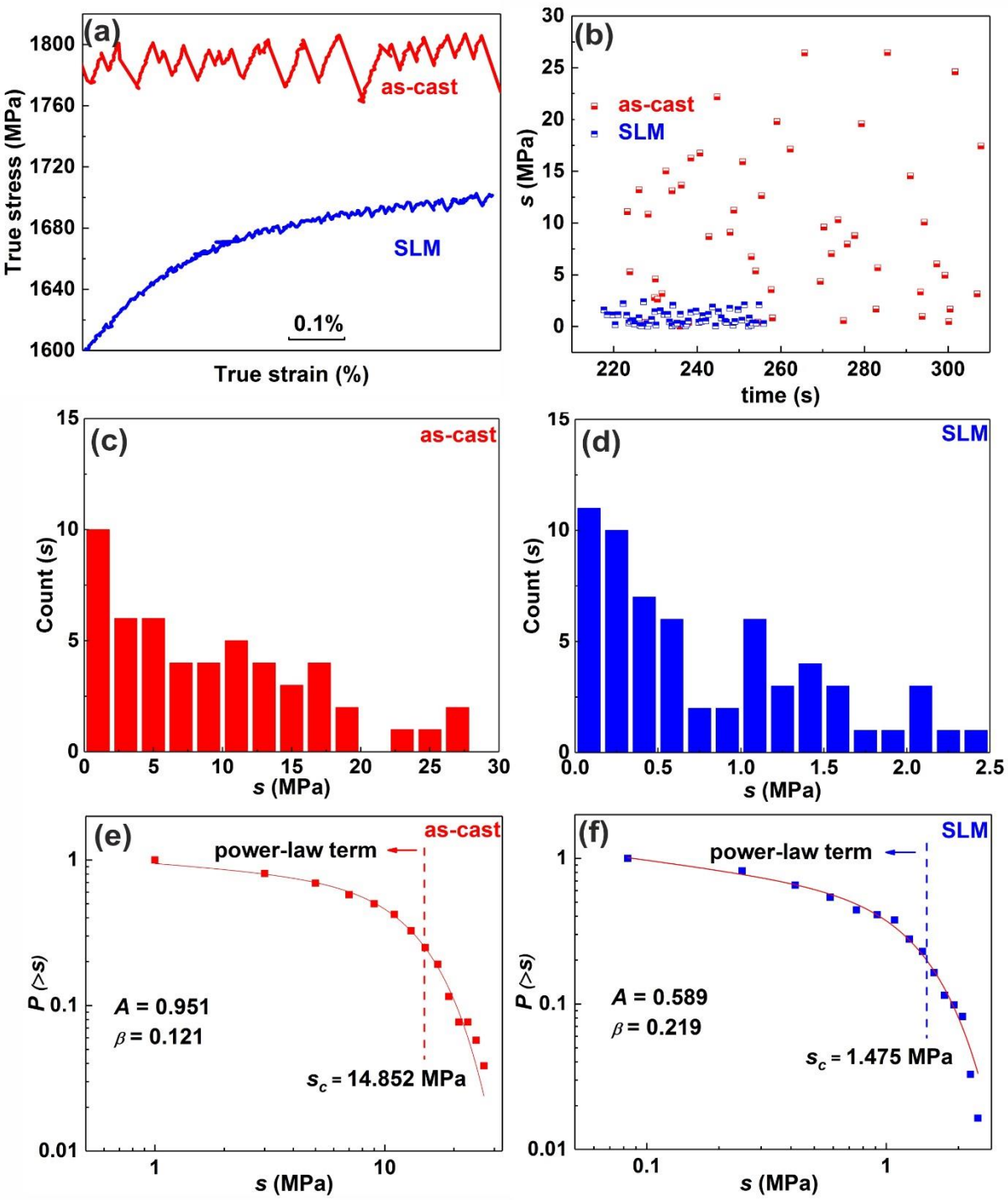

Figure 3.22: (a) An enlarged view of the serrated region in stress-strain curve shown in Fig. 3.17 (a). (b) The normalized stress drop magnitude, *s*, is given as a function of time. The stress drops in the SLM sample are much smaller than the as-cast one. The histograms of the normalized stress drop magnitude for (c) the as-cast sample and (d) the SLM sample. Please note the different ranges for *s*. The cumulative probability density for the as-cast (R = 0.995) and the SLM (R = 0.994) sample are depicted in (e) and (f), respectively. Equation (3.1) (solid line) describes the data well.

Indeed, the probability of a normalized stress drop magnitude, *s*, to occur in both the as-cast and the SLM samples can be properly captured by equation (3.1). We now want to briefly

discuss the fitting parameters β and s_c, which characterize the dynamics of shear banding [294]. Both are in the range reported for BMGs of comparable compositions [108, 110] but caution should be exercised when directly comparing the values because the sample dimensions, sample alignment and the machine stiffness strongly affect plasticity and serrated flow [108, 110]. It has been demonstrated that β decreases with an increase in plasticity banding [294], a trend also observed here (Figs. 3.22 (e) and (f)). In contrast, s_c, is significantly smaller in the SLM sample than in the as-cast glass (Figs. 3.22 (e) and (f)). A smaller cut-off value has been associated with a reduced shear avalanche size because more shear bands accommodate the imposed shear [294]. This distributes the strain more homogeneously and also holds here. Therefore, the shear band dynamics differ in the differently prepared glasses.

To facilitate visualization of the shear bands, a rectangular SLM sample was produced and one side was polished prior to uniaxial compression. Afterwards, the polished lateral surfaces of the cuboid-like specimens after fracture were examined in a SEM to gain insights regarding the macroscopic propagation of shear bands. Fig. 3.23 (a) depicts the true stress-strain curve of the rectangular SLM sample in compression. It yields at 1420 ± 20 MPa and fractures at 1540 ± 10 MPa both of which is lower than what is measured for the cylindrical SLM rods. Since the µ-CT reconstruction (inset to Fig. 3.23 (a)) shows a similar defect size distribution as the cylindrical specimen and both specimens are fully amorphous, stress concentrations arising at the edges could be the cause for the lower strength and the reduced plastic deformability [295]. The rectangular SLM sample fractures at an angle of about 45° (Fig. 3.23 (a), inset), i.e. along the plane of maximum shear stress [296]. The fracture surfaces of the rectangular SLM sample show multiple interlaced planes and vein-like patterns similar to the cylindrical SLM samples (Fig. 3.23 (b)). As discussed above, one might expect "interfaces" (about 40 µm thick, Fig. 3.23 (c)) between the regions with different thermal history (c.f. heat-affected zone) [207]. One could conjecture that such structural heterogeneities affect the propagation and orientation of shear bands since both are very sensitive to structural heterogeneities [70, 297]. However, in Fig. 3.23 (c) only straight shear bands can be observed, and they form an angle of 45° with respect to the loading direction.

During the activation of shear transformation zones (STZs) ahead of the shear band tip, antisymmetric stress-fields (vortices) evolve and they are transferred to adjacent non-activated STZs (see section 1.2.2) [55]. Both processes are very susceptible to the presence of structural heterogeneities even when the structure remains amorphous. More precisely, such heterogeneities in the amorphous state can be fluctuations in the local packing density or composition [70, 298, 299]. From this perspective, it is somewhat remarkable, that the shear

bands propagate in a straight manner and are not affected by the layerwise processing, since this is a strong implication for the fact that the SLM samples are homogeneous even beyond the atomic level.

Fig. 3.23 (d) depicts multiple shear bands, which interact with each other and with pores. At a higher magnification, the interaction between the pores and shear bands becomes more obvious: The shear bands either transect the pores, a process, which is accompanied by a small displacement of the shear band (Fig. 3.23 (e)). Alternatively, major shear bands terminate near a pore (Fig. 3.23 (f)) while multiple horizontal shear bands are generated around the pore. Even without a major shear band in its vicinity, pores clearly act as initiation sites for shear bands (Fig. 3.23 (g)) [64]. The altered stress state around the pore [64, 66] apparently affects shear band initiation as well as propagation, similar as it is known for other second phases being embedded in a metallic glass [107]. These findings help to explain the apparent differences in the serrated flow. At the initial stage of plastic deformation, the pores lead to a higher density of shear bands, each having a smaller shear offset. Consequently, shear banding is more stable and the stress drops, s, are smaller for the SLM sample than for the as-cast glass. Two aspects, however, remain intriguing and shall be briefly discussed below: (i) Why do the SLM samples fail at comparatively low stresses/strains and (ii) why are the shear bands macroscopically straight?

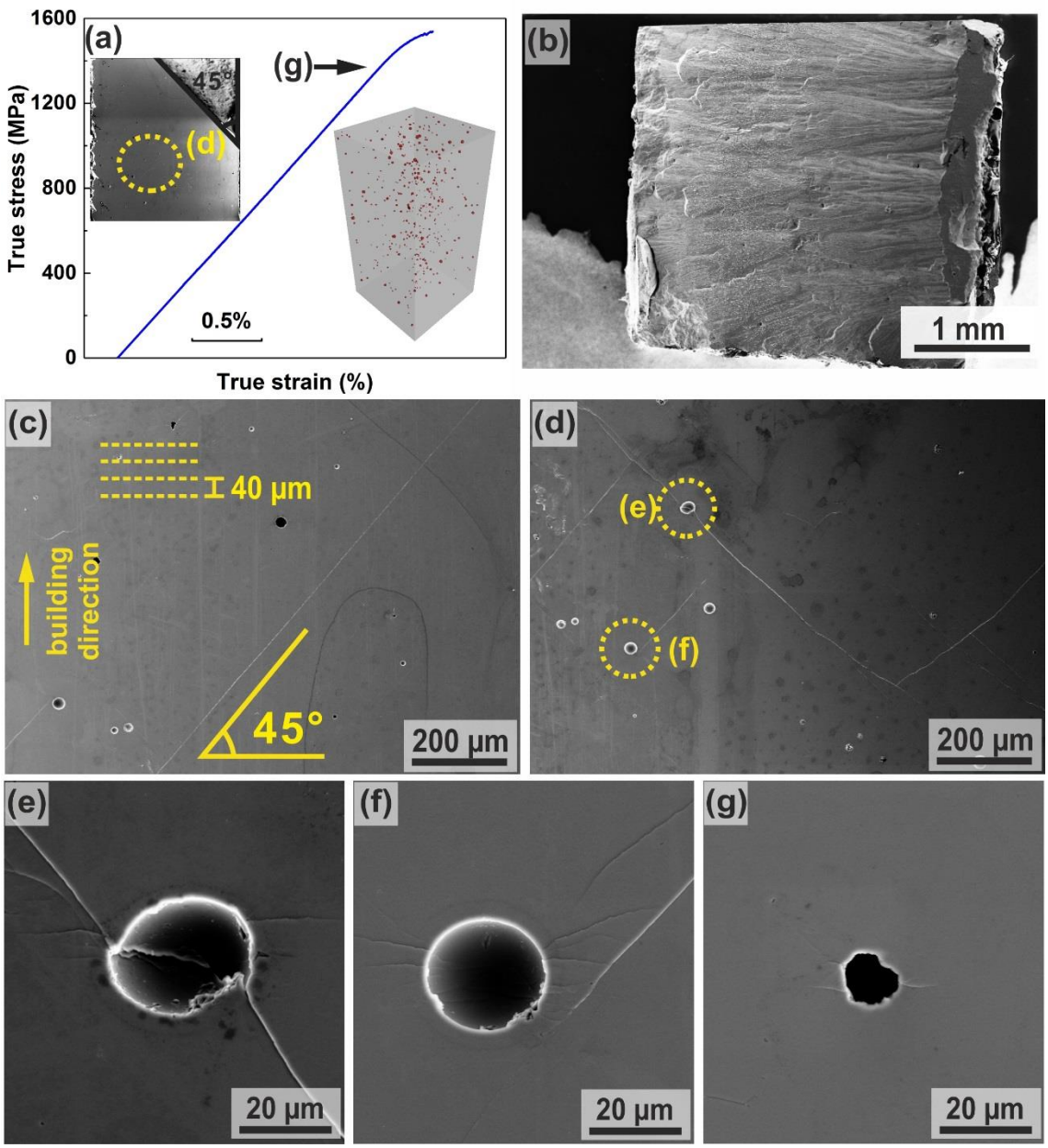

Figure 3.23: (a) True stress-strain curve of a rectangular SLM sample corroborates its plastic deformability. The insets depict the fracture angle of about 45° and the corresponding µ-CT reconstruction. (b) Fracture surfaces of the rectangular samples prepared via SLM. The morphology of fracture surfaces reveals interlaced fracture planes. There exist vein-like patterns. (c) A straight shear band observed on the lateral surface of fractured SLM cuboid sample. (d) SEM image depicts multiple shear bands interacting with each other and with pores. The regions of interest (encircled) are shown at higher magnification in (e) and (f). (g) Shear band initiation at a pore for a sample loaded until plastic deformation, as indicated in (a).

The distribution of pore sizes (Fig. 3.16 and 3.23 (a)) indicates that there are a few exceptionally large pores present and the µ-CT reconstruction implies that some of the pores have an irregular shape. These large pores possibly having sharp edges concentrate the stresses during loading and might, thus, be responsible for early failure [49, 280]. This phenomenon cannot be counterbalanced by the altered stress state and the more uniform shear band

generation around the smaller pores. Simultaneously, the fracture stress must be lower for the SLM samples than for the as-cast samples because of their lower relative density.

In conclusion, shear banding appears to be more stable in the SLM samples and the structural heterogeneity probed by nanoindentation as well as the uniform distribution of pores can account for this observation. Especially the pores alter the stress state, which entails a more uniform generation of shear bands. In spite of the overall higher amount of free volume and the structural heterogeneity of the SLM samples, they tend to fail earlier than the as-cast material. Most likely, the presence of few but relatively large pores accounts for the reduced damage tolerance.

3.2.5 Tribological and corrosion properties

Since SLM generally yields much higher cooling rates than copper mould casting (10^3 - 10^8 K/s) [198], one can anticipate differences in the wear behaviour (see section 1.2.4) [123]. In addition, the presence of µm-scale pores in the SLM samples might also play an important role. Yet, data on these aspects are still scarce [222] and the detailed mechanism has not been elucidated.

The sliding wear experiments were conducted to explore, whether the manufacturing process affects the wear behaviour and the wear mechanisms. The coefficient of friction as a function of time for an as-cast specimen, is shown in Figs. 3.24 (a) and (b). The coefficient of friction reaches a steady state with a value of about 0.4 within the first 35 minutes of testing. Between 35 and 120 minutes, the coefficient increases, as does its scatter. This is indicative of a transformation in the wear mode [300]. The worn surfaces of the as-cast $Zr_{52.5}Cu_{17.9}Ni_{14.6}Al_{10}Ti_5$ glass after different sliding times are shown in Figs. 3.24 (c) to (f). Only slim grooves are visible (Fig. 3.24 (c)) and their evolution indicates a distinct abrasive mechanism at the early stage of wear. With increasing sliding time, some fine debris forms (Fig. 3.24 (d)), and more material is ploughed out of the surface. This coincides with the drastic increase in the scattering of the coefficient of friction (Figs. 3.24 (a) and (b)) and suggests a transition in the wear mode. Plastically deformed grooves and adhering debris can be observed at later stages of wear (Figs. 3.24 (e) and (f)). The resulting typical mixed worn morphology indicates an abrasive and adhesive wear mechanism [126, 300].

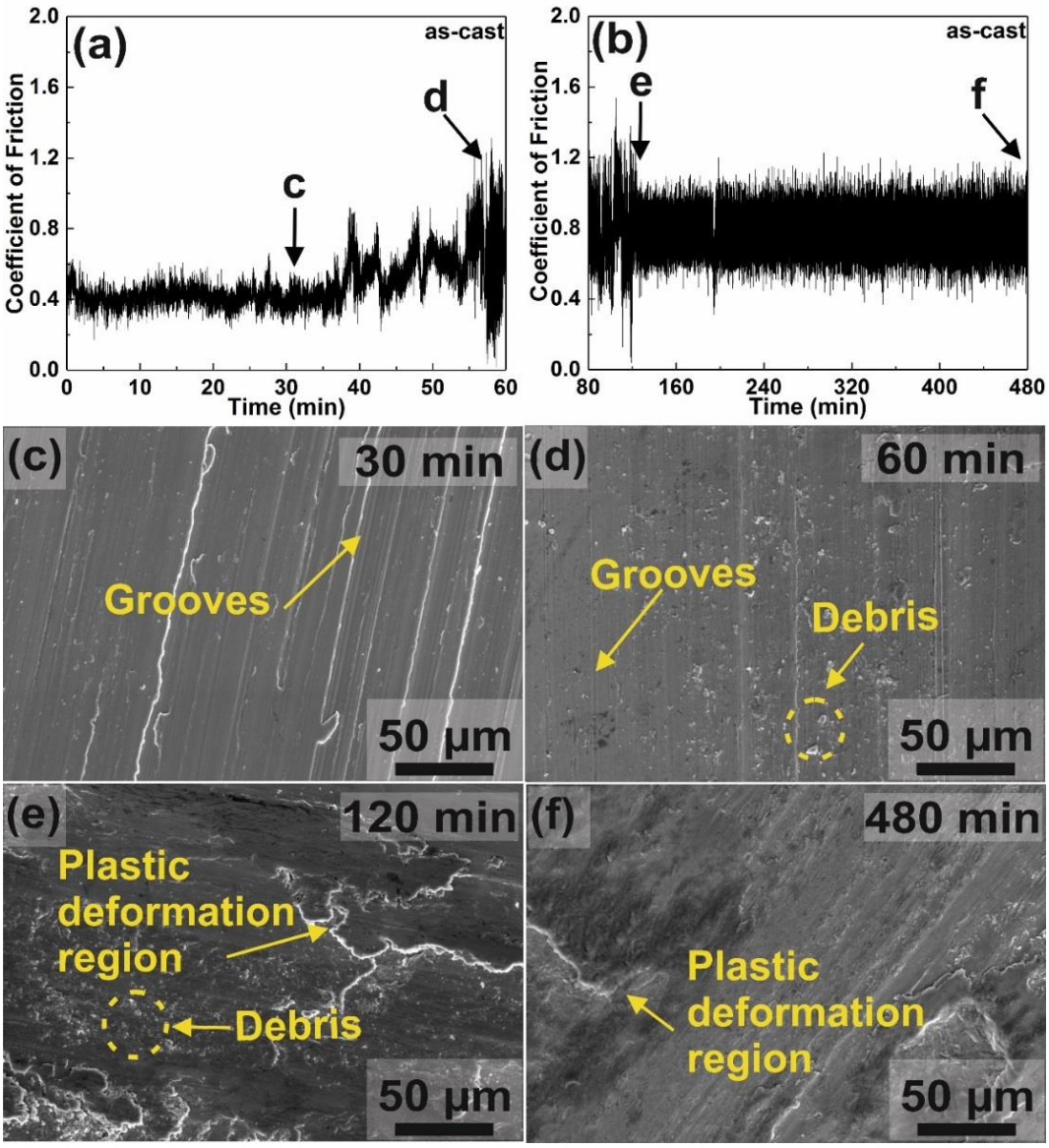

Figure 3.24: (a) and (b) depict the coefficient of friction as a function of sliding time for the as-cast $Zr_{52.5}Cu_{17.9}Ni_{14.6}Al_{10}Ti_5$ sample. Its variation, suggests a change in the wear mode. (c) to (f) show the morphologies of the worn surfaces after 30, 60, 120, 480 min of sliding. Grooves and debris can be clearly seen after the first 60 min (shown in (c) and (d)). In (e) and (f), plastically deformed regions dominate the surface.

The coefficient of friction and the surfaces of the SLM samples at different stages of wear testing are illustrated in Fig. 3.25. The coefficient of friction (Figs. 3.25 (a) and (b)) shows a similar trend like for the as-cast specimen. Again, a change in the wear mode occurs after 35 minutes when the initial steady state ends. However, the fluctuations in the coefficient of friction after 80 minutes are more pronounced than for the as-cast sample and the maximum values are distinctly higher than for the as-cast glass. As long as the wear mode is purely abrasive (within the first 60 minutes), the worn surfaces of the SLM sample (Figs. 3.25 (c) and (d)) cannot be distinguished from the as-cast sample. More but smaller regions of plastically

deformed material are found at the later stages of wear ((Figs. 3.25 (e) and (f)). The wear mode in metallic glasses has been reported to transform to the "brittle and ductile" mixed stage at the later stages of wear (see section 1.2.4) [120]. This is expected to lead to the coexistence of softer and harder regions in the glass [120], which can reflect in a larger fluctuation of the coefficient of friction [120]. It is noteworthy that the scattering of the coefficient of friction is more pronounced for the SLM sample than for the as-cast material. This could be either related to the higher degree of porosity or to intrinsic structural heterogeneities on small length scales (see Fig. 3.20).

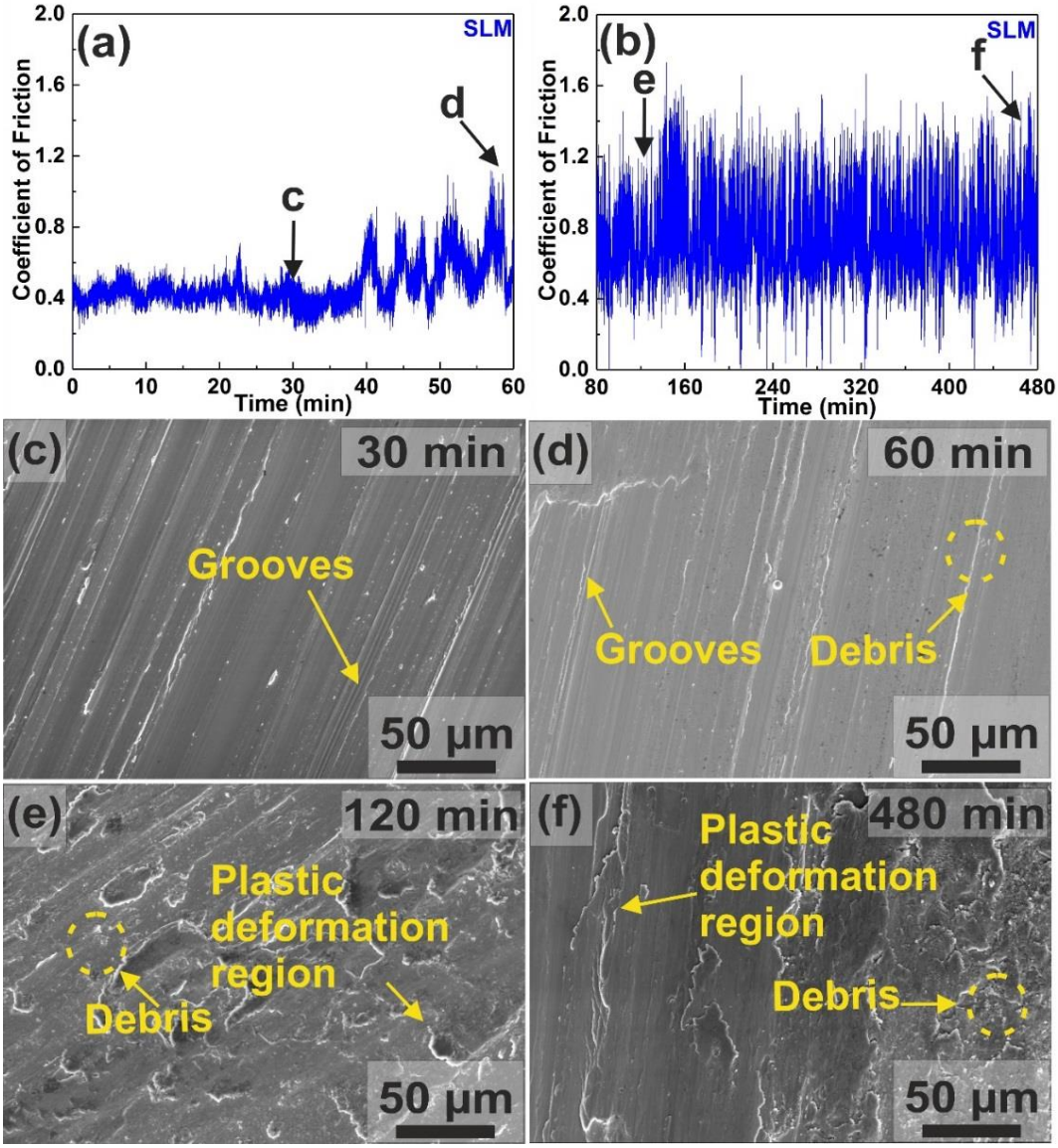

Figure 3.25: (a) and (b) display the coefficient of friction for the $Zr_{52.5}Cu_{17.9}Ni_{14.6}Al_{10}Ti_5$ sample produced by SLM. A similar trend as in Fig.6 (a) and (b) becomes obvious. (c) to (f) show the SEM images of the worn surfaces after 30, 60, 120, 480 min of wear testing. The SLM samples exhibit a comparable wear performance as the as-cast samples.

The coefficient of friction plays an important role for determining the wear resistance. A smaller value generally indicates higher wear resistance [118, 120, 121, 123-128]. Fig. 3.26 (a) compares the average coefficient of friction for the SLM and the as-cast samples at different sliding times. The average coefficient increases with sliding time, also due to the varying wear mechanism. Even though the coefficient of friction distinctly scatters for the SLM samples, the average COF is slightly lower than for the as-cast sample after long testing times (i.e. 480 minutes), indicating a slightly better wear resistance for the SLM sample. At the early and intermediate stages of wear, the average COF is comparable for both $Zr_{52.5}Cu_{17.9}Ni_{14.6}Al_{10}Ti_5$ samples (Fig. 3.26 (a)).

The specific wear rate for a SLM and an as-cast sample is shown in Fig. 3.26 (b) and it can be calculated as follows:

$$K_w = \frac{V}{F \times L} \tag{3.2}$$

where K_w is the wear rate; V is the loss volume determined by $V = (m_o - m_w)/\rho$ where m_o and m_w is the mass prior to and after testing, respectively, ρ is the density of the material; F is the load applied on the sample; L is the sliding distance given by $L = 2\pi rvt$, where r is the radius of the wear track, v is the rotating speed and t is the sliding duration [123]. The trend of the time-dependent specific wear rate agrees with the average COF (Fig. 3.26 (a)). Moreover, the wear rate for specimens prepared by the two different techniques is within the experimental error -at least for the early and intermediate stages of wear testing.

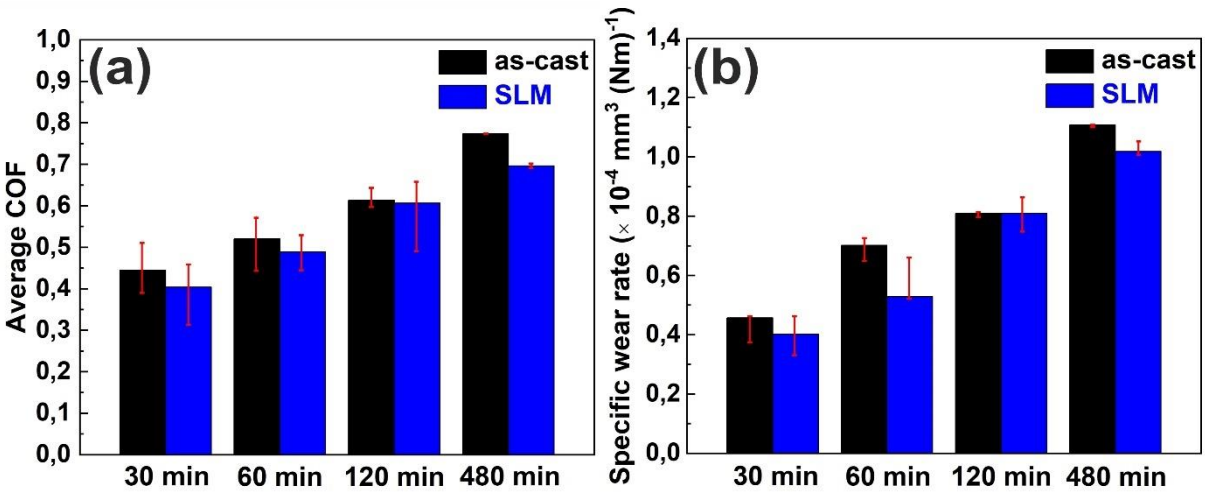

Figure 3.26: (a) Average coefficient of friction (COF) of the $Zr_{52.5}Cu_{17.9}Ni_{14.6}Al_{10}Ti_5$ SLM and as-cast samples dependent on time. The COF-values for samples prepared by both process conditions are similar except for the longest testing duration. (b) The specific wear rate of the SLM and as-cast specimen. The wear rate is in high agreement with the average COF (shown in (a)).

As outlined above, the wear behaviour of additively manufactured BMGs is comparable with the as-cast ones, indicating a great potential of application for BMGs produced via SLM.

Another crucial point in terms of potential applications is the corrosion behaviour of BMGs produced by SLM. As outlined in section 1.3, the chemically homogeneous nature of a single-phase glassy state is another reason for the enhanced corrosion resistance [134, 301, 302]. The powder used for additive manufacturing might suffer from chemical heterogeneities and the SLM process imposes completely different solidification conditions on the metallic melt (see sections 3.1.1 and 3.1.2). They could even promote chemical heterogeneities and structural heterogeneities (e.g. crystalline precipitates) (section 3.1.2). Moreover, the oxygen uptake during SLM process (around 430 ppm) also may influence the corrosion resistance of the SLM sample [303]. Finally, uniformly dispersed pores are present after selective laser melting and all these factors are expected to leave their traces in the corrosion behaviour.

Fig. 3.27 shows the anodic polarization curves of selected additively manufactured and as-cast $Zr_{52.5}Cu_{17.9}Al_{10}Ni_{14.6}Ti_5$ glasses recorded in 0.01 M Na_2SO_4 + 0.1 M NaCl solution. Please note that the presented curves were selected as one representative from 5-7 independent measurements for each material state. The repeatability of the characteristic potential values is intrinsically limited. To account for the experimental error, the typical scattering of corrosion potential (ΔE_{corr}), pitting potential (ΔE_{pit}) and repassivation potential (ΔE_R) are indicated in the plot. While ΔE_{corr} must be mainly ascribed to the individual history of each prepared sample surface, ΔE_{pit} and ΔE_R may be indicative for the manufacturing-related pitting susceptibility and repassivation ability of the different sample types [274].

The air-aged as-cast sample states reveal very low corrosion current densities, i_{corr} (determined by graphical Tafel extrapolation methods) on the order of 0.005 µA/cm² at E_{corr} values ranging from -0.23 to -0.35 V vs. SCE upon initial polarization [304]. This results from the beginning oxide formation during air exposure and immersion in the electrolyte under OCP conditions. The current density increases gradually up to 2 µA/cm² during anodic polarization. Consequently, the corrosive dissolution is rather low and it is superimposed by the anodic growth of passive films with a strong barrier-type effect [137, 274]. A sudden steep rise of the anodic current density at E_{pit} is due to local passive film breakdown, pit initiation and rapid pit growth [137]. A significant overshoot of the real current density above the current density limit of 1 mA/cm², which was set as threshold value to reverse the polarization direction for surface repassivation, as well as a very wide potential range in the reverse scan with a quite high current density correspond to a very pronounced pit propagation into the glassy matrix and a very limited surface healing ability. Since the reverse scanning of the potential reduces the driving force for anodic dissolution, the current density drops and a second minimum at E_R occurs reflecting repassivation of the previously damaged surface. The underlying surface reaction

mechanisms were in detail described in previous works [130, 133, 135-137]. As the local breakdown of the very thin passive film on the sample surface (= excavated sample cross section) is a more or less random event, which mainly depends on the number, distribution and nature of defects in the BMG, the E_{pit}-value strongly varies in independent measurements of different as-cast samples and results in a rather large ΔE_{pit}. By contrast, the following strong current density hysteresis and the subsequent minimum at E_R show a much better repeatability. Once the sensitive pit initiation took place, the following pit growth and repassivation steps proceed at quite similar rates for all cast sample states of the considered alloy.

The polarization curves of the samples prepared by SLM reveal quite a similar overall behaviour with characteristic steps described above for the as-cast BMG samples. However, the variation of the pitting potential, ΔE_{pit}, is less pronounced reflecting a narrower potential range of passive film breakdown and pit initiation. Furthermore, the current density overshoot above the set limit is much smaller and during reverse scanning the current density plateau is lower and the minimum of E_R is reached at more positive potentials. These facts indicate a somewhat less pronounced pit propagation rate and easier surface repassivation [133, 137, 274].

Altogether, this indicates a slightly reduced pitting corrosion susceptibility and slightly improved surface healing ability for BMGs prepared by SLM. The result is similar with that obtained in the Ti-based BMG (section 3.1.4). As in the case of the Ti-based BMG, this could be related to a better chemical homogeneity in comparison to as-cast BMGs of the same composition. Yet, these differences appear to be rather subtle and it is challenging to try to identify those by conventional chemical analysis or electron microscopy.

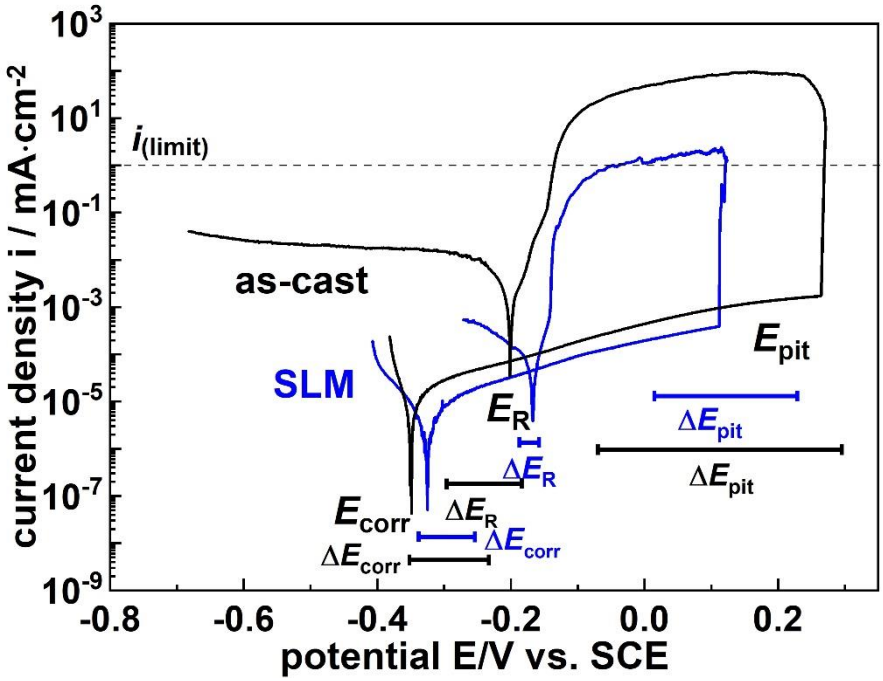

Figure 3.27: Anodic polarization curves recorded for $Zr_{52.5}Cu_{17.9}Ni_{14.6}Al_{10}Ti_5$ SLM and as-cast samples in 0.01 M Na_2SO_4 + 0.1 M NaCl solution. Corrosion potential (ΔE_{corr}), pitting potential (ΔE_{pit}) and repassivation potential (ΔE_R) bars represent the scattering of the values within 5 - 7 repeated measurements. Both samples show similar corrosion behaviour. The SLM sample performs slightly better than the as-cast sample during pitting corrosion.

After the corrosion tests, the surfaces were investigated in a scanning electron microscope to better understand the degradation phenomena. Fig. 3.28 shows the surface morphologies of damaged cross-sectional regions of an as-cast (Fig. 3.28 (a)) and an additively manufactured BMG sample (Fig. 3.28 (b)), respectively. The principal damage morphology is for both sample types similar and points to similar local corrosion processes, which are well described for this glassy alloy type synthesized by casting (see section 1.3) [135]. In case of the as-cast material, three individual pits with diameters between 30 - 50 µm having irregular edges and rather rough walls are shown in Fig. 3.28 (a). The size of a pit on a SLM sample cross section, in contrast, reaches dimensions of about 200 µm (Fig. 3.28 (b)). One can also detect small cracks and openings, which are similar to features observed for the corroded as-cast sample. The pit walls of the SLM sample show “honeycomb micromesh”-like regions, which is typical after repassivation [133]. The openings in the bottom of both sample types indicate that strong local dissolution occurs deep below the cross-sectional surface. The cavity morphology of the damages can catalyze the corrosion process since it can provide a shortcut for the electrolyte and thus, enable local enrichment of chloride ions and acidification.

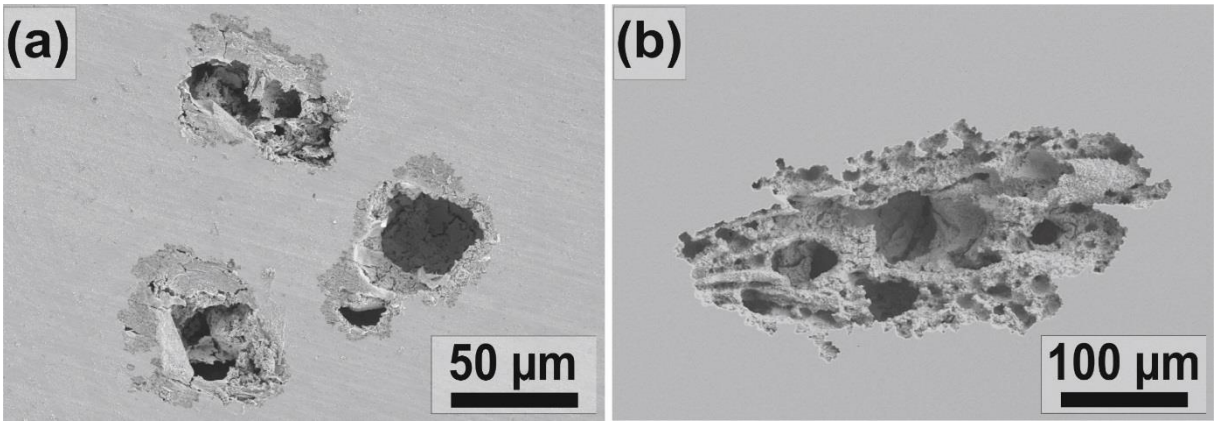

Figure 3.28: Surface morphologies of $Zr_{52.5}Cu_{17.9}Ni_{14.6}Al_{10}Ti_5$ as-cast sample (a) and SLM sample (b) after repassivation. Pits formed during linear anodic polarization to pitting potential (E_{pit}) and reverse scanning to repassivation potential (E_R). The as-cast sample has more but smaller pitted regions than the SLM sample. Both samples show rough pit walls.

From these very first tests comparing the corrosion behaviour of SLM vs. as-cast glassy samples in a selected electrolyte one may assume, that the structural defects typically occurring in as-cast samples are more detrimental for the corrosion stability than the pore-type defects, which are characteristic of SLM samples. While the former represent chemical discontinuities with sharp phase boundaries to the glassy matrix, the latter are geometrical discontinuities yielding a lower driving force for the chloride attack resulting in pit initiation and propagation. This can be regarded similar to findings from earlier studies, i.e. that mechanically induced defects such as microindents have to exceed a certain critical size to become preferred pit initiation sites rather than crystalline defects occurring at the same glassy sample cross-section [32]. However, besides their nature also the number and distribution of defects throughout the sample volume is decisive.

In the light of this, additional investigations are needed to clarify the impact of the manufacturing route on the corrosion mechanism and the overall corrosion properties for glassy alloys.

3.3 Structural heterogeneities of BMGs produced by SLM

Sections 3.1 and 3.2 cover the parameter optimization and the observed mechanical and chemical properties of a $Ti_{47}Cu_{38}Zr_{7.5}Fe_{2.5}Sn_2Si_1Ag_2$ and a $Zr_{52.5}Cu_{17.9}Ni_{14.6}Al_{10}Ti_5$ glass produced by selective laser melting. One central point in the respective discussions was the structural heterogeneity, which results from the SLM process and the inherent complex thermal history itself. It is, therefore, of avail to look into the structural heterogeneity in more detail and to directly compare both alloys. A striking difference between the additively manufactured Ti-based and the additively manufactured Zr-based glass is the apparent difference in the

nanohardness values measured at the cross and longitudinal sections (cf. Figs. 3.11 and 3.20). There might be a distinct influence of the alloy composition on the local structure of the glass after selective laser melting. To explore this possibility, finite volume modelling was applied to calculate the heat flow and temperature distribution during the SLM process.

In the first step, however, we compare the X-ray diffractions patterns of the as-cast glasses with the corresponding SLM samples. Fig. 3.29 displays the representative diffraction patterns of the SLM and as-cast samples for both alloys. Only broad scattering maxima can be observed characteristic of disordered systems, revealing nearly fully amorphous structures of the samples.

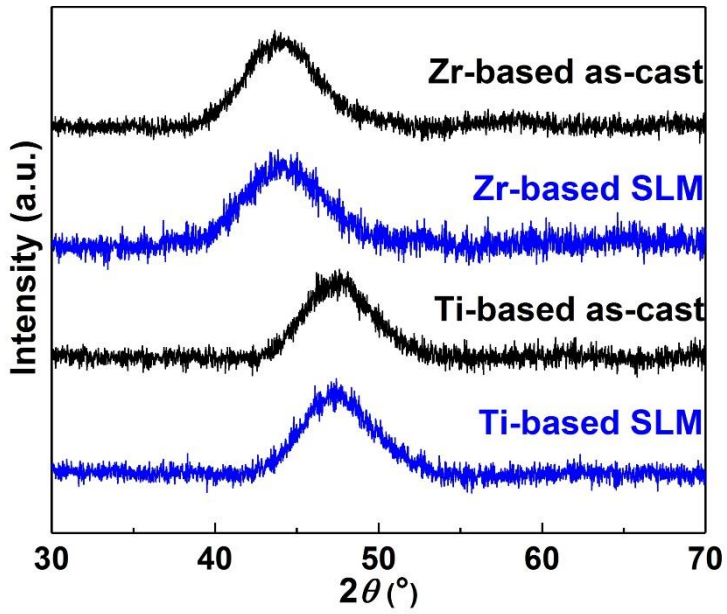

Figure 3.29: X-ray diffraction patterns of the $Zr_{52.5}Cu_{17.9}Ni_{14.6}Al_{10}Ti_5$ and $Ti_{47}Cu_{38}Zr_{7.5}Fe_{2.5}Sn_2Si_1Ag_2$ SLM and as-cast samples. All samples only show a major broad diffraction maximum, indicating a nearly full-amorphous structure.

In the next step, in order to reveal the structural relaxation imparted during SLM processing, DSC was carried out for various specimens taken from the SLM sample along its cylindrical axis, i.e. along the building direction (Fig. 2.4). Magnified sections of the corresponding curves demonstrate the exothermic relaxation occurs between 450 K and 675 K (Figs. 3.30 (a) and (b)). All SLM samples show larger relaxation enthalpies than the as-cast samples, indicating that higher cooling rates are effective during SLM, since more free volume is trapped in the SLM sample as they vitrify [266] and literature corroborates this finding [198].

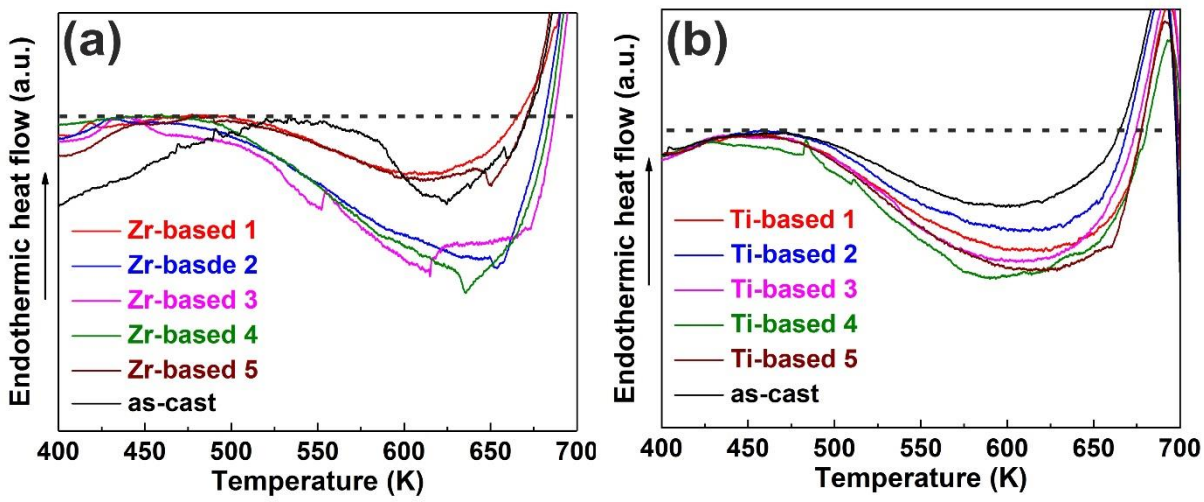

Figure 3.30: Sections of the DSC curves for (a) $Zr_{52.5}Cu_{17.9}Ni_{14.6}Al_{10}Ti_{5,}$ (b) $Ti_{47}Cu_{38}Zr_{7.5}Fe_{2.5}Sn_2Si_1Ag_2$ SLM and as-cast samples magnify the exothermic structural relaxation.

The relaxation enthalpies for all DSC specimens taken from the additively manufactured rods along their cylindrical axis are presented in Table 3.4. The relaxation enthalpies within the $Zr_{52.5}Cu_{17.9}Ni_{14.6}Al_{10}Ti_5$ SLM sample range between ΔH_{relax} = 3.31 J/g and 11.37 J/g and the corresponding values for $Ti_{47}Cu_{38}Zr_{7.5}Fe_{2.5}Sn_2Si_1Ag_2$ SLM samples range between ΔH_{relax} = 4.91 J/g and 12.15 J/g. One could speculate that the relaxation enthalpies increase from bottom to top of the SLM sample: The bottom part of the sample is built first and subsequently annealed for the longest duration owing to the heat input coming from subsequently processed layers (see section 1.4.2). Yet, as shown in Fig. 3.31, no obvious trend along the sample height (i.e. no effect of building duration) can be observed for both alloys. It seems that the temperature rise in the SLM samples is not sufficient or too short in order to allow for substantial structural relaxation. Therefore, no special caution has to be exercised when choosing samples for the evaluation of structural relaxation.

Table 3.4 Relaxation enthalpies of additively manufactured $Zr_{52.5}Cu_{17.9}Ni_{14.6}Al_{10}Ti_5$ and $Ti_{47}Cu_{38}Zr_{7.5}Fe_{2.5}Sn_2Si_1Ag_2$ samples. Samples for DSC measurements were taken along the building direction (bottom to top). Three rods for each composition were measured. It is notable that positions (1 - 5) represent the same height in each rod.

	Relaxation enthalpy ΔH_{relax} (J/g)				
Bottom to Top	**Pos. 1**	**Pos. 2**	**Pos. 3**	**Pos. 4**	**Pos. 5**
Zr-based S1	3.31	9.42	11.37	10.71	4.03
Zr-based S2	9.86	7.85	4.74	6.34	4.42
Zr-based S3	4.77	8.28	5.56	3.48	9.48
Ti-based S1	8.78	7.19	9.22	10.29	10.36
Ti-based S2	6.32	7.29	8.26	6.80	5.35
Ti-based S3	9.72	5.83	4.91	12.15	9.72

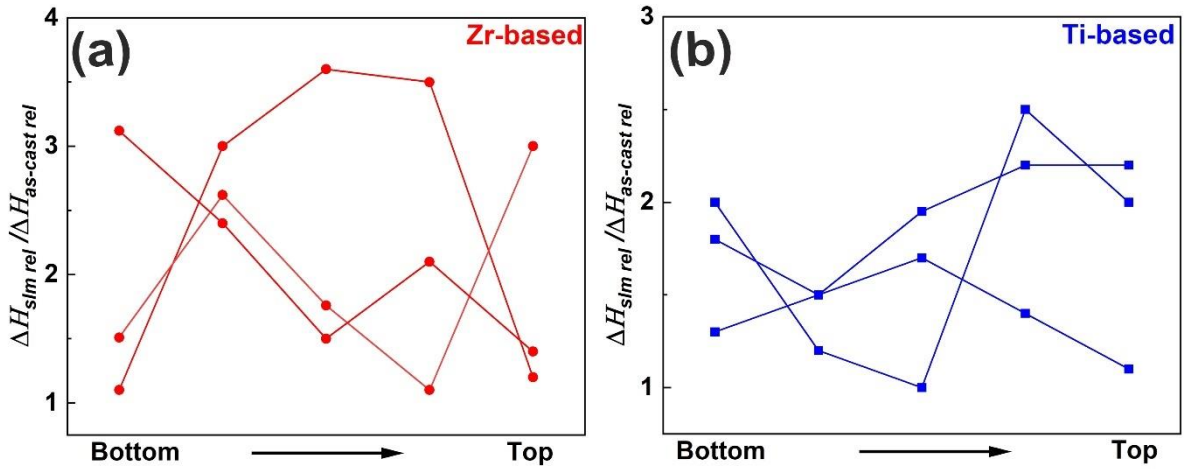

Figure 3.31: The relaxation enthalpies taken from the (a) $Zr_{52.5}Cu_{17.9}Ni_{14.6}Al_{10}Ti_5$, (b) $Ti_{47}Cu_{38}Zr_{7.5}Fe_{2.5}Sn_2Si_1Ag_2$ SLM samples are normalized by using the relaxation enthalpy of the corresponding as-cast sample, to compare both alloys. No clear correlation between relaxation enthalpy and sample position can be observed.

As already discussed above, nanoindentation was performed on the cross and longitudinal sections of both BMGs produced by selective laser melting. In order to clearly compare the results for the $Zr_{52.5}Cu_{17.9}Ni_{14.6}Al_{10}Ti_5$ and $Ti_{47}Cu_{38}Zr_{7.5}Fe_{2.5}Sn_2Si_1Ag_2$ glass, the results in Figs. 3.11 and 3.20 were concluded in Fig. 3.32. As shown in Fig. 3.32 (b), in contrast to the $Zr_{52.5}Cu_{17.9}Ni_{14.6}Al_{10}Ti_5$, in the nanoindentation maps of the $Ti_{47}Cu_{38}Zr_{7.5}Fe_{2.5}Sn_2Si_1Ag_2$ sample, both sections show similar hardness values, indicating a clearly more heterogeneous structure.

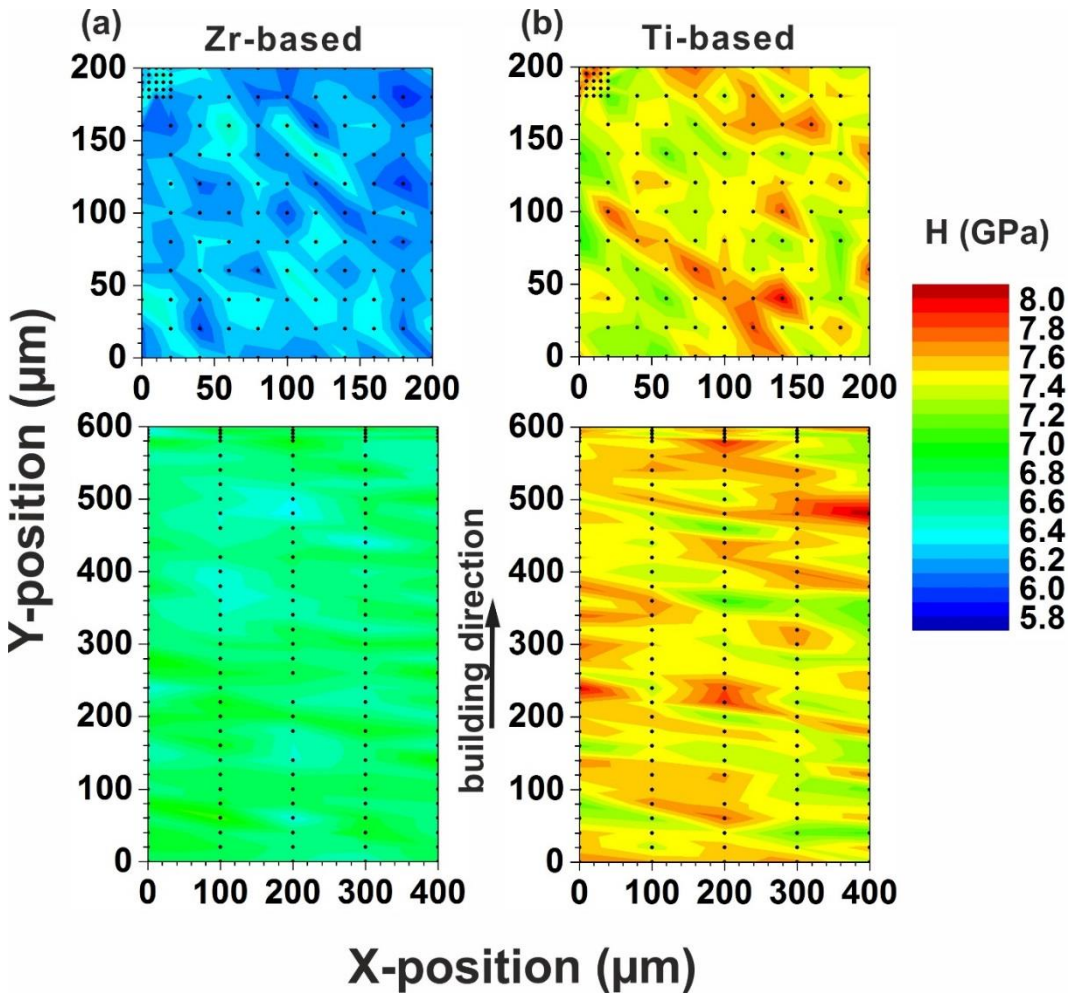

Figure 3.32: Hardness contour maps of cross sections (upper) and longitudinal sections (down) of the $Zr_{52.5}Cu_{17.9}Ni_{14.6}Al_{10}Ti_5$ (a) and $Ti_{47}Cu_{38}Zr_{7.5}Fe_{2.5}Sn_2Si_1Ag_2$ (b) additively manufactured samples. The $Ti_{47}Cu_{38}Zr_{7.5}Fe_{2.5}Sn_2Si_1Ag_2$ specimen produced via SLM shows a more heterogeneous structure.

One would expect the hardness values of the longitudinal map (along the building direction) to be even more heterogeneously distributed, owing to the layer-by-layer processing involving the evolution of the heat affected zone (HAZ). Therefore, a statistical analysis was used to show the heterogeneity in the samples. As shown in Figs. 3.33 (a) and (b), both longitudinal and cross section are relatively more heterogeneous for the Ti-based glass than for the Zr-based glass. The cross-section of the additively manufactured Zr-based BMG is more homogeneous, whereas its longitudinal section is relatively nonuniform. The different extents of homogeneity for these two additively manufactured BMGs might be attributed to the different thermal histories during SLM processing. Thus, in the following we elaborate on the spherical and temporal extent of the HAZ in both additively manufactured BMGs utilizing thermal field simulations.

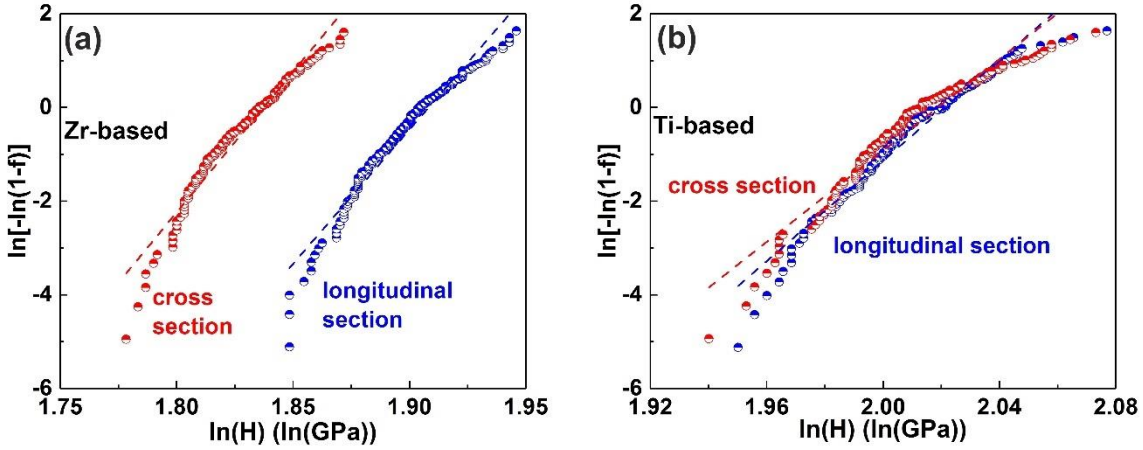

Figure 3.33: Weibull plot of the hardness values shown in Fig. 3.32 for additively manufactured (a) $Zr_{52.5}Cu_{17.9}Ni_{14.6}Al_{10}Ti_5$ and (b) $Ti_{47}Cu_{38}Zr_{7.5}Fe_{2.5}Sn_2Si_1Ag_2$ samples. The Weibull modulus, *m*, is derived from the slope of the linear regression curve of ln[-ln(1-*f*)] over ln(*H*), marked by the dashed lines.

A volumetric heat source was employed and the boundary condition of the top surface is defined by [249]:

$$-\kappa_{\text{eff}}\left(\frac{\partial T}{\partial z}\right)_{z=0} = \frac{3AP}{\pi\omega^2}\exp\left(-\frac{3(x^2+y^2)}{\omega^2}\right)_{z=0} - h_{\text{c}}(T-T_0) - \sigma_{\text{e}}\varepsilon(T^4-T_0^4) \tag{3.3}$$

where *A* is the laser absorptivity of powder system, which is set as 0.5. The thermal conductivity, specific heat capacity, density, and viscosity of the system were considered as temperature-dependent. Other thermophysical properties were regarded constant in order to simplify the simulations. Considering the initial porosity of the powder, the effective thermal conductivity of the powder system can be expressed by [249]:

$$\frac{\kappa_{\text{eff}}}{\kappa_g} = (1-\sqrt{1-\varphi})(1+\frac{\varphi\kappa_{\text{r}}}{\kappa_{\text{g}}}) + \sqrt{1-\varphi}\{\frac{2}{1-\frac{\kappa_g}{\kappa_s}}[\frac{1}{1-\frac{\kappa_g}{\kappa_s}}\text{In}(\frac{\kappa_{\text{g}}}{\kappa_s})-1]+\frac{\kappa_r}{\kappa_g}\} \tag{3.4}$$

where κ_{g} is the thermal conductivity of the ambient gas (W m^{-1} K^{-1}), κ_{s} is the thermal conductivity of the solid (W m^{-1} K^{-1}), and the radiative heat transfer among powder particles κ_{r} can be defined by [249]:

$$\kappa_{\text{r}} = 4F_0\sigma_{\text{e}}T_{\text{P}}^3D_{\text{P}} \tag{3.5}$$

where F_0 is the view factor which is set at 1/3 in this simulation, σ_{e} is the Stefan-Boltzmann constant, T_{P} is the temperature of powders (K) and D_{P} is the diameter of powder particles (m) which is set at 2×10^{-5} m. The effective thermal conductivity of the powder system, κ_{eff}, equals

κ_{powder} when the working temperature is below the melting point. After scanning, κ_{eff} equals κ_s due to the transformation from powder material to bulk material.

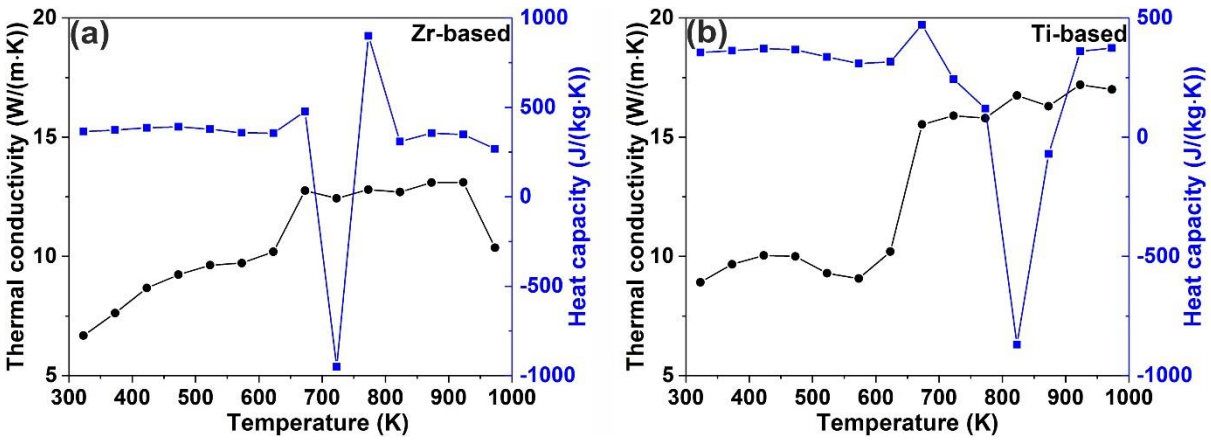

Figure 3.34: Thermophysical properties of both glass-forming alloy. The thermal conductivity and heat capacity are given for the (a) $Zr_{52.5}Cu_{17.9}Ni_{14.6}Al_{10}Ti_5$ and (b) $Ti_{47}Cu_{38}Zr_{7.5}Fe_{2.5}Sn_2Si_1Ag_2$ alloys.

The thermophysical properties of Zr- and Ti-based BMGs are displayed in Fig. 3.34 and other parameters used for the present simulation are listed in Table 3.5. It is notable that our FVM-model only considers one single melt track. In such case, the line energy densities of the additively manufactured Zr-based and Ti-based BMGs are 2.74 J/mm^2 and 2.16 J/mm^2, respectively.

Table 3.5: Parameters used in the finite volume simulation of $Zr_{52.5}Cu_{17.9}Ni_{14.6}Al_{10}Ti_5$ and $Ti_{47}Cu_{38}Zr_{7.5}Fe_{2.5}Sn_2Si_1Ag_2$ samples.

Parameters	$Zr_{52.5}Cu_{17.9}Ni_{14.6}Al_{10}Ti_5$	$Ti_{47}Cu_{38}Zr_{7.5}Fe_{2.5}Sn_2Si_1Ag_2$
density	6.7 g/cm^3	6.3 g/cm^3
melting point	1100 K	1116 K
ambient temperature	300 K	300 K
radius of laser beam	50 µm	50 µm
laser power	109 W	67.5 W
scanning velocity	1000 mm/s	780 mm/s
layer thickness	40 µm	40 µm

Figs. 3.35 (a) and (b) depict the temperature distribution in and around the molten pool during selective laser melting of $Zr_{52.5}Cu_{17.9}Ni_{14.6}Al_{10}Ti_5$ and $Ti_{47}Cu_{38}Zr_{7.5}Fe_{2.5}Sn_2Si_1Ag_2$ BMGs, respectively. The molten pool has an asymmetrical shape during processing of both alloys in agreement with other simulations [249], mainly because the thermal conductivity of the

solidified part is higher than that of powder. The heat is transferred faster through the solidified region than the powder [305]. The highest temperatures reach more than 2200 K and 2000 K for the Zr- and the Ti-based BMG, respectively. These temperatures clearly exceed their melting points (see Table 3.5). The molten region during the synthesis of the selectively-laser melted $Zr_{52.5}Cu_{17.9}Ni_{14.6}Al_{10}Ti_5$ glass extends to about 260 µm in width and 100 µm in thickness. Compared to that, the molten pool during the SLM of the $Ti_{47}Cu_{38}Zr_{7.5}Fe_{2.5}Sn_2Si_1Ag_2$ sample is clearly smaller in width (170 µm) and height (70 µm). The different extents of the molten pool for both alloys originates from the different processing parameters, where a higher power and scanning velocity for the Zr-based BMG was used and also from the different thermophysical properties of both glass-forming alloys (see Fig. 3.35). Owing to high cooling rates effective during SLM, the heat from the molten pool is extracted fast through the previously vitrified material. This heat extraction is reflected within the thermal field surrounding the molten pool, readily characterized by a steep negative temperature gradient. This gradient is typical of the heat-affected zone (HAZ), whose dimensions in Y- and Z-direction amounts to about 80 µm and 120 µm for the $Zr_{52.5}Cu_{17.9}Ni_{14.6}Al_{10}Ti_5$ SLM sample, respectively. For the $Ti_{47}Cu_{38}Zr_{7.5}Fe_{2.5}Sn_2Si_1Ag_2$ SLM sample, the HAZ is distinctly smaller and stretches about 40 µm in the Y-direction and 45 µm in the Z-direction. Unlike the $Zr_{52.5}Cu_{17.9}Ni_{14.6}Al_{10}Ti_5$ BMG produced via SLM, the HAZs in the Y- and Z-direction of $Ti_{47}Cu_{38}Zr_{7.5}Fe_{2.5}Sn_2Si_1Ag_2$ SLM sample are similar.

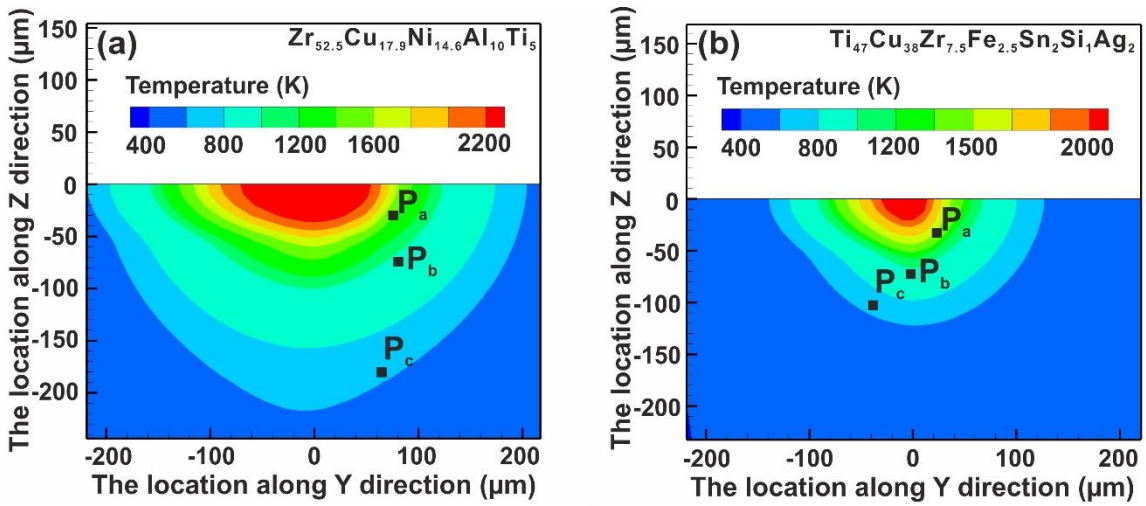

Figure 3.35: The side views of FVM simulated temperature field for (a) $Zr_{52.5}Cu_{17.9}Ni_{14.6}Al_{10}Ti_5$ and (b) $Ti_{47}Cu_{38}Zr_{7.5}Fe_{2.5}Sn_2Si_1Ag_2$ SLM samples. The additively manufactured $Zr_{52.5}Cu_{17.9}Ni_{14.6}Al_{10}Ti_5$ sample shows a larger heat-affected zone than the $Ti_{47}Cu_{38}Zr_{7.5}Fe_{2.5}Sn_2Si_1Ag_2$ sample produced via SLM.

A possible explanation for the different hardness values of cross and longitudinal sections in $Zr_{52.5}Cu_{17.9}Ni_{14.6}Al_{10}Ti_5$ SLM sample is that the larger HAZ in the Z-direction results in a more

relaxed structure. Therefore, the hardness shown in cross and longitudinal sections is different. Generally speaking, the overlap and HAZs in the Y- and Z-direction might influence the mechanical properties of the longitudinal and cross section for the SLM samples.

In order to clarify the influence of the thermal field on crystallization and structural relaxation, three representative positions were taken and analysed for each sample. As shown in Figs. 3.35 (a) and (b), P_a represents the position in the molten pool, P_b is in the HAZ near the molten pool and P_c is at the margins of the HAZ. Their temperature-time curves are shown in Figs. 3.36 (a) and (b) and allows us to determine the temporal evolution of the temperature at different locations in the sample. The melting temperature (T_m), crystallization temperature (T_x) and glass transition temperature (T_g) are indicated by dashed lines.

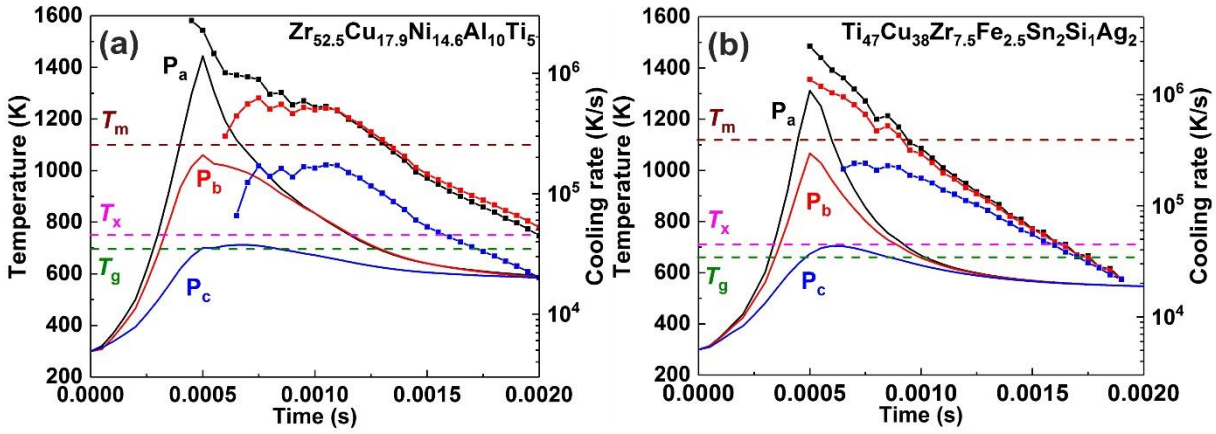

Figure 3.36: The heating and cooling traces at different positions of the temperature field (black rectangles in Fig. 3.35) for (a) $Zr_{52.5}Cu_{17.9}Ni_{14.6}Al_{10}Ti_5$ and (b) $Ti_{47}Cu_{38}Zr_{7.5}Fe_{2.5}Sn_2Si_1Ag_2$ additively manufactured BMGs. The grass-transition (T_g), crystallization (T_x), and melting (T_m) temperatures of the SLM samples are also indicated with dash lines.

In Fig. 3.36 (a), although the temperature within the HAZ (P_b) surpasses T_x, such high temperatures only prevail for about 0.9 ms. In the case of the $Ti_{47}Cu_{38}Zr_{7.5}Fe_{2.5}Sn_2Si_1Ag_2$ sample a temperature above T_x exists only for 0.5 ms (Fig. 3.36 (b)). Such a short crystallization window is insufficient for the crystallization. The cooling rates (traces with dots) were also calculated according to the curves (i.e. the derivatives of the T-t-curves).

The minimum cooling rates of the $Zr_{52.5}Cu_{17.9}Ni_{14.6}Al_{10}Ti_5$ and $Ti_{47}Cu_{38}Zr_{7.5}Fe_{2.5}Sn_2Si_1Ag_2$ samples are over 10^4 K/s. These values provide a lower boundary for the actual cooling rate of the (supercooled) melt. The high cooling rates ensure the formation of a fully glassy structure and are highly consistent with the estimations based on microstructural analysis (Fig. 3.29) [220, 306]. Comparing to the $Zr_{52.5}Cu_{17.9}Ni_{14.6}Al_{10}Ti_5$ SLM sample, the $Ti_{47}Cu_{38}Zr_{7.5}Fe_{2.5}Sn_2Si_1Ag_2$ SLM sample has a shorter duration of anneal. One can speculate that the overall shorter anneal leads to a less relaxed structure in the longitudinal direction. Thus, the

$Ti_{47}Cu_{38}Zr_{7.5}Fe_{2.5}Sn_2Si_1Ag_2$ sample produced via SLM exhibit similar nanohardness values on both sections. Whereas the $Zr_{52.5}Cu_{17.9}Ni_{14.6}Al_{10}Ti_5$ SLM sample shows different nanohardness values on cross and longitudinal sections.

CHAPTER 4 Selective laser melting of *ex-situ* Zr-based BMG matrix composites

Alloying elements, which stabilize the β-phase (e.g. Nb, Mo, Ta), are crucial ingredients for the development of Zr/Ti-based bulk metallic glass matrix composites reinforced with ductile β-type dendrites (see section 1.2.2.2) [77, 307-312]. Such composites with improved plasticity are usually obtained by casting or semi-solid processing. Precise control over the crystallization process and, consequently, control over the resulting microstructures is not straightforward and generally only feasible for alloys with outstanding glass-forming ability [313, 314]. These alloys often contain toxic Be [313, 314].

Thus, mixing glass-forming and conventional alloy powder prior to selective laser melting is a promising way to produce *ex-situ* BMG-composites. In this chapter, the glass-forming alloy $Zr_{52.5}Cu_{17.9}Ni_{14.6}Al_{10}Ti_5$ (at.%) was selected as matrix for the preparation of ex-situ BMG matrix composites. Two different contents of the β stabilizer Nb (2 wt.% and 10 wt.%) were added as the second, crystalline phase. The microstructural evolution and mechanical properties of the BMG matrix composites as obtained by selective laser melting will be systematically discussed in the following.

4.1 Phase formation

As revealed in section 3.2.1, the actual composition of $Zr_{52.3}Cu_{18}Ni_{14.6}Al_{10.1}Ti_5$ is in excellent agreement with the nominal composition, $Zr_{52.5}Cu_{17.9}Ni_{14.6}Al_{10}Ti_5$ (at.%). Therefore, we will only refer to the nominal composition in the following. The oxygen content of the $Zr_{52.3}Cu_{18}Ni_{14.6}Al_{10.1}Ti_5$ powder is 487 ± 5 ppm and the Nb powder contains 324 ± 17 ppm oxygen. After selective laser melting, the oxygen content reaches about 920 ± 20 ppm in the final samples. Since there is some residual oxygen in the chamber and Zr-based BMGs are prone to oxidation, there is an oxygen uptake during processing [87, 275].

In the first step, the phase formation in the different as-cast and additively manufactured samples was investigated by means of X-rays. Fig. 4.1 shows the X-ray diffraction patterns of the samples with varying Nb contents. The $Zr_{52.5}Cu_{17.9}Ni_{14.6}Al_{10}Ti_5$ SLM sample without any Nb additions exhibits only a broad diffraction maximum and no sharp reflections can be observed, suggesting that a single glassy phase has formed (Fig. 4.1(a)) [220]. The diffraction pattern of the SLM sample with 2 wt.% Nb, in contrast, exhibits a few additional sharp Bragg peaks, which can be ascribed to niobium. The corresponding as-cast sample containing 2 wt.% Nb ($Zr_{51.7}Cu_{17.6}Ni_{14.4}Al_{9.8}Ti_{4.9}Nb_{1.6}$ (at.%)) only shows a broad maximum (Fig. 4.1 (a)). During

repeated arc-melting and suction casting, niobium is completely dissolved, which can be inferred from the absence of Nb reflections, and, thus, a homogeneous alloy forms. This Nb content apparently does not reduce the critical casting thickness to below 3 mm, which is why the alloy still vitrifies during suction casting.

In the SLM sample with 10 wt.% Nb, one can detect Nb reflections but additional, relatively broad reflections appear being superimposed on a broad scattering background (Fig. 4.1(a)). Despite the high cooling rates during selective laser melting, this powder blend does not vitrify. In other words, its tendency to congeal into a glass is lower than of the base composition, $Zr_{52.3}Cu_{18}Ni_{14.6}Al_{10.1}Ti_5$. This might originate from the diffusion of Nb into the matrix, which then stimulates the precipitation of new crystalline phases, thus deteriorating the glass-forming ability. In order to assess the effect of 10 wt.% of Nb on the glass-forming ability of the alloy, an as-cast $Zr_{52.5}Cu_{17.9}Ni_{14.6}Al_{10}Ti_5$ sample with 10 wt.% Nb ($Zr_{48.3}Cu_{16.5}Ni_{13.4}Al_{9.2}Ti_{4.6}Nb_8$) was prepared and also investigated (Fig. 4.1(a)). No Nb reflections are present anymore, which indicates that Nb is again completely dissolved during repeated arc-melting. Yet, in stark contrast to the as-cast sample with 2 wt.% Nb, multiple crystalline reflections are visible and the XRD pattern does not imply that a glassy phase is left. The critical casting thickness of this composition certainly is below 3 mm [311].

The unambiguous identification of the crystalline phases is rather challenging because of the complex alloy composition in combination with the extended widths of the crystalline reflections. Even for the base alloy, i.e. $Zr_{52.5}Cu_{17.9}Ni_{14.6}Al_{10}Ti_5$, the crystallization products are subject to controversy [286, 315, 316]. Therefore, a detailed phase identification is beyond the scope of the present work, especially since it is not required for the discussion below. Instead, qualitative aspects of the crystallization process by comparing the as-cast $Zr_{52.5}Cu_{17.9}Ni_{14.6}Al_{10}Ti_5$ glass annealed for 24 h at 873 K and at 973 K with the as-cast sample with 10 wt.% Nb annealed at 973 K for 24 h were merely concentrated on. In Fig. 4.1 (b), a section (2θ-range from 12 ° - 24 °) of the respective XRD patterns is shown.

After annealing the as-cast $Zr_{52.5}Cu_{17.9}Ni_{14.6}Al_{10}Ti_5$ glass at 873 K for 24 h, only few crystalline reflections are found. The strongest ones can be attributed to $CuZr_2$ [285, 286, 316]. When annealed at 100 K more, this alloys precipitates additional phases, which might come from the tetragonal $NiZr_2$ phase, which is known to precipitate at the later stages of crystallization [286]. The big cube phase (fcc, $NiTi_2$-type) [287] cannot be detected in these as-cast samples. It is a metastable phase (in this alloy) and has to be stabilized by a substantial amount of oxygen [276, 277, 285, 287]. Yet, the oxygen content in the as-cast $Zr_{52.5}Cu_{17.9}Ni_{14.6}Al_{10}Ti_5$ glass (77 $\pm$ 5 ppm) is too low for this to happen. When the as-cast

$Zr_{52.5}Cu_{17.9}Ni_{14.6}Al_{10}Ti_5$ sample with 10 wt.% Nb is annealed at 973 K for 24 h, the diffraction pattern reveals distinct differences with respect to the annealed base composition (Fig. 4.1 (b)): $CuZr_2$ does not precipitate any more, and instead, tetragonal/fcc $NiZr_2$, Ti_2NbAl and Al_5Ti are detected. The fcc $NiZr_2$ (big cube) phase is stabilized in these samples owing to their relatively high oxygen contents (as-cast: 95 ± 6 ppm ppm, SLM: 1118 ± 17 ppm), while the Nb-containing crystalline phase forms because of the relatively high Nb content. It appears that the same crystalline phases are also found in the $Zr_{52.5}Cu_{17.9}Ni_{14.6}Al_{10}Ti_5$ sample with 10 wt.% Nb processed by selective laser melting (Fig. 4.1 (b)). However, the reflections are less intense and much broader, indicating a smaller crystal size. In addition, one strong Nb reflection appears in the SLM sample due to incomplete dissolution of the Nb powder particles during selective laser melting.

To summarize these findings, a substantial amount of Nb leads to the formation of Ti_2NbAl and the elevated oxygen content stabilizes the big cube phase next to tetragonal $NiZr_2$. The phase formation in $Zr_{52.5}Cu_{17.9}Ni_{14.6}Al_{10}Ti_5$ with 10 wt.% Nb produced by selective laser melting, hence, becomes even more complex than for oxygen-lean $Zr_{52.5}Cu_{17.9}Ni_{14.6}Al_{10}Ti_5$. Especially the volume fraction and the distribution of these brittle intermetallic phases is crucial for the deformation behaviour and will be discussed below.

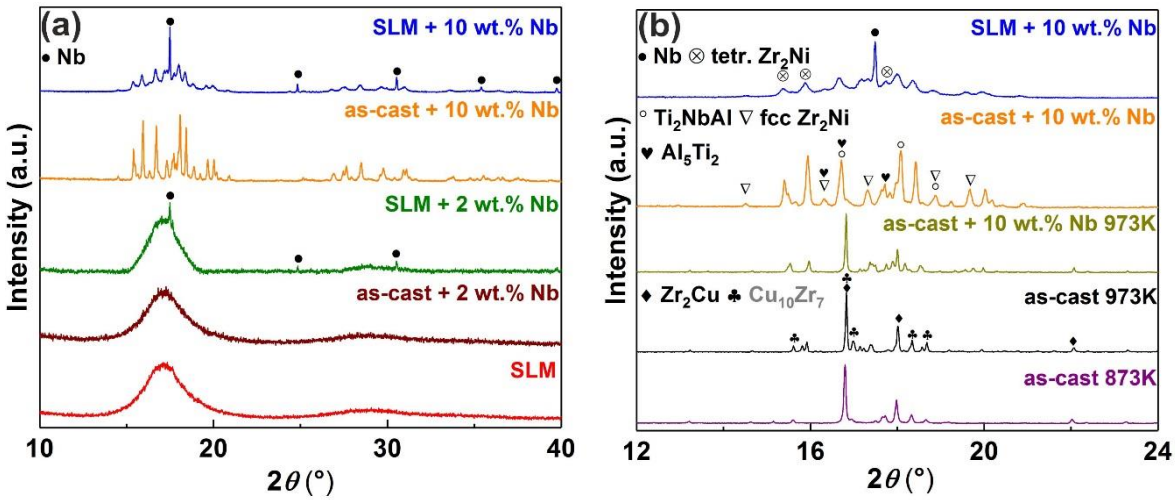

Figure 4.1: X-ray diffraction patterns of the pure $Zr_{52.5}Cu_{17.9}Ni_{14.6}Al_{10}Ti_5$ powder processed with SLM as well as of $Zr_{52.5}Cu_{17.9}Ni_{14.6}Al_{10}Ti_5$ with 2 and 10 wt.% Nb obtained by casting and SLM. Only the $Zr_{52.5}Cu_{17.9}Ni_{14.6}Al_{10}Ti_5$ sampled produced by SLM and as-cast sample with 2 wt.% Nb exhibit the broad reflection typical of metallic glasses. For the SLM sample containing 2 wt.% Nb, only Nb can be detected pointing to the fact that a BMG matrix composite has been obtained. In the SLM and as-cast sample with 10 wt.% Nb several intermetallic phases precipitate.

To unambiguously prove the presence of a glassy phase in these samples, differential scanning calorimetry was carried out. The DSC traces of all specimens are displayed in Fig. 4.2

and the glass-transition temperature (T_g) as well as the crystallization temperature (T_x) are indicated. All thermal data are additionally summarized in Table 4.1. The as-cast and SLM samples of both pure $Zr_{52.5}Cu_{17.9}Ni_{14.6}Al_{10}Ti_5$ and $Zr_{52.5}Cu_{17.9}Ni_{14.6}Al_{10}Ti_5$ with 2 wt.% Nb exhibit the typical features of metallic glasses, i.e. a glass transition followed by a supercooled liquid region and exothermic events associated with crystallization. The inset to Fig. 4.2 depicts an enlarged view of the temperature regime around T_g for the SLM sample with 10 wt.% Nb. Even though the endothermic event is not as pronounced as for the other samples, one can still reveal a glass transition proving the presence of small volume fraction of glass. Only in the as-cast $Zr_{52.5}Cu_{17.9}Ni_{14.6}Al_{10}Ti_5$ sample with 10 wt.% Nb, the glass transition is absent (Fig. 4.2). The slight differences in T_g and T_x for the additively manufactured and the as-cast $Zr_{52.5}Cu_{17.9}Ni_{14.6}Al_{10}Ti_5$ samples imply that the SLM state is somewhat different from the as-cast state, which may originate from the higher oxygen content found in the SLM samples.

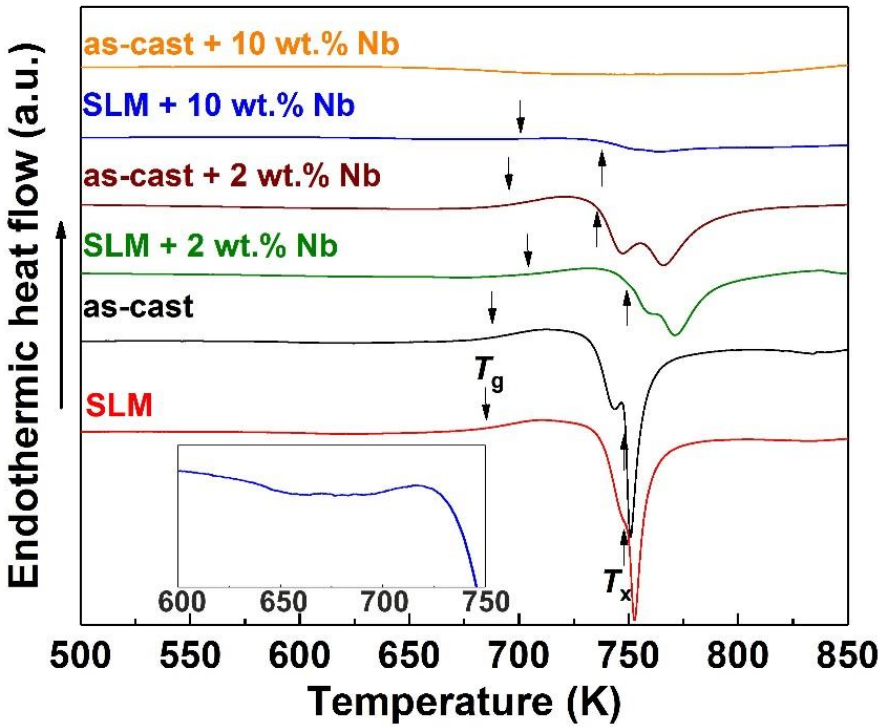

Figure 4.2: DSC traces of $Zr_{52.5}Cu_{17.9}Ni_{14.6}Al_{10}Ti_5$ with different Nb contents. and as-cast monolithic glass as well as BMG-matrix composites. Apart from as-cast sample with 10 wt.% Nb, all samples exhibit endothermic glass transition at glass-transition temperature, followed by an exothermic crystallization event. The glass-transition temperature, T_g and the onset of crystallization, T_x, are marked by arrows. For all the SLM samples, the crystallization peak is shifted to a slightly higher temperature and the shoulder of the first crystallization event becomes weaker than the as-cast sample. The inset indicates the glass transition in SLM sample with 10 wt.% Nb.

With increasing Nb content, the crystallization peaks become broader and shallower so that the enthalpy of crystallization decreases markedly compared to the fully amorphous SLM

samples. Based on the crystallization enthalpies the corresponding crystalline volume fractions were estimated (Table 4.1). The results corroborate the XRD data (Fig. 4.1) and prove that Nb additions reduce the glass-forming ability of $Zr_{52.5}Cu_{17.9}Ni_{14.6}Al_{10}Ti_5$ and promote the precipitation of crystals.

Table 4.1: Summary of the thermal parameters of the additively manufactured as well as of the as-cast samples.

sample	$T_g \pm 2$ (K)	$T_x \pm 2$ (K)	$\triangle T \pm 2$ (K)	$\triangle H_{cryst} \pm 2$ (J/g)	Cryst. Vol. fract. after SLM ± 5%
SLM	683	748	65	56	
as-cast	687	747	60	59	
SLM + 2 wt.% Nb	704	748	44	44	21%
as-cast + 2 wt.% Nb	696	736	40	64	
SLM + 10 wt.% Nb	700	738	38	20	64%
as-cast + 10 wt.% Nb				29	

4.2 Microstructures

The cross-sections of the additively manufactured $Zr_{52.5}Cu_{17.9}Ni_{14.6}Al_{10}Ti_5$ with 2 and 10 wt.% Nb are displayed in Figs. 4.3 (a) and (b), respectively. The Nb particles have an irregular shape and are uniformly distributed in the matrix. The shape of the particles is rather similar to that of the original Nb powder (cf. inset to Fig. 4.4 (a)), which suggests that the Nb particles did not melt during selective laser melting but only the glass-forming $Zr_{52.5}Cu_{17.9}Ni_{14.6}Al_{10}Ti_5$ powder. This can be explained by the significant difference in the melting temperatures, T_m (T_m (Nb) = 2750 K and T_m ($Zr_{52.5}Cu_{17.9}Ni_{14.6}Al_{10}Ti_5$) = 1085 K) [317, 318]. The matrix of the SLM sample with 10 wt.% Nb appears to be marbled (Fig. 4.3 (b)), which could be the result of abundant Nb diffusion into the matrix. This aspect will be discussed in more detail below.

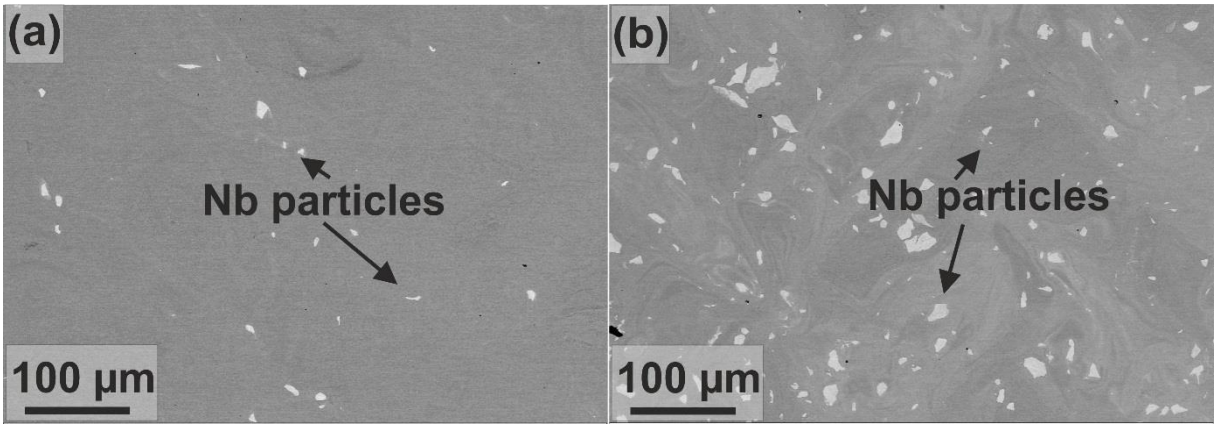

Figure 4.3: Scanning electron micrograph of the cross-sections of a $Zr_{52.5}Cu_{17.9}Ni_{14.6}Al_{10}Ti_5$ sample produced by SLM (a) with 2 wt.% Nb and (b) with 10 wt.% of Nb particles. The Nb particles with an irregular shape distribute inhomogeneously. There exhibit continuous ripple-like dark region around Nb particles.

First, the sizes and distribution of the Nb particles in the different SLM samples shall be analysed. The particle size distribution of the unprocessed Nb powder is displayed in Fig. 4.4 (a) together with a SEM micrograph of the powder. The particle size distribution resembles a Poisson distribution having its maximum at a particle size around 13 µm. The maximum equivalent diameters (particle sizes) are around 55 µm. The size distribution of the Nb particles is altered after the SLM process (Figs. 4.4 (b) and (c)): The maximum of the distribution is now around 8 µm and the maximum particle size detected is reduced to about 35 µm, independent of the amount of Nb particles added to the $Zr_{52.5}Cu_{17.9}Ni_{14.6}Al_{10}Ti_5$ powder. These changes imply that there is substantial diffusion of Nb into the matrix during SLM. The full µ-CT reconstructions of the samples shown in the according insets of Fig. 4.4 prove that the Nb particles are indeed uniformly distributed in the entire specimen. X-ray tomography bears the great advantage that interparticle spacings can be directly measured avoiding the complications of stereology [16]. We apply an approach known from the analysis of the short- and medium-range order in glassy materials [319, 320] and calculate the radial distribution function, $g(D)$ [321]:

$$g(D) = \rho(D) / \rho_0 \tag{4.1}$$

where $\rho(D)$ is the local particle density at distance D and ρ_0 is the average density of the system. The function can be interpreted as the probability of finding a particle at distance D in the sample.

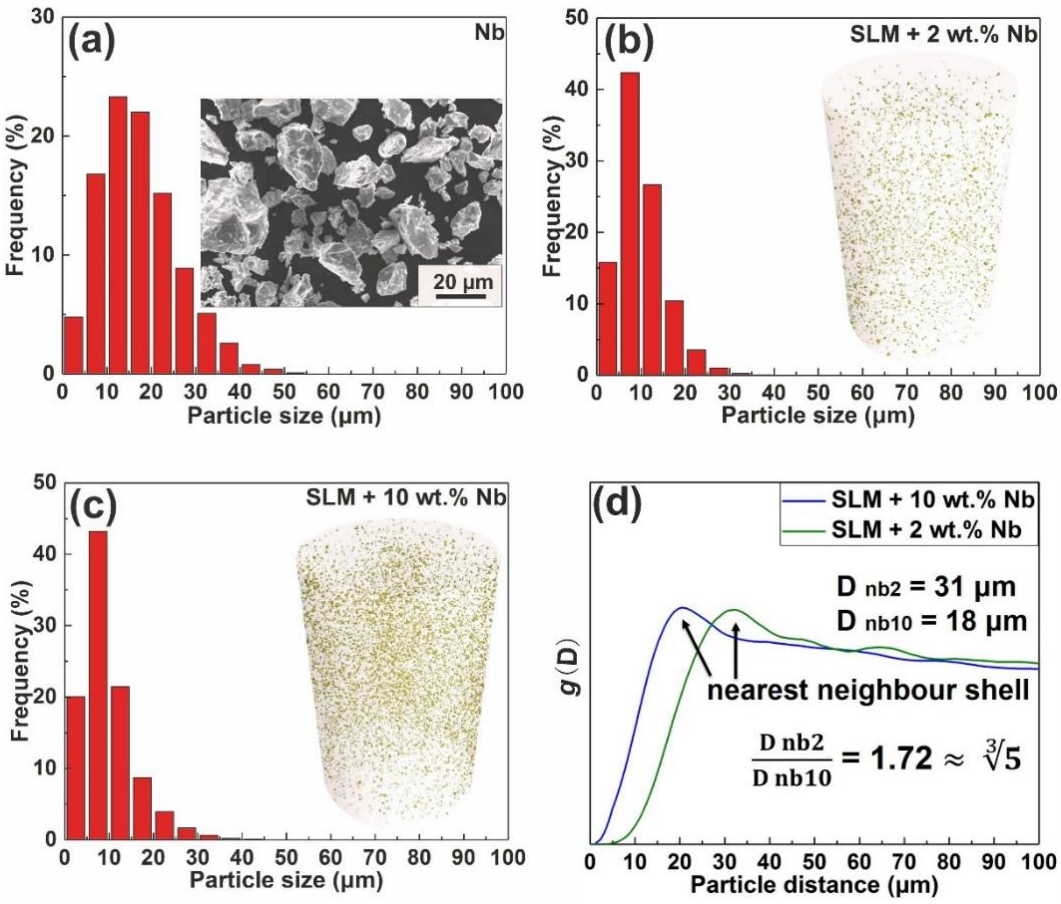

Figure 4.4: Nb particle distribution (a) before, (b) and (c) after SLM processing. SEM image of original Nb particles is shown as inset in (a); µ-CT reconstruction of the additively manufactured $Zr_{52.5}Cu_{17.9}Ni_{14.6}Al_{10}Ti_5$ with 2 wt. % (b) and 10 wt. % (c) Nb are also shown as insets; (d) distance of nearest neighbour particles are calculated based on a radial distribution function. It should be stressed that the initial Nb powder was analysed by using CAMSIZER, the Nb particles in SLM samples were detected with µ-CT.

The results for the SLM samples with 2 and 10 wt.% of Nb are depicted in Fig. 4.4 (d). Because of the irregular particle shapes and the random distribution of the Nb particles in the matrix, the oscillations typically found in radial distribution function [319, 320] are not very pronounced. Yet, the distance between nearest neighbours is at about 31 ± 3 µm for the sample with 2 wt.% Nb and about 18 ± 2 µm in the case of the sample with 10 wt.% Nb. This yields a ratio for the nearest neighbour distance of d_{nn}(2 wt.% Nb)/ d_{nn}(10 wt.% Nb) = 31/18 ≈ 1.72. This is in agreement with the value derived from a simplified geometrical consideration one can apply as an estimate for small volume or weight fractions of Nb: If one assumes a certain a matrix volume represented by a cube around each Nb particle of fixed size, located in the centre of each cube, then the spacing between these Nb particles is roughly the edge length of the according cube. A decrease from 10 wt.% Nb to 2 wt.% Nb is almost equivalent to an increase in the "matrix cube" volume by a factor of 5, which increases the interparticle spacing

accordingly. Because the edge length of the matrix cubes increases by a factor of $\sqrt[3]{5} \approx 1.71$, the interparticle spacing increases by the same factor. This estimate implies that the particles distribute homogeneously in the matrix.

Next to the distribution of the Nb particles in the present glass matrix composites also the presence and distribution of pores is of importance. Fig. 4.5 combines the µ-CT reconstruction (insets) and the extracted pore size distribution for the $Zr_{52.5}Cu_{17.9}Ni_{14.6}Al_{10}Ti_5$ SLM sample (Fig. 4.5 (a)) and for the $Zr_{52.5}Cu_{17.9}Ni_{14.6}Al_{10}Ti_5$ SLM sample with 2 wt.% as well as with 10 wt.% Nb (Figs. 4.5 (b) and (c)). In the $Zr_{52.5}Cu_{17.9}Ni_{14.6}Al_{10}Ti_5$ sample (Fig. 4.5 (a)), the majority of pores has sizes between 15 and 35 µm. The maximum pore size is around 90 µm, which seems to result from the coalescence of smaller pores in adjacent layers. These larger defects are very few and mainly detected in the centre of the rod. Nonetheless, the measured relative density reaches 99.5%, which exceeds the value of 98.5% measured via the Archimedean method. The limited resolution of the µ-CT measurement often leads to an overestimation of the relative density and could be responsible for the observed discrepancy here as well. As the inset of Fig. 4.5 (a) depicts, the small pores distribute randomly in the sample. The relative densities measured independently for the SLM sample with 2 wt.% Nb reach 99.1% (µ-CT) and 98.2% (Archimedean measurement) respectively. For the SLM sample with 10 wt.% Nb, the relative densities are determined as 99% (µ-CT) and 98% (Archimedean measurement). The pore size distributions of the SLM samples with 2 and with 10 wt.% Nb (Figs. 4.5 (b) and (c)) reach their maximum between 20 to 45 µm. The tails of the distributions towards larger pore sizes do not change significantly and also in these two samples, the pores are uniformly dispersed (insets to Figs. 4.5 (b) and (c)). Like for the $Zr_{52.5}Cu_{17.9}Ni_{14.6}Al_{10}Ti_5$ sample, the pores tend to stretch over several layers -especially in the centre of the sample with 10 wt.% Nb (Fig. 4.5 (c)). The slight reduction in the relative density of the Nb containing samples implies that the processing parameter used for $Zr_{52.5}Cu_{17.9}Ni_{14.6}Al_{10}Ti_5$ might have to be mildly adjusted. Nevertheless, the processability and the quality of the SLM samples is hardly reduced by the presence of Nb particles.

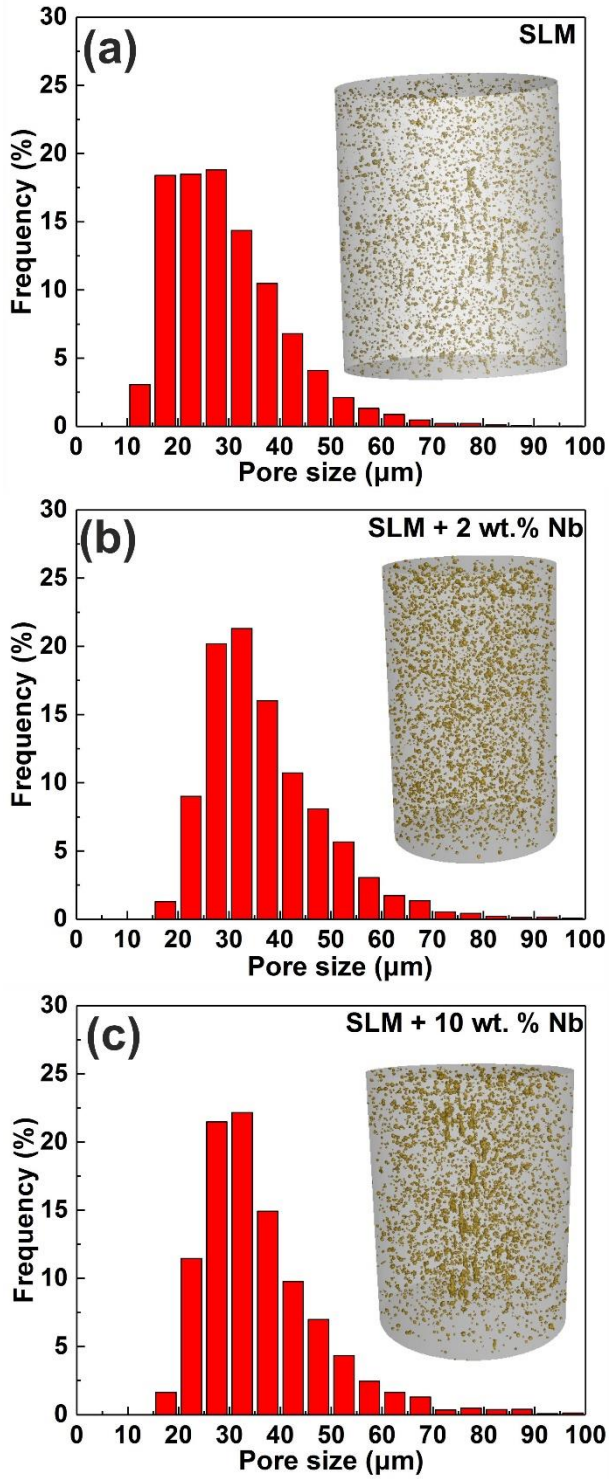

Figure 4.5: Pore distribution of the additively manufactured $Zr_{52.5}Cu_{17.9}Ni_{14.6}Al_{10}Ti_5$ (a), with 2 wt. % (b) and 10 wt. % (c) Nb determined by µ-CT. µ-CT reconstruction of all the SLM samples are shown as insets. Even though the samples have high relative density, the pores are still displayed. The porosity increased after adding Nb addition.

The focus of the next paragraphs is on the diffusion of Nb into the matrix, the phase formation and the interface characteristics in the additively manufactured $Zr_{52.5}Cu_{17.9}Ni_{14.6}Al_{10}Ti_5$ samples containing Nb. The Nb particles are well bonded to the matrix and one cannot observe any

cracks or voids at the interface (Fig. 4.6 (a)), an indication for good wettability between solid Nb and liquid $Zr_{52.5}Cu_{17.9}Ni_{14.6}Al_{10}Ti_5$. The mixing enthalpy, ΔH_{mix}, of Nb with the constituent elements of the glass-forming powder is mostly negative or only slightly positive (ΔH_{mix}(Nb-Al) = -18 kJ/mol, ΔH_{mix}(Nb-Ni) = -30 kJ/mol, ΔH_{mix}(Nb-Ti) = 2 kJ/mol, ΔH_{mix}(Nb-Cu) = 3 kJ/mol and ΔH_{mix}(Nb-Zr) = 4 kJ/mol) [322]. This favours local diffusion of Nb into the molten $Zr_{52.5}Cu_{17.9}Ni_{14.6}Al_{10}Ti_5$ powder during selective laser melting.

However, other than intended, Nb does not stabilize a β-type phase (see section 4.1) [89, 323], which would be very desirable with respect to the mechanical properties (see section 1.2.2.2). Instead, relatively complex intermetallic phases form (Fig. 4.1). In the micrographs, crystals with a darker contrast than the Nb particles are found in the matrix near the Nb particles. The region, in which the dark crystals precipitate, typically stretches about 10 µm into the matrix around each Nb particle. Their size ranges from 100 - 500 nm and, interestingly, they are not detected by XRD (Fig. 4.1 (a)). Presumably, their volume fraction is too low. In order to investigate the change in composition across the interface an EDS line-scan was performed and the results are shown in Fig. 4.6 (b). Over a distance of about 5 µm from the interface into the matrix especially the Nb and Zr content change.

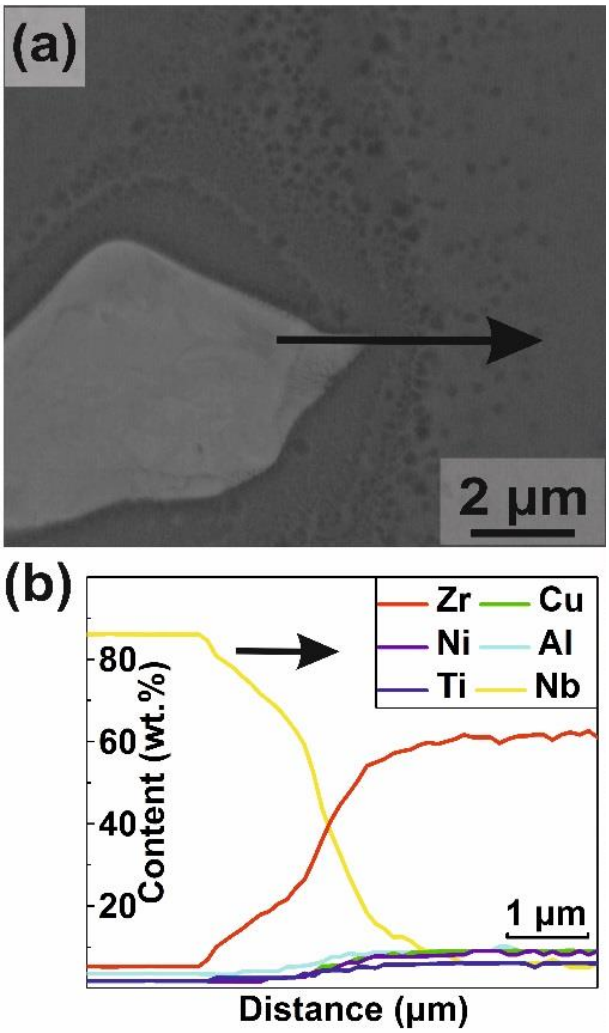

Figure 4.6: (a) SEM micrograph and corresponding (b) EDS line scan for the SLM sample with 2 wt.% Nb. In the vicinity of the Nb particle different crystalline phases precipitate having a typical size of 100 - 500 nm. Along the line scan (from Nb particle to the matrix), the Nb and Zr content has significant change.

The $Zr_{52.5}Cu_{17.9}Ni_{14.6}Al_{10}Ti_5$ SLM sample with 10 wt.% Nb ($Zr_{48.3}Cu_{16.5}Ni_{13.4}Al_{9.2}Ti_{4.6}Nb_8$) also contains the small dark crystals in the vicinity of the Nb particles (Fig. 4.7). However, additional bright crystals form. The EDS maps for this sample show that the regions with these bright crystals is Nb-rich. Moreover, they contain more Ti, Ni and Zr than the matrix. The larger amount of Nb particles in the melt enhances the diffusion of Nb into the matrix during SLM and, therefore, Nb-rich crystals are able to form in this sample. The diffusion coefficient of Nb in Zr-alloys ranges between 10^{-11} and 10^{-15} m^2/s [324, 325]. With increasing the temperature, the diffusion coefficient becomes higher [324, 325]. Moreover, diffusion is faster in the liquid state and, therefore, the majority dissolution of Nb most likely occur in the molten glass-forming powder.

In the present study, the lifetime of the molten pool is about 0.002 s (see section 3.3). The lifetime of the melt pool is neither sufficient to result in complete dissolution of Nb in the surrounding melt nor to uniformly distribute Nb in the melt. As a consequence, a chemical gradient is detected (Fig. 4.6 (b)). Thus, diffusion of the Nb particles induced the composition changes in the vicinity, leading to the formation of various crystalline phases. As discussed above, the elevated Nb content around the Nb particles deteriorates the glass-forming ability and stimulates the precipitation of various crystalline phases. These crystalline phases seem to be tetragonal $NiZr_2$, fcc $NiZr_2$ (big cube) and $CuZr_2$ (Fig. 4.1 (b)). One could now try to reduce the dissolution of Nb by increasing the scanning velocity for example, but in the present work the energy input was kept constant (compared to the fabrication of monolithic $Zr_{52.5}Cu_{17.9}Ni_{14.6}Al_{10}Ti_5$ glasses) in order to maintain the rather high relative density and to reduce the risk of crystallizing the glass-forming powder [220].

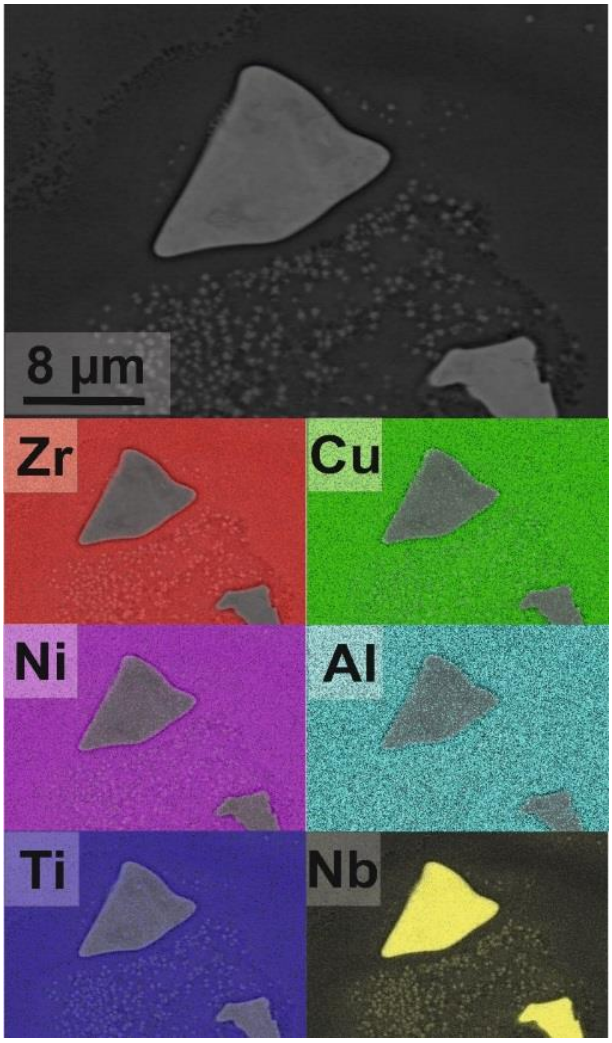

Figure 4.7: SEM micrograph and corresponding EDS maps for the SLM sample with 10 wt.% Nb. In the vicinity of the Nb particle, there is crystalline phases precipitate in nano scale. The EDS data indicates that there is mostly Nb diffusion into the matrix and that Cu and Al react with the Nb particles at the matrix-particle interface.

The particle-matrix interface was additionally characterized by transmission electron microscopy (TEM). Fig. 4.8 (a) depicts a bright-field TEM micrograph of the SLM sample with 2 wt.% Nb. A part of a relatively large crystal can be found in the lower left region of the image. The selected area electron diffraction (SAED) pattern (the upper right inset) proves that the particle is a Nb crystal, which is oriented along the $[111]_{bcc}$ direction. In the high-resolution TEM (HRTEM) image (the lower right inset), the lattice fringes become evident. The surrounding matrix is featureless. Fig. 4.8 (b) displays a magnified TEM image of the interface between the Nb particle and the matrix in the SLM sample with 2 wt.% Nb. A relatively sharp particle-matrix interface can be seen. The SAED pattern taken about 150 nm away from the interface (upper right inset) only shows a broad and diffuse halo typical of a glassy phase. The HRTEM image taken from the interface region is shown as the second inset. In the upper right corner of the image, the sample exhibits a homogeneous maze-like pattern corresponding to the glass. The left part of the image, in contrast, contains lattice fringes. No atomically sharp interface can be observed in the HRTEM image. As Fig. 4.8 (c) indicates, several nanocrystals precipitate near the crystal-glass interface of the SLM sample with 10 wt.% Nb particles. The nanocrystals have sizes between 5 and 80 nm and are surrounded by an amorphous matrix, as the SAED and the HRTEM image (insets) prove. It is unlikely that such large crystals form during ion-milling in these samples but not in the samples with 2 wt.% Nb. Consequently, the higher Nb content resulting in the enhanced diffusion during SLM must be the origin of this phenomenon.

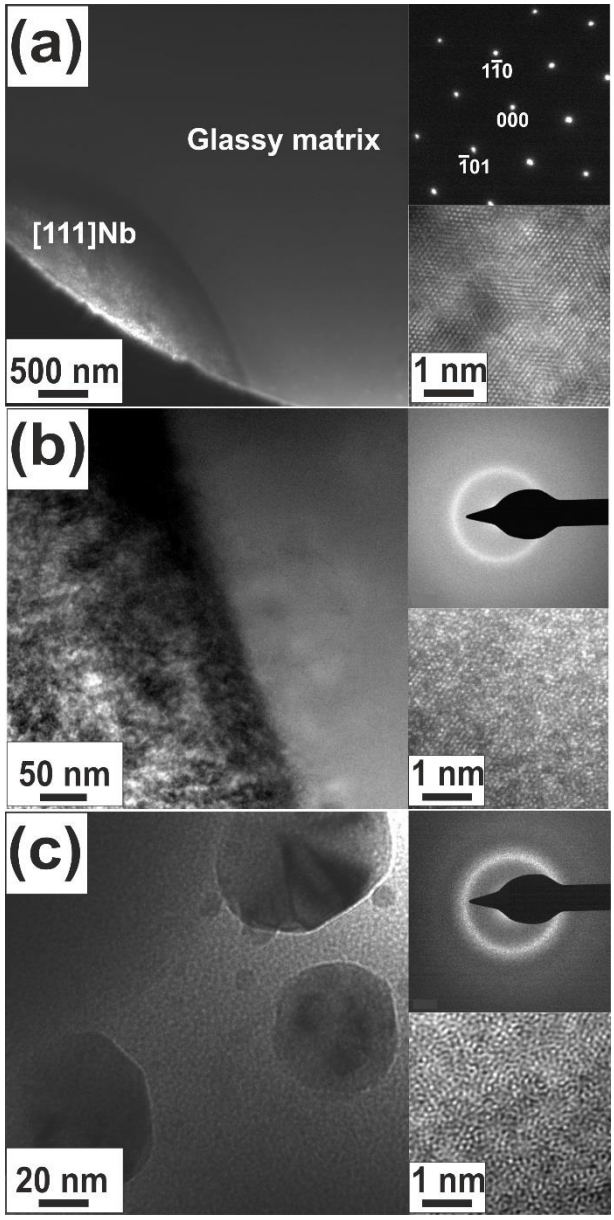

Figure 4.8: TEM micrograph and corresponding SAED patterns of (a) Nb particle in the SLM $Zr_{52.5}Cu_{17.9}Ni_{14.6}Al_{10}Ti_5$ with 2 wt. % Nb; (b) interface between Nb particle and glassy matrix in the SLM $Zr_{52.5}Cu_{17.9}Ni_{14.6}Al_{10}Ti_5$ with 2 wt.% Nb; (c) nanocrystals in the SLM $Zr_{52.5}Cu_{17.9}Ni_{14.6}Al_{10}Ti_5$ with 10 wt.% Nb.

4.3 Mechanical properties

Microhardness maps (Fig. 4.9) were obtained from the cross-sections of the additively manufactured $Zr_{52.5}Cu_{17.9}Ni_{14.6}Al_{10}Ti_5$ and $Zr_{52.5}Cu_{17.9}Ni_{14.6}Al_{10}Ti_5$ with 2 wt.% and 10 wt.% Nb in order to study the heterogeneity of the samples. The typical size of the indents is about 30 μm, which is larger than most of the Nb particles. The hardness values of the $Zr_{52.5}Cu_{17.9}Ni_{14.6}Al_{10}Ti_5$ sample produced via SLM (Fig. 4.9 (a)) do not scatter much and are in the range of 504 HV0.2 to 512 HV0.2. At the present resolution, it is not possible to reveal differences between the heat-affected zone and the melt track centres [245] and, therefore, the

hardness map appears rather uniform. The hardness values found in the SLM sample with 2 wt.% Nb (Fig. 4.9 (b)) vary between 475 HV0.2 and 586 HV0.2. The according map clearly points to an increased structural heterogeneity [245]. The lower hardness values must be a result of the Nb particles and the larger hardness must originate from the formation of strong intermetallic phases (cf. Fig. 4.6 and see discussion above). Finally, the SLM sample with 10 wt.% Nb (Fig. 4.9 (c)) exhibits the largest spread of hardness values (427 HV0.2 to 689 HV0.2). The corresponding map reveals a rather heterogeneous behaviour. Soft regions are surrounded by comparatively hard regions. While the former result from the presence of Nb crystals, the latter are those regions around the Nb particles, in which the intermetallic phases precipitate (Fig. 4.7). These intermetallics apparently are even harder than the $Zr_{52.5}Cu_{17.9}Ni_{14.6}Al_{10}Ti_5$ glass.

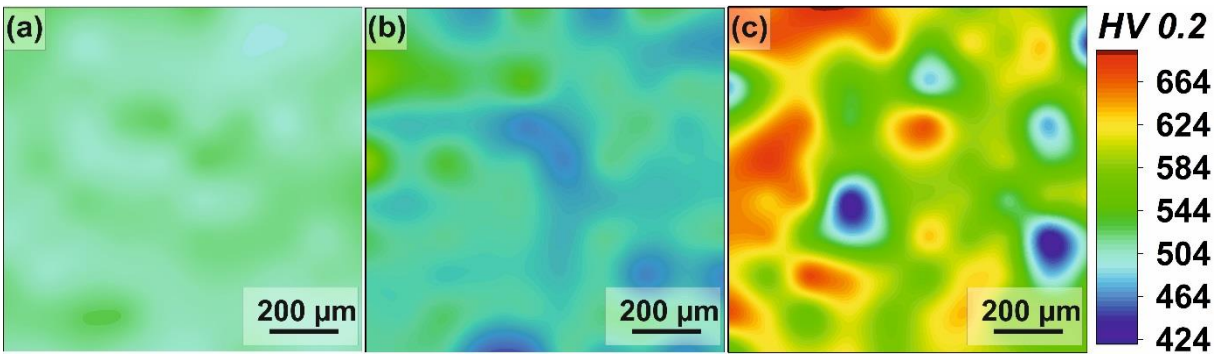

Figure 4.9: Micro-hardness maps carried out on the cross-section of (a) the additively manufactured $Zr_{52.5}Cu_{17.9}Ni_{14.6}Al_{10}Ti_5$, (b) with 2 wt.% and (c) 10 wt.% Nb. With the increase of the Nb content, the samples became more inhomogeneous. Some regions with high micro-hardness formed, at the meantime some softer regions appeared.

Subsequently, each material was uniaxially compressed. Fig. 4.10 compares the compressive stress-strain curves of all as-cast and SLM samples. As shown in Table 4.2, all additively manufactured specimens have a similar Young's modulus (77 GPa to 80 GPa), whereas the Nb-containing as-cast samples exhibit a higher value around 90 GPa. The $Zr_{52.5}Cu_{17.9}Ni_{14.6}Al_{10}Ti_5$ SLM sample typically fails at stresses around 1800 MPa. However, after the addition of Nb particles, the samples fracture at significantly lower stresses (1510 MPa for $Zr_{52.5}Cu_{17.9}Ni_{14.6}Al_{10}Ti_5$ with 2 wt.% Nb and 1000 MPa for $Zr_{52.5}Cu_{17.9}Ni_{14.6}Al_{10}Ti_5$ with 10 wt.% Nb).

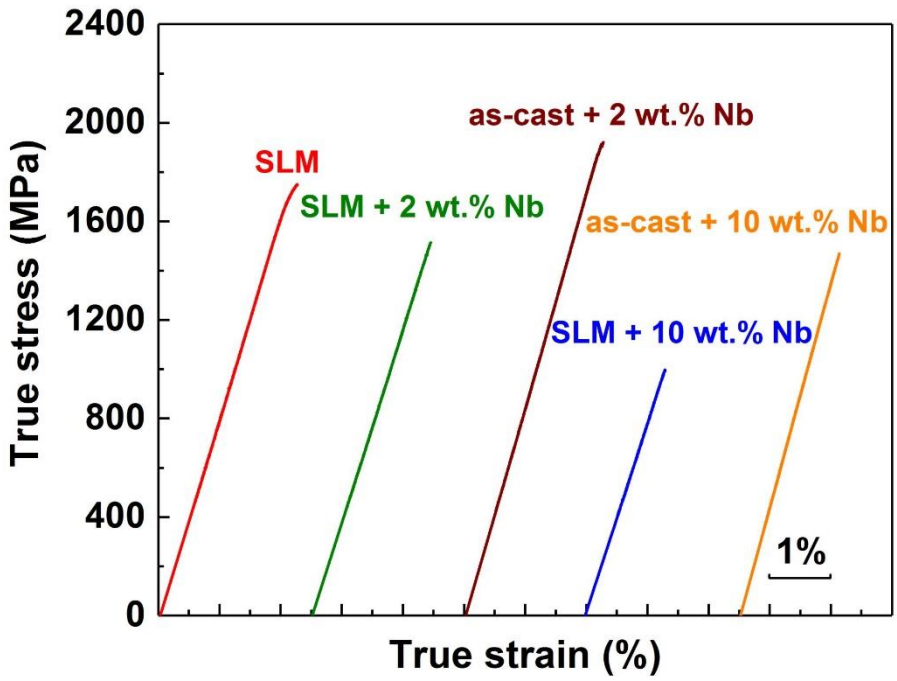

Figure 4.10: Representative stress-strain curves of the additively manufactured $Zr_{52.5}Cu_{17.9}Ni_{14.6}Al_{10}Ti_5$, SLM as well as as-cast samples with 2 wt.% and 10 wt.% Nb rods with a diameter of 3 mm. All the samples show no plasticity upon yielding.

Table 4.2: Summary of the mechanical properties of SLM and as-cast samples.

sample	Young's modulus (GPa)	Fracture strength (MPa)
SLM	79 ± 1	1800 ± 50
SLM + 2 wt.% Nb	78 ± 1	1500 ± 70
as-cast + 2 wt.% Nb	90 ± 2	1920 ± 40
SLM + 10 wt.% Nb	77 ± 1	1000 ± 40
as-cast + 10 wt.% Nb	87 ± 2	1300 ± 20

In addition, none of the samples fabricated by SLM shows any significant plastic deformation. Three factors might be responsible for this: (i) as discussed above, the amount of pores tends to increase with the Nb content, which is known to reduce plasticity [49] (ii) the relatively pointy corners and edges of some Nb particles could act as stress concentrators during mechanical loading [49] and (iii) the precipitation of hard but brittle intermetallic phases could induce premature failure. Especially the last aspect is decisive, as shown in the following.

For comparison, also the according as-cast samples were compressed (Fig. 4.10). The as-cast samples with 2 wt.% and 10 wt.% Nb, show a measurably higher maximum compressive strength (1920 MPa and 1300 MPa, respectively). Yet, also these samples fail in a brittle manner.

It is not clear why this applies to the fully amorphous as-cast $Zr_{52.5}Cu_{17.9}Ni_{14.6}Al_{10}Ti_5$ sample with 2 wt.% of Nb, since glassy $Zr_{52.5}Cu_{17.9}Ni_{14.6}Al_{10}Ti_5$ is malleable to some extent (see section 4.1). It seems that Nb has a negative bearing on plasticity in this alloy. When 10 wt.% Nb are added to $Zr_{52.5}Cu_{17.9}Ni_{14.6}Al_{10}Ti_5$, the melt does not vitrify any more on casting and, instead, several intermetallic phases form (Fig. 4.1(b)). Because of their complex composition and low crystal symmetry most of the phases, which precipitate in this alloy, are inherently brittle [326, 327].

Fractography provides valuable information regarding the failure mechanism and the role of the intermetallic phases, which form around the Nb particles. Figs. 4.11 (a), (b) and (c) show the additively manufactured $Zr_{52.5}Cu_{17.9}Ni_{14.6}Al_{10}Ti_5$ samples without, with 2 wt.% and with 10 wt% Nb, respectively. The Nb-free samples fail along the plane of maximum shear stress characteristic of metallic glasses (Fig. 4.11 (a)) [117]. When 2 wt.% are added to the alloy, the fracture surface becomes more complex and the material does not fail along a single plane anymore (Fig. 4.11 (b)). At the largest Nb content, however, the samples shatter into multiple small pieces (Fig. 4.11 (c)). A network of cracks must form on mechanical loading, which eventually fragments the entire specimens.

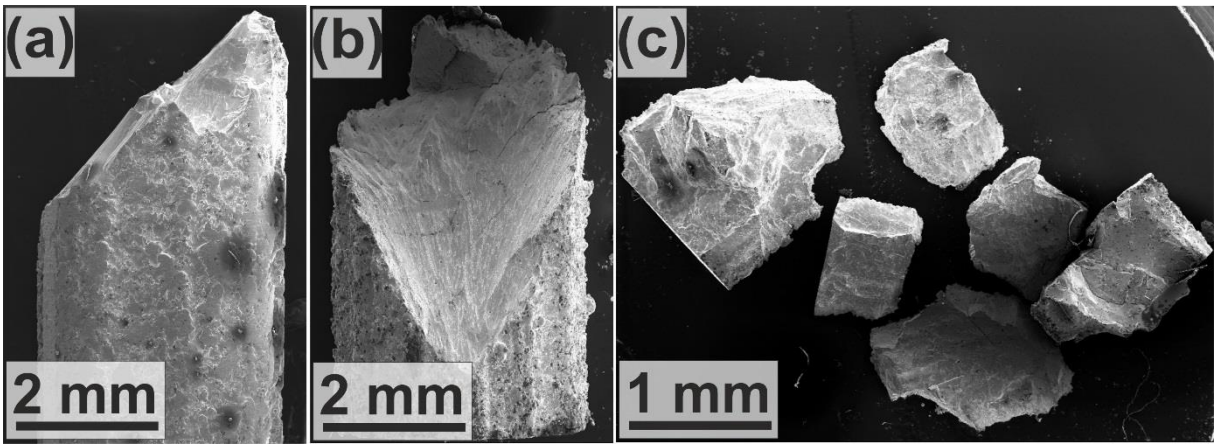

Figure 4.11: The SEM images of the broken (a) SLM $Zr_{52.5}Cu_{17.9}Ni_{14.6}Al_{10}Ti_5$ sample, (b) the SLM sample with 2 wt.% Nb and (c) SLM sample with 10 wt.% Nb. The SLM sample with 10 wt.% Nb for compression test broke into small pieces.

It is reasonable to assume that the brittle crystalline precipitates are the cause of this behaviour and the possible fracture mechanism is schematically depicted in Figs. 4.12 (a) and (b). The brittle crystals preferentially form around the Nb particles (Fig. 4.12 (a)) and because of the relatively large content of Nb particles (10 wt.%), they begin to coalesce and form a network. On compression the crystals yield first [108, 109, 326, 327] and owing to their brittleness, multiple cracks form in the sample. These cracks grow and propagate along the

network of brittle precipitates on further deformation until the entire sample fails eventually (Fig. 4.12 (b)).

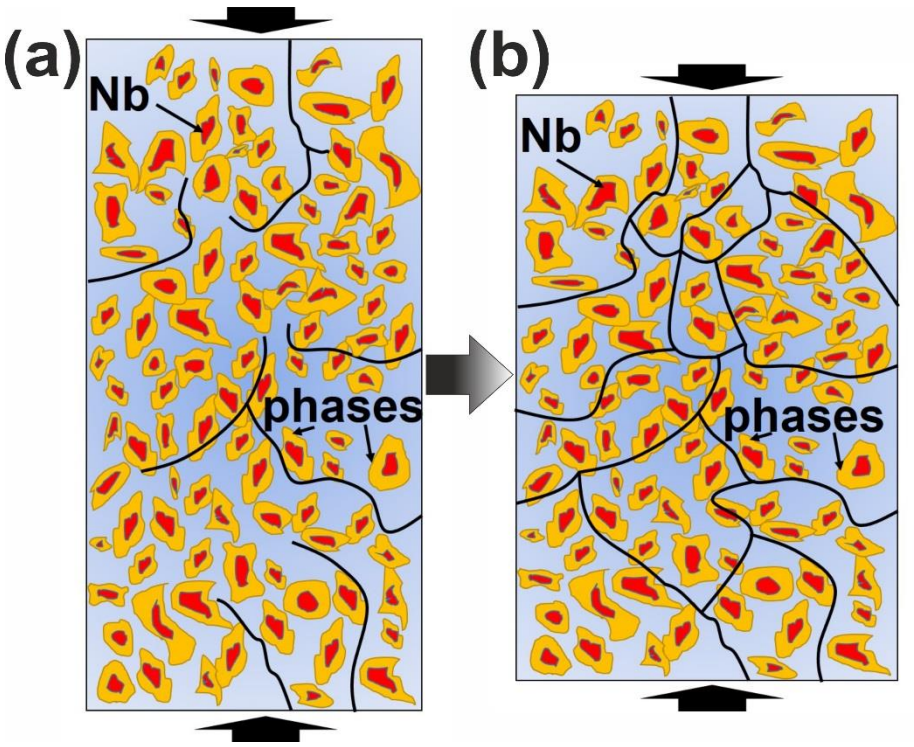

Figure 4.12: Schematic of fracture process for the SLM sample with 10 wt.% Nb at (a) early stage and (b) late stage of deformation.

CHAPTER 5 Selective laser melting of *in-situ* CuZr-based BMG matrix composites

$Cu_{50}Zr_{50}$-based BMG matrix composites are peculiar, since they additionally work-harden, owing to the deformation-induced martensitic transformation of the embedded B2 CuZr crystals. The martensitic transformation overcompensates the work softening of the glass [93, 117, 328, 329]. SLM seems to be a promising method to prepare BMG and its composites [128, 200, 217, 219-239]. By optimizing the process parameters, one can not only control the volume fraction of crystalline phase(s), but also their distribution. In-situ BMG matrix composites were not deliberately fabricated by SLM, though the layer-by-layer synthesis could bear great potential in this respect [231]. Thus, in this chapter a glass-forming $Cu_{46}Zr_{46}Al_8$ (at.%) powder was selected to produce a monolithic BMG and a BMG matrix composite via SLM. Properties like the relative density, structural heterogeneities, the formation of phases and mechanical properties will be systematically discussed in this chapter.

5.1 Powder analysis

As shown in Table 5.1, the actual composition of the gas-atomized powder only slightly deviates from the nominal composition of $Cu_{46}Zr_{46}Al_8$ (at. %). Thus, the gas atomization did not affect the chemical composition. The oxygen content of the initial powder is 332 ± 11 ppm and increases to 491 ± 15 ppm for the final specimens. Since the used composition is rich in Zr, which is highly affine to oxygen [87, 275] and residual oxygen prevails in the building chamber, it is incorporated into the powder during selective laser melting.

Table 5.1 Chemical composition of the gas-atomized $Cu_{46}Zr_{46}Al_8$ powder.

Element (wt.%)	Cu	Zr	Al
nominal	39.85	57.21	2.94
powder	39.76 ± 0.20	56.83 ± 0.10	2.92 ± 0.01

The detailed powder information such as powder size distribution and morphology provide important hints for setting the initial scanning strategy. The powder size distribution shown in Fig. 5.1 (a) demonstrates that the particle size is equally distributed between 10 and 80 µm. The fraction of the powder with a diameter ranging from 10 to 80 µm amounts to about 90%. The powder only contains about 2.5% small-sized particles, which effectively prevents particle agglomeration [171]. Based on heuristics obtained sections 3.1 and 3.2 and the powder characteristics, the layer thickness and hatch distance was selected to 40 and 180 µm,

respectively [220]. Fig. 5.1 (b) depicts the powder morphology. It can be clearly seen that spherical powder particles constitute the majority resulting in an improved flowability of the powder. Only a few agglomerated particles (satellites) very small in size, which adhere to larger particles, can be observed from the corresponding SEM image.

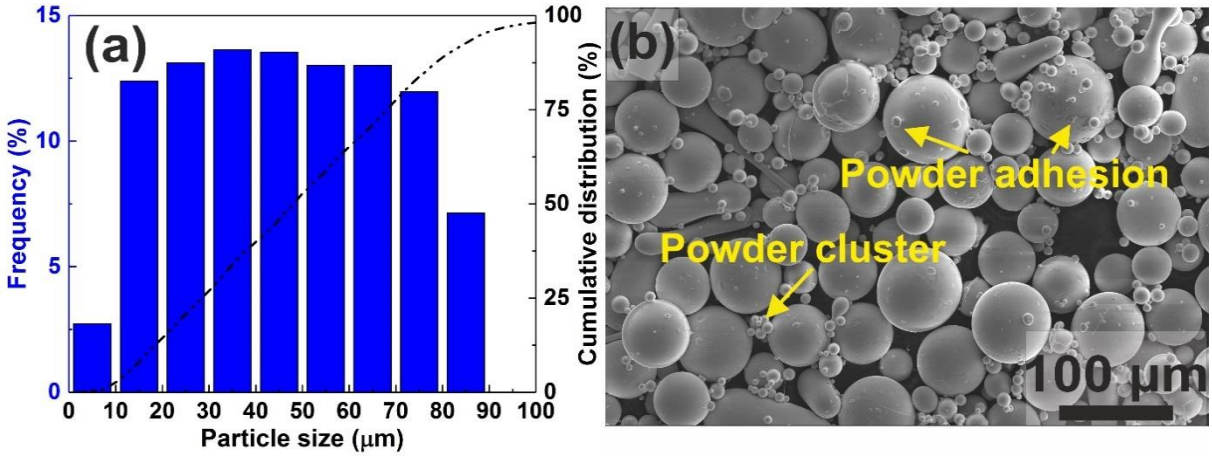

Figure 5.1: (a) Particle size distribution of the $Cu_{46}Zr_{46}Al_8$ powder after sieving. The diameters of the powder particles are almost equally distributed between 10 and 80 μm in diameter. (b) Scanning electron micrograph of the sieved gas-atomized powder. Mostly, spherical powder particles with a minor amount of satellites can be observed.

5.2 Parameter optimization

A high relative density is the prerequisite for additively manufactured components for being used as structural material and we first aim to identify the optimum processing conditions in terms of porosity. Fig. 5.2 displays the contour map of the relative density of $Cu_{46}Zr_{46}Al_8$ samples produced by SLM as a function of scanning velocity and laser power. The SLM specimens were produced with a constant layer thickness (l = 40 μm) and a constant hatch distance (h = 180 μm).

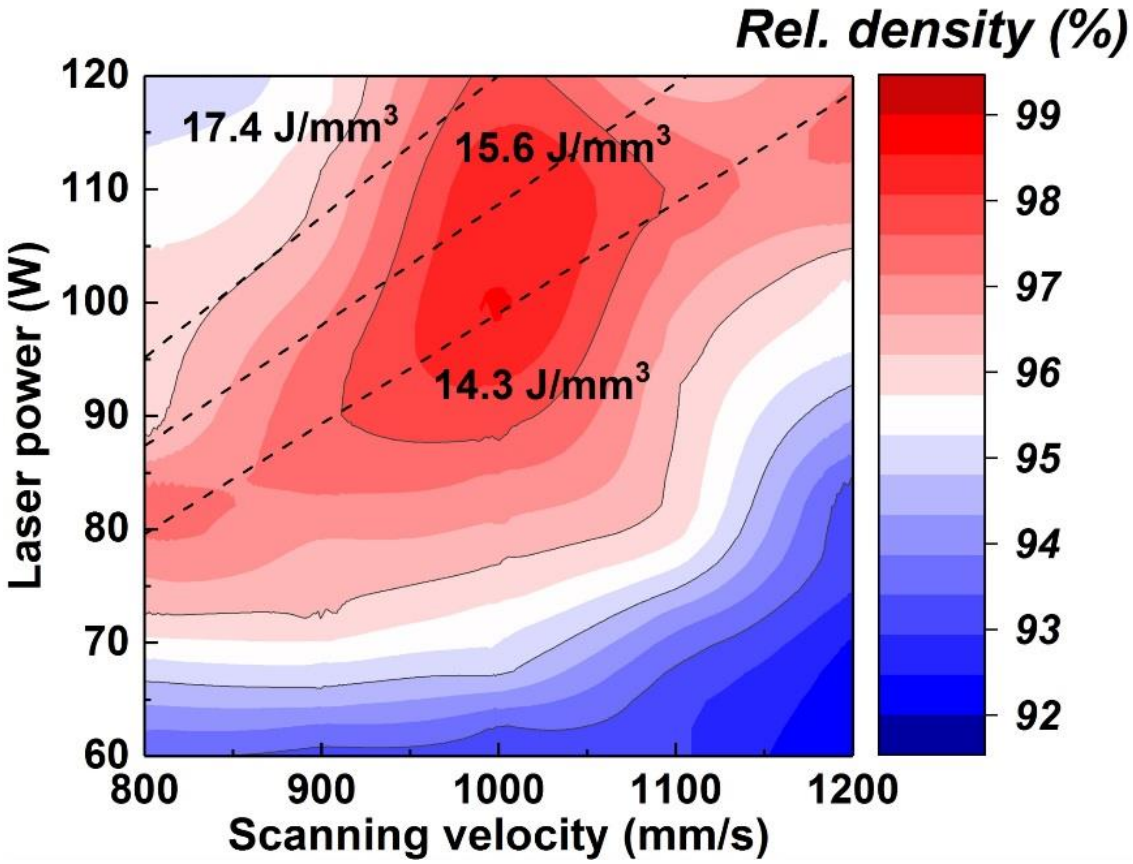

Figure 5.2: Contour map of the relative density of the additively manufactured $Cu_{46}Zr_{46}Al_8$ samples as a function of the scanning velocity and the laser power at a constant layer thickness (l = 40 µm) and a constant hatch distance (h = 180 µm). The dashed lines indicate values of constant volume energy input. The relative density was measured with Archimedean method.

By varying the laser power and scanning speed, optimum processing conditions are identified resulting in the preparation of relatively dense specimens. Fig. 5.2 illustrates the interrelation between the process parameters and the resulting relative densities of the SLM samples. The dashed lines in Fig. 5.2 represent a constant energy input along which the relative density strongly varies. As in the case of the Ti-based (section 3.1.2), these results do not show a monotonous correlation between the density of the selectively laser-melted specimens and the energy density criterion. However, the details of the relative density maps strongly vary for the different glass-forming compositions, which makes it very difficult to make any predictions. So far, empirical parameter optimization seems to be the only possibility to identify the optimum parameters. For laser powers ranging from 93 W to 114 W at a scanning velocity around 1000 mm/s, a high relative density above 98% can be achieved. This relatively wide area represents the optimum processing window for $Cu_{46}Zr_{46}Al_8$ and the maximum relative density reaches 98.6%. Such a rather wide parameter window is desirable for selective laser melting.

In order to better understand the interrelation between the energy input and the pore distribution, µ-CT experiments were carried out. Fig. 5.3 depicts the µ-CT reconstruction and pore distribution of the SLM samples produced with the following parameters:
(i) E_V = 14.3 J/mm^3 (P = 99 W, v = 1000 mm/s, h = 180 µm, l = 40 µm),
(ii) E_V = 17.4 J/mm^3 (P = 120 W, v = 1000 mm/s, h = 180 µm, l = 40 µm) and
(iii) a sample for which a re-melting step [192-194] was implemented (P_1 = 99 W, P_2 = 120 W v = 1000 mm/s, h = 180 µm, l = 40 µm). P_1 is the power for the first scanning and P_2 is the power for re-melting.

For the re-melted sample, each powder layer was initially processed with the following parameters: E_V = 14.3 J/mm^3 (P_1 = 99 W, v = 1000 mm/s, h = 180 µm, l = 40 µm). After the layers solidified, they were re-melted with a higher laser power (P_2 = 120 W), while the remaining processing conditions (v = 1000 mm/s, h = 180 µm) were not altered. A re-melting step is often applied to increase the relative density [194, 195] and it shall be assessed if this also applies to the present glass-forming alloy. In the following, the energy input is used to refer to all three fabricated sample batches.

As shown in Fig. 5.3, the pores are randomly distributed. Only few pores can be seen in the sample fabricated with an energy input of E_V = 14.3 J/mm^3 (Fig. 5.3 (a)) and its relative density is 98.6% (Archimedes). Both the number and the sizes of the pores increase when the alloy is prepared with a slightly higher energy input of E_V = 17.4 J/mm^3 or when each layer is re-melted (Figs. 5.3 (b) and (c)). The relative densities for the sample with energy input of E_V = 17.4 J/mm^3 and re-melted sample are 98% and 98.2%, respectively. The relative density of re-melted sample is lower than that of the sample produced with a lower energy input of E_V =14.3 J/mm^3. Consequently, it seems that the relative density of the re-melted sample is primarily determined by the first melting procedure. Unlike the previous works [194, 195],the second scanning does not seem to have a positive effect on the relative density in the present work. To obtain a more quantitative picture, a statistical analysis of the pore sizes was conducted.

As shown in Fig. 5.3 (a), the pore sizes range from 10 to 90 µm and most pores (over 50%) have an equivalent diameter of 15 and 30 µm. The pore sizes of the specimens produced at E_V = 17.4 J/mm^3 (Rel. density = 98%) mainly range between 20 µm and 35 µm (Fig. 5.3 (b)) and the pore size distribution of the re-melted sample (Rel. density = 98.2%) is rather similar. However, the peak of the appendant pore size distribution is located between 30 µm and 35 µm (Fig. 5.3 (c)), suggesting that a rising energy input leads to a slight increase in pore size. Yet, a too high energy input may overheat the material, leading to a larger defect size. The amount of large pores (over 65 µm) decreases as the energy input augments. The large pores usually stretch

over several layers and contain unmelted powder particles. At a sufficient energy input, these unmelted particles are fused and, hence, the evolution of larger pores is mitigated. A comparison between Figs. 5.3 (a) and (c) reveal that the main pore size increases, whereas large pores appear less. This result indicates that one can modify the distribution of defect size by a suitable re-melting treatment.

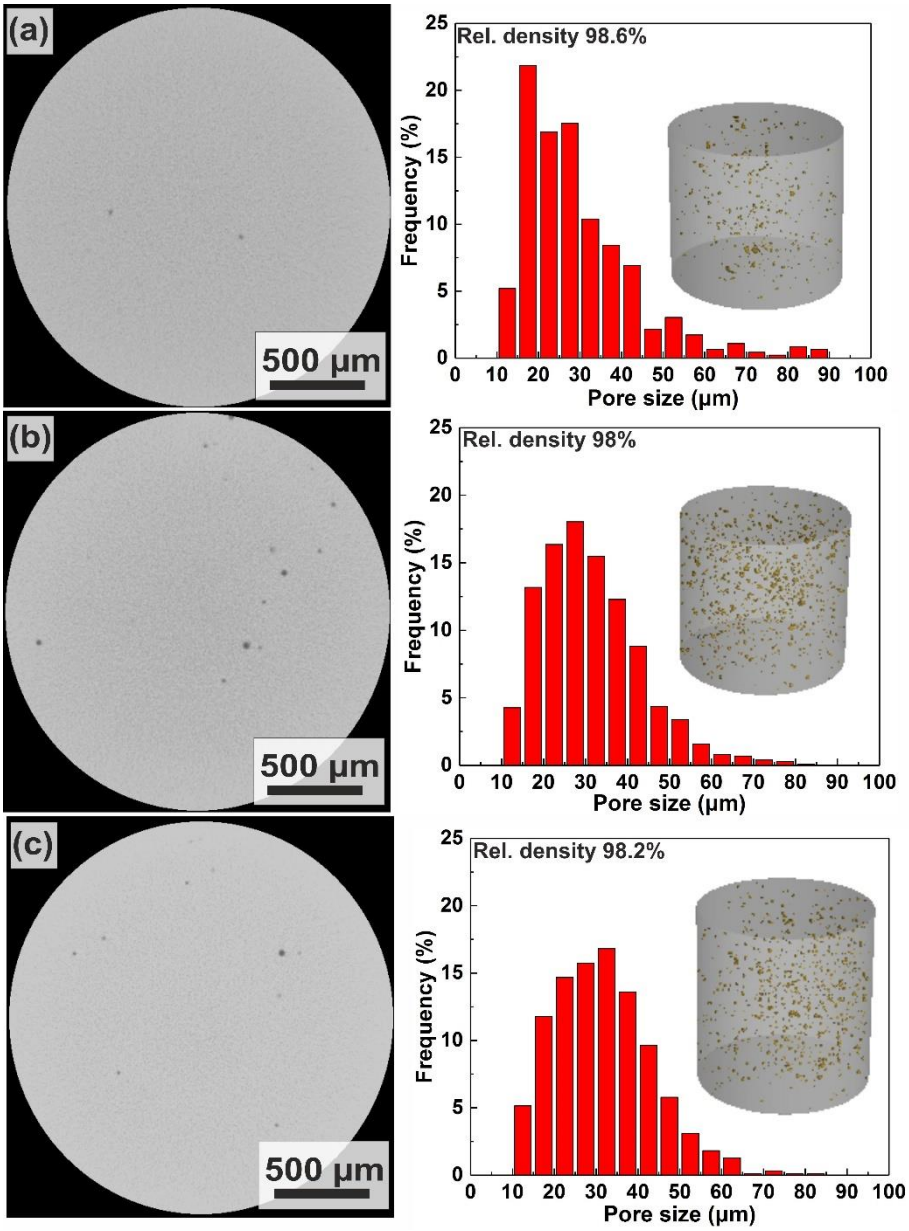

Figure 5.3: µ-CT images of cross-sections (upper), corresponding reconstructions (inset) and pore size distribution histograms of SLM samples prepared with different parameters: (a) P = 99 W, v = 1000 mm/s, h = 180 µm, l =40 µm, (b) P = 120 W, v = 1000 mm/s, h = 180 µm, l =40 µm, (c) Re-melted sample (P_1 = 99 W, P_2 = 120 W, v = 1000 mm/s, h = 180 µm, l =40 µm).

5.3 Microstructure

After having explored the interrelation between the processing parameters and porosity (or, equivalently: relative density), the phase formation and microstructure of the fabricated specimens shall be investigated next. Additionally, the powder and the as-cast material of identical chemical composition were characterized, which serves as reference states. The phase formation of the as-cast samples, the initial powder and the final SLM samples synthesized at different energy inputs was investigated first using XRD (Fig. 5.4).

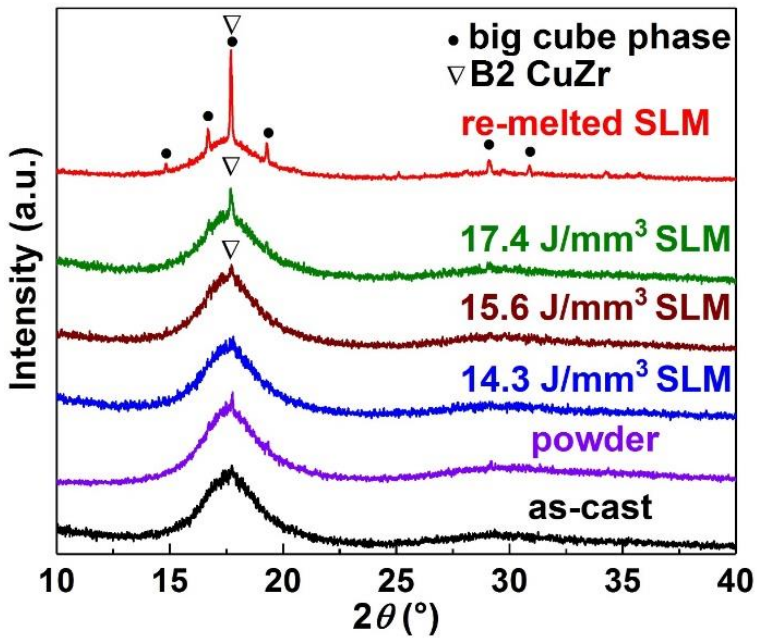

Figure 5.4: X-ray diffraction patterns of the $Cu_{46}Zr_{46}Al_8$ powder, the as-cast rods and rods produced by SLM with different energy inputs. All cylindrical specimens were produced with a diameter of 3 mm. By increasing the energy input, sharp peaks corresponding to the presence of crystalline phases, are visible.

The XRD pattern of the initial powder shows a broad maximum superposed by one weak crystalline reflection, which can be allocated to the B2 CuZr phase. As already known from as-cast CuZr-based BMG composites, small B2 CuZr crystals can form prior to the vitrification of the supercooled liquid when insufficient cooling rates are applied [93]. This, apparently, is also the case during gas atomization. The XRD pattern of the SLM sample synthesized at an energy input of E_V = 14.3 J/mm^3 only depicts a broad scattering maxima at 2θ = 17.5 ° indicating a fully glassy microstructure similar to the as-cast state (Fig. 5.4). The high cooling rates (see section 1.4.2) [198] ensure the suppression of crystallization on solidification of the melt during selective laser melting. The cooling rates during SLM appear to exceed the ones of gas atomization, which is why the $Cu_{46}Zr_{46}Al_8$ appears to be fully glassy after SLM.

When the additively manufactured samples are produced with an energy input of E_V = 15.6 J/mm^3, crystallization occurs. A relatively weak crystalline reflection appears on top of the broad scattering maximum of the glass. It can be allocated again to the B2 CuZr phase, suggesting that a higher energy input leads to lower cooling rates resulting in partial crystallization. At even higher energy input (Fig. 5.4, E_V = 17.4 J/mm^3), the intensity of this sharp reflection increases. As discussed in section 1.4.1.2, re-melting treatment can not only improve the relative density, but also be used to design the microstructure. Thus, in order to obtain and increase the volume fraction of B2 CuZr, re-melting treatment was conducted.

In the XRD pattern of re-melted sample, various sharp reflections can be observed and all of them can be allocated to the B2 CuZr phase. However, the intensity of the main reflection at about 2θ = 18 ° is comparatively high, so that one can suspect either a texture effect or the crystallization of an additional phase which is more likely. The position of this strong reflection can be also allocated to the big cube phase [330] and previous works on as-cast $Cu_{50}Zr_{50}$-based BMG matrix composites report on its formation, particularly at high temperatures and elevated oxygen content, as in the present case. In order to verify this assumption, TEM was employed.

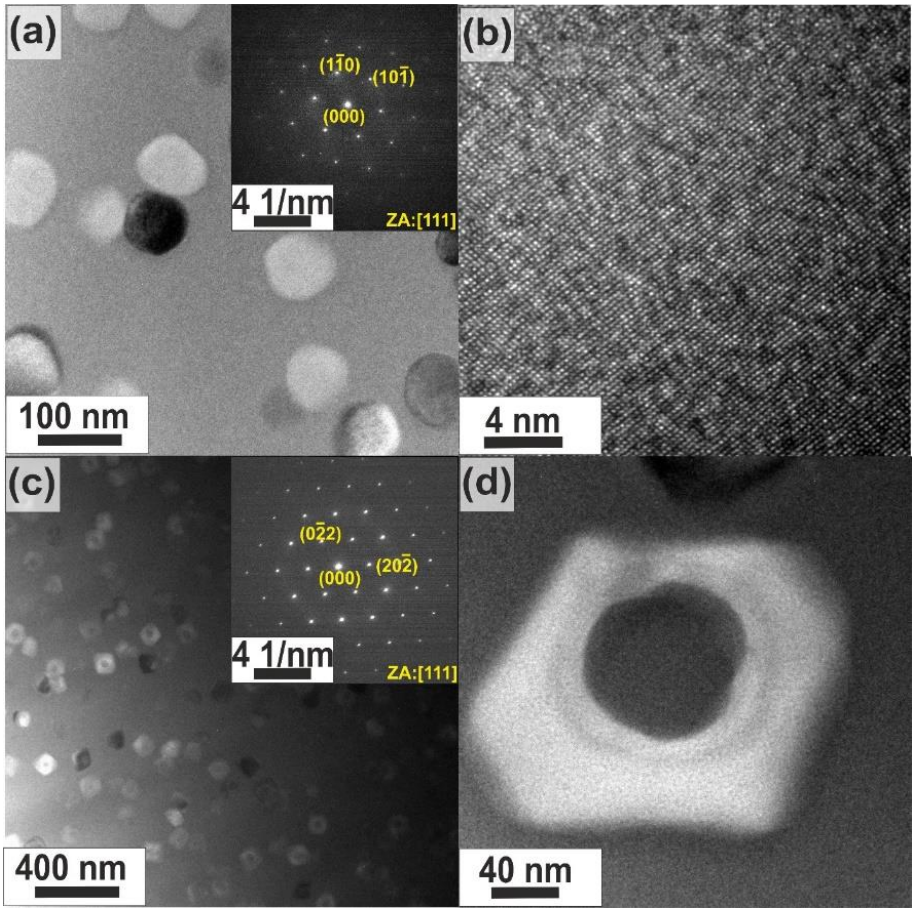

Figure 5.5: (a) Bright-field TEM micrograph of the SLM sample produced at an energy input of E_V =17.4 J/mm^3 shows spherical entities, which are identified as B2 CuZr crystals according to the selected area electron diffraction (SAED) pattern (inset). (b) High-resolution TEM image of the B2 CuZr nanocrystals (shown in a) confirms long-range ordering. (c) TEM micrograph of the re-melted SLM sample depicts almost square entities and they are identified as the big cube phase by means of the corresponding SAED pattern (inset). (d) At higher magnification, it can be seen that the big cube phase is centred around another phase, which most likely served as heterogeneous nuclei.

Fig. 5.5 (a) displays the bright-field TEM image of the SLM sample fabricated at an energy input of E_V = 17.4 J/mm^3. Only spherical crystals are visible and by means of electron diffraction (Fig. 5.5 (a), inset), they can be clearly identified as B2 CuZr (Pm$\bar{3}$m). The indicated lattice spacings of B2 CuZr were determined along the [111] zone axis and they match the observed lattice spacings obtained from the high-resolution TEM image (Fig. 5.5 (b)). The diameter of the B2 CuZr crystals ranges from 30 nm and 100 nm. The evolution of such small particles can be attributed to the high cooling rates inherent in SLM [198], which strongly inhibit crystal growth.

The re-melted specimen was also characterized by TEM and Fig. 5.5 (c) represents the bright-field micrograph. A high number of crystals with edged shape is visible, clearly differing from the morphology of the B2 CuZr crystals shown in Fig. 5.5 (a). According to the corresponding

SAED pattern (inset of Fig. 5.5 (c)), the edged phases are identified as the big cube phase (Fd$\overline{3}$m, NiT_2-type). The big cube phase usually precipitates in alloys having an elevated oxygen content [277, 286, 287] which indeed holds for the present $Cu_{46}Zr_{46}Al_8$ alloy. However, the oxygen content of about 500 ppm is comparatively low and generally the big cube phase is stabilized by larger oxygen contents [277, 286, 287]. It seems that its formation is nucleated by the crystallization of B2 CuZr (Fig. 5.5 (d)): One edged-shaped big cube crystal is shown and it is centred around a crystal with spherical morphology. Since the corresponding XRD pattern (Fig. 5.4) only confirms the presence of the big cube phase and the B2 CuZr phase, the central crystal shown in Fig. 5.5 (d) should be B2 CuZr.

B2 CuZr nanocrystals most likely act as heterogeneous nuclei for the big cube phase. Therefore, the big cube phase has to overcome a lower activation energy for its formation and can form at lower oxygen contents [220]. The big cube phase then most likely nucleates after the formation of B2 CuZr phase during the re-melting process.

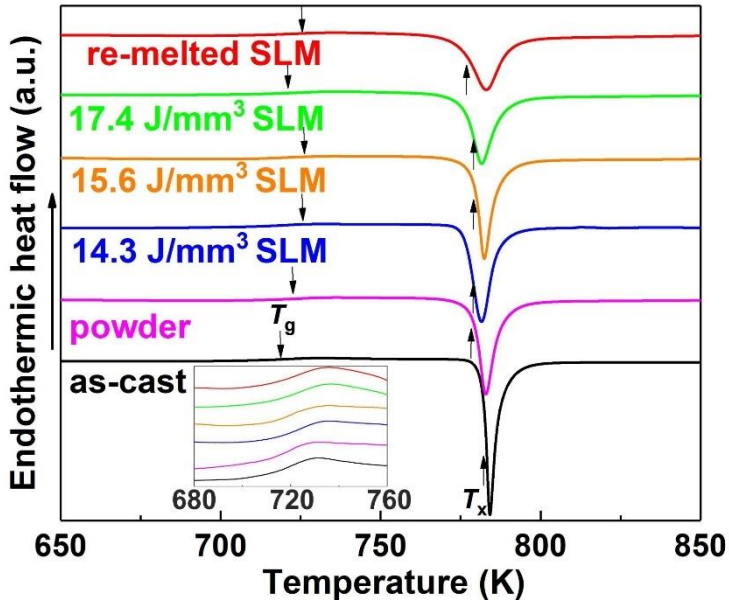

Figure 5.6: DSC traces of the $Cu_{46}Zr_{46}Al_8$ powder, as-cast and SLM samples obtained at different energy inputs. As indicated in the inset, all samples exhibit an endothermic glass transition, followed by an exothermic crystallization event. The glass transition temperature, (T_g) and crystallization temperature (T_x) are marked by arrows.

The DSC curves shown in Fig. 5.6 confirm the (partially) glassy nature of the $Cu_{46}Zr_{46}Al_8$ powder, as-cast and SLM samples. All the specimens show a clear typical glass-transition event and a supercooled liquid region followed by an exothermic event associated with crystallization. The re-melted SLM sample shows a broader exothermic peak, most likely due to the formation of the big cube phase [277]. It can be seen that the glass-transition temperature (T_g) and the crystallization temperature (T_x) marked by arrows, are slightly differing. This implies that the

processing method (gas atomization, SLM and casting) can affect the states of the glassy samples and all thermal data is listed in Table 5.2. Additively manufactured sample at higher energy input, leads to samples with a lower crystallization enthalpy (ΔH_{cryst}), suggesting the formation of crystals. The corresponding crystalline volume fractions are also shown in Table 5.2. The re-melting process dramatically enhanced the crystalline volume fraction to 12.5%.

Table 5.2: Overview over the thermal data obtained from DSC measurements of as-cast and SLM samples fabricated at different energy densities. The glass transition temperature, (T_g), crystallization temperature (T_x), width of the supercooled liquid ($\Delta T = T_x - T_g$) and the crystallization enthalpy (ΔH_{cryst}) are listed and the typical errors are given.

sample	$T_g \pm 1$ **(K)**	$T_x \pm 1$ **(K)**	$\Delta T \pm 2$ **(K)**	ΔH_{cryst} **± 2 (J/g)**	$(\Delta H_{slm} - \Delta H_{slmc})/\Delta H_{slm}$
powder	721	776	55	58	
as-cast sample	717	782	65	57	
SLM (E_V = 14.3 J/mm^3)	725	779	54	56	
SLM (E_V = 15.6 J/mm^3)	721	779	58	52	7.1%
SLM (E_V = 17.4 J/mm^3)	727	776	49	52	7.1%
SLM (re-melted)	725	775	50	49	12.5%

5.4 Mechanical properties

5.4.1 Compression tests

The SLM samples produced with energy input of E_V = 14.3 J/mm^3 and 17.4 J/mm^3 as well as the re-melted samples, which were used for μ-CT reconstruction (Fig. 5.3) were subjected to uniaxial compression. As-cast cylindrical BMGs were also subjected to uniaxial compression and serve as a reference. Fig. 5.7 depicts the compressive stress-strain curves for all samples. Three specimens for each processing condition were tested all having fairly reproducible properties. As shown in Fig. 5.7, the as-cast samples exhibit yield stresses ranging between 1890 MPa and 1950 MPa. The respective fracture strain ranges between 2.11% and 2.45%. The Young's modulus of the as-cast samples amounts to about 98 and 100 GPa. After yielding, the as-cast samples show distinct plastic deformation with visible serration. By contrast, no plastic strain can be observed for the additively manufactured BMGs regardless the processing conditions. The SLM samples with energy input E_V = 14.3 J/mm^3 fracture at stresses ranging from 1470 to 1560 MPa, and their Young's modulus ranges between 79 and 84 GPa. For additively manufactured BMGs synthesized at a higher energy input of E_V = 17.4 J/mm^3, the

fracture stress is in a range of 1310 MPa and 1400 MPa. The values of the Young's modulus are between 76 and 83 GPa. The re-melted SLM samples show the lowest fracture stresses (1179 MPa to 1262 MPa), while their Young's modulus is unchanged (77 GPa to 82 GPa). According to μ-CT results, all different SLM samples have similar relative densities. However, the samples produced at E_V = 17.4 J/mm^3 and re-melted samples have larger pore size, which might be a cause for the lower fracture stresses. Moreover, structural relaxation affects the mechanical properties, particularly the plastic deformability of metallic glasses [70]. One could speculate that more relaxed structure of the additively manufacture sample obtained at E_V = 17.4 J/mm^3 and re-melted sample is also the cause for yielding at lower stresses. To clarify this speculation, the relaxation enthalpies will be discussed in section 5.4.2. As discussed in section 5.3, the crystalline phases were found in the samples produced at E_V = 17.4 J/mm^3 and re-melted samples. This also might cause the earlier fracture.

Compared to the as-cast BMGs, all SLM samples fail in a brittle manner at lower yielding stresses. In contrast to the as-cast BMGs, which are fully dense, the structure of additively manufactured BMGs shows pores. These defects act as stress concentrators, when the sample is loaded [49] and lead to yielding at lower stresses followed by immediate brittle failure [49].

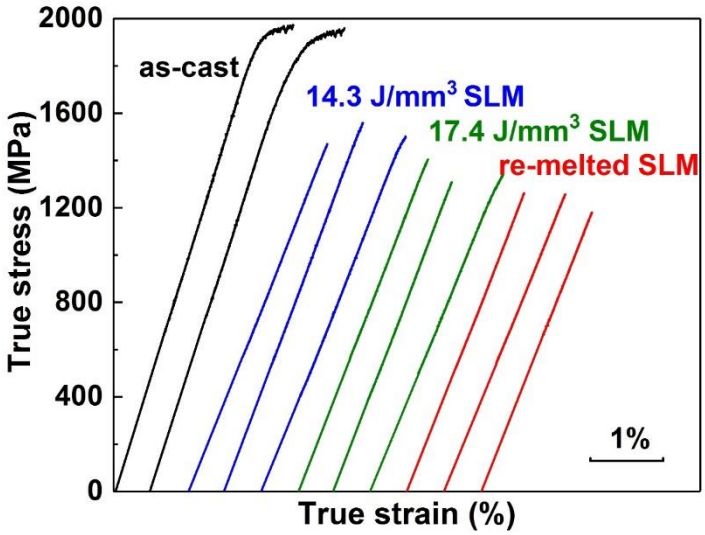

Figure 5.7: Compressive true stress-strain curves of the as-cast and SLM samples produced at different process parameters: E_V = 14.3 J/mm^3 (P = 99 W, v = 1000 mm/s, h = 180 μm, l =40 μm), E_V = 17.4 J/mm^3 (P = 120 W, v = 1000 mm/s, h = 180 μm, l =40 μm), re-melted (P_1 = 99 W, P_2 = 120 W, v = 1000 mm/s, h = 180 μm, l =40 μm).

Mechanical properties and the associated deformation mechanisms of as-cast $Cu_{46}Zr_{46}Al_8$ BMGs have been already studied in a systematic manner [331-333]. However, the fracture mechanism of additively manufactured $Cu_{46}Zr_{46}Al_8$ BMGs is still unknown. The underlying mechanism is elucidated by analysing the fracture morphologies (Fig. 5.8). Only fully

amorphous SLM samples with energy input of E_V = 14.3 J/mm^3 were considered and compared with the as-cast sample. Figs. 5.8 (a), (b) and (c) reveal the fracture surface of the compressed SLM sample. As displayed in Fig. 5.8 (a), the fracture surface is rugged and multiple fracture planes can be observed, indicating a complex fracture process differing from a pure shear fracture. A crack, which started from the lateral surface and stopped within the glass, can be observed. The crack most likely initiated from stress concentrators at the rough lateral surface and subsequently propagated towards the interior of the glass where it stopped. The distinct vein-like pattern typical of fractured as-cast BMGs can be seen, as Fig. 5.8 (d) confirms. However, the vein-like pattern on the fracture surface of the additively manufactured BMG is inhomogeneous and discontinuous. Fig. 5.8 (c)) depicts further fractographical features: instead of vein-like patterns, steps and dimples are visible and they are indicators for a hysterical failure. Cavity structures comprising the so-called mist zone (Fig. 5.8 (c)) whose size can extend to few hundred nanometres, can be seen as well. The different morphologies shown in Figs. 5.8 (b) and (c) can be attributed to the different velocities of crack propagation [263]. The larger propagating velocity for region c results in a higher stress intensity factor, the magnitude of which depends on the size and shape of the crack [263]. These obvious markings left on the fracture surface indicate a complicated stress field, inducing the hysterical fracture in the compressive test.

Further defects are visible and Fig. 5.8 (b) depicts a region (b marked in Fig. 5.8 (a)) at higher magnification. There are small unmelted powder particles on the fracture surface next to rather large pores. Pores alter the stress state during compression testing and act as concentrators. As in accordance with previous works [128, 219, 220, 306] and the results shown in section 3.2.3, the random distributed large pores are the main cause for this complex fracture process and brittle behaviour of additively manufactured BMGs.

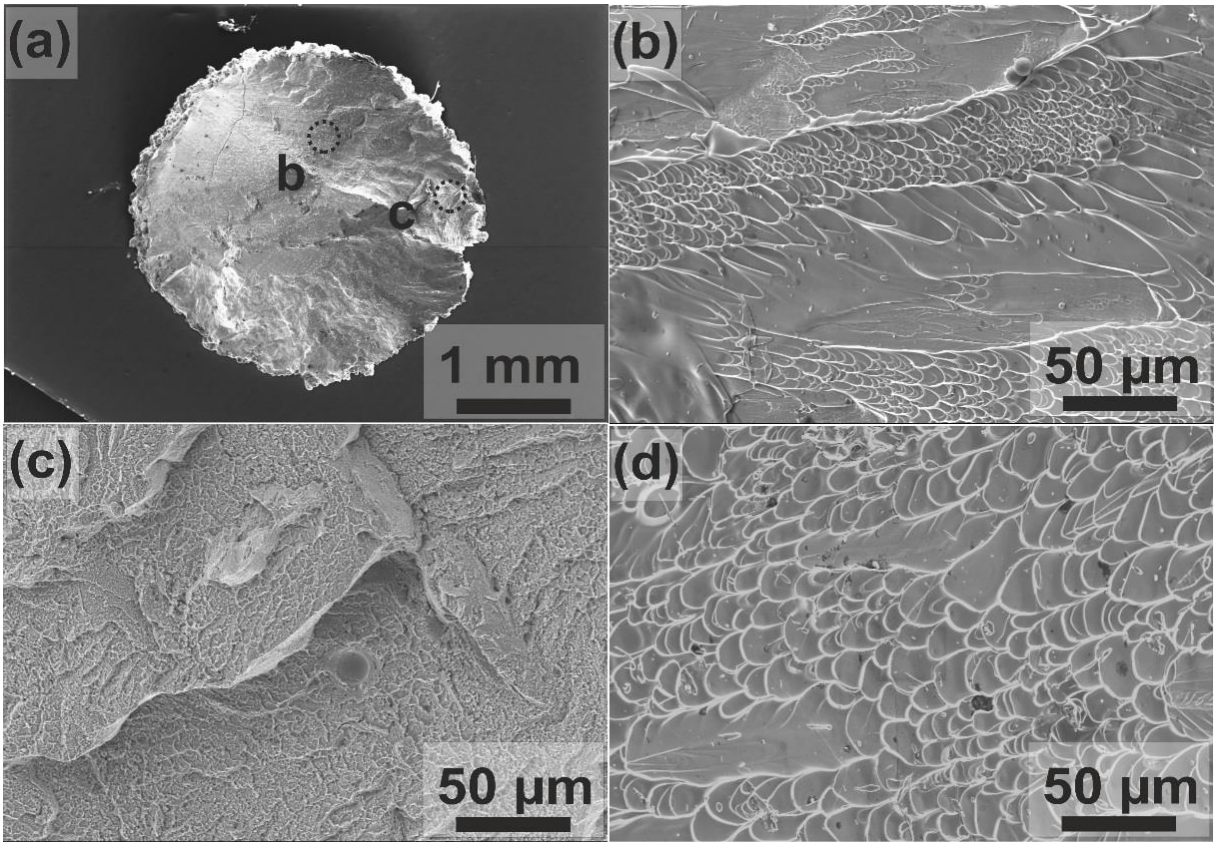

Figure 5.8: The morphologies of the fracture surfaces of the SLM sample fabricated at an energy input of E_V = 14.3 J/mm^3 (a, b and c) and an as-cast sample (d). The rugged surface reveals a complicated fracture process of the SLM sample.

5.4.2 Microhardness and structural relaxation

Microhardness measurements were conducted on as-cast and SLM samples produced at an energy input of E_V = 14.3 J/mm^3 (P = 99 W, v = 1000 mm/s, h = 180 µm, l = 40 µm), which was identified as fully amorphous (Fig. 5.4). Hardness maps were recorded for the as-cast and SLM specimens in order to investigate the influence of the processing methods on the structure of the glassy samples and indicate their mechanical properties (Fig. 5.9). Fig. 5.9 (a) depicts the positions where the indents were placed. Since there is a slight gradient in the cooling rate and the surface solidifies faster than the central part for the as-cast sample [70], all the indents were selected near the central part of both cross- and longitudinal sections. Figs. 5.9 (a) and (b) display the hardness maps of the cross- and longitudinal sections for as-cast sample, respectively. Both sections show similar values between 610 and 637 HV0.2. The hardness maps of cross- and longitudinal sections of the SLM sample are shown in Figs. 5.9 (c) and (d), respectively. The cross section of the SLM sample shows lower hardness values ranging 512 and 545 HV0.2. The hardness values determined from the longitudinal section are higher and range between 532 and 563 HV0.2. The overall hardness of the cross- and longitudinal sections

indicates a slightly inhomogeneous structure of the SLM specimen. A possible cause is the differently pronounced heat-affected zone (HAZ) within the cross section and longitudinal section where the latter is larger. The hatch distance h = 180 µm is much larger than the layer thickness l = 40 µm, leading to a larger HAZ in the longitudinal and, thus, to a more intense structural relaxation, as FVM simulations corroborate (see section 3.3).

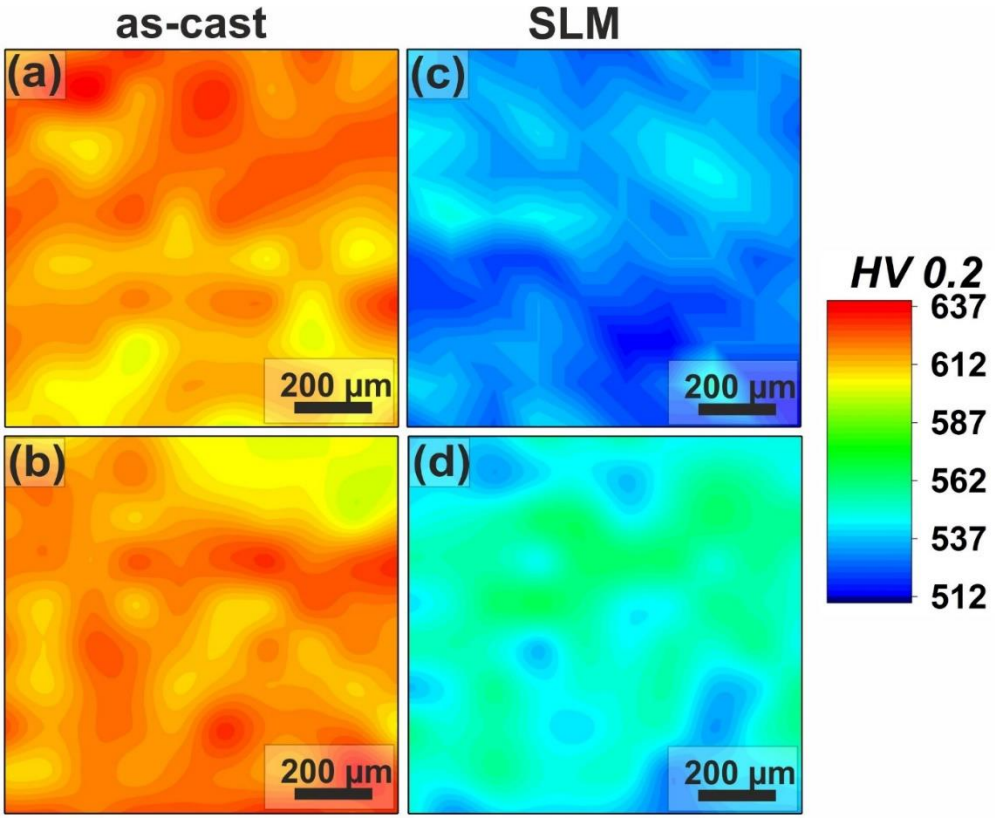

Figure 5.9: (a) and (c) display the hardness contour maps for the cross sections of as-cast and SLM samples, respectively. (b) and (d) depict the hardness contour maps of the corresponding longitudinal section for as-cast and SLM specimens, respectively.

Since the relaxation enthalpies are sensitive to the thermal history, the values of the relaxation enthalpies can reveal more or less relaxed structures. Therefore, a section of the DSC curve revealing the structural relaxation enthalpy below T_g is depicted in Fig. 5.10. The relaxation enthalpies of the as-cast samples have values between ΔH_{relax} = 5.24 J/g and ΔH_{relax} = 8.72 J/g, which is lower than the range of SLM samples obtained at E_V = 14.3 J/mm^3 between ΔH_{relax} = 14.33 J/g and ΔH_{relax} = 22.32 J/g. Additionally, ΔH_{relax} of the SLM sample with an energy input of E_V = 17.4 J/mm^3 ranges between 11.00 J/g and 11.05 J/g. ΔH_{relax} of re-melted SLM sample ranges between 8.12 J/g and 10.42 J/g. The results are similar with the cases of Ti-based and Zr-based BMGs (Chapter 3). Although structural relaxation of the glass might occur in the HAZ to a certain extent, the SLM sample still has a higher free volume content than the as-cast sample. Either the maximum temperatures present in the HAZ does not suffice for relaxing the structure

of the additively manufactured BMGs and FVM simulation (see section 3.3) refute this assumption, or the heat within the HAZ is extracted through the surrounding volume so quickly, that structural relaxation is kinetically hampered. Thus, in comparison to the additively manufactured BMG, the as-cast BMG is overall harder (Fig. 5.9). It is notable that as increasing the energy input or re-melting the sample, the relaxation enthalpy decreases, indicating that the excessive heat and subsequent thermal treatment (re-melting) relaxes the structure of the SLM samples, which might account for the lower fracture stresses of the re-melted samples and samples produced at E_V = 17.4 J/mm^3 (section 5.4.1).

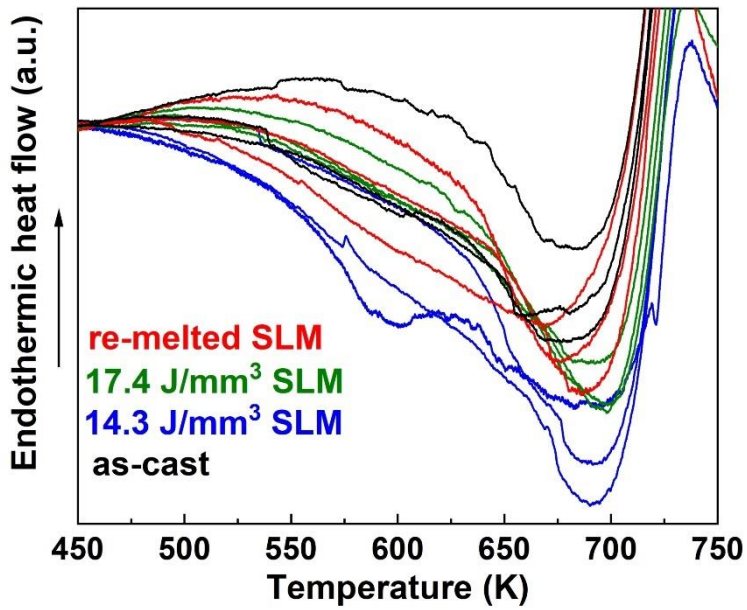

Figure 5.10: Parts of the DSC curves of the as-cast and SLM samples focussing on the exothermic structural relaxation. The enlarged DSC curves of the SLM samples fabricated at the indicated energy inputs highlight the region in which the exothermic structural relaxation occurs.

5.4.3 Nanoindentation

Calorimetry provides only average information about the free volume content of BMGs and the spatial resolution of microhardness measurements is not sufficient to detect nanoscale structural heterogeneities. Therefore, complementary nanoindentation was carried out. Figs. 5.11 (a) to (c) depict nanohardness contour maps of the longitudinal sections for SLM samples synthesized at different energy inputs to reveal the influence of the SLM processing conditions on the amorphous structure. The SLM sample produced at an energy input of E_V = 14.3 J/mm^3 shows an average hardness value of 7.41 ± 0.18 GPa. Compared to that, the SLM sample with an input of E_V = 17.4 J/mm^3 is harder (7.46 ± 0.17 GPa). The hardness value further increases for the re-melted SLM sample up to 7.52 ± 0.21 GPa. Thus, SLM of $Cu_{46}Zr_{46}Al_8$ powder at

increasing energy inputs results in the preparation of harder BMGs. As shown in the hardness maps (Figs. 5.11 (a) to (c)), the layer-like hardness distribution becomes more pronounced when selectively melted with increasing the energy input, since more relaxed glassy structures result.

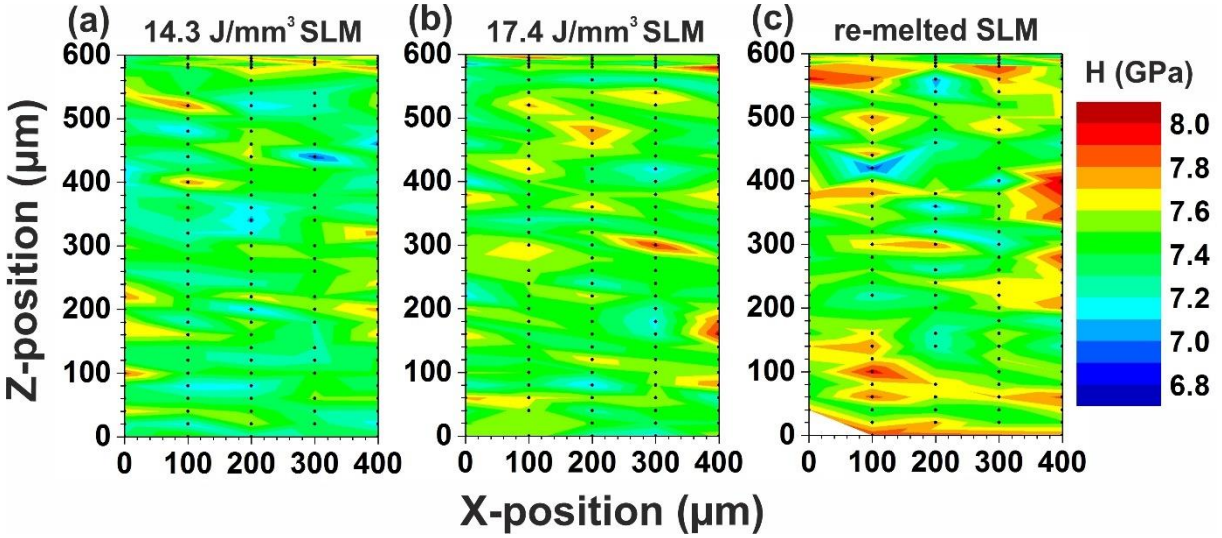

Figure 5.11: Nanohardness contour maps for the longitudinal section of the SLM samples synthesized at energy inputs of (a) E_V = 14.3 J/mm^3 (P = 99 W, v = 1000 mm/s, h = 180 µm, l =40 µm), (b)17.4 J/mm^3 (P = 120 W, v = 1000 mm/s, h = 180 µm, l =40 µm), (c) re-melted (P_1 = 99 W, P_2 = 120 W, v = 1000 mm/s, h = 180 µm, l =40 µm).

In order to investigate the degree of structural heterogeneity of SLM samples as a function of the processing conditions, namely energy input, the hardness distribution of all additively manufactured BMGs was analysed. Fig. 5.12 shows the Weibull plot of the hardness values. Although no obvious heat-affected zone (HAZ) is visible in the hardness maps (Fig. 5.11 (c)), the re-melted SLM sample has a much lower Weibull modulus (m = 43.44 ± 0.98) than the samples synthesized with an energy input of 14.3 J/mm^3 (m = 51 ± 0.93) and 17.4 J/mm^3 (m = 53.54 ± 0.95). The lower Weibull modulus reveals a more heterogeneous structure of the re-melted SLM sample. Consequently, the additional heat caused by the re-melting process not only triggers crystallization and overall relaxes the structure of the additively manufactured BMGs, but also seems to relax it in a more heterogeneous manner.

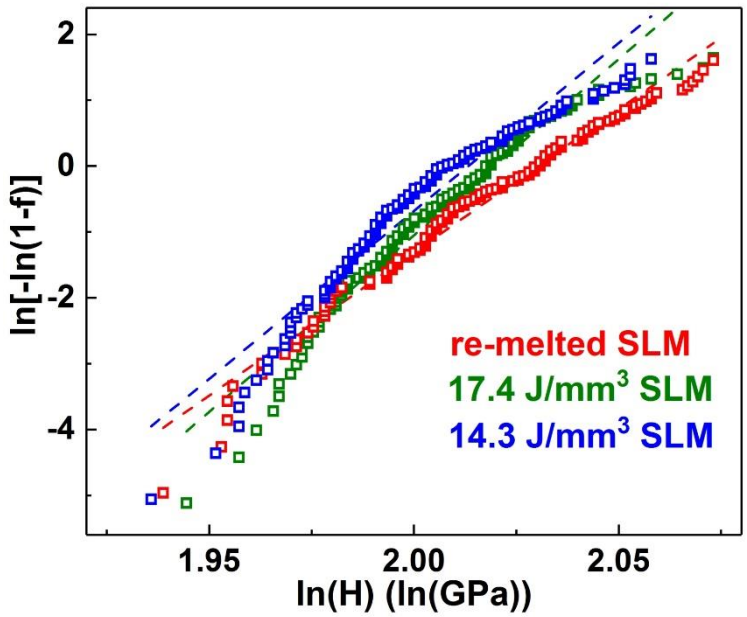

Figure 5.12: Weibull plot of hardness values for the SLM samples. The Weibull modulus (*m*) is derived from the slope of the linear regression curve of ln[-ln(1-f)] over ln(*H*) and indicated by the dashed line.

CHAPTER 6 Summary

The aim of the present thesis is to study the processing optimization, microstructure, physical and chemical properties of bulk metallic glasses (BMGs) and their composites produced via selective laser melting (SLM). The nearly fully dense BMGs and BMG matrix composites (BMGCs) were successfully prepared and the associated physical and chemical properties were systematically investigated.

For the purpose mentioned above, the compositions of $Zr_{52.5}Cu_{17.9}Ni_{14.6}Al_{10}Ti_5$ (at.%) and $Ti_{47}Cu_{38}Zr_{7.5}Fe_{2.5}Sn_2Si_1Ag_2$ (at.%) were used to produce additively manufactured BMGs.

Fully glassy $Ti_{47}Cu_{38}Zr_{7.5}Fe_{2.5}Sn_2Si_1Ag_2$ samples with a high relative density from 98.5% - 98.7%, good thermal stability and high compressive strength around 1700 MPa were obtained by selective laser melting. The processing maps indicate that no single process parameter has a linear effect on the relative density of the additively manufactured $Ti_{47}Cu_{38}Zr_{7.5}Fe_{2.5}Sn_2Si_1Ag_2$ samples, which provides a new clue to study the process parameters. The microhardness results reveal that the macroscopic homogeneity of SLM samples is comparable to that of as-cast BMGs. Similar corrosion performance was obtained in the as-cast and SLM samples. Moreover, the SLM sample shows slightly better surface healing ability and reduced pitting corrosion susceptibility.

The relative density of $Zr_{52.5}Cu_{17.9}Ni_{14.6}Al_{10}Ti_5$ SLM sample reaches values above 98.7%. Compared to the yield strength of as-cast BMGs (about 1830 MPa), additively manufactured BMGs yield at lower stresses of about 1710 MPa. A detectable plastic strain (about 0.5%) after yielding was determined for all SLM specimens, which is still lower than for the as-cast glass of identical composition. The residual porosity in the SLM samples is believed to be responsible for the premature failure of the BMGs prepared by selective laser melting. Further investigations of the deformation mechanism of SLM samples reveal its structure to be homogeneous, also on an atomic length scale. Moreover, apparent pores play an important role for the formation and affect the propagation of shear bands. Nonetheless, the effect of these pores on the microhardness is negligible and the hardness values of the SLM samples and the as-cast samples hold similar distributions. Also the complex thermal history of the SLM samples, thus, has no evident influence on the microhardness. A similar wear performance for SLM and as-cast BMG specimens can be deduced from the time-dependent coefficients of friction, wear rates and surface morphologies after wear. In other words, SLM processing has no negative effect on these mechanical properties. Finally, the comparable anodic polarization curves and pitting behaviour of the SLM and as-cast samples suggest that they have a similar

corrosion resistance. The slightly improved surface healing ability and reduced pitting corrosion susceptibility is an advantage inherent in additively manufactured BMGs and could originate from a chemically more uniform glassy structure. Apart from the still limited plastic deformability, additively manufactured BMGs demonstrate mechanical properties and corrosion resistance very similar to as-cast BMGs. By means of the DSC measurements, nanoindention tests and thermal field simulation of $Zr_{52.5}Cu_{17.9}Ni_{14.6}Al_{10}Ti_5$ and $Ti_{47}Cu_{38}Zr_{7.5}Fe_{2.5}Sn_2Si_1Ag_2$ additively manufactured BMGs, the homogeneity of SLM BMGs were studied. The varied structural homogeneities of the SLM BMGs can be attributed to the different thermophysical properties and processing parameters.

In order to further design the microstructure and illustrate the processability of additively manufacturing BMGCs, the *ex-situ* and *in-situ* methods were carried out to fabricate BMGCs via SLM.

Glass matrix composites were produced by selective laser melting by processing a blend of glass-forming $Zr_{52.5}Cu_{17.9}Ni_{14.6}Al_{10}Ti_5$ powder and Nb particles. Even without refining the process parameters, relative densities above 98% are possible. The formation of crystalline phases in the investigated specimens strongly depends on the Nb content in both SLM and as-cast samples. Nb clearly reduces the glass-forming ability of the alloy system and stimulates the precipitation of brittle phases around the Nb particles. The larger the fraction of Nb particles, the more pronounced the diffusion of Nb into the matrix. This is why in the sample with 10 wt.% Nb a Nb-rich crystalline phase could be detected, which seems absent in the samples with 2 wt.% Nb. μ-CT measurements were used to analyse the size changes of the Nb particles after selective laser melting. This data was used to extract radial distribution functions in order to analyse the Nb particle distribution, which provided a gist to adjust the distance between particles by changing the amount of additional particles. It also provides a possibility to predict the propagation of the shear bands and calculate the activity space of the shear bands, thereby helping to design the material. According to the micro-hardness map, the homogeneity of the samples became worse after adding Nb particles. In addition, with the increase of Nb content, the range of microhardness became larger, implying that the crystalline volume fraction increased. Meanwhile, the brittle phases accelerated the propagation of shear bands and the generation of cracks, leading to a brittle fracture of the specimens. The current work outlines a possibility of producing BMG matrix composites by SLM. It also illustrates the selection of additional material plays an important role to a global ductile BMG-matrix composites. An ideal addition and optimized processing parameter should be discovered in further studies. Additive manufacturing of powder blends proves to be a powerful tool for designing BMG matrix

composites and this study highlights some of the pitfalls associated with this approach. Therefore, this work will help to facilitate the selection of future alloy systems and to optimize the properties of additively manufactured BMG matrix composites. It is, consequently, feasible to produce uniform BMG matrix composites with finely dispersed soft crystals. This work also reveals that in order to avoid the formation of unstable brittle phases, the additional materials which cannot react with the matrix should be selected carefully. If reactions between the additional element and the matrix occur in certain temperature. An optimal parameter should be found in order to avoid the reaction. The amount of additional element should also be taken in consideration because diffusion will impact the chemical homogeneity of the BMG matrix. In brief, the fraction of the suitable additional materials plays a very important role in processing BMG matrix composites by SLM.

$Cu_{46}Zr_{46}Al_8$ (at.%) bulk metallic glass and composites have been successfully fabricated via SLM. The nearly fully glassy SLM samples and additively manufactured BMGCs samples have a high relative density (over 98%). By optimizing the process parameters, the B2 CuZr phase can be partially and particularly deliberately crystallized. Consequently, SLM represents a new *in-situ* method of producing BMGCs. Next to B2 CuZr, the big cube phase formed when processing conditions with higher energy input are endeavoured. The glassy structure of additively manufactured BMGs was characterized in detail and compared to as-cast BMGs of the same composition. Additively manufactured BMGs vitrify at distinctly higher cooling rates than the as-cast material. Owing to the resulting higher free volume content trapped in SLM samples during vitrification, they are overall softer than the as-cast samples, as inferred from microindentation. Cross and longitudinal section were investigated for the as-cast and additively manufactured BMGs. In contrast to the as-cast BMG, the cross and longitudinal sections of SLM sample differ in overall hardness indicating a less uniform structure. Most likely, the extent of the heat-affected zone (HAZ) differs in cross and longitudinal sections. The additional heat from the new layer relaxed the previous solidified layers. With increasing the energy input, the relaxation becomes more obvious. However, the duration of relaxation is too short. The free volume trapped in the SLM sample is higher than the as-cast sample. The fracture strength of fully glassy SLM sample is about 1500 MPa, which is less than for the as-cast BMGs (about 1900 MPa). Although the additively manufactured BMGCs consist B2 phase, which is usually considered to be beneficial for the mechanical properties, the strength of the additively manufactured BMGCs can only reach 1400 MPa. Next to crystals, also pores pose structural heterogeneities and latter are inherent to the structure of additively manufactured BMGs. Moreover, randomly distributed large pores act as stress concentrators during loading.

Thus, porosity is considered to be the main cause for the premature failure of additively manufactured BMGs and structural relaxation accounts for the decreased fracture stresses of additively manufactured BMGCs. Since SLM can vitrify and especially also partially vitrify small volumes of supercooled liquid (microscale) “layer-by-layer”, crystalline phase(s) are considered to distribute homogeneously in the glassy matrix.

CHAPTER 7 Outlook

The results shown in the present work reveal that SLM is a promising method for synthesizing BMGs and BMGCs. Even though the chemical and physical properties of additively manufactured BMGs and BMGCs can compare to the as-cast ones, more in-depth work needs to be done in the future in order to achieve the practical application of the additively manufactured BMGs and BMGCs. The further ideas, open questions and possible experiments are listed in the following:

(i) Since the inherent porosity of additively manufactured BMGs and BMGCs induced the premature failure in the compression tests. The fatigue behaviour should be further studied for practical applications.

(ii) To study the effect of thermal history from the "layer-by-layer" processing, the building direction can be changed to the angle of 30°, 45°, 60° and 90° with the substrate. By investigating the propagation of the shear bands in the compression tests, the thermal history can be revealed.

(iii) By optimizing the processing parameters, the "layer by layer" structure composites can be produced. The effect of the structure on the deformation process of such additively manufactured BMGCs should be studied in depth.

(iv) By the means of modifying the parameters, the particle size of crystals in additively manufactured BMGCs can be adjusted. The relation of crystal particle size and the mechanical properties of additively manufactured BMGCs needs to be studied.

(v) Introduce a new addition, which cannot react with the BMG matrix. The distance between the secondary phases can be changed by altering the amount of the addition. The influence of the distance on the propagation and initiation of shear bands can be investigated.

Acknowledgements

"Seek truth from facts."- Book of Han

As the quote from the Book of Han illustrated, my PhD study is a journey of seeking truth from facts. Before the start, I was so lucky that I got the financial support from Chinese Scholarship Council (CSC). I really appreciate their funding for supporting my life in Germany. During this journey I met many people, who helped me a lot. Without their favour, I would not have been able to finish this dissertation successfully.

First and foremost, I would like to express my deep sense of gratitude Prof. Dr. Martina Zimmermann for her supervision and support. I also would like to give my thanks to Prof. Dr. Jürgen Eckert for providing me the opportunity to work in Leibniz Institute for Solid State and Material Research (IFW Dresden), where I can work with top-level devices and discuss with brilliant and talented people.

I equally express my sincere gratitude to my direct supervisor Prof. Dr. Simon Pauly. He always gives me constructive advices not only in academic field but also in daily life. Even though he left Dresden to Aschaffenburg, he still helped and encouraged me when I was lost. Simon, you treated me as a little brother. I have to thank you for your patience. A few sentences are insufficient to describe my acknowledgements for you. Vielen Dank, man!

The outcome of my PhD study should be attributed to the supportive atmosphere inherent to Institute for Complex Materials (ICM). Sincere thanks go to my department leader, Dr. Uta Kühn for her support. She always has an open ear open for me. When I need help, she always stands by me. Particularly, I want to thank Dr. Konrad Kosiba and Dr. Pei Wang for the valuable suggestions, support and the happy time during my PhD study. As seniors, they guide me and encourage when I am lost.

I also would like thank Dr. Thomas Gemming for his financial support at the end of my study. I am also grateful to Dr. Annett Gebert and Dr. Sergio Scudino for their technical support and insightful discussions. I have to give my sincere thanks to Marion Johne for the corrosion tests, Birgit Bartusch for DSC measurements, Dr. Alexander Funk for μ-CT measurements, Dr. Rene Limbach for nanoindentation tests, Kerstin Schröder and Christiane Mix for the help in metallography lab, Alexander Schultze for wear tests, Dr. Horst Wendrock for SEM instruction. Juliane Scheiter for heat treatment, Andrea Voß, for the chemical composition measurement, Heike Bußkamp for the oxygen content measurement Heike Bußkamp and Birgit Opitz for the XRD measurements. Particularly, I have to thank my colleagues in department 3401, Nicole

Geißler, Hans Weber, Romy Keller, Michael Frey, Sven Donath, Harald Merker and Baumgart Kai-Uwe for their help. They never say “No” to me, when I need help. I extent my gratitude to the colleagues in SLM lab, Dr. Tobias Gustmann, Dr. Jan Sander, Dr. Holger Schwab, Dr. Omar Oday Salman and Fabian Kochta for their inspiring discussions and kindly help.

I sincerely thank all the former colleagues who helped me in academic and daily life, Dr. Lixia Xi, Dr. Long Zhang, Yanfei Sui, Bo Gao, Prof. Dr. Shenghai Wang, Dr. Haichao Li, Mo Li, Zichao Li, Dr. Daniel Sopu, Dr. Parthiban, Dr. Pramote Thirathipviwat, Dr. Rub Nawaz Shalid, Dr. Xiaolei Sun, Dr. Jinbo Pang and Dr. Xueyi Lu.

I also have to express my great thanks to my Chinese colleagues and friends, Ju Wang, Tianbing He, Qiongqiong Lu, Dr. Ran He, Ling Ding, Peng Xue, Hongyu Chen, Tiwen Lu, Kang Sun, Xiaoliang Han, Xiaoru Cai, Dr. Jing Guo, Dr. Ye Liu, Dr. Bin Cai, Dr. Tao Zhang, Dr. Lanfa Liu, Min Ji, Dr. Tianyi Li, Dr. Kangfa Deng, Dr. Yangxi Fu, Bo Yin, Jiawen Zhang, Qin Liu, Hanjing Zhang, Yuchen Wang, Xinyu Wang, Diyu You, Jin Zhao, Qiaoyuan Liu, Zhenyu Xie, Jun Bai, Huan Wu, Bowen Xue, Yifan Lu, Jitong Zhao, Decen Song, Liao Chen, Ya Jiang, Jiachuan Liang, Peng Yu, Boyu Dong, Haisong Wang, Tianxiang Deng and all the members of AFG football team. Particularly, I would like to give my special thanks to Dr. Zhao Qu for her guidance and encouragement. Dear friends, I will never forget the happy time we spent in Germany. May our friendship last forever.

The sincere gratitude should be given to the ladies at the secretariat, Brit Präßler-Wüstling and Janette Schuster for their administrative help.

Finally, I would like to express great thanks to all the family members, my parents, aunts, uncles and cousins for their constant support and encouragements during the last years. Profound gratitude goes to my beloved, Rebecca, for her support, love and patience. “Ever thine, Ever mine, Ever ours.”

Liang Deng
06.02.2020

Bibliography

[1] J.Q. Wang, Y. Shen, J.H. Perepezko, M.D. Ediger, Increasing the kinetic stability of bulk metallic glasses, Acta Mater. 104 (2016) 25-32.

[2] H.M. Lin, J.K. Wu, C.C. Wang, P.Y. Lee, The corrosion behavior of mechanically alloyed Cu–Zr–Ti bulk metallic glasses, Mater. Lett. 62 (2008) 2995-2998.

[3] J.K. Lee, H.J. Kim, T.S. Kim, S.Y. Shin, Y.C. Kim, J.C. Bae, Deformation behavior of Ni-based bulk metallic glass synthesized by spark plasma sintering, J. Mater. Process. Tech. 187 (2007) 801-804.

[4] S. Yoon, H.J. Kim, C. Lee, Deposition behavior of bulk amorphous NiTiZrSiSn according to the kinetic and thermal energy levels in the kinetic spraying process, Surf Coat Technol. 200 (2006) 6022-6029.

[5] W.H. Wang, C. Dong, C.H. Shek, Bulk metallic glasses, Mater. Sci. Eng. R 44 (2004) 45-89.

[6] C.A. Angell, Formation of glasses from liquids and biopolymers, Science 267 (1995) 1924-1935.

[7] J.C. Dyre, Colloquium: The glass transition and elastic models of glass-forming liquids, Rev. Mod. Phys. 78 (2006) 953.

[8] R. Busch, J. Schroers, W.H. Wang, Thermodynamics and kinetics of bulk metallic glass, MRS Bull. 32 (2007) 620-623.

[9] C. Suryanarayana, A. Inoue, Bulk metallic glasses, CRC press 2017.

[10] J.E. Hilliard, J.W. Cahn, On the nature of the interface between a solid metal and its melt, Acta Metall. 6 (1958) 772-774.

[11] J.W. Cahn, Theory of crystal growth and interface motion in crystalline materials, Acta Metall. 8 (1960) 554-562.

[12] D. Turnbull, Under what conditions can a glass be formed? Contemp. Phys. 10 (1969) 473-488.

[13] D.E. Polk, D. Turnbull, Flow of melt and glass forms of metallic alloys, Acta Metall. 20 (1972) 493-498.

[14] M.H. Cohen, G.S. Grest, Liquid-glass transition, a free-volume approach, Phys. Rev. B 20 (1979) 1077.

[15] M.H. Cohen, D. Turnbull, Molecular transport in liquids and glasses, J. Chem. Phys. 31 (1959) 1164-1169.

[16] K. Kosiba, Flash-Annealing of Cu-Zr-Al-based Bulk Metallic Glasses (2017).

[17] Y.Q. Cheng, E. Ma, Atomic-level structure and structure–property relationship in metallic glasses, Prog. Mater. Sci. 56 (2011) 379-473.

[18] H.S. Chen, Glassy metals, Rep. Prog. Phys. 43 (1980) 353.

[19] A. Peker, W.L. Johnson, A highly processable metallic glass: $Zr_{41.2}Ti_{13.8}Cu_{12.5}Ni_{10.0}Be_{22.5}$, Appl. Phys. Lett. 63 (1993) 2342-2344.

[20] H.W. Kui, A.L. Greer, D. Turnbull, Formation of bulk metallic glass by fluxing, Appl. Phys. Lett. 45 (1984) 615-616.

[21] A. Inoue, N. Nishiyama, Extremely low critical cooling rates of new Pd-Cu-P base amorphous alloys, Mater. Sci. Eng. A 226 (1997) 401-405.

[22] Z.P. Lu, C.T. Liu, Glass formation criterion for various glass-forming systems, Phys. Rev. Lett. 91 (2003) 115505.

[23] Z.P. Lu, C.T. Liu, A new glass-forming ability criterion for bulk metallic glasses, Acta Mater. 50 (2002) 3501-3512.

[24] W.K. Jun, R.H. Willens, P. Duwez, Non-crystalline structure in solidified gold–silicon alloys, Nature 187 (1960) 869.

[25] P. Duwez, R.H Willens. Rapid quenching of liquid alloys. Defense Technical Information Center, US, 1962.

[26] R.B. Pond. Metallic filaments and method of making same. Google Patents; 1958.

[27] A. Inoue, N. Nishiyama, H. Kimura, Preparation and thermal stability of bulk amorphous $Pd_{40}Cu_{30}Ni_{10}P_{20}$ alloy cylinder of 72 mm in diameter, Mater. Trans. JIM 38 (1997) 179-183.

[28] A. Inoue, T. Nakamura, N. Nishiyama, T. Masumoto, Mg-Cu-Y bulk amorphous alloys with high tensile strength produced by a high-pressure die casting method, Mater. Trans. JIM 33 (1992) 937-945.

[29] N. Nishiyama, A. Inoue, Glass-forming ability of bulk $Pd_{40}Ni_{10}Cu_{30}P_{20}$ alloy, Mater. Trans., JIM 37 (1996) 1531-1539.

[30] E.S. Park, D.H. Kim, Formation of Ca-Mg-Zn bulk glassy alloy by casting into cone-shaped copper mold, J. Mater. Res. 19 (2004) 685-688.

[31] Y. Yokoyama, E. Mund, A. Inoue, L. Schultz, Production of $Zr_{55}Cu_{30}Ni_5Al_{10}$ glassy alloy rod of 30 mm in diameter by a cap-cast technique, Mater. Trans. 48 (2007) 3190-3192.

[32] A. Inoue, T. Zhang, Fabrication of bulky Zr-based glassy alloys by suction casting into copper mold, Mater. Trans. JIM 36 (1995) 1184-1187.

[33] T. Zhang, A. Inoue, Mechanical properties of Zr-Ti-Al-Ni-Cu bulk amorphous sheets prepared by squeeze casting, Mater. Trans. JIM 39 (1998) 1230-1237.

[34] W.G. Pfann, Zone melting, John Wiley & Sons, New York, 1958.

[35] T. Tamura, K. Amiya, R.S. Rachmat, Y. Mizutani, K. Miwa, Electromagnetic vibration process for producing bulk metallic glasses, Nat. Mater. 4 (2005) 289.

[36] D. Geissler, J. Grosse, S. Donath, D. Ehinger, M. Stoica, J. Eckert, U. Kühn. Granulation of bulk metallic glass forming alloys as a feedstock for thermoplastic forming and their compaction into bulk samples. Mater. Sci. Forum 879 (2017) 589-594.

[37] J. Schroers, W.L. Johnson, Highly processable bulk metallic glass-forming alloys in the Pt-Co-Ni-Cu-P system, Appl. Phys. Lett. 84 (2004) 3666-3668.

[38] J. Shen, Q. Chen, J. Sun, H. Fan, G. Wang, Exceptionally high glass-forming ability of an FeCoCrMoCBY alloy, Appl. Phys. Lett. 86 (2005) 151907.

[39] A. Inoue, W. Zhang, T. Zhang, K. Kurosaka, High-strength Cu-based bulk glassy alloys in Cu-Zr-Ti and Cu-Hf-Ti ternary systems, Acta Mater. 49 (2001) 2645-2652.

[40] A. Inoue, Stabilization of metallic supercooled liquid and bulk amorphous alloys, Acta Mater. 48 (2000) 279-306.

[41] D.B. Miracle, W.S. Sanders, O.N. Senkov, The influence of efficient atomic packing on the constitution of metallic glasses, Philos Mag. 83 (2003) 2409-2428.

[42] D.B. Miracle, A structural model for metallic glasses, Nat. Mater. 3 (2004) 697.

[43] E. Axinte, Metallic glasses from “alchemy” to pure science: Present and future of design, processing and applications of glassy metals, Mater. De. 35 (2012) 518-556.

[44] M. Chen, A brief overview of bulk metallic glasses, NPG Asia Mater. 3 (2011) 82.

[45] A. Inoue, A. Takeuchi, Recent development and application products of bulk glassy alloys, Acta Mater. 59 (2011) 2243-2267.

[46] M.M. Trexler, N.N. Thadhani, Mechanical properties of bulk metallic glasses, Prog. Mater. Sci. 55 (2010) 759-839.

[47] T. Masumoto, R. Maddin, The mechanical properties of palladium 20 a/o silicon alloy quenched from the liquid state, Acta Metall. 19 (1971) 725-741.

[48] A.L. Greer, Metallic glasses, Science 267 (1995) 1947-1953.

[49] A.L. Greer, Y.Q. Cheng, E. Ma, Shear bands in metallic glasses, Mater. Sci. Eng. R 74 (2013) 71-132.

[50] M. Telford, The case for bulk metallic glass, Mater Today 7 (2004) 36-43.

[51] M.F. Ashby, A.L. Greer, Metallic glasses as structural materials, Scr. Mater. 54 (2006) 321-326.

[52] D. Pan, A. Inoue, T. Sakurai, M.W. Chen, Experimental characterization of shear transformation zones for plastic flow of bulk metallic glasses, PNAS 105 (2008) 14769-14772.

[53] E. Ma, Tuning order in disorder, Nat. Mater. 14 (2015) 547.

[54] A.S. Argon, Plastic deformation in metallic glasses, Acta Metall. 27 (1979) 47-58.

[55] D. Şopu, A. Stukowski, M. Stoica, S. Scudino, Atomic-level processes of shear band nucleation in metallic glasses, Phys. Rev. Lett. 119 (2017) 195503.

[56] S. Ogata, F. Shimizu, J. Li, M. Wakeda, Y.J.I. Shibutani, Atomistic simulation of shear localization in Cu–Zr bulk metallic glass, Intermetallics 14 (2006) 1033-1037.

[57] M.L. Falk, J.S. Langer, Dynamics of viscoplastic deformation in amorphous solids. Phys. Rev. E 57 (1998) 7192.

[58] C.A. Schuh, A.C. Lund, Atomistic basis for the plastic yield criterion of metallic glass, Nat. Mater. 2 (2003) 449.

[59] A.S. Argon, H.Y. Kuo, Plastic flow in a disordered bubble raft (an analog of a metallic glass), Mater. Sci. Eng. 39 (1979) 101-109.

[60] A.S. Argon, L.T. Shi, Development of visco-plastic deformation in metallic glasses, Acta Metall. 31 (1983) 499-507.

[61] F. Spaepen, A microscopic mechanism for steady state inhomogeneous flow in metallic glasses, Acta Metall. 25 (1977) 407-415.

[62] Y. Zhang, A.L. Greer, Thickness of shear bands in metallic glasses, Appl. Phys. Lett. 89 (2006) 071907.

[63] S. Pauly, M.H. Lee, D.H. Kim, K.B. Kim, D.J. Sordelet, J. Eckert, Crack evolution in bulk metallic glasses, J. Appl. Phys. 106 (2009) 103518.

[64] T. Wada, A. Inoue, A.L. Greer, Enhancement of room-temperature plasticity in a bulk metallic glass by finely dispersed porosity, Appl. Phys. Lett. 86 (2005) 251907.

[65] A. Inoue, T. Wada, D.V. Louzguine-Luzgin, Improved mechanical properties of bulk glassy alloys containing spherical pores, Mater. Sci. Eng. A 471 (2007) 144-150.

[66] R.T. Qu, J.X. Zhao, M. Stoica, J. Eckert, Z.F. Zhang, Macroscopic tensile plasticity of bulk metallic glass through designed artificial defects, Mater. Sci. Eng. A 534 (2012) 365-373.

[67] J. Qiao, In-situ dendrite/metallic glass matrix composites: a review, J. Mater. Sci. Technol. 29 (2013) 685-701.

[68] Z. Zhu, H. Zhang, Z. Hu, W. Zhang, A. Inoue, Ta-particulate reinforced Zr-based bulk metallic glass matrix composite with tensile plasticity, Scr. Mater. 62 (2010) 278-281.

[69] C. Liu, R. Maaß, Elastic fluctuations and structural heterogeneities in metallic glasses, Adv. Funct. Mater. 28 (2018) 1800388.

[70] K. Kosiba, D. Şopu, S. Scudino, L. Zhang, J. Bednarcik, S. Pauly, Modulating heterogeneity and plasticity in bulk metallic glasses: Role of interfaces on shear banding, Int. J. Plast. 119 (2019) 156-170.

[71] J. Shen, Y.J. Huang, J.F. Sun, Plasticity of a TiCu-based bulk metallic glass: Effect of cooling rate, J. Mater. Res. 22 (2007) 3067-3074.

[72] S.V. Ketov, Y.H. Sun, S. Nachum, Z. Lu, A. Checchi, A.R. Beraldin, H.Y. Bai, W.H. Wang, D.V. Louzguine-Luzgin, M.A. Carpenter, Rejuvenation of metallic glasses by non-affine thermal strain, Nature 524 (2015) 200.

[73] Y. Chen, M.Q. Jiang, L.H. Dai, How does the initial free volume distribution affect shear band formation in metallic glass? Sci. China Phys., Mech. Astron. 54 (2011) 1488-1494.

[74] Z.Y. Zhang, Y. Wu, J. Zhou, W.L. Song, D. Cao, H. Wang, X.J. Liu, Z.P. Lu, Effects of Sn addition on phase formation and mechanical properties of TiCu-based bulk metallic glass composites, Intermetallics, 42 (2013) 68-76.

[75] R.D. Conner, R.B. Dandliker, W.L. Johnson, Mechanical properties of tungsten and steel fiber reinforced $Zr_{41.25}Ti_{13.75}Cu_{12.5}Ni_{10}Be_{22.5}$ metallic glass matrix composites, Acta Mater. 46 (1998) 6089-6102.

[76] H. Choi-Yim, S.Y. Lee, R.D. Conner, Mechanical behavior of Mo and Ta wire-reinforced bulk metallic glass composites, Scr. Mater. 58 (2008) 763-766.

[77] F. Szuecs, C.P. Kim, W.L. Johnson, Mechanical properties of $Zr_{56.2}Ti1_{3.8}Nb_{5.0}Cu_{6.9}Ni_{5.6}Be_{12.5}$ ductile phase reinforced bulk metallic glass composite, Acta Mater. 49 (2001) 1507-1513.

[78] K.M. Flores, W.L. Johnson, R.H. Dauskardt, Fracture and fatigue behavior of a Zr–Ti–Nb ductile phase reinforced bulk metallic glass matrix composite, Scr. Mater. 49 (2003) 1181-1187.

[79] A. Inoue, Mechanical properties of Zr-based bulk glassy alloys containing nanoscale compound particles, Intermetallics 8 (2000) 455-468.

[80] M. Kinaka, H. Kato, M. Hasegawa, A. Inoue, High specific strength Mg-based bulk metallic glass matrix composite highly ductilized by Ti dispersoid, Mater. Sci. Eng. A 494 (2008) 299-303.

[81] J. Eckert, M. Seidel, A. Kübler, U.T. Klement, L. Schultz, Oxide dispersion strengthened mechanically alloyed amorphous Zr-Al-Cu-Ni composites, Scr. Mater. 38 (1998) 595-602.

[82] H. Fu, H. Zhang, H. Wang, Q. Zhang, Z. Hu, Synthesis and mechanical properties of Cu-based bulk metallic glass composites containing in-situ TiC particles, Scr. Mater. 52 (2005) 669-673.

[83] P. Wadhwa, J. Heinrich, R. Busch, Processing of copper fiber-reinforced $Zr_{41.2}Ti_{13.8}Cu_{12.5}Ni_{10.0}Be_{22.5}$ bulk metallic glass composites, Scr. Mater. 56 (2007) 73-76.

[84] M.E. Siegrist, J.F. Löffler, Bulk metallic glass–graphite composites, Scr. Mater. 56 (2007) 1079-1082.

[85] H. Choi-Yim, R. Busch, U. Köster, W.L. Johnson, Synthesis and characterization of particulate reinforced $Zr_{57}Nb_5Al_{10}Cu_{15.4}Ni_{12.6}$ bulk metallic glass composites, Acta Mater. 47 (1999) 2455-2462.

[86] H. Choi-Yim, W.L. Johnson, Bulk metallic glass matrix composites, Appl. Phys. Lett. 71 (1997) 3808-3810.

[87] W.H. Wang, Roles of minor additions in formation and properties of bulk metallic glasses, Prog. Mater. Sci. 52 (2007) 540-596.

[88] S.V. Madge, D.V. Louzguine-Luzgin, A. Inoue, A.L. Greer, Large compressive plasticity in a La-based glass-crystal composite, Metals, 3 (2013) 41-48.

[89] D.C. Hofmann, J.Y. Suh, A. Wiest, G. Duan, M.L. Lind, M.D. Demetriou, W.L. Johnson, Designing metallic glass matrix composites with high toughness and tensile ductility, Nature, 451 (2008) 1085.

[90] K. Kosiba, S. Pauly, Inductive flash-annealing of bulk metallic glasses, Sci. Rep. 7 (2017) 2151.

[91] M. Ferry, K.J Laws, C. White, D.M. Miskovic, K.F. Shamlaye, W. Xu, O. Biletska, Recent developments in ductile bulk metallic glass composites, MRS Commun. 3 (2013) 1-12.

[92] J.W. Seo, D. Schryvers, TEM investigation of the microstructure and defects of CuZr martensite. Part I: Morphology and twin systems, Acta Mater. 46 (1998) 1165-1175.

[93] S. Pauly, G. Liu, G. Wang, U. Kühn, N. Mattern, J. Eckert, Microstructural heterogeneities governing the deformation of $Cu_{47.5}Zr_{47.5}Al_5$ bulk metallic glass composites, Acta Mater. 57 (2009) 5445-5453.

[94] J. Eckert, J. Das, S. Pauly, C. Duhamel, Mechanical properties of bulk metallic glasses and composites, J. Mater. Res. 22 (2007) 285-301.

[95] D. Schryvers, J.W. Seo, G.S. Firstov, Y.N. Koval, J.V. Humbeeck, Unit cell determination in CuZr martensite by electron microscopy and X-ray diffraction, Scr. Mater. 36 (1997) 1119-1125.

[96] K.K. Song, S. Pauly, Y. Zhang, R. Li, S. Gorantla, N. Narayanan, U. Kühn, T. Gemming, J. Eckert, Triple yielding and deformation mechanisms in metastable $Cu_{47.5}Zr_{47.5}Al_5$ composites, Acta Mater. 60 (2012) 6000-6012.

[97] Z.Q. Liu, R. Li, G. Liu, K.K. Song, S. Pauly, T. Zhang, J. Eckert, Pronounced ductility in CuZrAl ternary bulk metallic glass composites with optimized microstructure through melt adjustment, AIP Adv. 2 (2012) 032176.

[98] E.M. Carvalho, I.R. Harris, Constitutional and structural studies of the intermetallic phase, ZrCu, J. Mater. Sci. 15 (1980) 1224-1230.

[99] A.V. Zhalko-Titarenko, M.L Yevlashina, V.N Antonov, B.Y. Yavorskii, Y.N. Koval, G.S. Firstov, Electronic and crystal structure of the ZrCu intermetallic compound close to the point of structural transformation, Phys. Status Solidi B 184 (1994) 121-127.

[100] Y.N. Koval, G.S. Firstov, A.V. Kotko, Martensitic transformation and shape memory effect in ZrCu intermetallic compound. Scr. Metall. Mater. 27 (1992) 1611-1616.

[101] X. Ren, N. Miura, K. Taniwaki, K. Otsuka, T. Suzuki, K. Tanaka, Y.I. Chumlyakov, M. Asai, Understanding the martensitic transformations in TiNi-based alloys by elastic constants measurement, Mater. Sci. Eng. A 273 (1999) 190-194.

[102] F.F. Wu, K.C. Chan, S.S. Jiang, S.H. Chen, G. Wang, Bulk metallic glass composite with good tensile ductility, high strength and large elastic strain limit, Sci. Rep. 4 (2014) 5302.

[103] K.K. Song, S. Pauly, Y. Zhang, P. Gargarella, R. Li, N.S. Barekar, U. Kühn, M. Stoica, J. Eckert, Strategy for pinpointing the formation of B2 CuZr in metastable CuZr-based shape memory alloys, Acta Mater. 59 (2011) 6620-6630.

[104] Y. Wu, H. Wang, H.H. Wu, Z.Y. Zhang, X.D. Hui, G.L. Chen, D. Ma, X.L. Wang, Z.P. Lu, Formation of Cu-Zr-Al bulk metallic glass composites with improved tensile properties. Acta Mater. 59 (2011) 2928-2936.

[105] J.M. Liu, H.F. Zhang, H.M. Fu, Z.Q. Hu, X.G. Yuan, In situ spherical B2 CuZr phase reinforced ZrCuNiAlNb bulk metallic glass matrix composite. J. Mater. Res. 25 (2010) 1159-1163.

[106] Y.Y. Cheng, S.J. Pang, C. Chen, T. Zhang, Size-dependent enhancement of plasticity by laser surface melting in $Zr_{55}Al_{10}Ni_5Cu_{30}$ bulk metallic glass, J. Alloys Compd. 658 (2016) 49-54.

[107] K. Kosiba, S. Scudino, R. Kobold, U. Kühn, A.L. Greer, J. Eckert, S. Pauly, Transient nucleation and microstructural design in flash-annealed bulk metallic glasses, Acta Mater. 127 (2017) 416-425.

[108] B.A. Sun, S. Pauly, J. Tan, M. Stoica, W.H. Wang, U. Kühn, J. Eckert, Serrated flow and stick–slip deformation dynamics in the presence of shear-band interactions for a Zr-based metallic glass, Acta Mater. 60 (2012) 4160-4171.

[109] B.A. Sun, K.K. Song, S. Pauly, P. Gargarella, J. Yi, G. Wang, C.T. Liu, J. Eckert, Y. Yang, Transformation-mediated plasticity in CuZr based metallic glass composites: A quantitative mechanistic understanding, Int. J. Plast. 85 (2016) 34-51.

[110] C. Wang, B.A. Sun, W.H. Wang, H.Y. Bai, Chaotic state to self-organized critical state transition of serrated flow dynamics during brittle-to-ductile transition in metallic glass, J. Appl. Phys. 119 (2016) 054902.

[111] F.H. Dalla Torre, D. Klaumünzer, R. Maaß, J.F. Löffler, Stick–slip behavior of serrated flow during inhomogeneous deformation of bulk metallic glasses, Acta Mater. 58 (2010) 3742-3750.

[112] J.L. Ren, C. Chen, G. Wang, N. Mattern, J. Eckert, Dynamics of serrated flow in a bulk metallic glass, AIP Adv. 1 (2011) 032158.

[113] D. Klaumünzer, R. Maaß, J.F. Löffler, Stick-slip dynamics and recent insights into shear banding in metallic glasses, J. Mater. Res. 26 (2011) 1453-1463.

[114] J.J. Lewandowski, W.H. Wang, A.L. Greer, Intrinsic plasticity or brittleness of metallic glasses, Phil. Mag. Lett. 85 (2005) 77-87.

[115] J. Tan, Y. Zhang, B.A. Sun, M. Stoica, C.J. Li, K.K. Song, U. Kühn, F.S. Pan, J. Eckert, Correlation between internal states and plasticity in bulk metallic glass, Appl. Phys. Lett. 98 (2011) 151906.

[116] B.A. Sun, H.B. Yu, W. Jiao, H.Y. Bai, D.Q. Zhao, W.H. Wang, Plasticity of ductile metallic glasses: A self-organized critical state, Phys. Rev. Lett. 105 (2010) 035501.

[117] K.K. Song, S. Pauly, B.A. Sun, J. Tan, M. Stoica, U. Kühn, J. Eckert, Correlation between the microstructures and the deformation mechanisms of CuZr-based bulk metallic glass composites, AIP Adv. 3 (2013) 012116.

[118] C.Y. Tam, C.H. Shek, Abrasive wear of $Cu_{60}Zr_{30}Ti_{10}$ bulk metallic glass, Mater. Sci. Eng. A 384 (2004) 138-142.

[119] A.L. Greer, K.L. Rutherford, I.M. Hutchings, Wear resistance of amorphous alloys and related materials, Int. Mater. Rev. 47 (2002) 87-112.

[120] M.L. Rahaman, L.C. Zhang, H.H. Ruan, Understanding the friction and wear mechanisms of bulk metallic glass under contact sliding, Wear 304 (2013) 43-48.

[121] D.R. Maddala, A. Mubarok, R.J. Hebert, Sliding wear behavior of $Cu_{50}Hf_{41.5}Al_{8.5}$ bulk metallic glass, Wear 269 (2010) 572-580.

[122] M. Ishida, H. Takeda, N. Nishiyama, K. Kita, Y. Shimizu, Y. Saotome, A. Inoue, Wear resistivity of super-precision microgear made of Ni-based metallic glass, Mater. Sci. Eng. A 449 (2007) 149-154.

[123] Y.J. Huang, H.B. Fan, D.J. Wang, Y. Sun, F.Y. Liu, J. Shen, J.F. Sun, J. Mi, The effect of cooling rate on the wear performance of a ZrCuAlAg bulk metallic glass, Mater. Des. 58 (2014) 284-289.

[124] M.E. Siegrist, E.D. Amstad, J.F. Löffler, Tribological properties of graphite-and ZrC-reinforced bulk metallic glass composites, Intermetallics 15 (2007) 1228-1236.

[125] Y.B. Wang, H.F. Li, Y. Cheng, Y.F. Zheng, L.Q. Ruan, In vitro and in vivo studies on Ti-based bulk metallic glass as potential dental implant material, Mater. Sci. Eng. C 33 (2013) 3489-3497.

[126] M.L. Rahaman, L.C. Zhang, M. Liu, W.D. Liu, Surface roughness effect on the friction and wear of bulk metallic glasses, Wear 332 (2015) 1231-1237.

[127] M. Rahaman, L.C. Zhang, H.H. Ruan, Effects of environmental temperature and sliding speed on the tribological behaviour of a Ti-based metallic glass, Intermetallics 52 (2014) 36-48.

[128] D. Ouyang, N. Li, W. Xing, J.J. Zhang, L. Liu, 3D printing of crack-free high strength Zr-based bulk metallic glass composite by selective laser melting, Intermetallics 90 (2017) 128-134.

[129] F.X. Qin, X.M. Wang, A. Kawashima, S.L. Zhu, H. Kimura, A. Inoue, Corrosion behavior of Ti-based metallic glasses, Mater. Trans. 47 (2006) 1934-1937.

[130] J.R. Scully, A. Gebert, J.H. Payer, Corrosion and related mechanical properties of bulk metallic glasses, J. Mater. Res. 22 (2007) 302-313.

[131] M. Stratmann, G.S. Frankel. Encyclopedia of Electrochemistry, vol. 4: Corrosion and Oxide Films. Wiley-VCH, Weinheim, 2003.

[132] F.X. Qin, M. Yoshimura, X.M Wang, S.L. Zhu, A. Kawashima, K. Asami, A. Inoue, Corrosion behavior of a Ti-based bulk metallic glass and its crystalline alloys, Mater. Trans. 48 (2007) 1855-1858.

[133] U.K. Mudali, S. Baunack, J. Eckert, L. Schultz, A. Gebert, Pitting corrosion of bulk glass-forming zirconium-based alloys, J. Alloys Compd. 377 (2004) 290-297.

[134] A. Kawashima, W.P. Yu, B.P. Zhang, H. Habazaki, K. Asami, K. Hashimoto, Pitting Corrosion of Amorphous Ni-Zr Alloys in Chloride Ion Containing Sulfuric Acid Solutions, Mater. Trans. JIM 38 (1997) 443-450.

[135] A. Gebert, P.F. Gostin, M. Uhlemann, J. Eckert, L. Schultz, Interactions between mechanically generated defects and corrosion phenomena of Zr-based bulk metallic glasses, Acta Mater. 60 (2012) 2300-2309.

[136] J. Paillier, C. Mickel, P.F. Gostin, A. Gebert, Characterization of corrosion phenomena of Zr-Ti-Cu-Al-Ni metallic glass by SEM and TEM, Mater. Charact. 61 (2010) 1000-1008.

[137] P.F. Gostin, D. Eigel, D. Grell, J. Eckert, E. Kerscher, A. Gebert, Comparing the pitting corrosion behavior of prominent Zr-based bulk metallic glasses, J. Mater. Res. 30 (2015) 233-241.

[138] L. Huang, Y. Yokoyama, W. Wu, P.K. Liaw, S.J. Pang, A. Inoue, T. Zhang, W. He, Ni-free Zr-Cu-Al-Nb-Pd bulk metallic glasses with different Zr/Cu ratios for biomedical applications, J. Biomed. Mater. Res. Part B 100 (2012) 1472-1482.

[139] T. Wang, Y.D. Wu, J.J. Si, Y.H. Cai, X.H. Chen, X.D. Hui, Novel Ti-based bulk metallic glasses with superior plastic yielding strength and corrosion resistance, Mater. Sci. Eng. A 642 (2015) 297-303.

[140] Y.B. Wang, H.F. Li, Y. Cheng, S.C. Wei, Y.F. Zheng, Corrosion performances of a Nickel-free Fe-based bulk metallic glass in simulated body fluids, Electrochem. Commun. 11 (2009) 2187-2190.

[141] X.L. Zhang, G. Chen, T. Bauer, Mg-based bulk metallic glass composite with high bio-corrosion resistance and excellent mechanical properties, Intermetallics 29 (2012) 56-60.

[142] B. Vishwanadh, R. Balasubramaniam, D. Srivastava, G.K. Dey, Effect of surface morphology on atmospheric corrosion behaviour of Fe-based metallic glass, $Fe_{67}Co_{18}Si_{14}B_1$, Bull. Mater. Sci. 31 (2008) 693-698.

[143] A. Gebert, K. Mummert, J. Eckert, L. Schultz, A. Inoue, Electrochemical investigations on the bulk glass forming $Zr_{55}Cu_{30}Al_{10}Ni_5$ alloy, Mater Corros. 48 (1997) 293-297.

[144] B. Vishwanadh, G.J. Abraham, S. Neogy, R.S. Dutta, G.K. Dey, Effect of structural defects, surface irregularities, and quenched-in defects on corrosion of Zr-based metallic glasses, Metall. Mater. Trans. A 40 (2009) 1131-1141.

[145] M.L. Morrison, R.A. Buchanan, A. Peker, P.K. Liaw, J.A. Horton, Electrochemical behavior of a Ti-based bulk metallic glass, J. Non-cryst. Solids 353 (2007) 2115-2124.

[146] J. Fornell, E. Pellicer, N. Van Steenberge, S. González, A. Gebert, S. Suriñach, M. Baró, J. Sort, Improved plasticity and corrosion behavior in Ti-Zr-Cu-Pd metallic glass with minor additions of Nb: An alloy composition intended for biomedical applications, Mater. Sci. Eng. A 559 (2013) 159-164.

[147] S. Pang, Y. Liu, H. Li, L. Sun, Y. Li, T. Zhang, New Ti-based Ti–Cu–Zr–Fe–Sn–Si–Ag bulk metallic glass for biomedical applications, J. Alloys Compd. 625 (2015) 323-327.

[148] F.X. Qin, X.M. Wang, S.L. Zhu, A. Kawashima, K. Asami, A. Inoue, Fabrication and corrosion property of novel Ti-based bulk glassy alloys without Ni, Mater. Trans. 48 (2007) 515-518.

[149] W.H. Peter, R.A. Buchanan, C.T. Liu, P.K. Liaw, M.L. Morrison, J.A. Horton, C.A. Carmichael Jr, J.L. Wright, Localized corrosion behavior of a zirconium-based bulk metallic glass relative to its crystalline state, Intermetallics 10 (2002) 1157-1162.

[150] K. Mondal, B.S. Murty, U.K. Chatterjee, Electrochemical behavior of multicomponent amorphous and nanocrystalline Zr-based alloys in different environments, Corros. Sci. 48 (2006) 2212-2225.

[151] Standard terminology for additive manufacturing technologies (2012).

[152] A.J. Pinkerton, Lasers in additive manufacturing, Opt. Laser Technol. 78 (2016) 25-32.

[153] C.Y. Yap, C.K. Chua, Z.L. Dong, Z.H. Liu, D.Q. Zhang, L.E. Loh, S.L. Sing, Review of selective laser melting: Materials and applications, Appl. Phys. Rev.2 (2015) 041101.

[154] W. Meiners, K. Wissenbach, A. Gasser, Shaped body especially prototype or replacement part production, DE Patent 19 (1998).

[155] G. Ziółkowski, E. Chlebus, P. Szymczyk, J. Kurzac, Application of X-ray CT method for discontinuity and porosity detection in 316L stainless steel parts produced with SLM technology, Arch. Civ. Mech. Eng. 14 (2014) 608-614.

[156] E.O. Olakanmi, R.F. Cochrane, K.W. Dalgarno, A review on selective laser sintering/melting (SLS/SLM) of aluminium alloy powders: Processing, microstructure, and properties, Prog. Mater. Sci. 74 (2015) 401-477.

[157] A. Strondl, O. Lyckfeldt, H. Brodin, U. Ackelid, Characterization and control of powder properties for additive manufacturing, JOM 67 (2015) 549-554.

[158] E.O. Olakanmi, Selective laser sintering/melting (SLS/SLM) of pure Al, Al–Mg, and Al–Si powders: Effect of processing conditions and powder properties, J. Mater. Process. Tech. 213 (2013) 1387-1405.

[159] H.J Gong, H.F. Gu, K. Zeng, J.J.S. Dilip, D. Pal, B. Stucker, D. Christiansen, J. Beuth, J.J. Lewandowski. Melt pool characterization for selective laser melting of Ti-6Al-4V pre-alloyed powder. Solid Freeform Fabrication Symposium (2014) 256-267.

[160] P. Wang, H.C. Li, K.G. Prashanth, J. Eckert, S. Scudino, Selective laser melting of Al-Zn-Mg-Cu: Heat treatment, microstructure and mechanical properties, J. Alloys Compd. 707 (2017) 287-290.

[161] G. Yablokova, M. Speirs, J. Van Humbeeck, J.P. Kruth, J. Schrooten, R. Cloots, F. Boschini, G. Lumay, J. Luyten, Rheological behavior of β-Ti and NiTi powders produced by atomization for SLM production of open porous orthopedic implants, Powder Technol. 283 (2015) 199-209.

[162] T. Marcu, M. Todea, I. Gligor, P. Berce, C. Popa, Effect of surface conditioning on the flowability of Ti6Al7Nb powder for selective laser melting applications, Appl. Surf. Sci. 258 (2012) 3276-3282.

[163] W. Reschetnik, J.P. Brüggemann, M.E. Aydinöz, O. Grydin, K.P. Hoyer, G. Kullmer, H.A. Richard, Fatigue crack growth behavior and mechanical properties of additively processed EN AW-7075 aluminium alloy, Procedia Struct. Integrity 2 (2016) 3040-3048.

[164] M. Khan, P. Dickens, Selective laser melting (SLM) of gold (Au), Rapid Prototyping J. 18 (2012) 81-94.

[165] T. Gustmann, A. Neves, U. Kühn, P. Gargarella, C.S. Kiminami, C. Bolfarini, J. Eckert, S. Pauly, Influence of processing parameters on the fabrication of a Cu-Al-Ni-Mn shape-memory alloy by selective laser melting, Addit. Manuf. 11 (2016) 23-31.

[166] R.M. German, Particle packing characteristics, Metal Powder Industry, Princeton, New Jersey (1989).

[167] H.H. Zhu, J.Y.H. Fuh, L. Lu, The influence of powder apparent density on the density in direct laser-sintered metallic parts, Int. J. Mach. Tools Manuf. 47 (2007) 294-298.

[168] J. Mazumder, D. Dutta, N. Kikuchi, A. Ghosh, Closed loop direct metal deposition: art to part, Opt. Laser. Eng. 34 (2000) 397-414.

[169] B. Liu, R. Wildman, C. Tuck, I. Ashcroft, R. Hague, Investigation the effect of particle size distribution on processing parameters optimisation in selective laser melting process, Additive manufacturing research group, Loughborough University (2011) 227-238.

[170] A.B. Spierings, N. Herres, G. Levy, Influence of the particle size distribution on surface quality and mechanical properties in AM steel parts, Rapid Prototyping J. 17 (2011) 195-202.

[171] A. Simchi, The role of particle size on the laser sintering of iron powder, Metall. Mater. Trans. B 35 (2004) 937-948.

[172] R. Li, Y.S. Shi, Z.G. Wang, L. Wang, J.H. Liu, W. Jiang, Densification behavior of gas and water atomized 316L stainless steel powder during selective laser melting, Appl. Surf. Sci. 256 (2010) 4350-4356.

[173] K.G. Prashanth, S. Scudino, T. Maity, J. Das, J. Eckert, Is the energy density a reliable parameter for materials synthesis by selective laser melting? Mate. Res. Lett. 5 (2017) 386-390.

[174] R. Chou, J. Milligan, M. Paliwal, M. Brochu, Additive manufacturing of Al-12Si alloy via pulsed selective laser melting, JOM 67 (2015) 590-596.

[175] U.S. Bertoli, A.J. Wolfer, M.J. Matthews, J.P.R. Delplanque, J.M. Schoenung, On the limitations of volumetric energy density as a design parameter for selective laser melting, Mater. Des. 113 (2017) 331-340.

[176] I. Tolosa, F. Garciandía, F. Zubiri, F. Zapirain, A. Esnaola, Study of mechanical properties of AISI 316 stainless steel processed by “selective laser melting”, following different manufacturing strategies, Int. J. Adv. Manuf. Technol. 51 (2010) 639-647.

[177] G. Miranda, S. Faria, F. Bartolomeu, E. Pinto, S. Madeira, A. Mateus, P. Carreira, N. Alves, F.S. Silva, O. Carvalho, Predictive models for physical and mechanical properties of 316L stainless steel produced by selective laser melting, Mater. Sci. Eng. A 657 (2016) 43-56.

[178] H.Y. Chen, D.D. Gu, D.H. Dai, C.L. Ma, M.J. Xia, Microstructure and composition homogeneity, tensile property, and underlying thermal physical mechanism of selective laser melting tool steel parts, Mater. Sci. Eng. A 682 (2017) 279-289.

[179] S. Ghouse, S. Babu, R.J. Van Arkel, K. Nai, P.A. Hooper, J.R.T. Jeffers, The influence of laser parameters and scanning strategies on the mechanical properties of a stochastic porous material, Mater. Des. 131 (2017) 498-508.

[180] D.Z. Wang, C.F. Yu, J. Ma, W. Liu, Z.J. Shen, Densification and crack suppression in selective laser melting of pure molybdenum, Mater. Des. 129 (2017) 44-52.

[181] X.Z. Shi, S.Y. Ma, C.M. Liu, Q.R. Wu, Parameter optimization for Ti-47Al-2Cr-2Nb in selective laser melting based on geometric characteristics of single scan tracks, Opt. Laser Technol. 90 (2017) 71-79.

[182] W. Li, J. Liu, Y. Zhou, S. Li, S.F. Wen, Q.S. Wei, C.Z. Yan, Y.S. Shi, Effect of laser scanning speed on a Ti-45Al-2Cr-5Nb alloy processed by selective laser melting: microstructure, phase and mechanical properties, J. Alloys Compd. 688 (2016) 626-636.

[183] J.-P. Kruth, B. Vandenbroucke, J. Van Vaerenbergh, I. Naert, Rapid manufacturing of dental prostheses by means of selective laser sintering/melting, Proceedings of the AFPR S4 (2005) 176-186.

[184] P. Hanzl, M. Zetek, T. Bakša, T. Kroupa, The influence of processing parameters on the mechanical properties of SLM parts. Procedia Eng.100 (2015) 1405-1413.

[185] D. Wang, Di, Y.Q. Yang, X.B. Su, Y.H. Chen, Study on energy input and its influences on single-track, multi-track, and multi-layer in SLM, Int. J. Adv. Manuf. Technol. 58 (2012) 1189-1199.

[186] Y.J. Lu, S.Q. Wu, Y.L. Gan, T.T. Huang, C.G. Yang, J.J. Lin, J.X. Lin, Study on the microstructure, mechanical property and residual stress of SLM Inconel-718 alloy manufactured by differing island scanning strategy, Opt. Laser Technol. 75 (2015) 197-206.

[187] L.N. Carter, C. Martin, P.J. Withers, M.M. Attallah, The influence of the laser scan strategy on grain structure and cracking behaviour in SLM powder-bed fabricated nickel superalloy, J. Alloys Compd. 615 (2014) 338-347.

[188] F. Geiger, K. Kunze, T. Etter, Tailoring the texture of IN738LC processed by selective laser melting (SLM) by specific scanning strategies, Mater. Sci. Eng. A 661 (2016) 240-246.

[189] B. Cheng, S. Shrestha, K. Chou. Stress and deformation evaluations of scanning strategy effect in selective laser melting, Addit. Manuf. 12 (2016) 240-251.

[190] R. Rashid, S.H. Masood, D. Ruan, S. Palanisamy, R.A.R. Rashid, M. Brandt, Effect of scan strategy on density and metallurgical properties of 17-4PH parts printed by Selective Laser Melting (SLM), J. Mater. Process. Tech. 249 (2017) 502-511.

[191] K.G. Prashanth, S. Scudino, J. Eckert, Defining the tensile properties of Al-12Si parts produced by selective laser melting, Acta Mater. 126 (2017) 25-35.

[192] A.G. Demir, B. Previtali, Investigation of remelting and preheating in SLM of 18Ni300 maraging steel as corrective and preventive measures for porosity reduction, Int. J. Adv. Manuf. Technol. 93 (2017) 2697-2709.

[193] L. Pantělejev, D. Koutný, D. Paloušek, J. Kaiser. Mechanical and Microstructural Properties of 2618 Al-Alloy Processed by SLM Remelting Strategy, Mater. Sci. Forum 891 (2017) 343-349.

[194] J. Vaithilingam, R.D. Goodridge, R.J. Hague, S.D.R. Christie, S. Edmondson, The effect of laser remelting on the surface chemistry of Ti6al4V components fabricated by selective laser melting, J. Mater. Process. Tech. 232 (2016) 1-8.

[195] J.P. Kruth, J. Deckers, E. Yasa. Experimental investigation of laser surface remelting for the improvement of selective laser melting process, Solid Freeform Fabrication Symposium (2008) 321-332.

[196] R.E. Russo, Laser ablation, Appl. Spectrosc. 49 (1995) 14A-28A.

[197] Y.L. Li, D.D. Gu, Parametric analysis of thermal behavior during selective laser melting additive manufacturing of aluminum alloy powder, Mater. Des.63 (2014) 856-867.

[198] S. Pauly, P. Wang, U. Kühn, K. Kosiba, Experimental determination of cooling rates in selectively laser-melted eutectic Al-33Cu, Addit. Manuf. 22 (2018) 753-757.

[199] D.H. Dai, D.D. Gu, Influence of thermodynamics within molten pool on migration and distribution state of reinforcement during selective laser melting of AlN/AlSi10Mg composites, Int. J. Mach. Tools Manuf. 100 (2016) 14-24.

[200] S. Pauly, L. Löber, R. Petters, M. Stoica, S. Scudino, U. Kühn, J. Eckert, Processing metallic glasses by selective laser melting, Mater. Today. 16 (2013) 37-41.

[201] Q. Lei, B.P. Ramakrishnan, S.J. Wang, Y.C. Wang, J. Mazumder, A. Misra, Structural refinement and nanomechanical response of laser remelted Al-Al_2Cu lamellar eutectic, Mater. Sci. Eng. A 706 (2017) 115-125.

[202] D.H. Dai, D.D. Gu, R. Poprawe, M.J. Xia, Influence of additive multilayer feature on thermodynamics, stress and microstructure development during laser 3D printing of aluminum-based material, Sci. Bull. 62 (2017) 779-787.

[203] Y.J. Liu, Z. Liu, Y. Jiang, G.W. Wang, Y. Yang, L.C. Zhang, Gradient in microstructure and mechanical property of selective laser melted AlSi10Mg, J. Alloys Compd. 735 (2018) 1414-1421.

[204] H. Rao, S. Giet, K. Yang, X.H. Wu, C.H.J. Davies, The influence of processing parameters on aluminium alloy A357 manufactured by Selective Laser Melting, Mater. Des.109 (2016) 334-346.

[205] S.N. Cao, D.D. Gu, Q.M. Shi, Relation of microstructure, microhardness and underlying thermodynamics in molten pools of laser melting deposition processed TiC/Inconel 625 composites, J. Alloys Compd. 692 (2017) 758-769.

[206] T. Mukherjee, W. Zhang, T. DebRoy, An improved prediction of residual stresses and distortion in additive manufacturing, Comp. Mater. Sci. 126 (2017) 360-372.

[207] P. Wang, L. Deng, K.G. Prashanth, S. Pauly, J. Eckert, S. Scudino, Microstructure and mechanical properties of Al-Cu alloys fabricated by selective laser melting of powder mixtures, J. Alloys Compd. 735 (2018) 2263-2266.

[208] A. Zinoviev, O. Zinovieva, V. Ploshikhin, V. Romanova, R. Balokhonov, Evolution of grain structure during laser additive manufacturing. Simulation by a cellular automata method, Mater. Des.106 (2016) 321-329.

[209] P. Laakso, T. Riipinen, A. Laukkanen, T. Andersson, A. Jokinen, A. Revuelta, K. Ruusuvuori, Optimization and simulation of SLM process for high density H13 tool steel parts, Physics Procedia 83 (2016) 26-35.

[210] Y.L. Li, D. Gu, Thermal behavior during selective laser melting of commercially pure titanium powder: Numerical simulation and experimental study, Addit. Manuf. 1 (2014) 99-109.

[211] L.E. Loh, C.K. Chua, W.Y. Yeong, J. Song, M. Mapar, S.L. Sing, Z.H. Liu, D.Q. Zhang, Numerical investigation and an effective modelling on the Selective Laser Melting (SLM) process with aluminium alloy 6061, Int. J. Heat Mass. Tran. 80 (2015) 288-300.

[212] K.H. Leitz, P. Singer, A. Plankensteiner, B. Tabernig, H. Kestler, L.S. Sigl, Multi-physical simulation of selective laser melting, Met. Powder Rep. 72 (2017) 331-338.

[213] M. Masoomi, S.M. Thompson, N. Shamsaei, A. Elwany, L. Bian. An experimental-numerical investigation of heat transfer during selective laser melting. International Solid Freeform Fabrication Symposium (2015).1-14.

[214] L. Van Belle, G. Vansteenkiste, J.C. Boyer. Comparisons of numerical modelling of the Selective Laser Melting. Key Eng Mater, 504 (2012) 1067-1072.

[215] C. Tang, J.L. Tan, C.H. Wong, A numerical investigation on the physical mechanisms of single track defects in selective laser melting, Int. J. Heat Mass. Tran. 126 (2018) 957-968.

[216] A. Gebhardt, M. Fateri, J.S. Hötter, M. Knothe, F.M. Schmidt, H. Rieper. Numerical and experimental investigation of selective laser melting of silver. Fraunhofer Direct Digital Manufacturing Conference (DDMC) 2012.

[217] D. Ouyang, N. Li, L. Liu, Structural heterogeneity in 3D printed Zr-based bulk metallic glass by selective laser melting, J. Alloys Compd. 740 (2018) 603-609.

[218] H. Attar, L. Löber, A. Funk, M. Calin, L.C. Zhang, K.G. Prashanth, S. Scudino, Y.S. Zhang, J. Eckert, Mechanical behavior of porous commercially pure Ti and Ti-TiB composite materials manufactured by selective laser melting, Mater. Sci. Eng. A 625 (2015) 350-356.

[219] X.P. Li, M.P. Roberts, S. O'Keeffe, T.B. Sercombe, Selective laser melting of Zr-based bulk metallic glasses: Processing, microstructure and mechanical properties, Mater. Des. 112 (2016) 217-226.

[220] S. Pauly, C. Schricker, S. Scudino, L. Deng, U. Kühn, Processing a glass-forming Zr-based alloy by selective laser melting, Mater. Des. 135 (2017) 133-141.

[221] N. Li, J.J. Zhang, W. Xing, D. Ouyang, L. Liu, 3D printing of Fe-based bulk metallic glass composites with combined high strength and fracture toughness, Mater. Des. 143 (2018) 285-296.

[222] P. Bordeenithikasem, M. Stolpe, A. Elsen, D.C. Hofmann, Glass forming ability, flexural strength, and wear properties of additively manufactured Zr-based bulk metallic glasses produced through laser powder bed fusion, Addit. Manuf. 21 (2018) 312-317.

[223] X. Lin, Y.Y. Zhang, G.L. Yang, X.H. Gao, Q. Hu, J. Yu, L. Wei, W.D. Huang, Microstructure and compressive/tensile characteristic of large size Zr-based bulk metallic glass prepared by laser solid forming, J. Mater. Sci. Technol. 35 (2019) 328-335.

[224] D.C. Hofmann, P. Bordeenithikasem, A. Pate, S.N. Roberts, E. Vogli, Developing processing parameters and characterizing microstructure and properties of an additively manufactured FeCrMoBC metallic glass forming alloy, Adv. Eng. Mater. 20 (2018) 1800433.

[225] X.P. Li, C.W. Kang, H. Huang, L.C. Zhang, T.B. Sercombe, Selective laser melting of an $Al_{86}Ni_6Y_{4.5}Co_2La_{1.5}$ metallic glass: processing, microstructure evolution and mechanical properties, Mater. Sci. Eng. A 606 (2014) 370-379.

[226] G.L. Yang, X. Lin, F.C. Liu, Q. Hu, L. Ma, J.F. Li, W.D. Huang, Laser solid forming Zr-based bulk metallic glass, Intermetallics 22 (2012) 110-115.

[227] H.Y. Jung, S.J. Choi, K.G. Prashanth, M. Stoica, S. Scudino, S. Yi, U. Kühn, D.H. Kim, K.B. Kim, J. Eckert, Fabrication of Fe-based bulk metallic glass by selective laser melting: a parameter study, Mater. Des. 86 (2015) 703-708.

[228] W. Xing, D. Ouyang, N. Li, L. Liu, Insight into micro-cracking in 3D-printed Fe-based BMGs by selective laser melting, Intermetallics 103 (2018) 101-106.

[229] D. Ouyang, W. Xing, N. Li, Y.C. Li, L. Liu, Structural evolutions in 3D-printed Fe-based metallic glass fabricated by selective laser melting, Addit. Manuf. 23 (2018) 246-252.

[230] J.P. Best, J. Ast, B. Li, M. Stolpe, R. Busch, F. Yang, X.P. Li, J. Michler, J.J. Kruzic, Relating fracture toughness to micro-pillar compression response for a laser powder bed additive manufactured bulk metallic glass, Mater. Sci. Eng. A 770 (2020) 138535.

[231] X.Y. Lu, M. Nursulton, Y.L. Du, W.H. Liao, Structural and Mechanical Characteristics of $Cu_{50}Zr_{43}Al_7$ Bulk Metallic Glass Fabricated by Selective Laser Melting, Materials 12 (2019) 775.

[232] X.D. Gao, Z.L. Liu, J.H. Li, E.F. Liu, C.M. Yue, K. Zhao, G. Yang, Selective laser melting of CuZr-based metallic glass composites, Mater. Lett. 259 (2020) 126724.

[233] X.D. Nong, X.L. Zhou, Y.X. Ren, Fabrication and characterization of Fe-based metallic glasses by Selective Laser Melting, Opt. Laser Technol. 109 (2019) 20-26.

[234] Ł. Żrodowski, B. Wysocki, R. Wróblewski, A. Krawczyńska, B. Adamczyk-Cieślak, J. Zdunek, P. Błyskun, J. Ferenc, M. Leonowicz, W. Święszkowski, New approach to amorphization of alloys with low glass forming ability via selective laser melting, J. Alloys Compd. 771 (2019) 769-776.

[235] P.C. Zhang, D. Ouyang, L. Liu, Enhanced mechanical properties of 3D printed Zr-based BMG composite reinforced with of Ta precipitates, J. Alloys Compd. 803 (2019) 476-483.

[236] L. Wang, H. Wang, Y.K. Liu, Z.X. Fu, T.J. Peng, J. Shen, S.Y. Zhou, M. Yan, G. Wang, Y.H. Dai, Selective laser melting helps fabricate record-large bulk metallic glass: Experiments, simulation and demonstrative part, J. Alloys Compd. 808 (2019) 151731.

[237] Y.G. Nam, B. Koo, M.S. Chang, S.S. Yang, J.H. Yu, Y.H. Park, J.W. Jeong, Selective laser melting vitrification of amorphous soft magnetic alloys with help of double-scanning-induced compositional homogeneity, Mater. Lett. (2019) 127068.

[238] X.H. Gao, X. Lin, J. Yu, Y.L. Li, Y.L. Hu, W. Fan, S.Q. Shi, W.D. Huang, Selective Laser Melting (SLM) of in-situ beta phase reinforced Ti/Zr-based bulk metallic glass matrix composite, Scr. Mater. 171 (2019) 21-25.

[239] C. Zhang, X.M. Li, S.Q. Liu, H. Liu, L.J. Yu, L. Liu, 3D printing of Zr-based bulk metallic glasses and components for potential biomedical applications, J. Alloys Compd. 790 (2019) 963-973.

[240] V. Molokanov, M. Petrzhik, T. Mikhailova, T. Sviridova, N. Djakonova, Formation of bulk (Zr, Ti)-based metallic glasses, J. Non-cryst. Solids. 250 (1999) 560-565.

[241] X.P. Li, M. Roberts, Y.J. Liu, C.W. Kang, H. Huang, T.B. Sercombe, Effect of substrate temperature on the interface bond between support and substrate during selective laser melting of Al–Ni–Y–Co–La metallic glass, Mater.Des. (1980-2015). 65 (2015) 1-6.

[242] W. Xing, D. Ouyang, N. Li, L. Liu, Estimation of residual stress in selective laser melting of a Zr-based amorphous alloy, Materials 11 (2018) 1480.

[243] P. Mercelis, J.P. Kruth, Residual stresses in selective laser sintering and selective laser melting, Rapid prototyping J. 12 (2006) 254-265.

[244] R. Mertens, S. Dadbakhsh, J. Van Humbeeck, J.P. Kruth, Application of base plate preheating during selective laser melting, Procedia CIRP. 74 (2018) 5-11.

[245] J.P. Best, Z. Evenson, F. Yang, A.C. Dippel, M. Stolpe, O. Gutowski, M.T. Hasib, X.P. Li, J.J. Kruzic, Structural periodicity in laser additive manufactured Zr-based bulk metallic glass, Appl. Phys. Lett. 115 (2019) 031902.

[246] P. Ramasamy, Soft Ferromagnetic Bulk Metallic Glasses with Enhanced Mechanical Properties (2018).

[247] R. Limbach, B.P. Rodrigues, L. Wondraczek, Strain-rate sensitivity of glasses, J. Non-Cryst. Solids 404 (2014) 124-134.

[248] S. Sawamura, R. Limbach, H. Behrens, L. Wondraczek, Lateral deformation and defect resistance of compacted silica glass: Quantification of the scratching hardness of brittle glasses, J. Non-Cryst. Solids 481 (2018) 503-511.

[249] D.H. Dai, D.D. Gu, Thermal behavior and densification mechanism during selective laser melting of copper matrix composites: simulation and experiments. Mater. Des. 55 (2014) 482-491.

[250] M. Geetha, A.K. Singh, R. Asokamani, A.K. Gogia, Ti based biomaterials, the ultimate choice for orthopaedic implants - A review, Prog. Mater. Sci. 54 (2009) 397-425.

[251] M. Long, H.J. Rack, Titanium alloys in total joint replacement - a materials science perspective, Biomater. 19 (1998) 1621-1639.

[252] B. Zberg, P.J. Uggowitzer, J.F. Löffler, MgZnCa glasses without clinically observable hydrogen evolution for biodegradable implants, Nat. Mater. 8 (2009) 887-891.

[253] H.F. Li, Y.F. Zheng, Recent advances in bulk metallic glasses for biomedical applications, Acta Biomater. 36 (2016) 1-20.

[254] L.E. Tanner, R. Ray, Physical properties of $Ti_{50}Be_{40}Zr_{10}$ glass, Scr. Metall. 11 (1977) 783-789.

[255] P. Gong, L. Deng, J.S. Jin, S.B. Wang, X.Y. Wang, K.F. Yao, Review on the Research and Development of Ti-Based Bulk Metallic Glasses, Metals 6 (2016) 264.

[256] L. Zhang, M.Q. Tang, Z.W. Zhu, H.M. Fu, H.W. Zhang, A.M. Wang, H. Li, H.F. Zhang, Z.Q. Hu, Compressive plastic metallic glasses with exceptional glass forming ability in the Ti-Zr-Cu-Fe-Be alloy system, J. Alloys Comp. 638 (2015) 349-355.

[257] S.J. Pang, Y. Liu, H.F. Li, L.L. Sun, Y. Li, T. Zhang, New Ti-based Ti-Cu-Zr-Fe-Sn-Si-Ag bulk metallic glass for biomedical applications, J. Alloys Comp. 625 (2015) 323-327.

[258] K.F. Kelton, W.J. Kim, R.M. Stroud, A stable Ti-based quasicrystal, Appl. Phys. Lett. 70 (1997) 3230-3232.

[259] J.L. Libbert, J.Y. Kim, K.F. Kelton, Oxygen in Ti-(Cr, Mn)-Si icosahedral phases and approximants, Phil. Mag. A 79 (1999) 2209-2225.

[260] P.S. Grant, Spray forming, Progr. Mater. Sci. 39 (1995) 497-545.

[261] P.P. Yuan, D.D. Gu, Molten pool behaviour and its physical mechanism during selective laser melting of TiC/AlSi10Mg nanocomposites: simulation and experiments, J. Phys. D: Appl. Phys. 48 (2015) 035303.

[262] D.D. Gu, W. Meiners, K. Wissenbach, R. Poprawe, Laser additive manufacturing of metallic components: materials, processes and mechanisms, Int. Mater. Rev. 57 (2012) 133-164.

[263] G. Wang, Y.T. Wang, Y.H. Liu, M.X. Pan, D.Q. Zhao, W.H. Wang, Evolution of nanoscale morphology on fracture surface of brittle metallic glass, Appl. Phys. Lett. 89 (2006) 121909.

[264] A. Concustell, F.O. Méar, S. Surinach, M.D. Baró, A.L. Greer, Structural relaxation and rejuvenation in a metallic glass induced by shot-peening, Phil. Mag. Lett. 89 (2009) 831-840.

[265] Y.H. Sun, A. Concustell, A.L. Greer, Thermomechanical processing of metallic glasses: extending the range of the glassy state, Nat. Rev. Mater. 1 (2016) 16039.

[266] A. Van den Beukel, J. Sietsma, The glass transition as a free volume related kinetic phenomenon, Acta Metall. Mater. 38 (1990) 383-389.

[267] T. Egami, Understanding the properties and structure of metallic glasses at the atomic level, JOM 62 (2010) 70-75.

[268] R.M. Srivastava, J. Eckert, W. Löser, B.K. Dhindaw, L. Schultz, Cooling rate evaluation for bulk amorphous alloys from eutectic microstructures in casting processes, Mater. Trans. 43 (2002) 1670-1675.

[269] J.C. Qiao, J.M. Pelletier, Dynamic mechanical relaxation in bulk metallic glasses: a review, J. Mater. Sci. Technol. 30 (2014) 523-545.

[270] R. Limbach, K. Kosiba, S. Pauly, U. Kühn, L. Wondraczek, Serrated flow of CuZr-based bulk metallic glasses probed by nanoindentation: Role of the activation barrier, size and distribution of shear transformation zones, J. Non-cryst. Solids 459 (2017) 130-141.

[271] H. Gleiter, Nanoglasses: a new kind of noncrystalline material and the way to an age of new technologies? Small 12 (2016) 2225-2233.

[272] Z. Śniadecki, D. Wang, Y. Ivanisenko, V. Chakravadhanula, C. Kübel, H. Hahn, H. Gleiter, Nanoscale morphology of $Ni_{50}Ti_{45}Cu_5$ nanoglass, Mater. Charact. 113 (2016) 26-33.

[273] W.H. Liu, B.A. Sun, H. Gleiter, S. Lan, Y. Tong, X.L. Wang, H. Hahn, Y. Yang, J.J. Kai, C.T. Liu, Nanoscale Structural Evolution and Anomalous Mechanical Response of Nanoglasses by Cryogenic Thermal Cycling, Nano Lett. 18 (2018) 4188-4194.

[274] A. Gebert, P. Gostin, L. Schultz, Effect of surface finishing of a Zr-based bulk metallic glass on its corrosion behaviour, Corros. Sci. 52 (2010) 1711-1720.

[275] Z.P. Lu, H. Bei, Y. Wu, G.L. Chen, E.P. George, C.T. Liu, Oxygen effects on plastic deformation of a Zr-based bulk metallic glass, Appl. Phys. Lett. 92 (2008) 011915.

[276] L. He, Z.G. Wu, F. Jiang, J. Sun, Enhanced thermal stability of $Zr_{65}Cu_{17.5}Ni10Al_{7.5}$ metallic glass at temperature range near glass transition by oxygen impurity, J. Alloys Compd. 456 (2008) 181-186.

[277] A.A. Kündig, M. Ohnuma, T. Ohkubo, K. Hono, Early crystallization stages in a Zr-Cu-Ni-Al-Ti metallic glass, Acta Mater. 53 (2005) 2091-2099.

[278] Z.F. Zhang, G. He, J. Eckert, L. Schultz, Fracture mechanisms in bulk metallic glassy materials, Phys. Rev. Lett. 91 (2003) 045505.

[279] A.H. Brothers, D.C. Dunand, Ductile bulk metallic glass foams, Adv. Mater. 17 (2005) 484-486.

[280] F. Shimizu, S. Ogata, J. Li, Yield point of metallic glass, Acta Mater. 54 (2006) 4293-4298.

[281] S.V. Madge, T. Wada, D.V. Louzguine-Luzgin, A.L. Greer, A. Inoue, Oxygen embrittlement in a Cu-Hf-Al bulk metallic glass, Scr. Mater. 61 (2009) 540-543.

[282] Y. Yokoyama, A. Kobayashi, K. Fukaura, A. Inoue, Oxygen embrittlement and effect of the addition of Ni element in a bulk amorphous Zr-Cu-Al alloy, Mater. Trans. 43 (2002) 571-574.

[283] R.D. Conner, R.E. Maire, W.L. Johnson, Effect of oxygen concentration upon the ductility of amorphous $Zr_{57}Nb_5Al_{10}Cu_{15.4}Ni_{12.6}$, Mater. Sci. Eng. A 419 (2006) 148-152.

[284] C.T. Liu, M.F. Chisholm, M.K. Miller, Oxygen impurity and microalloying effect in a Zr-based bulk metallic glass alloy, Intermetallics 10 (2002) 1105-1112.

[285] A. Gebert, J. Eckert, L. Schultz, Effect of oxygen on phase formation and thermal stability of slowly cooled $Zr_{65}Al_{7.5}Cu_{17.5}Ni_{10}$ metallic glass, Acta Mater. 46 (1998) 5475-5482.

[286] K. Kajiwara, M. Ohnuma, T. Ohkubo, D.H. Ping, K. Hono, APFIM/TEM/SAXS studies of early stage crystallization of a $Zr_{52.5}Cu_{17.9}Ni_{14.6}Al_{10}Ti_5$ metallic glass, Mater. Sci. Eng. A 375 (2004) 738-743.

[287] M. Baricco, S. Spriano, I. Chang, M.I. Petrzhik, L. Battezzati, "Big cube" phase formation in Zr-based metallic glasses, Mater. Sci. Eng. A 304 (2001) 305-310.

[288] V. Keryvin, C. Bernard, J.C. Sangleboeuf, Y. Yokoyama, T. Rouxel, Toughness of $Zr_{55}Cu_{30}Al_{10}Ni_5$ bulk metallic glass for two oxygen levels, J. Non-cryst. Solids 352 (2006) 2863-2868.

[289] Z.J. Ma, S.B. Lei, T.L. Yeung, P. Wang, Y.C. Guo, Z. Yang, J.P. Li, P.H. Gao, Plasticity Improvement of Zr-Based Bulk Metallic Glasses by Adjusting Oxygen Content and Cooling Rate, Mater. Trans. 58 (2017) 423-426.

[290] F. Qiu, Y.Y. Liu, R.F. Guo, Z.H. Bai, Q.C. Jiang, Effect of oxygen content on the microstructure, compression properties and work-hardening behaviors of ZrCuAlNi glassy composites, Mater. Sci. Eng. A 580 (2013) 13-20.

[291] P.S. Babu, D.S. Rao, L.R. Krishna, G. Sundararajan, Weibull analysis of hardness distribution in detonation sprayed nano-structured WC-12Co coatings, Surf Coat Technol. 319 (2017) 394-402.

[292] F.F. Csikor, C. Motz, D. Weygand, M. Zaiser, S. Zapperi, Dislocation avalanches, strain bursts, and the problem of plastic forming at the micrometer scale, Science 318 (2007) 251-254.

[293] J.M. Carlson, J.S. Langer, Properties of earthquakes generated by fault dynamics, Phys. Rev. Lett. 62 (1989) 2632.

[294] G. Wang, K.C. Chan, L. Xia, P. Yu, J. Shen, W.H. Wang, Self-organized intermittent plastic flow in bulk metallic glasses, Acta Mater. 57 (2009) 6146-6155.

[295] S. Scudino, K.B. Surreddi, G. Wang, G. Liu, Effect of stress concentration on plastic deformation of $Zr_{41.2}Ti_{13.8}Cu_{12.5}Ni_{10}Be_{22.5}$ bulk metallic glass under compressive loading, Mater. Lett. 179 (2016) 202-205.

[296] M. Stolpe, J.J. Kruzic, R. Busch, Evolution of shear bands, free volume and hardness during cold rolling of a Zr-based bulk metallic glass, Acta Mater. 64 (2014) 231-240.

[297] S. Scudino, J.J. Bian, H.S. Shahabi, D. Şopu, J. Sort, J. Eckert, G. Liu, Ductile bulk metallic glass by controlling structural heterogeneities, Sci. Rep. 8 (2018) 9174.

[298] H. Wagner, D. Bedorf, S. Küchemann, M. Schwabe, B. Zhang, W. Arnold, K. Samwer, Local elastic properties of a metallic glass, Nat. Mater. 10 (2011) 439-442.

[299] K.B. Kim, J. Das, F. Baier, M.B. Tang, W.H. Wang, J. Eckert, Heterogeneity of a $Cu_{47.5}Zr_{47.5}Al_5$ bulk metallic glass, Appl. Phys. Lett. 88 (2006) 051911.

[300] H. Wu, I. Baker, Y. Liu, X.L. Wu, P.R. Munroe, J.G. Zhang, Tribological studies of a Zr-based bulk metallic glass, Intermetallics 35 (2013) 25-32.

[301] S.M. Gravano, S. Torchio, F. Mazza, E. Angelini, M. Baricco, The effects of quenching conditions on the electrochemical behaviour of $Fe_{34}Ni_{36}Cr_{10}P_{14}B_6$ amorphous alloys, Corros. Sci. 33 (1992) 1227-1241.

[302] R.S. Dutta, G.K. Dey, Effects of partial crystallinity and quenched-in defects on corrosion of a rapidly solidified Ti-Cu alloy, Bull. Mater. Sci. 26 (2003) 477-482.

[303] X.P. Nie, X.H. Yang, L.Y. Chen, K.B. Yeap, K.Y. Zeng, D. Li, J.S. Pan, X.D. Wang, Q.P. Cao, S.Q. Ding, J.Z. Jiang, The effect of oxidation on the corrosion resistance and mechanical properties of a Zr-based metallic glass, Corros. Sci. 53 (2011) 3557-3565.

[304] E. McCafferty, Validation of corrosion rates measured by the Tafel extrapolation method, Corros. Sci. 47 (2005) 3202-3215.

[305] M. Rombouts, L. Froyen, A.V. Gusarov, E.H. Bentefour, C. Glorieux, Light extinction in metallic powder beds: Correlation with powder structure, J. Appl. Phys. 98 (2005) 013533.

[306] L. Deng, S.H. Wang, P. Wang, U. Kühn, S. Pauly, Selective laser melting of a Ti-based bulk metallic glass, Mater. Lett. 212 (2018) 346-349.

[307] C.C. Hays, C.P. Kim, W.L. Johnson, Microstructure controlled shear band pattern formation and enhanced plasticity of bulk metallic glasses containing in situ formed ductile phase dendrite dispersions, Phys. Rev. Lett. 84 (2000) 2901.

[308] S.Y. Lee, C.P. Kim, J.D. Almer, U. Lienert, E. Ustundag, W.L. Johnson, Pseudo-binary phase diagram for Zr-based in situ β phase composites, J. Mater. Res. 22 (2007) 538-543.

[309] D.C. Hofmann, J.Y. Suh, A. Wiest, M.L. Lind, M.D. Demetriou, W.L. Johnson, Development of tough, low-density titanium-based bulk metallic glass matrix composites with tensile ductility, PNAS 105 (2008) 20136-20140.

[310] L. Zhang, S. Pauly, M.Q. Tang, J. Eckert, H.F. Zhang, Two-phase quasi-equilibrium in β-type Ti-based bulk metallic glass composites, Sci. Rep. 6 (2016) 19235.

[311] U. Kühn, J. Eckert, N. Mattern, L. Schultz, Microstructure and mechanical properties of slowly cooled Zr-Nb-Cu-Ni-Al composites with ductile bcc phase, Mater. Sci. Eng. A 375 (2004) 322-326.

[312] P. Gargarella, S. Pauly, M. Stoica, G. Vaughan, C. M. Afonso, U. Kühn, J. Eckert, Structural evolution in Ti-Cu-Ni metallic glasses during heating, APL materials 3 (2015) 016101.

[313] L. Zhang, H.F. Zhang, W.Q. Li, T. Gemming, P. Wang, M. Bönisch, D. Şopu, J. Eckert, S. Pauly, β-type Ti-based bulk metallic glass composites with tailored structural metastability, J. Alloys Compd. 708 (2017) 972-981.

[314] L. Zhang, H.M. Fu, H. Li, Z.W. Zhu, H.W. Zhang, W.R. Li, Y.D. Li, H.F. Zhang, Developing β-type bulk metallic glass composites from Ti/Zr-based bulk metallic glasses by an iteration method, J. Alloys Compd. 740 (2018) 639-646.

[315] X.L. Wang, J. Almer, C.T. Liu, Y.D. Wang, J.K. Zhao, A.D. Stoica, D.R. Haeffner, W.H. Wang, In situ synchrotron study of phase transformation behaviors in bulk metallic glass by simultaneous diffraction and small angle scattering, Phys. Rev. Lett. 91 (2003) 265501.

[316] G. He, Z. Bian, G.L. Chen, Structures and properties of a Zr-based bulk glass alloy after annealing, Mater. Sci. Eng. A 270 (1999) 291-298.

[317] S. Mukherjee, Z. Zhou, J. Schroers, W.L. Johnson, W.K. Rhim, Overheating threshold and its effect on time-temperature-transformation diagrams of zirconium based bulk metallic glasses, Appl. Phys. Lett. 84 (2004) 5010-5012.

[318] S.C. Glade, R. Busch, D.S. Lee, W.L. Johnson, R.K. Wunderlich, H.J. Fecht, Thermodynamics of $Cu_{47}Ti_{34}Zr_{11}Ni_{8}$, $Zr_{52.5}Cu_{17.9}Ni_{14.6}Al_{10}Ti_{5}$ and $Zr_{57}Cu_{15.4}Ni_{12.6}Al_{10}Nb_{5}$ bulk metallic glass forming alloys, J. Appl. Phys. 87 (2000) 7242-7248.

[319] F. Li, J.S. Lannin, Radial distribution function of amorphous carbon, Phys. Rev. Lett. 65 (1990) 1905.

[320] J. Fortner, J.S. Lannin, Radial distribution functions of amorphous silicon, Phys. Rev. B. 39 (1989) 5527.

[321] K. Younge, C. Christenson, A. Bohara, J. Crnkovic, P. Saulnier, A model system for examining the radial distribution function, Am. J. Phys. 72 (2004) 1247-1250.

[322] A. Takeuchi, A. Inoue, Calculations of mixing enthalpy and mismatch entropy for ternary amorphous alloys, Mater. Trans. JIM 41 (2000) 1372-1378.

[323] D.C. Hofmann, H. Kozachkov, H.E. Khalifa, J.P. Schramm, M.D. Demetriou, K.S. Vecchio, W.L. Johnson, Semi-solid induction forging of metallic glass matrix composites, JOM 61 (2009) 11.

[324] R. Piotrkowski, F. Dyment, Nb^{95} and Ni^{63} diffusion along the $\alpha_{|}^{|}$ β interphase boundaries of A Zr-2.5 wt% Nb alloy, J. Nucl. Mater. 137 (1986) 94-99.

[325] C. Herzig, U. Köhler, S. Divinski, Tracer diffusion and mechanism of non-Arrhenius diffusion behavior of Zr and Nb in body-centered cubic Zr-Nb alloys, J. Appl. Phys. 85 (1999) 8119-8130.

[326] J.T. Fan, Z.F. Zhang, F. Jiang, J. Sun, S.X. Mao, Ductile to brittle transition of $Cu_{46}Zr_{47}Al_7$ metallic glass composites, Mater. Sci. Eng. A 487 (2008) 144-151.

[327] Y.F. Sun, S.K. Guan, B.C. Wei, Y.R. Wang, C.H. Shek, Brittleness of Zr-based bulk metallic glass matrix composites containing ductile dendritic phase, Mater. Sci. Eng. A 406 (2005) 57-62.

[328] S. Pauly, S. Gorantla, G. Wang, U. Kühn, J. Eckert, Transformation-mediated ductility in CuZr-based bulk metallic glasses, Nat. Mater. 9 (2010) 473.

[329] Y.J. Liu, H.W. Yao, T.W. Zhang, Z. Wang, Y.S. Wang, J.W. Qiao, H.J. Yang, Z.H. Wang, Designing ductile CuZr-based metallic glass matrix composites, Mater. Sci. Eng. A 682 (2017) 542-549.

[330] B. Escher, U. Kühn, J. Eckert, C. Rentenberger, S. Pauly, Influence of Ag and Co additions on glass-forming ability, thermal and mechanical properties of Cu-Zr-Al bulk metallic glasses, Mater. Sci. Eng. A 673 (2016) 90-98.

[331] Y.S. Qin, X.L. Han, K.K. Song, L. Wang, Y. Cheng, Z.Q. Zhang, Q.S. Xue, N.Z. Sun, J.G. Wang, B.A. Sun, B. Sarac, F. Spieckermann, G. Wang, I. Kaban, J. Eckert, Stability of shear banding process in bulk metallic glasses and composites, J. Mater. Res. 32 (2017) 2560-2569.

[332] Y. Zhang, N. Mattern, J. Eckert, Study of structural anisotropy in $Cu_{50}Zr_{45}Al_5$ metallic glass under uniaxial compression by molecular dynamics simulations, Intermetallics 30 (2012) 154-157.

[333] J.C. Qiao, S.D. Feng, J.M. Pelletier, D. Crespo, E. Pineda, Y. Yao, Physical aging effects on the dynamic relaxation behavior and mechanical properties of $Cu_{46}Zr_{46}Al_8$ metallic glass, J. Alloys Compd. 726 (2017) 195-200.

Publications

1. **L. Deng**, S. Wang, P. Wang, U. Kühn, S. Pauly, Selective laser melting of a Ti-based bulk metallic glass, Materials Letters 212(2018)346-349.

2. **L. Deng**, A. Gebert, L. Zhang, H.Y. Chen, D.D. Gu, U. Kühn, M. Zimmermann, K. Kosiba, S. Pauly, Mechanical performance and corrosion behaviour of Zr-based bulk metallic glass produced by selective laser melting, Materials & Design 189(2020)108532.

3. P. Wang, **L. Deng**, K.G. Prashanth, S. Pauly, J. Eckert, S. Scudino, Microstructure and mechanical properties of Al-Cu alloys fabricated by selective laser melting of powder mixtures, Journal of Alloys and Compounds 735(2018)2263-2266.

4. B. Sarac, C. Gammer, **L. Deng**, E. Park, Y. Yokoyama, M. Stoica, J. Eckert, Elastostatic reversibility in thermally formed bulk metallic glasses: nanobeam diffraction fluctuation electron microscopy, Nanoscale 10(2018)1081-1089.

5. S. Pauly, C. Schricker, S. Scudino, **L. Deng**, U. Kühn, Processing a glass-forming Zr-based alloy by selective laser melting, Materials & Design 135(2017)133-141.

Eidesstattliche Erklärung

Hiermit versichere ich, dass ich die vorliegende Arbeit ohne unzulässige Hilfe Dritter und ohne Benutzung anderer als der angegebenen Hilfsmittel angefertigt habe; die aus fremden Quellen direkt oder indirekt übernommenen Gedanken sind als solche kenntlich gemacht. Bei der Auswahl und Auswertung des Materials sowie bei der Herstellung des Manuskripts habe ich Unterstützungsleistungen von folgenden Personen erhalten: Prof. Dr.-Ing. M. Zimmermann und Prof. Dr. S. Pauly. Weitere Personen waren an der geistigen Herstellung der vorliegenden Arbeit nicht beteiligt. Insbesondere habe ich nicht die Hilfe eines kommerziellen Promotionsberaters in Anspruch genommen. Dritte haben von mir keine geldwerten Leistungen für Arbeiten erhalten, die in Zusammenhang mit dem Inhalt der vorgelegten Dissertation stehen. Die Arbeit wurde bisher weder im Inland noch im Ausland in gleicher oder ähnlicher Form einer anderen Prüfungsbehörde vorgelegt und ist auch noch nicht veröffentlicht worden. Die Dissertation wurde an der TU Dresden am Institut für Werkstoffwissenschaft der Fakultät Maschinenwesen unter der wissenschaftlichen Betreuung von Prof. Dr.-Ing. M. Zimmermann angefertigt. Die Promotionsordnung der Fakultät Maschinenwesen der TU Dresden aus dem Jahre 2001 erkenne ich an.

M.Eng. Liang Deng